

# Printed Organic Thin Film Transistors, Photodiodes, and Phototransistors for Sensing and Imaging

*Adrien Pierre*



Electrical Engineering and Computer Sciences  
University of California at Berkeley

Technical Report No. UCB/EECS-2017-180

<http://www2.eecs.berkeley.edu/Pubs/TechRpts/2017/EECS-2017-180.html>

December 1, 2017

Copyright © 2017, by the author(s).  
All rights reserved.

Permission to make digital or hard copies of all or part of this work for personal or classroom use is granted without fee provided that copies are not made or distributed for profit or commercial advantage and that copies bear this notice and the full citation on the first page. To copy otherwise, to republish, to post on servers or to redistribute to lists, requires prior specific permission.

**Printed Organic Thin Film Transistors, Photodiodes, and Phototransistors for  
Sensing and Imaging**

by

Adrien Pierre

A dissertation submitted in partial satisfaction of the  
requirements for the degree of

Doctor of Philosophy

in

Engineering - Electrical Engineering & Computer Sciences

in the

Graduate Division

of the

University of California, Berkeley

Committee in charge:

Professor Ana Claudia Arias, Chair

Professor Vivek Subramanian

Professor Paul K. Wright

Fall 2016

The dissertation of Adrien Pierre, titled Printed Organic Thin Film Transistors, Photodiodes, and Phototransistors for Sensing and Imaging, is approved:

Chair	_____	Date	_____
	_____	Date	_____
	_____	Date	_____

University of California, Berkeley



**Printed Organic Thin Film Transistors, Photodiodes, and Phototransistors for  
Sensing and Imaging**

Copyright 2016  
by  
Adrien Pierre

## Abstract

Printed Organic Thin Film Transistors, Photodiodes, and Phototransistors for Sensing and Imaging

by

Adrien Pierre

Doctor of Philosophy in Engineering - Electrical Engineering & Computer Sciences

University of California, Berkeley

Professor Ana Claudia Arias, Chair

Light and image sensors are ubiquitous and used in a wide variety of applications ranging from consumer products to healthcare and industrial applications. The signal-to-noise ratio (SNR) from a photodetector element increases with larger photoactive area, which is costly to scale up using silicon wafers and wafer-based microfabrication. On the other hand, the performance of solution-processed photodetectors and transistors is advancing considerably. It is proposed that the printability of these devices on plastic substrates can enable low-cost areal scaling for high SNR light and image sensors.

This thesis advances the performance of printed organic thin film transistor (OTFT), photodiode (OPD), and phototransistor (OPT) devices optimized for light and image sensing applications by developing novel printing techniques and creating new device architectures. An overview is first given on the essential figures of merit for each of these devices and the state of the art in solution-processed image sensors. A novel surface energy-patterned doctor blade coating technique is presented to fabricate OTFTs on flexible substrates over large areas. Using this technique, OTFTs with average mobility and on-off ratios of  $0.6 \text{ cm}^2/\text{Vs}$  and  $10^5$  are achieved, which is competitive with amorphous silicon TFTs. High performance OPDs are also fabricated using doctor blade coating and screen printing. These printing processes give high device yield and good controllability of photodetector performance, enabling an average specific detectivity of  $3.45 \times 10^{13} \text{ cm} \cdot \text{Hz}^{0.5} \cdot \text{W}^{-1}$  that is higher than silicon photodiodes ( $10^{12-13}$ ). Finally, organic charge-coupled devices (OCCDs) and a novel OPT device architecture based on an organic heterojunction between a donor-acceptor bulk heterojunction blend and a high mobility semiconductor that allows for a wide absorption spectrum and fast charge transport are discussed. The OPT devices not only exhibit high transistor and photodetector performance, but are also able to integrate photogenerated charge at video frame rates up to 100 frames per second with external quantum efficiencies above 100%. Applications of these devices include screen printed OTFT backplanes, large-area OPDs for pulse oximeter applications, and OPT-based image sensors.

To Grandma & Lena  
Who brought me joy in what I do

# Contents

<b>Contents</b>	<b>ii</b>
<b>List of Figures</b>	<b>iv</b>
<b>List of Tables</b>	<b>xiv</b>
<b>1 Introduction</b>	<b>1</b>
1.1 Introduction . . . . .	1
1.2 Fundamental Operation Principles of Image Sensors . . . . .	2
1.3 Thin Film Transistors & Photodetectors . . . . .	6
1.4 Passive Pixel Image Sensors without Charge Integration . . . . .	18
1.5 Passive Pixel Image Sensors Capable of Charge Integration . . . . .	22
1.6 Fabrication Techniques . . . . .	29
1.7 Thesis Outline . . . . .	32
<b>2 Printed Organic Thin Film Transistors</b>	<b>34</b>
2.1 Introduction . . . . .	34
2.2 Doctor Blade Coating & Device Process Flow . . . . .	35
2.3 Source-Drain Electrode Optimization . . . . .	41
2.4 Semiconductor Optimization . . . . .	44
2.5 Dielectric Optimization . . . . .	53
2.6 OTFT Array Performance & Reliability . . . . .	54
2.7 Conclusion . . . . .	56
<b>3 Printed Organic Photodiodes</b>	<b>58</b>
3.1 Introduction . . . . .	58
3.2 Cathode Design . . . . .	63
3.3 Active Layer Design . . . . .	66
3.4 Anode Design . . . . .	68
3.5 Performance & Reliability . . . . .	71
3.6 Conclusion . . . . .	79
<b>4 Organic Charge-coupled Devices &amp; Charge-integrating Phototransistors</b>	<b>80</b>

4.1	Introduction . . . . .	80
4.2	Organic Charge-coupled Devices . . . . .	80
4.3	Organic Phototransistors . . . . .	87
4.4	Conclusion . . . . .	100
<b>5</b>	<b>Printed Interconnects &amp; Devices for Sensing &amp; Imaging Applications</b>	<b>101</b>
5.1	Introduction . . . . .	101
5.2	Integration of Organic Photodiodes for Applications in Pulse Oximetry . . .	102
5.3	Addressable Organic Thin Film Transistors & Phototransistor Arrays for Im- age Sensing . . . . .	116
5.4	Conclusion . . . . .	123
<b>6</b>	<b>Conclusion &amp; Future Work</b>	<b>124</b>
	<b>Bibliography</b>	<b>128</b>

# List of Figures

1.1	(a) Schematic view of an image sensor depicting the flow of photogenerated charge from charge integration in the pixel (step 1), to discharging in the column for either passive or active pixels (step 2), and finally readout from external circuits sensing voltage, charge, or current (step 3). (b) Rolling shutter addressing and readout scheme. (c) Global shutter addressing and readout scheme. . . . .	4
1.2	Upper and lower bounds on the dynamic range of a photogenerated signal starting from generation in the photodetector, to storage in the pixel, and finally readout on the column line after discharge from the pixel. . . . .	5
1.3	(a) Operation and biasing of TFTs with n- and p-type semiconductors. (b) Figures of merit and carrier behavior in transfer characteristic sweep (constant $V_{DS}$ , changing $V_{GS}$ ) for a p-type TFT. (c) Figures of merit and carrier behavior in output characteristic sweep (constant $V_{GS}$ , changing $V_{DS}$ ) for a p-type TFT. . . . .	7
1.4	(a) Band diagram of an organic photodiode depicting charge generation and collection and the equivalent circuit. (b) Qualitative depiction of external quantum efficiency (EQE) and responsivity ( $R$ ) for a photodetector. (c) Typical photodiode current-voltage characteristics in dark and under illumination. (d) Illustration of dynamic range for a photodetector. . . . .	9
1.5	(a) Organic blocking layers in a Perovskite photodiode and its dynamic response. (b) Filterless organic photodiodes enabled through thick active layers and the resulting EQE spectrum. Reprinted with permission from [6]. Copyright 2015 Nature Publishing Group. (c) Detectivity as a function of applied field across the device for various photodiodes cited in this review along with the bias stress stability of an organic photodiode. (a) and (c) Reprinted with permission from [41] and [137], respectively. Copyright 2015 John Wiley and Sons. . . . .	13
1.6	(a) Hole (red) and electron (yellow) movement in a hole-transporting phototransistor with photoconductive gain and the dynamic response shown to the right. (b) Charge carrier movement in the same phototransistor but operating in a long-term charge-trapping regime. . . . .	15

1.7	(a) Interfacial trapping of photogenerated carriers used to inject charge from an electrode as a gain mechanism. Reprinted with permission from [55]. Copyright 2012 Nature Publishing Group. (b) Broadband bulk heterojunction phototransistor. Reprinted with permission from [59]. Copyright 2015 Nature Publishing Group. (c) Fabrication steps for an all-printed phototransistor. Reprinted with permission from [87]. Copyright 2014 Elsevier. . . . .	17
1.8	(a) Photodiode and (b) phototransistor-based passive pixel architecture for image sensors not using intra-pixel charge integration. . . . .	18
1.9	(a) Reproduced color image scanned by a linear array of organic photodiodes. Reprinted with permission from [189]. Copyright 1999 John Wiley and Sons. (b) An array of phototransistors based on charge transfer to a semiconductor from a light-absorbing dye. Reprinted with permission from [112]. Copyright 2016 American Chemical Society. (c) Light-programmable organic phototransistor memory devices and an imaging array. Reprinted with permission from [194]. Copyright 2013 Nature Publishing Group. . . . .	20
1.10	(a) 1T pixel architecture, a charge-integrating passive pixel, showing the integrating capacitor of the photodiode ( $C_{PD}$ ) and parasitic capacitances. (b) Drive voltage ( $V_G$ ), photodiode node voltage ( $V_{PD}$ ), and charge on the column line ( $Q_C$ ) during pixel operation with parasitic effects. . . . .	24
1.11	(a) Monolithic integration of an organic thin film transistor (TFT) and organic photodiode (OPD) to form a 1T pixel along with the dynamic response. Reprinted with permission from [172]. Copyright 2011 Elsevier. (b) Flexible organic photodiode-carbon nanotube TFT 1T image sensor. Reprinted with permission from [168]. Copyright 2013 American Chemical Society. (c) Top-illuminated spray-coated organic photodiodes on top of a CMOS chip to form a hybrid image sensor. Reprinted with permission from [11]. Copyright 2012 Nature Publishing Group. . . . .	26
1.12	(a) Inkjet printing process for a continuous line. (b) Blade coating technique showing ink dispensing followed by coating. (c) Screen printing process depicting flooding of the ink over the screen followed by transfer of the ink through openings in the screen onto a substrate. . . . .	32
2.1	Doctor blade coating process (a) and the movement and rupture of fluid on a surface energy-patterned surface (b) (Reprinted with permission from [111]. Copyright 1997 Springer.). The contact angles of water measured on various SAMs (c) showing the liquid (L), gas (G), and solid (S) interface energy interactions on a droplet. . . . .	36
2.2	The surface energy-patterned doctor blade coating process flow on a substrate (a) and tunable printing parameters (b). . . . .	38
2.3	Process flow for all-printed OTFT arrays on flexible plastic substrates. . . . .	40
2.4	The surface energy-patterned inkjet printing process for the gate electrode (a) and the final architecture of the OTFT device (b). . . . .	40

2.5	SEP source-drain electrode yield as a function of dimensions (a) for as-received ink (b) and optimized ink (c). The profile of a 30 $\mu\text{m}$ $L$ channel with 100 $\mu\text{m}$ LW is measured (d). Film thickness as a function of coating speed (e) and yield as a function of SAM hydrophobicity (f) are quantified as a function of source-drain dimensions. . . . .	42
2.6	Optical micrographs and histogram distribution of channel lengths for source-drain electrodes printed from as-received ink (a,c, respectively) and optimized ink (b,d, respectively). Histogram distribution of channel lengths for various inks for the whole and bottom $\frac{3}{4}$ of the array (e) along with the mean channel length measured in cross sections perpendicular to the direction of printing (f). . . . .	43
2.7	Optical micrographs of silver source-drain electrodes before (a) and after (b) coating with PEDOT:PSS with cross-sectional profiles (c). . . . .	44
2.8	Statistical (a) and optical (b) quantification of polymeric semiconductor pattern width along with cross-sections measured at the top left (c) and bottom right (d) of the array as measured through the red dashed line. . . . .	45
2.9	Transfer (a) and output (b) characteristics of polymeric SP220 OTFTs along with statistical distribution of saturation mobility (c), on-off ratio (d), and threshold voltage (e). . . . .	46
2.10	Schematic depiction of chamber used to control evaporation rate of toluene with optical micrographs (a) and cross-sectional profiles of TIPS-Pentacene crystals formed by fast (b) and slow (c) solvent evaporation. . . . .	48
2.11	Effect of blade coating direction (a) and dispensed ink volume (b and c) on TIPS-Pentacene film morphology and continuity between electrodes and the channel, respectively. The variability of on-current (d) and typical transfer (e) and output (f) curves for a TIPS-Pentacene OTFT. . . . .	49
2.12	An OTFT with a semiconductor composed of 1:1 TIPS-Pentacene : PTAA (a). The distribution of saturation mobility (b) and typical transfer (c) and output (d) plots are shown. . . . .	50
2.13	Chemical structure of semiconductor (a) and solvent (b) blends used in ink formulation. Polarized optical microscopy of semiconductor films (prior to gate electrode thermal evaporation) printed on plastic from inks composed of 1:0 and 9:1 (c), 9:1 and 9:1 (d), 1:1 and 2:1 (e) diF TES ADT:PTAA and mesitylene:tetralin, respectively. Transfer characteristics of these films (f) and polarized optical microscopy of semiconductor films in the channel regions printed from inks composed of 9:1 and 9:1 (g), 1:1 and 2:1 (h) diF TES ADT:PTAA and mesitylene:tetralin, respectively. . . . .	52
2.14	Poly(4-vinylphenol) dielectric film thickness along coating (y) and lateral (x) directions printed from a single intermediate vapor pressure solvent (a) and mixture of high and low vapor pressure solvent blend (b). The thickness of amorphous fluoropolymer using a blend of high and low boiling point solvents is also shown (c). . . . .	53



2.15	Mostly-printed OTFT array with evaporated gate electrodes (a) with mobility measured at various locations in the array (b). Saturation mobility (c and f), $\text{Log}(I_{\text{ON}}/I_{\text{OFF}})$ (d and g), and threshold voltage (e and h) histograms are shown before and after annealing the complete device (post-annealed) at 120°C for 10 minutes, respectively. . . . .	55
2.16	Zoomed-out photograph of the all-printed OTFT array (a) with the transfer (b) and output (c) characteristics of a typical device. The statistical distribution of saturation mobility (d), $\text{Log}(I_{\text{ON}}/I_{\text{OFF}})$ (e), subthreshold slope (f), and threshold voltage (g) is shown for the array. . . . .	56
2.17	Bias stress during measurements (a) and comparison of transfer characteristic before and after (b). Transfer characteristics measured during flex testing (c) showing change in on-current with bending radii (d) that eventually fail due to substrate cracking (e). . . . .	57
3.1	Kelvin probe force microscopy (KPFM) theory of operation, showing energy level alignment between the probe tip and sample with no connection (a), short circuit (b), and biased at the flat band potential (c). (d) The peak-to-peak (P-P) output signal characteristics of Kelvin probe measurement as a function of $V_B$ and denoting the minima that occurs at the flat band potential. . . . .	59
3.2	(a) Screen printing process showing the flood phase (step 1) and squeegee phase (step 2) with ink pushed through openings in the screen depositing on the substrate as the squeegee is dragged across the screen (step 3). (b) Illustration of a zoomed-in portion of a screen, which consists of an emulsion layer (orange) with openings that define the patterns that is supported by a stainless steel mesh (blue) that is angled 22.5° with respect to the printing direction. (c) Figurative illustration of viscosity ( $\eta$ ) as a function of shear rate for a shear thinning ink, showing regions that are relevant to the flood (step 1) and squeegee (step 2) phases. . . . .	61
3.3	(a) Fabrication steps for each layer in an all-printed organic photodiode (OPD) using doctor blade coating (red) and screen printing (yellow). (b) Band diagram and thickness of each layer of the all-printed OPD for a PCDTBT:PC <sub>71</sub> BM active layer. (c) Photograph of 32 × 32 pixel array on a flexible plastic substrate. . . . .	62
3.4	(a) Work function of PEDOT:PSS/PEIE cathode measured using KPFM as a function of PEIE solution concentration in 2-methoxyethanol printed with a blade height of 100 μm at a speed of 1.6 cm/s. (b) Atomic force microscopy (AFM) magnitude plot (top) and corresponding KPFM plot (bottom) on PEDOT:PSS coated with a 0.4 wt. % PEIE in solution. (c) KPFM measurements of 0.4 wt. % PEIE in solution coated on PEDOT:PSS and sheet resistance measurement done over centimetric scales depicting the location of the array (red dashed lines) on a polyethylene naphthalate (PEN) substrate. . . . .	64

- 3.5 (a) Light ( $1 \mu\text{W}/\text{cm}^2$  @ 532 nm) and dark current-voltage characteristics of all-printed OPDs with no PEIE and 0.05 wt. % PEIE in solution deposited for the cathode. (b) Light ( $1 \mu\text{W}/\text{cm}^2$  @ 532 nm) and dark current-voltage characteristics of all-printed OPDs with 0.4 wt. % and 1 wt. % PEIE solution deposited for the cathode. (c) All-printed OPD mean EQE and dark current dependence on PEDOT:PSS/PEIE cathode work function deposited in Figure 3.4a. (d) Light ( $1 \mu\text{W}/\text{cm}^2$  @ 532 nm) and dark current-voltage characteristics in log-scale of the all-printed OPD. . . . . 65
- 3.6 (a) Illustrative depiction of the chronological drying process of a blade coated wet film for ink concentrations well below the solubility limit and approaching the solubility limit that leave behind aggregates (black dots). (b) All-printed OPD device yield at an applied reverse bias field of 88 kV/cm and the corresponding dark current for functional devices. Current-voltage characteristics of all-printed OPDs plotted for active layer thicknesses of 235 nm (c) and 380 nm (d) under reverse bias for multiple devices. . . . . 67
- 3.7 (a) Illustrative depiction of a blend of screen printable PEDOT:PSS (SPP) with high work function AI 4083 PEDOT:PSS printed on the active layer. (b) Viscosity of undiluted SPP (courtesy of Agfa Gevaert) and diluted in AI 4083. (c) Dark current density (black) and EQE (red) of inverted OPDs printed with the optimal cathode and active layer for anodes made of gold and blends of SPP and AI 4083 showing the work function of each of these electrodes. (d) Optical micrographs of the anodes on top of the all-printed OPD array. . . . . 69
- 3.8 Screen printing quality of anode on top of active layer for 0 (a), 25 (b), 40 (c), and 50 (d) wt. % AI 4083 PEDOT:PSS added to SPP. (e) Optical micrograph of PEDOT:PSS blends printed on PEN substrate with at most 40 wt. % AI 4083 (e) and 50 wt. % (f) added to SPP. (g) Cross sectional profile of SPP + 25 wt. % AI 4083 anodes printed on top of the active layer. . . . . 70
- 3.9 (a) Band diagram of standard OPDs with printed anode (no PEIE) and active layer (570 nm-thick) with thermally evaporated aluminum and silver), and inverted OPDs with printed cathode (0.4 wt. % PEIE) and active layer with screen printed PEDOT:PSS (SPP + 25 wt. % AI 4083) or thermally evaporated gold. (b) Current-voltage characteristics of devices under dark and light conditions at 532 nm and  $1 \mu\text{W}/\text{cm}^2$ . . . . . 71
- 3.10 (a) Dynamic response of all-printed OPD at 532 nm biased at -5 V. (b) EQE spectral response of all-printed OPD under various  $V_{\text{Bias}}$  under  $3\text{-}6 \mu\text{W}/\text{cm}^2$ . Frequency response of all-printed OPDs with a 570 nm- (c) and 235 nm-thick (d) active layer and  $0.16 \text{ mm}^2$  active area under sine-modulated light at various biases. 74
- 3.11 (a) All-printed OPD device impedance model with the resistivity of the PEDOT:PSS electrodes and impedance of PEIE and active layers highlighted. (b) Nyquist plot of raw data (black) and fit to the model (red) for various light intensities. (c) Extracted parameters of the model based on the fitted data. (d)  $\tau_{\text{avg}}$  (Equation 3.5) measured at  $V_{\text{Bias}} = 0 \text{ V}$  for various light intensities. . . . . 75

3.12	(a) Schematic of photocurrent noise measurement setup. (b) Spectral noise density of photocurrent at 33 and 56 nA for all-printed OPDs (solid lines) measured at short circuit and theoretical value based on shot noise (dashed lines) as calculated from Equation 3.6. . . . .	77
3.13	(a) Comparison of specific detectivity ( $D^*$ ) calculated according to Equation 3.1 at various applied fields ( $V_{\text{Bias}}/t_{\text{OPD}}$ ) for the all-printed OPDs presented in this chapter and other OPDs published in literature. (b) An all-printed OPD (Figure 3.3b) biased continuously at -5 V for 20 hours in air alternating between light (532 nm) and dark with a 50% duty cycle. (c) Scatter plot of EQE, dark current and $D^*$ of all-printed OPDs that were left for 24 hours in the dark in air prior to measurement and exposed to the same conditions in Figure 3.13b. (d) EQE and dark current of a batch of all-printed OPDs measured the day of fabrication and after 211 days of storage in nitrogen while exposed to ambient light. . . . .	78
4.1	(a) Device architecture of an organic charge-coupled device (OCCD) with an active layer composition of 100:1 PCDTBT:PC <sub>71</sub> BM and the biasing polarities for such devices. (b) External quantum efficiency (EQE) of an all-printed organic photodiode (OPD) as a function of time and biased at -15 V using PEDOT:PSS/PEIE cathode and PEDOT:PSS anode as the device in Chapter 3. (c) Temporal response of the OCCD in (a) illuminated at various irradiances at 532 nm. (d) Bias stress stability in the dark of the OCCD in (a) with an initial run at -10 V immediately followed by a -5 V bias. . . . .	82
4.2	(a) Temporal response of an OCCD of the same structure as the device in Figure 4.1a but with an active layer composition of 1:3 PCDTBT:PC <sub>71</sub> BM. (b) Bias stress stability in the dark of the OCCD with 1:3 donor:acceptor with an initial run at -20 V immediately followed by a -5 V bias. (c) Capacitance as function of bias of the same OCCD in the dark and under an irradiance of 1.34 $\mu\text{W}/\text{cm}^2$ at 532 nm. (d) Frequency response of the capacitance for the same OCCD under various irradiances at 532 nm. . . . .	84
4.3	(a) Driving and readout circuit used to operate OCCDs as charge-integrating photodetector pixels. (b) Driving scheme used for assessing OCCD charge integration performance by ensuring the light is only on when the OCCD is biased in integration mode (high) and not during reset (low). (c) Temporal response of the OCCD in Figure 4.2 when periodically illuminated at various irradiances at 532 nm for 5 ms at a refresh rate of 100 Hz. (d) Temporal response of the same OCCD illuminated at 41 $\mu\text{W}/\text{cm}^2$ at 532 nm with a 50% duty cycle for a refresh rate of 100 Hz and 20 Hz. (e) Integrated charge as a function of illumination time at various irradiances. . . . .	86
4.4	(a) Dynamic range of integrated charge for a pixel using a photodiode (linear responsivity) and a phototransistor (sublinear responsivity with photoconductive gain). (b) Rolling shutter row addressing scheme used in commercial image sensors for integration and readout of photogenerated charge during a frame period. . . . .	87

4.5	Fabrication process flow for the organic phototransistor (OPT) with the final device schematic showing the source (S), drain (D), and gate (G) electrodes. . .	89
4.6	(a) Band diagram of the OPT channel along with the thickness of the migration of photogenerated charge and the thickness of each layer. (b,c, and d) Various test structures used to determine the impact of the heterojunction channel. (e) Comparison of transfer characteristics for the devices shown in (b-d). (f) Out-of-plane X-ray diffraction (XRD) measurements on the PCDTBT:PC <sub>71</sub> BM-DNTT channel with the inset showing the 2D diffraction pattern. . . . .	90
4.7	(a) Dark transfer characteristic of a phototransistor for forward and backward sweeps at a rate of 5V/s. (b) The transfer characteristic in (a) plotted as $\sqrt{I_{DS}}$ with respect to a linear fit. (c) Statistical distribution of mobility, on-off ratio, and threshold voltage ( $V_T$ ) for 40 devices. . . . .	91
4.8	(a) Output characteristics of an OPT in dark and under an irradiance of 40 $\mu\text{W}/\text{cm}^2$ at 532 nm along with the EQE for various $V_{GS}$ . (b) EQE of an OPD with the same BHJ as the OPT (45 nm of 1:3 PCDTBT:PC <sub>71</sub> BM) using a PEDOT:PSS anode and aluminum cathode as a function of applied electric field. . . . .	92
4.9	(a) Transfer characteristic of OPT at various irradiances at 532 nm. (b) Pixel schematic and equivalent circuit of an OPT-based pixel. (c) Drive ( $V_G$ ) and readout ( $Q_{int}$ ) scheme of pixel operation. The first phase and vast majority of the frame period is charge integration of electrons (blue) followed by a fast discharge of the electrons through recombination with injected holes (red) to quickly readout the signal. (d) Equivalent pixel circuit in the on- and off-state showing relevant parasitic capacitances ( $C_{GS}$ ) and nodal voltages. . . . .	94
4.10	(a) Dynamic response of integrating charge and EQE of the rate of integrating charge, labeled instantaneous EQE, at an irradiance of 40 and 323 $\mu\text{W}/\text{cm}^2$ at 532 nm. (b) Dynamic response of the discharge to readout light signals after an integration period of 32 ms for irradiances of 1.4, 40 and 323 $\mu\text{W}/\text{cm}^2$ at 532 nm. (c) Integrated charge as a function of readout delay at an irradiance of 40 $\mu\text{W}/\text{cm}^2$ at 532 nm. (d) EQE of integrated charge ( $\text{EQE}_{Int}$ ) measured at readout from 416-784 nm at irradiances varying between 5-10 $\mu\text{W}/\text{cm}^2$ at 30 fps. Also shown are the absorption coefficients of the DNTT and PCDTBT:PC <sub>71</sub> BM layers of the phototransistor. . . . .	95
4.11	(a) Optical micrograph of OPT-based pixel used to test the optoelectronic performance of the device with illumination only on the bias capacitor (black), channel (blue), and drain-gate overlap (green). (b) Equivalent circuit diagram highlighting the same test regions as shown in (a). (c) Discharge characteristics shown for restricted illumination to the regions highlighted in (a) and (b) at an irradiance of 41 $\mu\text{W}/\text{cm}^2$ at 532 nm. . . . .	97

4.12	(a) Dynamic range of readout signal from an OPT-based pixel measured at 5,30 and 100 fps with a 95% integration time duty cycle for light at 532 nm. (b) EQE <sub>Int</sub> measured at readout for the dynamic range measurements in (a). (c) Image lag at 30 fps normalized to imaged irradiance of the last illuminated frame by calibrating the pixel to the plot in (a). (d) Normalized response of pixel to steady illumination after dark. . . . .	98
4.13	(a) Schematic of OPD-based pixel (1T) showing the OPD and TFT element. (b) Driving and charge readout scheme of the 1T pixel, where $V_G$ , $V_{PD}$ , and $Q_C$ represent gate voltage, voltage at the OPD-TFT node, and collected charge at the drain, respectively, with the drain of the TFT set to ground. (c) Cross sectional profile of the 1T pixel in (a) showing the OPD and TFT regions. (d) Equivalent circuit of 1T pixel. (e) Dynamic response of 1T pixel (red) in comparison to the OPT-based pixel (black). (f) EQE <sub>Int</sub> measured at readout for the dynamic range measurements in (e). . . . .	99
5.1	(a) Measurement setup of transmission-mode pulse oximetry. (b) Molar absorptivity spectrum of deoxygenated hemoglobin (Hb) and oxygenated hemoglobin (HbO <sub>2</sub> ). (c) Schematic representation of a photoplethysmogram (PPG) and the various time-variant and -invariant components that contribute to the signal. (d) Measurement setup of reflectance-mode pulse oximetry. . . . .	103
5.2	(a) Schematic view of a printed array of discrete organic photodiode (OPDs) with the photoactive area highlighted in red. (b) Cross sectional view of an OPD. (c) Photograph of a printed array of discrete OPDs. . . . .	104
5.3	(a) Chemical structures of donor polymers (P2B and P3B) and acceptor (PC <sub>71</sub> BM) used to create infrared-sensing OPDs. (b) Band diagram of the OPD at flat band potential. (c) External quantum efficiency (EQE) spectra of various donor:acceptor wt. ratios dissolved in 1,2 dichlorobenzene and spin coated to form devices with the same band diagram as in (b). (d) Light and dark current-voltage characteristics of annealed and unannealed infrared OPDs processed in the same way as the devices in (c) in comparison to a high performance organic photovoltaic material system (P(TBT-DPP):PC <sub>71</sub> BM). . . . .	106
5.4	(a) EQE of a printed OPD using 1:2 P2B:PC <sub>71</sub> BM by weight dissolved in 2:1 chlorobenzene:1,2 dichlorobenzene by volume. (b) Light and dark current-voltage characteristics of the device in (a). (c) Transmission PPG measurement using near infrared (NIR) and red LEDs. . . . .	108
5.5	(a) Band diagram of PTB7:PC <sub>71</sub> BM (donor:acceptor) OPD at flat band potential. (b) EQE of the printed OPD in (a) cast from 95:5 chlorobenzene:1,8-diiodooctane by volume in relation to the electroluminescent (EL) spectra of the green and red organic light emitting diodes (OLEDs). (c) Light and dark current-voltage characteristics of the device in (a). (d) Attenuation of sine-modulated light dependence on frequency for various LED/OLED and silicon photodiode (PD)/OPD combinations. . . . .	109

5.6	(a) Measurement setup of transmission-mode pulse oximetry using all-organic devices. (b) System schematic diagram for driving and reading the oximeter. (c) Reference PPG measurement using LEDs and a silicon PD with the calculated heart rate and blood oxygen saturation ( $\text{SaO}_2$ ). (d) PPG measurement using all-organic devices with the calculated heart rate and $\text{SaO}_2$ . Reprinted with permission from [114]. Copyright 2014 Nature Publishing Group. . . . .	111
5.7	(a) Fabrication process for a four-pixel OPD module for reflectance-mode pulse oximetry. (b) EQE spectrum of a BHJ blend of 1:2 donor polymer: $\text{PC}_{71}\text{BM}$ by weight dissolved in 95:5 1,2,4-trimethylbenzene (TMB):benzyl benzoate (BB) by volume. (c) Light and dark current-voltage characteristics of a sample pixel in (a). (d) Signal attenuation of an OPD pixel as a function of the frequency of a sine-modulated light source. . . . .	113
5.8	(a) Schematic and picture of an eight-OPD pixel array for reflectance-mode pulse oximetry. (b) EQE spectra of the pixels in the array color coded according to row position in (a). (c) Dark current-voltage characteristics of the OPDs in the array color coded according to row position. (d) Signal attenuation of an OPD pixel as a function of the frequency of a sine-modulated light source. . . . .	115
5.9	Screen printed silver paste on polyethylene terephthalate (PET) (a) and plasma-treated amorphous fluoropolymer (AF) (b). Screen printed silver on plasma-treated AF with a snap-off distance (SOD) of 0.4 mm (c) and 1.6 mm (d). Screen printed features from a screen with a significant amount of drying (e) and negligible amount of solvent evaporation (f). . . . .	117
5.10	(a) Dark current-voltage characteristics of an all-printed OPD (reference Chapter 3) with and without dielectric or silver paste printed on the PEDOT:PSS anode. (b) Screen printing process on top of the BHJ active layer in order to create contact pads for OPD pixels without degrading device performance. (c) Optical micrograph of the final all-printed OPD with a contact pad. (d) Cross sectional profile of the contact pad. (e) Light and dark current-voltage characteristics of the pixel with contact pad. . . . .	118
5.11	(a) Schematic of organic thin film transistor (OTFT) array. (b),(c) Photographs of an array of OTFTs with screen printed interconnects. (d) Cross sectional profile of inkjet printed silver nanoparticle contact bump on a source-drain electrode used to create a conductive via through the gate dielectric (height shown by red dashed line). . . . .	119
5.12	(a) Transfer characteristics for OTFTs in the array with sufficient gate-source overlap. (b) Output characteristic of a sample device from (a). (c) Histogram of contact resistance ( $R_{\text{On}}$ ) and $\text{Log}_{10}(\text{I}_{\text{On}}/\text{I}_{\text{Off}})$ for the devices in (a). (d) Transfer characteristics for OTFTs in the array with insufficient gate-source overlap. (e) Output characteristic of a sample device from (d). (c) Histogram of $R_{\text{On}}$ and $\text{Log}_{10}(\text{I}_{\text{On}}/\text{I}_{\text{Off}})$ for the devices in (d). . . . .	120

5.13	(a) Fabrication process for screen printed interconnects on organic phototransistor (OPT)-based pixels. (b) Zoomed-in view of interconnect lines on the image sensor. (c) Photograph of the imager and equivalent circuit diagram. (d) Images taken by the imager at various irradiances. . . . .	122
------	---	-----

# List of Tables

1.1	Properties of solution-processed non-charge-integrating passive pixel image sensors.	21
1.2	Properties of solution-processed passive pixel image sensors capable of intra-pixel charge integration. . . . .	28
1.3	Properties of fabrication techniques. . . . .	30
1.4	Properties of printing techniques. . . . .	31
2.1	Yields and average saturation mobility, on-off ratio and threshold voltage standard deviation for devices with various diF TES ADT : PTAA and mesitylene:tetralin composition. . . . .	51
3.1	Work function of the PEDOT:PSS cathode coated with 0.6 wt. % PEIE in 2-methoxyethanol under various conditions. . . . .	63
3.2	OPD characteristics of the various structures illustrated in Figure 3.9a. Measurements were performed under $1 \mu\text{W}/\text{cm}^2$ at 532 nm at an applied reverse bias field of 88 kV/cm in air without encapsulation. . . . .	72
3.3	All-printed OPD cut off frequencies ( $f_{3\text{dB}}$ ) for various active layer thicknesses, $V_{\text{Bias}}$ , and $E_{\text{Int}}$ (Equation 3.3). . . . .	73
4.1	Rise time (reaches 90% of steady state) of discharge after integration at various irradiances at 532 nm. . . . .	96



## Acknowledgments

The research and writing put into this dissertation would not have been possible without the support of many people and organizations. I would first like to thank my thesis advisor, Ana Claudia Arias, for being the best possible academic advisor. Starting a PhD in a new research group, with no lab yet setup or projects from senior students, was a daunting task for her and everyone else in our group. I'm extremely grateful for her confidence in my abilities and let me pursue my own research interests from the first days research and supporting me since then. I would also like to thank various funding sources, especially the National Science Foundation Graduate Research Fellowship Program for financially supporting me through my last three years of my PhD. I'm also grateful for Systems On Nanoscale Information fabriCs (SONIC) center, Intel, Cambridge Display Technologies, the Department of Energy (DOE), and the Molecular Foundry for funding and enabling the research presented in this dissertation.

I would also like to thank all the individuals with whom I had the privilege of working alongside everyday. Vivek Subramanian and Paul Wright have not only been helpful by being on my dissertation committee, but also by sharing lab space and resources to facilitate research between all of our groups. I'm grateful for the support from the Cory Hall machine shop and Marvell NanoLab staff for setting up most of our equipment and responding to all the emergency repairs done in the early days of our lab. Various part suppliers were also critical in enabling the fabrication of my devices, especially Rachel Peglow and Yuhi Ogawa at Dynamesh who supplied my screen printing screens, Mark Devereaux and Don Peterson at Photo Etch Technology who supplied my surface energy-patterning and evaporation stencils, and Zehntner for providing doctor blade coaters. I also thank many individuals in the Arias and Subramanian research group who setup and maintained equipment that was critical to device fabrication and characterization. I would especially like to thank Joe Corea, Claire Lochner and Aminy Ostfeld who have been here with me from day one getting the lab up and running.

Many of the research projects presented in this dissertation were done in collaboration with others. I appreciate the exposure to the science community I got at Lawrence Berkeley National Laboratory in the first year of graduate school. I'm also grateful for the assistance I got from Mahsa Sadeghi on the fabrication of organic thin film transistors (OTFTs) since she was an undergraduate student and for her and Lilian Soares Cardoso bringing the implementation of these devices to the systems level in their doctoral research. I also thank Marcia Payne and John Anthony at the University of Kentucky, Antonio Facchetti at Polyera, and Monica Davis at EMD Millipore for the provision of OTFT materials. Igal Deckman and Pierre Balthazar Lechne provided me with indispensable insight that made the fabrication of high performance organic photodiodes (OPDs) possible. My thanks also extend to the chemists at St-Jean Photochimie who provided a customized batch of semiconducting polymer that enabled OPD and organic phototransistor (OPT) devices. I'm also grateful for the

support from Abhinav Gaikwad in characterizing my materials. Finally, I would like to offer thanks to Yasser Khan, Claire Lochner, Donggeon Han and Jonathan Ting who not only made all-organic pulse oximeters possible but an enjoyable experience.

Last but certainly not least, I would like to extend my deepest thanks to all who have made my five years in Berkeley an amazing and life-transforming experience. Past and present members of the Arias group, including all previously mentioned members and Natasha Yamamoto, Alla Zamarayeva, Maggie Payne, Felipe Pavinatto and Tae Hoon Kim, have been a pleasure to work with and are also some of the funnest and most trustworthy friends. I have also developed many close friendships with other members of the graduate student community. During graduate school, I began actively exercising and training and achieved amazing changes in strength, stamina and physique I never dreamed possible. I especially thank Kris and Melissa Bates at Grassroots Crossfit for not only making me a better version of myself, but creating a fun environment for completing challenging exercises and socializing with other members of the Berkeley community. I would also like to thank my parents for their immense support in my education and creating an encouraging environment for studying from preschool to the submission of this thesis. Without their motivation and encouragement, my entrance into Berkeley, let alone the submission of this dissertation, would not have been possible. Most importantly, I am eternally grateful for my wife, Ivy Tao, and the purpose and joy she brings everyday to my life. She is the source of all my inspirations, the motivation for my doings, and the love of my life with whom I grow more excited about our future each passing day.

# Chapter 1

## Introduction

### 1.1 Introduction

The mass production of image sensors has revolutionized the landscape of media broadcasting, surveillance, medicine and many other domains that benefits from captured photographs or videos. This proliferation of image sensors was strongly attributed to Moore's law, which continuously scaled down transistor size in order to increase the device speed but also to decrease the cost per device since more chips and sensors can be packed into one silicon wafer[67, 170]. Consequently, for a fixed number of pixels, the cost per image sensor decreased by shrinking the pixel dimensions. Furthermore, advances in silicon microfabrication technology enabled high performance transistors to be embedded in each pixel for amplifying the photo-accumulated charge. Despite such advances, the SNR (signal-to-noise ratio) and dynamic range (range of photographable light intensities) of image sensors with small pixels becomes limited by the quantized nature of light, known as shot noise[65, 147, 166]. For this reason high performance image sensors have larger pixels on the order of tens of micrometers in dimension, while inexpensive and low performance imagers have pixel dimensions of approximately  $1\text{ }\mu\text{m}$ [65, 166].

It becomes clear that alternatives to silicon wafer-based microfabrication technology are necessary in order to circumvent the trade-off between pixel size, which is correlated to performance, and cost. Processing techniques that scale favorably with area, such as printing, can leverage the superior performance of large pixels without increasing the cost. This is because sensor size is no longer limited by the area of a silicon wafer, but can be deposited on inexpensive substrates in a continuous roll-to-roll fashion[5, 96]. The most prevalent of these materials are solution processable organic compounds, Perovskites and inorganic nanomaterials that have highly tunable absorption spectrums and high absorption coefficients. This is in strong contrast to the poor absorption coefficient of silicon, which can only be improved upon in conventional microfabrication with the costly epitaxial deposition of a handful of materials. Furthermore, the ability to deposit functional materials on a variety of

flexible and deformable substrates can make conformal substrates which not only relax the requirements of the optics to focus the light, but also enable new methods of imaging never possible with planar sensors[63]. A significant amount of emerging literature can be found on solution processable and flexible image sensors with a wide variety of pixel architectures and operational modes. As such, it is important to assess the progress and shortcomings of this young field while emphasizing the figures of merit and most optimal way of designing devices and systems for image sensing.

## 1.2 Fundamental Operation Principles of Image Sensors

Image sensors are complex systems, composed of multiple types of devices such as the photodetectors and transistors in each pixel of the array along with the drivers and readout circuitry outside the sensor area. While printing large area and flexible image sensors can enable features and performance never possible with planar and compact versions, it is important to assess new systems by the same figures of merit used in conventional image sensors[65, 166]. Figure 1.1a shows the path of the light-induced photocurrent signal from the photodetector element in the pixel (black square), through the pixel circuitry (red square) and finally to the readout circuitry at the exterior of the array. Almost all commercialized image sensors employ a charge integrating pixel architecture[65, 67, 166] as illustrated in step 1 of Figure 1.1a. Placing a capacitor in series with the photocurrent source of the detector enables integration of the signal during for a period of time. The integration period ends when a signal from the row line triggers the pixel to discharge the photogenerated charge onto the column line in step 2. A passive pixel architecture directly transfers the photogenerated charge from the pixel to the column, giving it a charge output gain (labeled  $G$  in Figure 1.1a) of unity. Conversely, an active pixel utilizes multiple transistors to amplify the charge output from the pixel onto the column. Step 3 shows the injected charge is finally fed into the readout circuit at the base of the column to translate the photogenerated signal into a voltage so that it can be read by analog to digital converters. This conversion can be done by reading the voltage drop across a passive load such as a resistor, the output of a charge amplifier or the output of a transimpedance amplifier. The base of each column is equipped with readout circuitry in order to parallelize the readout process as each row is scanned.

The intra-pixel charge integration in step 1 offers a far higher SNR compared to looking at the instantaneous photocurrent of each pixel as it is scanned. Reading out the instantaneous photocurrent from each pixel means that the sampling period from each row must be very short in order to scan the array at an appreciable frame rate. On the other hand, Figure 1.1b shows photocurrent can be integrated in the pixel while it is switched off during most of the frame period (step 1), then discharged quickly into the column line for reading out the charge (steps 2 and 3). This simultaneous charge integration (image capturing)

and discharging of pixels in an array is known as rolling shutter operation. Global shutter operation on the other hand, as illustrated in Figure 1.1c, simultaneously integrates charge over the whole array for a period of time to prevent motion artifacts, holds the charge, then discharges it row by row. Intra-pixel integration using either of these schemes allows for the strength of the signal to increase linearly with time. The noise of the photocurrent and dark current of a photodetector must also be taken into account, which can be modeled as a statistical Poisson process[65, 147]. The noise of a current source is the standard deviation of integrated charge during a certain time period. In a Poisson process, the standard deviation and noise is the square root of the integrated charge, which is known as the shot noise of a device. Equation 1.1 illustrates the most important figure of merit for measuring sensitivity of an image sensor, signal to noise ratio (SNR) as a function of photocurrent ( $I_{Photo}$ ), dark current ( $I_{Dark}$ ), fixed readout noise ( $N_{RO}$ ) from steps 2 and 3 and integration time ( $T$ , which is very close to the frame period). The photocurrent and dark current are then decomposed into photocurrent density ( $J_{Photo}$ ) and dark current density ( $J_{Dark}$ ) multiplied by the photosensitive area per pixel ( $A$ ) to demonstrate how scaling photoactive area affects SNR. The equation is further simplified to show the case for short and long integration times where the shot noise from the photodetector element is negligible and significantly larger compared to the readout noise, respectively. In both cases it is desirable to have a lower dark current density, larger photoactive area and longer integration time for a fixed light flux (i.e. constant  $J_{Photo}$ ). The benefit of large area pixels is especially predominant for shorter integration times because small pixels easily result in readout noise dominating over shot noise[65]. As a result of this trend it is important to create image sensors with large pixel photoactive areas to obtain high performance at higher frame rates. Solution processable materials are advantageous in this regard since they can leverage performance and cost by significantly reducing the processing cost per unit area of image sensors.

$$\begin{aligned}
 SNR &= \frac{Signal}{Noise} = \frac{I_{Photo}T}{\sqrt{N_{RO}^2 + (I_{Photo} + I_{Dark})T}} = \frac{J_{Photo}AT}{\sqrt{N_{RO}^2 + (J_{Photo} + J_{Dark})AT}} \\
 \lim_{T \rightarrow 0} SNR &= \frac{J_{Photo}AT}{N_{RO}}, \quad \lim_{T \rightarrow \infty} SNR = \frac{J_{Photo}\sqrt{AT}}{\sqrt{J_{Photo} + J_{Dark}}}
 \end{aligned} \tag{1.1}$$

Another important figure of merit of an image sensor is dynamic range. It is defined as the difference between the lowest detectable signal (as limited by noise) and the highest. Figure 1.2 shows the limiting factors for the lower (noise floor) and upper end (saturation) of the dynamic range as the photogenerated charge passes through the three steps shown in Figure 1.1a; charge Photogeneration from the photodetector, pixel signal discharge, and readout from external circuitry. The photodetector is the element that generates the light signal. The upper bound on the signal from a photodetector is limited by effective series resistance, which can be in the form of either an actual resistance or significant charge recombination. However, these effects typically occur above sun light irradiance, well beyond

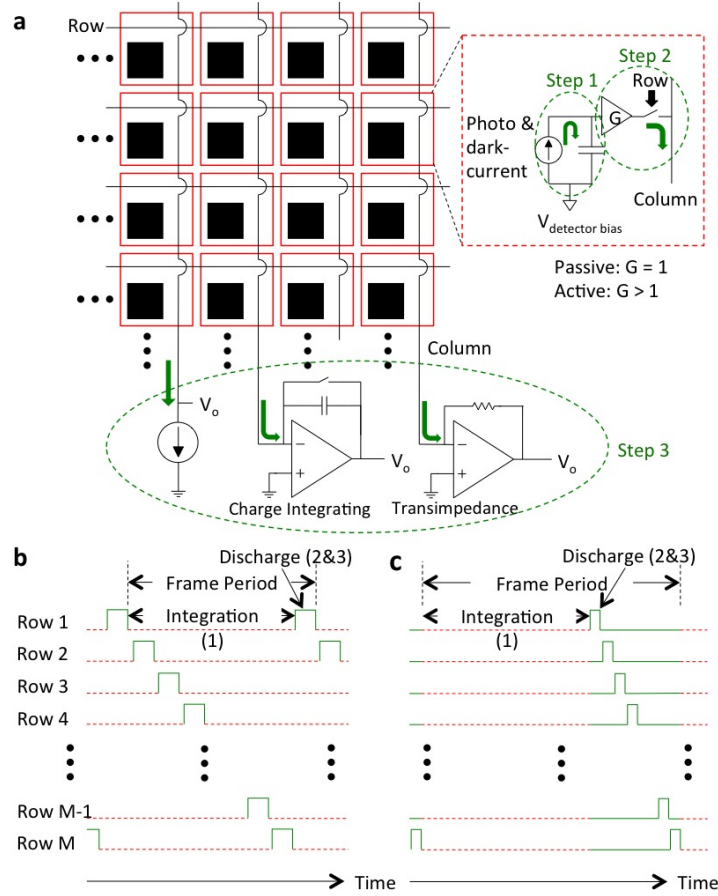


Figure 1.1: (a) Schematic view of an image sensor depicting the flow of photogenerated charge from charge integration in the pixel (step 1), to discharging in the column for either passive or active pixels (step 2), and finally readout from external circuits sensing voltage, charge, or current (step 3). (b) Rolling shutter addressing and readout scheme. (c) Global shutter addressing and readout scheme.

the range of irradiance used in photography or video. The lower bound is limited by the noise of the detector, whether from the shot noise of the dark current or  $1/f$  noise caused by trap states in the device. The main limiting factor in the dynamic range of an image sensor arises when the photogenerated signal from the photodetector is captured and stored in the pixel circuitry. The capacitive element used for photocharge integration can only store a finite amount of charge for a given supply voltage ( $Q=CV$ ), known as the well capacity. However, parasitic capacitances between transistors and the charge integration node severely deteriorate performance. Row and column lines, which are connected to transistor terminals, induce parasitic charge injection into the path of the photogenerated charge, which not only decreases well capacity but also raises the noise floor. Pixel-to-pixel leakage can also become

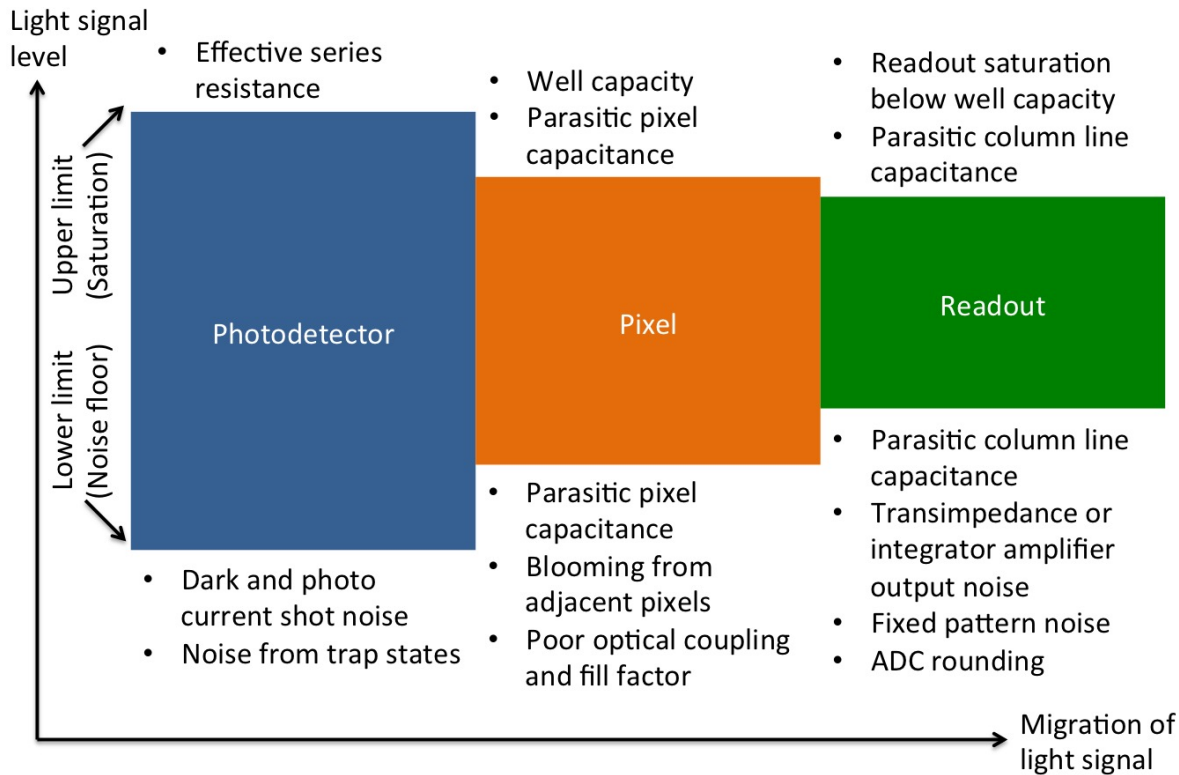


Figure 1.2: Upper and lower bounds on the dynamic range of a photogenerated signal starting from generation in the photodetector, to storage in the pixel, and finally readout on the column line after discharge from the pixel.

a limiting factor for the noise floor of image sensors when charge bleeds into the adjacent pixels, known as blooming. Consequently proper pixel-pixel isolation is needed in order to ensure that the noise floor of adjacent dark pixels does not become limited by blooming. Poor optics and fill factor, the percentage of the pixel's area that is photosensitive, also limit the amount of light reaching the photodetector element. In the final step, the integrated photocurrent is discharged from the pixel onto the column and read by the readout circuitry. Parasitic capacitance between the column and driver lines should be minimized as it can result in signal saturation at the readout and also noise. The design of the readout circuitry must avoid signal saturation by the well capacity of the pixel. Variability in the dark current, known as fixed pattern noise, must be kept at a minimum in order to establish a consistent background noise throughout the whole array.

In order to advance the field of solution processed large area image sensors, it is imperative to perform an assessment on the state-of-the-art of these systems with regards to photodetector devices, image sensors of various pixel architectures, and imaging optics. In

this chapter, the theory, figures of merit and state-of-the-art of photodiodes and phototransistors will first be overviewed. Following this, discussion on solution processed image sensors will be organized into passive non-charge integrating, passive charge integrating and active pixel systems. Finally, progress in optics compliant with large area and flexible sensors will be reviewed.

## 1.3 Thin Film Transistors & Photodetectors

### Thin Film Transistors & Figures of Merit

Thin film transistors (TFTs) are three terminal devices that are comprised of a gate electrode that is used to control the flow of charge from the source electrode to the drain electrode as shown in Figure 1.3a. A dielectric between the channel (semiconductor) and gate electrode allows for capacitive control of the amount of carriers in the channel. The channel region is a semiconductor that is either n-type or p-type that should have good electron and hole transport properties, respectively. This device is typically unipolar, which means either and electron or hole is transported in the channel in the lowest unoccupied molecular orbital (LUMO) or highest occupied molecular orbital (HOMO), respectively. Source-drain electrodes should also have a low injection barrier for majority carrier of the channel. Electrons and holes are injected into channel from the source electrode, which means current flows from drain to source and source to drain for n- and p-type devices, respectively. The gate voltage with respect to the voltage of the source electrode ( $V_{GS}$ ) modulates the conductivity of the channel as explained in Figure 1.3b. A  $V_{GS}$  less than the threshold voltage ( $V_T$ ) of the TFT biases the device in the subthreshold region. In this region the gate voltage affects the bulk charge of the semiconductor, which changes the amount of band bending at the dielectric interface. The Fermi distribution of free carriers decreases exponentially with increasing energy for a trap-free semiconductor. However, the abundance of trap states within the band gap of most solution-processed organic and inorganic semiconductors leads to a non-exponential or power-law behavior in the conductance of the channel as a function of  $V_{GS}$ . Accumulation occurs when the charge concentration of free carriers at the dielectric interface begins to out number the change in bulk charge of the semiconductor and marks the threshold voltage,  $V_T$ , of the device. During accumulation (the on-state of the device), drain-source bias ( $V_{DS}$ ) affects the voltage drop in the channel. Small  $V_{DS}$  results in resistor-like behavior, also known as the linear (a.k.a. triode) region as shown in Figure 1.3c. However, a sufficiently large  $V_{DS}$  creates a large voltage drop in the channel, which drops below the threshold voltage near the drain. This drop causes the channel to pinch off carriers and enter the saturation region, pinning the channel voltage drop to  $V_{GS}-V_T$ . Equations 1.2 and 1.3 describe the channel current in the linear and saturation regions, respectively, according to square-law theory[67, 170], where  $W$  (cm),  $L$  (cm),  $\mu$  ( $\text{cm}^2/\text{Vs}$ ), and  $C_{OX}$  ( $\text{F}/\text{cm}^2$ ) are channel width, channel length, mobility, and gate capacitance, respectively. However,



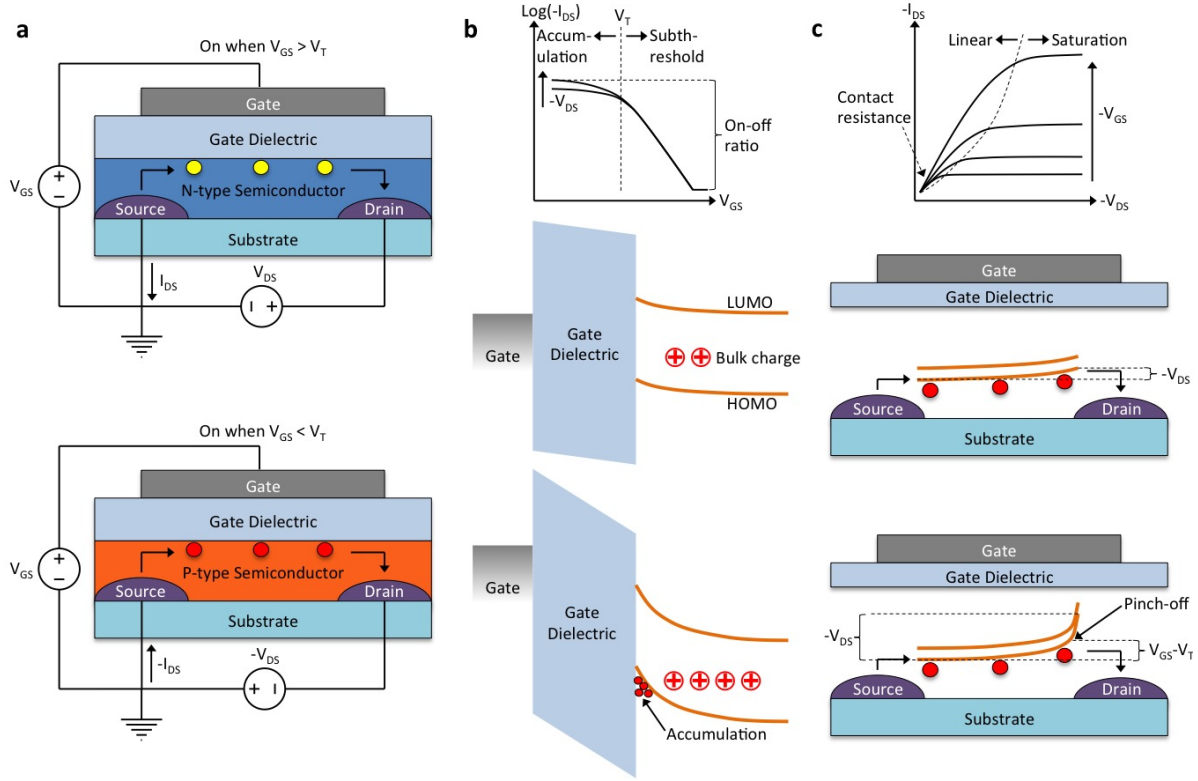


Figure 1.3: (a) Operation and biasing of TFTs with n- and p-type semiconductors. (b) Figures of merit and carrier behavior in transfer characteristic sweep (constant  $V_{DS}$ , changing  $V_{GS}$ ) for a p-type TFT. (c) Figures of merit and carrier behavior in output characteristic sweep (constant  $V_{GS}$ , changing  $V_{DS}$ ) for a p-type TFT.

square-law theory is an ideal approximation for TFT behavior since it neglects the effect of  $V_{GS}$ -dependent bulk-charge, thus overestimating the conductance of the channel. In addition, this model assumes negligible contact resistance. Constants such as  $\mu$  and  $C_{OX}$  also vary as a function of  $V_{GS}$  and sweep rate, respectively, in most solution-processed semiconductors.

$$I_{DS,linear} = \frac{W}{L} \mu C_{OX} (V_{GS} - V_T) V_{DS} \quad (1.2)$$

$$I_{DS,saturation} = \frac{W}{2L} \mu C_{OX} (V_{GS} - V_T)^2 \quad (1.3)$$

Mobility is the most commonly utilized figure of merit ascribed to TFTs in literature[9, 190] because it quantifies the conductivity of the channel in the on-state. This parameter directly affects the contact resistance of the device in the linear region, as shown in Figure

1.3c. Increasing  $C_{ox}$  or channel  $W/L$  ratio can further reduce this contact resistance. This reduction allows for faster discharge of image sensor pixel assuming the RC time constant of the pixel is limited by the resistance of the TFT channel and capacitance of the photodetector. In addition to mobility and contact resistance, on-off ratio, as shown in Figure 1.3b, is another important figure of merit. A high on-off ratio minimizes parasitic discharge of the pixel in the off-state while maintaining fast discharge in the on-state, allowing for higher SNR and arrays with larger number of rows.

Metal oxide TFTs are typically n-type and can be solution-processed[190]. However the high annealing temperatures of oxide semiconductors makes them incompatible with flexible plastic substrates. Organic semiconductors allow low-temperature solution processing that is compatible with plastic substrates[9]. While there exist high performance n-type solution-processed organic materials[187], the majority of organic semiconductor exhibit p-type behavior. Crystallization is an important factor for organic devices in order to maximize mobility and on-off ratio. Crystallization can be controlled by nucleation points[35, 52], solvent evaporation[121, 135], and surface energy modification via substrate self-assembled monolayers[94] or additives to promote vertical segregation[57, 159]. In addition to optimizing the channel of the device, minimizing the channel length also increases device speed provided a low contact barrier between the semiconductor’s HOMO and electrode work function for p-type devices. Solution processing techniques for achieving short channel lengths include highly scaled gravure printing[49, 92], offset printing [45], and surface energy patterned inkjet printing[152]. Other important optimization factors in organic devices include the semiconductor-dielectric interface, which must have as little scattering as possible in order to maximize mobility[83, 97]. There is a general correlation between large gate dielectric constants leading to poor mobility since the large polarization of these molecules induces more scattering of charge carriers at the channel-dielectric interface[97].

## Photodiodes & Figures of Merit

Photodiodes are two terminal devices that behave as a light-dependent current source in parallel with a diode as pictured in the inset of Figure 1.4a. This is the photodetector element implemented in most commercial visible light image sensors due to its high sensitivity, low leakage current and simplicity of fabrication. With regards to large area image sensors, it is advantageous to employ solution processable organic or Perovskite materials due to their low deposition cost per area and inherit flexibility [5, 95]. The photoactive layer of organic photodiodes uses donor (hole accepting) and acceptor (electron accepting) materials with LUMO and HOMO that serve as electron and hole transporting energy bands, respectively. Sandwiched across the photoactive layer is an anode, a hole selective electrode, and a cathode, an electron selective electrode. As shown in step 1 of Figure 1.4a, the low dielectric constant of organic materials causes photoexcited electron-hole pairs to become coulombically bound, which is known as an exciton. It’s only when this exciton diffuses towards a donor-acceptor

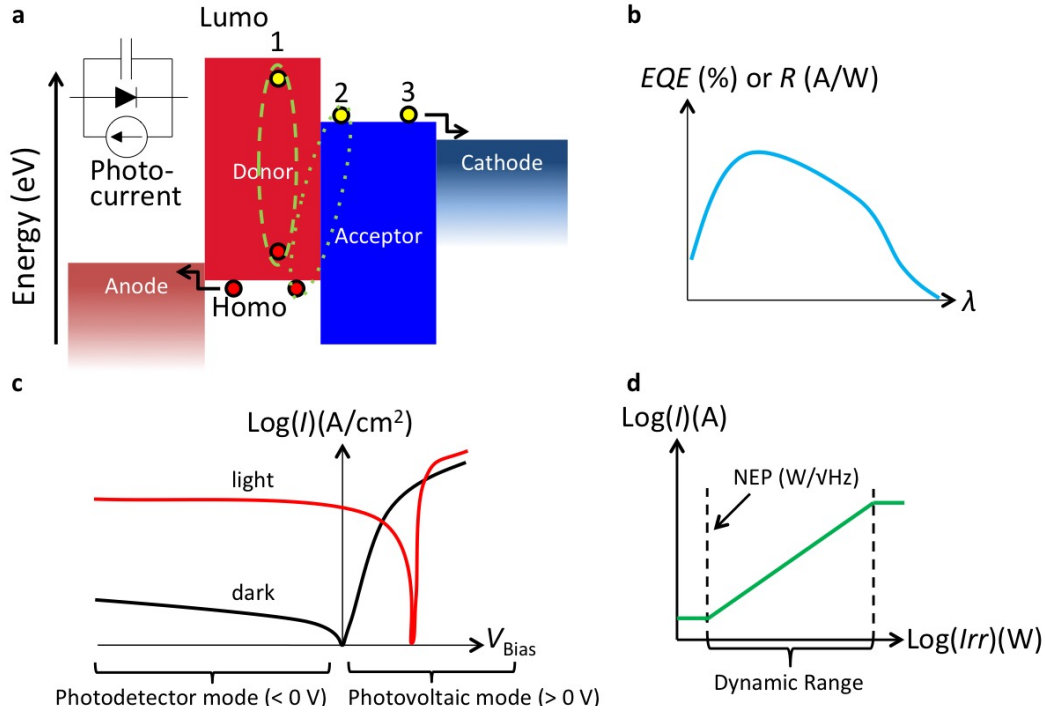


Figure 1.4: (a) Band diagram of an organic photodiode depicting charge generation and collection and the equivalent circuit. (b) Qualitative depiction of external quantum efficiency (EQE) and responsivity ( $R$ ) for a photodetector. (c) Typical photodiode current-voltage characteristics in dark and under illumination. (d) Illustration of dynamic range for a photodetector.

interface as shown in step 2 that the higher electron affinity (lower LUMO) of the acceptor material and lower ionization potential (higher HOMO) of the donor material causes the exciton to dissociate into a free electron and hole in the acceptor and donor, respectively. Most organic photodiodes use a bulk heterojunction (BHJ) active layer, which is the mixture of donor and acceptor materials in order to increase surface area across which excitons may be dissociated. The free electrons and holes are then transported through the acceptor and donor and collected at the cathode and anode, respectively, ideally without recombination. Perovskite materials are usually not composed of a donor or acceptor components as the dielectric constant for these materials is significantly higher than organics, which permits excitons to freely dissociate into free carriers via thermal energy[122].

The figures of merit used to assess photodiode performance also have a direct impact on image sensor performance. External quantum efficiency (EQE) is defined as the ratio of the rate of extracted photogenerated electrons from a device over the rate of incident photons radiated on the photoactive area. EQE is typically expressed as a function of incident light

wavelength as shown in Figure 1.4b. Alternatively, EQE can be equivalently expressed as the output current per watt of irradiance, this is known as responsivity ( $R$ ). Current density vs. bias voltage characteristics are also instrumental for assessing proper device in dark and illuminated conditions as shown in Figure 1.4c. Photodiodes are reversed biased ( $V_{\text{Bias}} < 0$  V) to create a larger electric field in the device to extract carriers before recombination. Additionally, reverse biasing the photodiode results in lower injection current in dark conditions (known as dark current) compared to the photovoltaic biasing regime ( $V_{\text{Bias}} > 0$  V). An ideal photodiode should have a high difference between light and dark current at a reverse bias in order to enable the highest SNR. In terms of device performance, the EQE should be high to create a large light current and the leakage across the diode should be minimal to minimize dark current. A photodiode that maintains a high SNR at large reverse bias translates into a larger well capacity since the capacitance of the diode itself is used to store charge (more details in the section on passive integrating image sensors). Observing current density as a function of light intensity enables the determination of dynamic range, which is the range of irradiance over which the photodiode exhibits a measurable change in photocurrent. This figure of merit can either be expressed as the ratio between the highest and lowest light intensity or that ratio in decibel format[65] as shown in Equation 1.4 and illustrated in Figure 1.4d.

$$\text{Dynamic Range (dB)} = 20 \log_{10} \left( \frac{I_{\text{upper}}}{I_{\text{lower}}} \right) \quad (1.4)$$

A linear dynamic range response (constant EQE across a wide range of irradiance) is usually desired for photodiodes. However, sublinear responses are often seen in disordered materials such as organics and nanomaterials[10, 19, 178]. While these responses may not be ideal for certain radiometric applications, they can be advantageous for improving the dynamic range of an imaging system[65] as will be later discussed in the section on passive charge integrating image sensors. The dynamic range of photodiodes is typically limited by the noise of dark current at low irradiances. The dark current noise in its simplest form is expressed as the shot noise of the current flow, which behaves according to Poisson statistics. The noise, or standard deviation, of a Poisson process is defined as the square root of the flux of electrons per second. Additionally, excessive trap states within the band gap of the photodiode can lead to  $1/f$  noise on top of shot noise. Equation 1.5 shows how dark current and charge trapping affect the noise spectral density ( $S$ ) of a photodiode.

$$S \left( \frac{\text{A}}{\sqrt{\text{Hz}}} \right) = \sqrt{N_{\text{Shot}}^2 + N_{\text{Trap}}^2} = \sqrt{(2qI_{\text{Dark}}) + N_{\text{Trap}}^2} \quad (1.5)$$

Two equivalent figures of merit used to express the performance of a photodiode at low irradiances are noise equivalent power ( $NEP$ ) and specific detectivity ( $D^*$ ).  $NEP$  is the theoretical lowest measurable irradiance (SNR=1) for a 1 Hz integration bandwidth

(or equivalently half second integration time according to Nyquist-Shannon sampling theory[147]). Figure 1.4d qualitatively shows that the *NEP* marks the lowest point on the dynamic range. *NEP* can be quantified by Equation 1.6, which is the noise spectral density divided by the responsivity of the photodiode. Specific detectivity is defined by Equation 1.7 and is inversely proportional to *NEP* and normalized to area (*A*) since  $S \propto \sqrt{I} \propto \sqrt{A}$ . This area normalization is important in order to allow a fair comparison between various photodiodes since, as previously discussed, SNR increases with area.

$$NEP \left( \frac{W}{\sqrt{Hz}} \right) = \frac{S}{R} \quad (1.6)$$

$$D^* \left( \frac{cm\sqrt{Hz}}{W} \right) = \frac{\sqrt{A}}{NEP} \quad (1.7)$$

The frequency response of a photodiode is a figure of merit applicable to image sensors. This is typically characterized by the cutoff frequency ( $f_{3dB}$ ), which is the frequency at which the peak output current from a sine-modulated light source is lowered by 3 dB from lower frequencies. A high cutoff frequency is indicative of fast charge extraction from the device, which minimizes image lag in image sensors[126, 166].

There have been many developments in the literature on solution processed photodiodes, which typically attain EQEs and dark currents anywhere from 20-60% and 10-1,000 nA/cm<sup>2</sup>, respectively[10, 50]. More recently, many studies have been aggressively investigating new physical mechanisms to create low noise, high frequency, spectrum selective and fully printable photodiodes.

Much of the prior art from the organic and Perovskite solar cell community on the effect of active layer film thickness, solvent composition and donor-acceptor ratio on morphology[14, 29, 60, 131] and device physics[19] was used to obtain similar EQEs in solution processed photodiodes. However, reverse bias dark current and frequency response was rarely investigated in the context of photovoltaics and has been optimized for photodiodes in several ways. Increasing the thickness of the active layer beyond a micrometer can significantly drop the dark current to values below 1 nA/cm<sup>2</sup> without a significant compromise in cut-off frequency[6, 126]. Reduced dark current also achieved when hole and electron blocking layers at the cathode and anode, respectively, are used to improve charge selectivity at the electrodes[10, 50]. This becomes especially important in low band gap systems where Schottky barrier at the electrodes is lower[18]. It has been shown that organic interlayers in Perovskite photodiode to decrease the dark current to between 1-10 nA/cm<sup>2</sup> under reverse bias while maintaining response times of approximately a microsecond[41, 109] as shown in Figure 1.5a. Subsequent power spectrum measurements revealed the noise spectral density of these devices is indeed very close to the shot noise theoretical limit, which is believed to

be the result of surface defect passivation from the interlayers[41]. Interface engineering is important when optimizing frequency response. Arca et. al. have shown that frequency response in BHJ organic photodiodes deteriorates significantly at low irradiances as a result of carrier trapping at interfaces, which can be ameliorated by choosing a suitable interlayer[3].

The absorption spectrum of a photodiode can be made broader to image at longer wavelengths. Conventional organic or Perovskite photovoltaic materials show a broad absorption with cutoff wavelengths typically around 900 nm. This is because the optimal band gap for power conversion efficiency is 1.34 eV ( 925 nm) according to the Shockley-Queisser limit[157]. Gong et. al. took the first step to synthesizing custom-made polymers for very broadband photodiodes with a spectral response from 300 to 1450 nm[51]. A later study synthesized a polymer with a low cutoff wavelength of 1000 nm for photodiode use[196]. By using a superior electron-blocking layer, the dark current was reduced to a few nA/cm<sup>2</sup> while maintaining an  $f_{3dB}$  of 400 kHz. Quantum dots, which can have low band gaps, can also be embedded in photodiodes to extend the responsivity of the device to wavelengths as long as 1800 nm[139].

Conversely, it is also possible to narrow the spectral response of photodiodes. The drive for color filter-less image sensors has led to the development of materials with narrow absorption bands in the red, green and blue regions[2, 154, 153]. Meredith et. al. have shown that even broadband materials can be used to create narrow spectral selectivity by significantly increasing the active layer thickness[6]. Figure 1.5b shows that the lower extinction coefficients of wavelengths near the absorption cutoff penetrate further and more uniformly into the device where electrons are more likely to be extracted at the cathode. However, the high absorption well below the cutoff wavelength results in a significant amount of recombination at the front of the device as a consequence of space charge accumulation of electrons.

The majority of literature on solution-processed photodiodes utilizes spin coated active layers with vacuum-deposited electrodes on rigid substrates. While synthesizing soluble functional materials is a pre-requisite to creating printable devices, it is important to create printed devices since the printing process can present challenges or new opportunities never realized with conventional microfabrication[5, 96]. The discovery of solution-processable work function reducing interlayers such as polyethylenimine ethoxylated (PEIE)[197] and conjugated polyfluorene electrolytes[70] opened many possibilities in printed electronics as soluble low work function conductors are not available. Caironi et. al. initially reported fully solution processed photodiodes using inkjet printing and PEIE to reduce the work function of the silver or PEDOT:PSS cathode[8, 130]. Organic photodiodes printed using a combination of blade coating and screen printing reported by Pierre et. al. showed mean dark currents as low as 150 pA/cm<sup>2</sup> and specific detectivities as high as  $3.4 \times 10^{13}$  [137]. As shown in Figure 1.5c, these devices displayed high specific detectivity under a large applied electric field in comparison to other devices[7, 40, 55, 100, 114], which is important for maximizing well capacity in image sensors as will be discussed in the section of passive charge

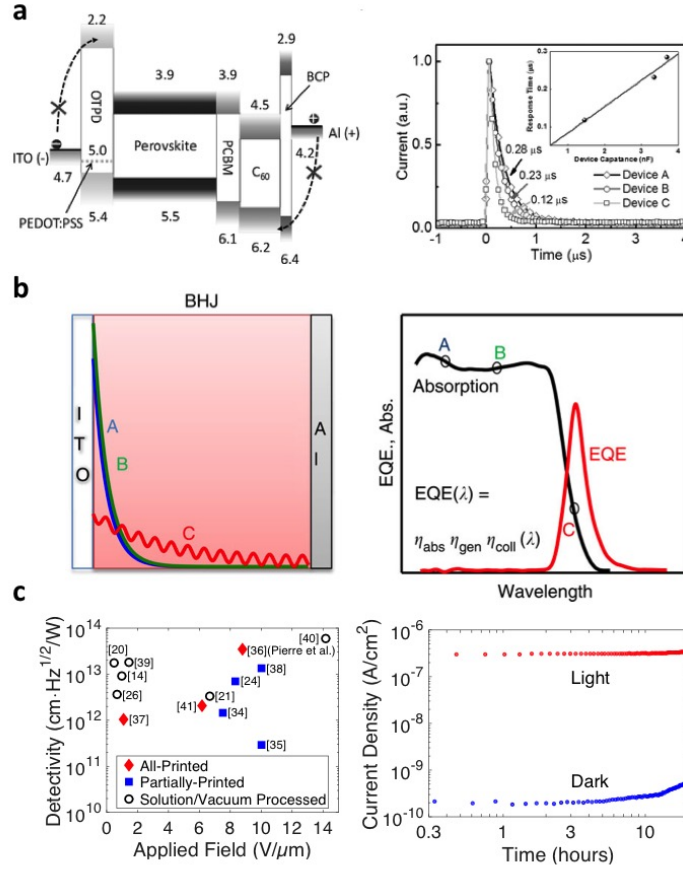


Figure 1.5: (a) Organic blocking layers in a Perovskite photodiode and its dynamic response. (b) Filterless organic photodiodes enabled through thick active layers and the resulting EQE spectrum. Reprinted with permission from [6]. Copyright 2015 Nature Publishing Group. (c) Detectivity as a function of applied field across the device for various photodiodes cited in this review along with the bias stress stability of an organic photodiode. (a) and (c) Reprinted with permission from [41] and [137], respectively. Copyright 2015 John Wiley and Sons.

integrating image sensors. The bias stability of these devices is shown in Figure 1.5c, which is an important consideration in imaging systems as photodiodes are biased continuously. More information on printing techniques for solution processable electronics can be found in a review by Krebs[96].

## Phototransistors & Figures of Merit

Phototransistors can also be used as the photodetector element in image sensors. This device has three terminals, unlike two-terminal photodiodes, and behaves like a regular thin film transistor (TFT) in the dark. Such devices consist of a conductive channel with unipolar source and drain electrodes on either side with the conductivity of the channel controlled by a gate terminal. However, the TFT behavior of these devices changes upon light exposure for a couple of reasons.

Phototransistors can operate as a photoconductor as shown in Figure 1.6a for a p-type device (hole transporting). The transverse field created by the gate electrode assists the spatial segregation of photogenerated electron-hole pairs. However, since both source and drain contacts are hole-selective, the photogenerated electron stays in the channel while the photogenerated hole is extracted at the drain. The accumulation of electrons in the channel results in a shift in threshold voltage, causing more holes to be injected in order to neutralize the electrons[10, 56]. New holes will be injected into the channel at the source electrode until a recombination event occurs between an injected hole and the photogenerated electron. If the transit time of a hole across the device ( $\tau_{transit}$ ) is less than the lifetime of the electron ( $\tau_{lifetime}$ ), then multiple holes can be injected into the channel of the phototransistor for a single photogenerated electron-hole pair. This phenomenon, known as photoconductive gain (G), can result in EQEs well over 100% as denoted by Equation 1.8[10, 24, 56].

$$G = \frac{\tau_{lifetime}}{\tau_{transit}} \quad (1.8)$$

The response time of phototransistors in the photoconductive regime is usually limited by the lifetime of the minority carrier and not the comparatively fast transit time of the majority carrier. Consequently, devices that exhibit high photoconductive gain cannot operate as quickly as a photodiode with the same transit time. Photoconductive gain decreases with increasing irradiance for a couple of reasons. The first is that electrons generated at low irradiances fill deeper trap states that have longer recombination lifetimes, with higher irradiances resulting in electrons filling shallower trap states that have shorter lifetimes[184]. The second reason is that the shift in threshold voltage is proportional to the logarithm of the irradiance[10, 169], resulting in decreased sensitivity at higher light intensities.

Phototransistors can also operate in a charge-trapping regime in which photogenerated electrons (in a hole-transporting device) become lodged in deep trap states in the channel of the device as shown in Figure 1.6b. This trapping results in a shift in the threshold voltage of the phototransistor during normal transistor bias sweeps, even after the illumination has stopped. The lifetime of these trap states may even be as long as days[194]. These electrons can be de-trapped through a large gate bias, effectively resetting the phototransistor. For this reason, phototransistors operating in charge-trapping mode with exceptionally long trap



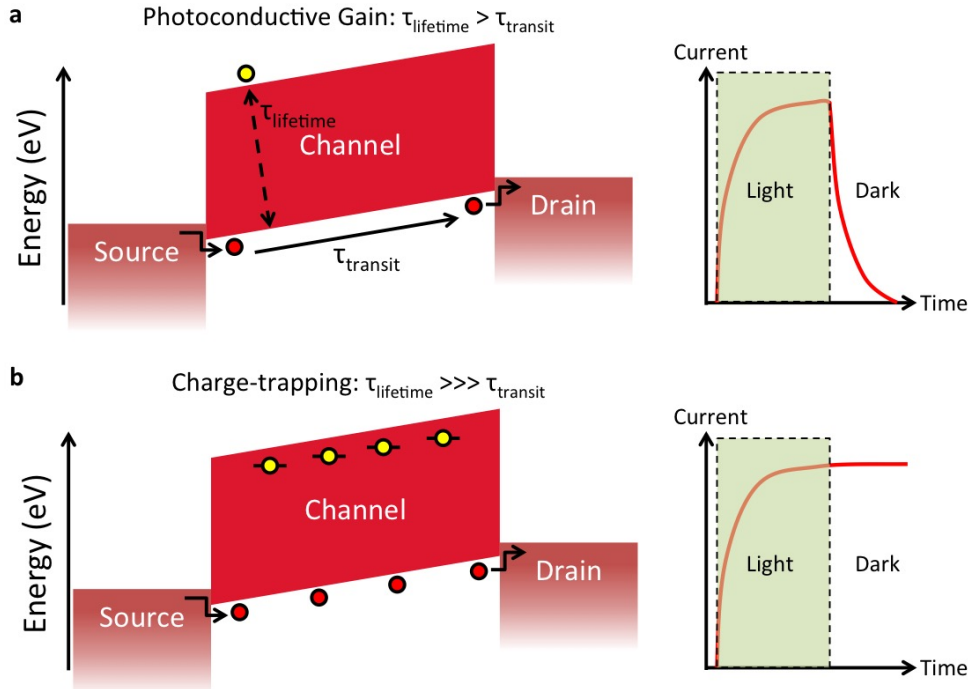


Figure 1.6: (a) Hole (red) and electron (yellow) movement in a hole-transporting phototransistor with photoconductive gain and the dynamic response shown to the right. (b) Charge carrier movement in the same phototransistor but operating in a long-term charge-trapping regime.

state lifetimes are sometimes referred to as memory devices[194]. Phototransistors often operate in a combination of both the photoconductive gain and charge-trapping regime since both of these mechanisms involve the lifetime of minority carriers but at different time scales.

Responsivity is frequently used as a figure of merit for phototransistors. Yuan et. al. have closely examined the behavior of C8-BTBT phototransistors, which provide the highest photoconductive gain seen in literature to the best of our knowledge[191]. One key observation is that the photoconductive gain is significantly higher in phototransistor than in a thin film photoconductor of the same device geometry. This difference in gain is speculated as a result of the transverse field induced by the gate segregating electrons and holes, thus reducing the probability of recombination. The very long recombination lifetime of electrons in C8-BTBT (seconds) and high mobility of  $20 \text{ cm}^2/\text{Vs}$  results in a responsivity over  $10^5 \text{ A/W}$ . The low defect density of the highly crystalline semiconductor also resulted in noise spectral density on par with the theoretical shot noise limit. However, the long electron lifetime means that the device takes hundreds of seconds to turn off unless a large gate pulse is applied. Yan et. al. have achieved high gain through embedding wide band gap metal

oxide nanoparticles in an organic semiconductor[186]. The gain obtained is at most an order of magnitude lower than Yuan et. al.'s, but the turnoff time was over  $10^2$  times faster.

Photoconductive gain mechanisms can also be implemented in a photodiode architecture using embedded nanoparticles. Guo et. al. initially demonstrated this concept by creating P3HT photodiodes with a sparse concentration of isolated ZnO nanoparticles[55]. Electron trapping in the ZnO under illumination creates photoconductive gain. Additionally, electron trapping near the anode causes significant band bending which results in trap-assisted hole injection to create higher gain as shown in Figure 1.7a. The short travel distance of the carriers in a photodiode structure also decreases recombination lifetimes to under 1 ms while retaining a responsivity of over 1000 A/W. It was shown in a later study that a trade-off exists between photoconductive gain and cut-off frequency in photodiodes[105]. Low nanoparticle concentrations led to high gain due to the good isolation of small nanoparticle clusters but significantly longer de-trapping times, whereas high nanoparticle concentrations led to a more continuous network which didn't promote good charge trapping but significantly decreased de-trapping times. Similar reports were shown for Perovskite[37] and organic[58] and hybrid[36, 155] photodetectors.

While conventional high-performance solution processable TFT semiconductors can be used as phototransistors, the wide band gap and low absorption coefficient of these materials limits their performance outside the UV spectrum. Several strategies have been shown in the literature to address the poor optical properties of conventional TFTs. The first strategy is to employ the same BHJ active layer morphology frequently used in OPDs in phototransistors. Xu et. al. have reported a BHJ phototransistor with a cutoff wavelength of 900nm and high responsivity of over  $10^5$  A/W at light intensities below 100 nW/cm<sup>2</sup> [184]. The hole mobility of their devices ( $0.3 \text{ cm}^2/\text{Vs}$ ) is significantly higher than that of conventional BHJ OPDs ( $\leq 10^{-4} \text{ cm}^2/\text{Vs}$ )[10], which enables a response time of 40 ms. A similar concept was later shown by Han et. al. demonstrated a BHJ phototransistor with a low cutoff wavelength of 1000 nm as shown in Figure 1.7b[59]. Another alternative to improve the optical properties of phototransistors is to use Perovskite materials, which typically show similar optical properties and improved charge carrier mobility in comparison to organics. Li et. al. have demonstrated a Perovskite ambipolar transistor with a responsivity of over  $10^2$  down to 800 nm [104]. The high charge carrier mobility of over  $1 \text{ cm}^2/\text{Vs}$  enabled very fast response times of under 7  $\mu\text{s}$ . A hybrid device scheme can also be used to leverage the electronic or photonic properties of each layer. For instance, Rim et. al. deposited a BHJ on top of a high mobility indium gallium zinc oxide (IGZO) TFT to form a phototransistor[143]. A specific detectivity over  $10^{12}$  Jones was demonstrated for their devices, with minimal persistence of photocurrent and at least 7 orders of magnitude linear dynamic range.

In addition to the channel of phototransistors, other layers of the device such as the electrodes and gate dielectric are printable. All-printed phototransistors on a flexible polyimide substrate demonstrated by Kim et. al. highlight several commonly used printing

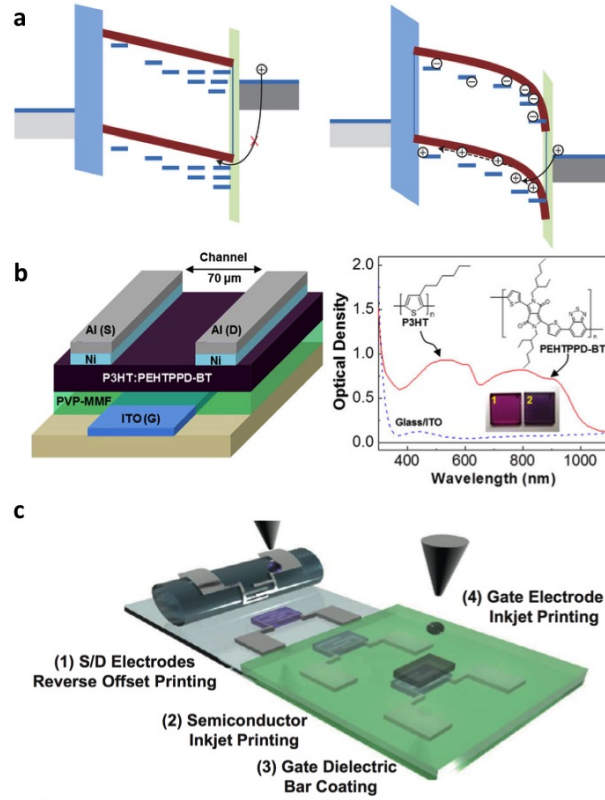


Figure 1.7: (a) Interfacial trapping of photogenerated carriers used to inject charge from an electrode as a gain mechanism. Reprinted with permission from [55]. Copyright 2012 Nature Publishing Group. (b) Broadband bulk heterojunction phototransistor. Reprinted with permission from [59]. Copyright 2015 Nature Publishing Group. (c) Fabrication steps for an all-printed phototransistor. Reprinted with permission from [87]. Copyright 2014 Elsevier.

techniques as shown in Figure 1.7c[87]. Inkjet printing was used to directly pattern the photoactive material and gate electrode with the gate dielectric uniformly bar coated in between. Reverse offset printing defined the channel geometry of  $W/L = 1000 \mu\text{m}/20 \mu\text{m}$ . This high throughput printing technique can even create channel lengths below  $1 \mu\text{m}$ [45]. Self-assembly processes can also achieve sub micron channel lengths. Wang et. al. utilized inkjet printing of solubilizing solvents on ultrathin PMMA (a photoresist) to create thick coffee-ring induced ridges[179]. Subsequent deposition of metal and removal of the PMMA defines channel lengths of  $700 \text{ nm}$ , which greatly enhanced the responsivity of longer channel devices since the transit time of injected holes is shorter. A high responsivity of  $10^6 \text{ A/W}$  with an average TFT mobility of  $1.2 \text{ cm}^2/\text{Vs}$  was reported.

## 1.4 Passive Pixel Image Sensors without Charge Integration

### Theory

Passive pixel sensors transfer the raw photogenerated signal from the photodetector element directly to the column line. This direct transfer of the photogenerated signal means that no amplification (gain of unity) of the signal occurs within the pixel as shown in Figure 1.1a. A passive pixel can integrate photogenerated charge during the frame period as previously discussed in the fundamental principles of image sensors. However, a passive pixel can also simply consist of a photodetector directly addressed by the row and read out instantaneously by the column line, rather than integrated, as symbolized for both a photodiode and phototransistor in Figure 1.8a and b, respectively. The inherent disadvantage of this design is that the SNR of a non-integrated pixel is significantly lower compared to an integrating one as mentioned previously in the fundamentals of image sensors. This compromise in the quality of the signal means that the array can only be scanned at impractically slow frame rates. Despite this disadvantage, constructing passive non-integrating image sensors is still a valuable step in demonstrating the scalability, functional device yield, uniformity and performance of photodetector elements.

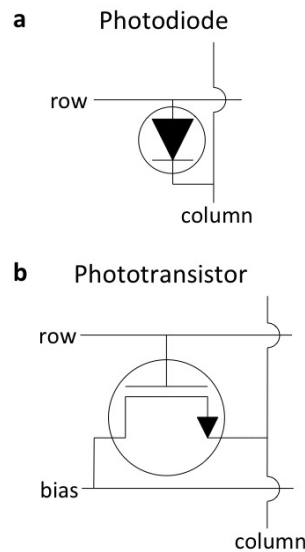


Figure 1.8: (a) Photodiode and (b) phototransistor-based passive pixel architecture for image sensors not using intra-pixel charge integration.

## Case Studies

Solution processable semiconducting polymers revolutionized the research field of photovoltaics by enabling the possibility of low-cost, large-area and flexible solar modules[53]. As such, the optimization of the materials to create high performance solar cells also enabled the development of arrays of photodiodes (pixel architecture of Figure 1.8a) used as image sensors. Yu et. al. were the first to demonstrate the capability of such solution processed solar cells to act as photodiodes in an image sensor by downscaling the electrode spacing between each solar cell and increasing the total pixel count along a linear array as shown in Figure 1.9a[189]. Poly(3-octylthiophene) (P3OT) was used as the donor polymer due to its absorption over the whole visible spectrum, which was difficult with the wider band gap polymers commonly used at the time of publication[53]. These devices showed good photodiode behavior ( $<10$  nA/cm<sup>2</sup> dark current and 45% EQE at -10 V bias) and sufficiently high uniformity over the 102 pixels in the linear array to be used as an image scanner. Additionally, the high resistivity and high absorptivity of organic materials enabled thin device active layers with negligible crosstalk between pixels even for an un-patterned active layer. A later account by Xu et. al. took advantage of the mechanical robustness of organic systems by implementing the same array architecture on a deformable plastic substrate[185]. This was motivated by the idea that conformable image sensors could minimize the amount of optics that are required to focus the image plane on conventional planar image sensors. Metal grid lines were deposited on the substrate by direct pattern transfer of thermally evaporated gold or silver from a deformed PDMS mold.

Flexible phototransistor arrays have also been implemented in a non-integrating passive pixel architecture as shown in Figure 1.8b. Saito et. al. utilized the photosensitivity of a conventional pentacene transistor to form a photodetector array with a microlens array on flexible substrate[145]. However, the poor absorption and responsivity of pentacene to light requires high irradiances ( $>2$  mW/cm<sup>2</sup>) in order to measure an appreciable change in on-current. However, Chu et. al. have recently shown that the choice of gate dielectric can tune the charge trapping properties of DNTT phototransistors to significantly improve imaging performance[33]. Using polylactide (PLA) as the gate dielectric significantly lowers mobility in the dark, but significantly increases it when photogenerated charges are trapped along with a positive shift in threshold voltage. This also results in a significantly faster response time of only 50 ms, which may be practical at video frame rates. The absorption spectrum of the aforementioned phototransistor image sensors is often limited to blue and UV wavelengths as a result of the large band gap of high performance organic semiconductors such as pentacene and DNTT. Liu et. al. have demonstrated that the responsivity of conventional phototransistors can be significantly enhanced by inserting a strong absorbing layer on top of a high mobility semiconductor as depicted in Figure 1.9b[112]. A ruthenium complex with a broad absorption spectrum is used to enhance the responsivity of the phototransistors by a factor of almost  $10^3$  in the off-regime with a drop in mobility by only a factor of 2 in the on-regime. This enables the capture of images at a relatively low light irradiance of 1.5  $\mu$ W/cm<sup>2</sup>.

Memory devices can also be used as passive pixel image sensors. These devices enable global shutter array operation, which is the simultaneous capture of light information on all pixels across an array, as shown in Figure 1.1c. Global shutter reduces motion artifacts seen in a rolling shutter sequence illustrated in Figure 1.1b since row addressing during image capture is not necessary. Nau et. al. have demonstrated a passive pixel array consisting of pixels with an organic non-volatile resistive switch in series with an organic photodiode[123]. A sufficiently large voltage pulse is supplied across the pixel during illumination. The voltage drop across the photodiode decreases with increasing illumination (due to its higher photoconductivity), which increases the voltage across the resistive switching element beyond a threshold voltage that then triggers a change in resistance. The irradiance that the pixel

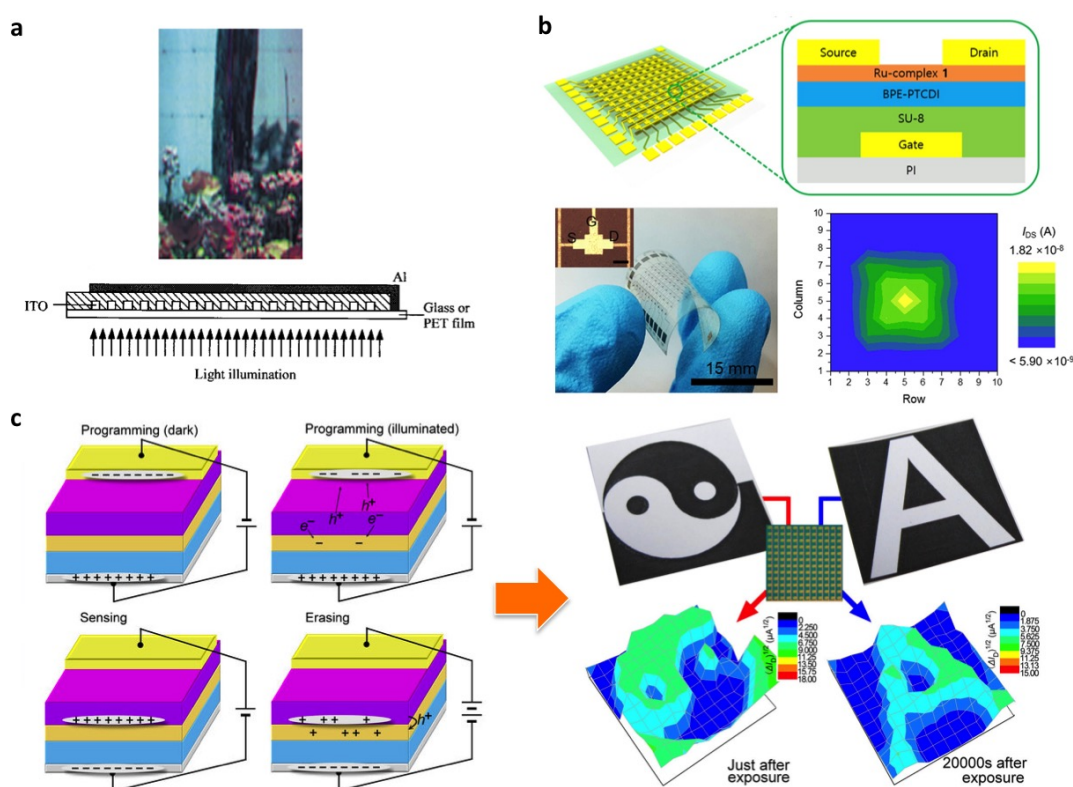


Figure 1.9: (a) Reproduced color image scanned by a linear array of organic photodiodes. Reprinted with permission from [189]. Copyright 1999 John Wiley and Sons. (b) An array of phototransistors based on charge transfer to a semiconductor from a light-absorbing dye. Reprinted with permission from [112]. Copyright 2016 American Chemical Society. (c) Light-programmable organic phototransistor memory devices and an imaging array. Reprinted with permission from [194]. Copyright 2013 Nature Publishing Group.

Type of Photodetector	Image Measurement	Pixel Device Processing & Materials	Lowest Imaged Irradiance ( $\mu\text{W}/\text{cm}^2$ ) @ $\lambda$	Bending Radius (mm)	Reference
Photodiode	Photodiode current	Soluble organic	$\simeq 10^{-3}$	Rigid substrate	[189]
	Photodiode current	Evaporated organic	2 @ 633 nm	10 (curved but not flexible)	[185]
Phototransistor	Channel current from $\Delta$ conductance	Evaporated organic	$2 \times 10^3$	20	[145]
	Channel current from $\Delta$ conductance & $V_T$	Evaporated organic	20 @ 450 nm	Flexible but not measured	[33]
	Channel current from $\Delta$ conductance	Soluble light absorber on evaporated organic	1.2 @ 450 nm	1	[112]
Memory	Photodiode current (after light exposure)	Evaporated resistive switch memory on soluble organic	1.5	Flexible but not measured	[123]
	Channel current from $\Delta V_T$ (after light exposure)	Evaporated organic on soluble organic	40	Flexible but not measured	[194]
Inorganic	Photoconductive current	Blade coated Perovskite	30 @ 550 nm	5	[34]
	Photodiode current	Sputtered ferroelectric	$10^5$ @ 658 nm	32	[30]
	Channel current from $\Delta$ conductance	CVD/sol-gel nanowires	$\simeq 100$	Rigid substrate	[113]

Table 1.1: Properties of solution-processed non-charge-integrating passive pixel image sensors.

sensed can then be readout at a later time by examining the resistance of the pixel at a small bias, and reset by applying a large bias for the next image. Charge trapping can also be used within a device to create long-term storage memory devices. Zhang et. al. have shown that inserting an electron acceptor at the semiconductor-dielectric interface of a phototransistor enables long-term storage of photogenerated electrons[194]. The electrons are accumulated at the interface with a positive gate bias as shown in Figure 1.9c. This accumulation results in a positive threshold voltage shift with increasing light intensity, which can be sensed at low gate voltages and reset at high negative biases. Optimization of the electron accepting layer led to long charge retention, with the sensed current only decreasing by 8% after 20,000 seconds, and high performance transistor properties with mobility over  $2 \text{ cm}^2/\text{Vs}$  and on-off ratios of  $5 \times 10^6$ . Such high performance transistor and photodetector properties in a single device could also enable active pixel circuits.

While organic materials have long been the choice of solution processable and flexible systems, photodiode image sensor arrays have recently been demonstrated with novel photoactive materials. Perovskites have been shown to form high performance photoconductor image sensors through blade coating by Deng et. al[34]. Not only is the material stable for weeks in air, it is extremely resilient to strain with no observable change in current-voltage behavior after 100,000 bending cycles. Ferroelectrics are a class of materials that have been extensively studied for applications of memory in microelectronics[73] but can also be used as large area image sensors as demonstrated by Chin et. al[30]. Their initial results show photodiodes constructed on flexible steel foil with low dark currents. Solution processable II-VI semiconductor nanowires have also been processed into a passive image sensor from sol-gel by Liu et. al[113]. Their phototransistors have mobilities ranging from 4 to  $28 \text{ cm}^2/\text{Vs}$  depending on the S:Se ratio, which also adjusts the band gap. Using these tunable band gaps, they were able to fabricate a multicolor imager without the need of optical filters.

## 1.5 Passive Pixel Image Sensors Capable of Charge Integration

### Theory

Passive image sensors have the capability to integrate photogenerated charge during the period of a frame. As previously mentioned, integration of photogenerated charge significantly improves the SNR of the light signal from a pixel compared to direct current sampling at a given frame rate. Figure 1.10a illustrates the array layout and pixel architecture for an integrating passive pixel sensor, a transistor in series with a photodiode (1T), and charge amplifier on each column to sample the integrated charge. The pixel circuit with all relevant capacitances is shown in Figure 1.10a as well. The intrinsic capacitance of the photodiode ( $C_{PD}$ ) is used as the integrating capacitor. Photodiodes are ideal for 1T pixels since the



large surface area and short spacing of the electrodes provides the large capacitance needed to maximize well capacity.

The ideal operation of a 1T pixel is illustrated in Figure 1.10b. When the TFT is on, the voltage of the photodiode anode ( $V_{PD}$ ) is set to zero while the cathode is biased at a positive voltage (making the device reverse biased). After the TFT is turned off,  $V_{PD}$  increases as  $C_{PD}$  accumulates photogenerated charge during the frame period. Opening the TFT discharges the accumulated photogenerated charge and resets the photodiode back to its original reverse bias for the next frame. The ideal discharge rate is governed by a time constant  $R_{on} C_{PD}$ , where  $R_{on}$  is the resistance of the TFT in the linear regime. The transistor typically remains open for several time constants in order to discharge as many carriers as possible to minimize image lag. The off-state resistance of the TFT,  $R_{off}$ , must also be high to ensure that  $R_{off} C_{PD}$  is much greater than the frame period to minimize discharge during the integration.

Parasitic capacitances substantially affect the performance of image sensors by inducing parasitic charge injection that creates readout noise and lower discharge rates. The drain-source capacitance is extremely small in thin film transistors and thus has a negligible effect on pixel performance. Additionally, minimal parasitic charge injection occurs from bias-column line capacitances since the column line is grounded and the bias voltage is constant. However, the gate-drain capacitance ( $C_{GD}$ ) slows the switching speed of the transistor and induces parasitic charge transfer onto the photodiode[166]. The time constant of the discharge changes to  $R_{on} (C_{PD} + C_{GD})$ , and  $V_{PD}$  decreases by  $(C_{GD} \Delta V_G) \times C_{PD}$  when the pixel enters integration mode (TFT off) as shown in Figure 1.10b, which limits well capacity. Gate-source ( $C_{GS}$ ) capacitance results from overlapping gate and source electrodes and also from intersecting row and column lines. Since the column line is connected to virtual ground from the charge integrator a parasitic charge of  $C_{GS} \Delta V_G$  is injected onto the column line when the TFT is turned on. It should be noted that the mean value of the charge on the column line during sampling time is the same for both the ideal and parasitic model shown in Figure 1.10b since  $V_G$  returns to the same value as at the start of the frame period. Despite the reset of the voltages, parasitic charge injection still induces noise that increases with  $C_{GD}$  and  $C_{GS}$  according to Equation 1.9. This will limit the SNR from the sensor in form of readout noise previously shown in Equation 1.1.

$$Q_{parasitic\ noise} = \sqrt{K_B T (C_{GS} + C_{GD})} \quad (1.9)$$

Additional considerations need to be taken into account when implementing disordered materials in a 1T image sensor architecture. Many organic, Perovskite and other disordered semiconductors exhibit decreased responsivity with increased irradiance or decreased applied bias. This nonlinear responsivity prevents early saturation under bright light and less photogenerated charge is added as well capacity is approached (since the photodiode voltage drop is low at well capacity). These effects can increase the dynamic range of a 1T image sensor

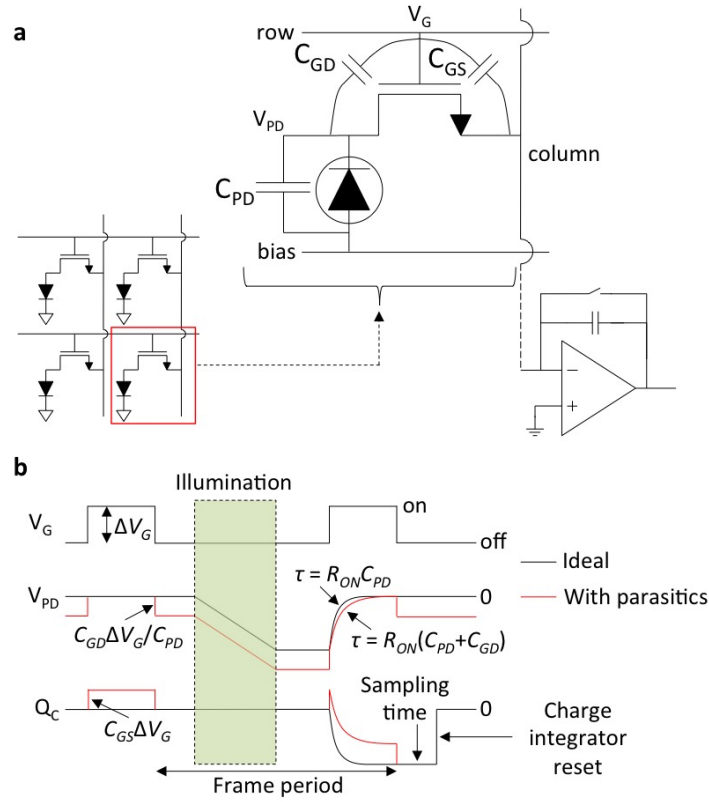


Figure 1.10: (a) 1T pixel architecture, a charge-integrating passive pixel, showing the integrating capacitor of the photodiode ( $C_{PD}$ ) and parasitic capacitances. (b) Drive voltage ( $V_G$ ), photodiode node voltage ( $V_{PD}$ ), and charge on the column line ( $Q_C$ ) during pixel operation with parasitic effects.

at a given frame rate. On the other hand disordered materials trap a significant amount of charge in slow-releasing deep states, leading to image lag effects between frames[166]. Bias stress, which is the gradual accumulation of trapped charge causing a drift in threshold voltage, is a concern in TFTs during prolonged use. While disordered TFTs with many trap states are used in large-area applications, it has been shown that low duty cycle operation of TFTs similar to the operation of such devices in a 1T image sensor significantly reduces bias stress as the short turn-on time prevents carriers from being lodged in deep trap states[165]. More details on passive pixel image sensor design and optimization using disordered materials can be found in literature on large-area amorphous silicon x-ray sensors[166].

## Case Studies

Many of the reported of 1T image sensors in the literature only measure performance in DC mode[75, 117, 124, 162, 168] despite the fact this architecture enables charge integration within a pixel, making it practical to capture images at video frame rates. Despite this drawback, the literature on solution processable, flexible and large area 1T image sensors and pixels shows tremendous efforts in the heterogeneous integration of high performance photodiodes and TFTs.

Horizontal (side-by-side) integration of the patterned photodiode and TFT is the simplest design from a fabrication layout perspective. However, horizontal integration of these two devices means that photodiode active area must be sacrificed to accommodate the TFT. This presents a reduction in fill factor, the fraction of an image sensor's surface area that is photosensitive. Nausieda et. al. created a 1T pixel using thermally evaporated pentacene TFTs and an inkjet printed photoconductor on inter-digitated electrodes[124]. One of the major tradeoffs for the horizontal integration was patterning the pentacene by etching to make room for the photoconductor, which decreased the on-off ratio and mobility by an order of magnitude. However, photoconductors are not ideal photodetectors for 1T architectures as the low capacitance of these devices limits the well capacity. Renshaw et. al. and Tong et. al. have shown monolithic integration of thermally evaporated TFTs and photodiodes on lithographically-patterned electrodes as depicted in Figure 1.11a[141, 172]. A discharge time constant of 400  $\mu$ s was achieved with a TFT mobility of 0.1  $\text{cm}^2/\text{Vs}$  and pixels were able to sense light levels as low 250  $\text{nW}/\text{cm}^2$  at DC[172]. Malinowski et. al.[117] used the same pixel design and device active materials (SubPc/ $\text{C}_{60}$  for the photodiode and pentacene for the TFTs) as the aforementioned publications[141, 172] to create a large area  $32 \times 32$  pixel image sensor. Image sensors with 200  $\mu\text{m}$  and 1 mm pixel pitch showed similar EQE but lower dark current density for the larger pixels.

Solution-processable organic photodiodes simplify the fabrication process of image sensors since several steps of vacuum deposition can be replaced with printing or spin coating. Additionally, solution-processed photodiodes achieve comparable or even better photodiode performance in comparison to their thermally evaporated counterparts[10]. For instance, Takahashi et. al. constructed a horizontally integrated 1T image sensor by spin coating a bulk heterojunction photoactive layer over an array of carbon nanotube TFTs for x-ray sensing[168]. Openings between the TFTs defined the photoactive area as shown in Figure 1.11b, a scintillator was placed in front of the array to down-convert x-rays to green light. Low light intensities approaching 1  $\mu\text{W}/\text{cm}^2$  were measured in DC, with negligible changes in performance down to a very small bending radius of 2 mm (such flexibility is made possible by a thin polyimide substrate of 24  $\mu\text{m}$ ). The high mobility of the TFTs (17  $\text{cm}^2/\text{Vs}$  average) enables a turn on time of approximately 1 ms, however the integration of photogenerated charge was not assessed. Gelinck et. al. assessed the performance of image sensors of a similar design to Takahashi et. al. but with organic TFTs in charge integra-

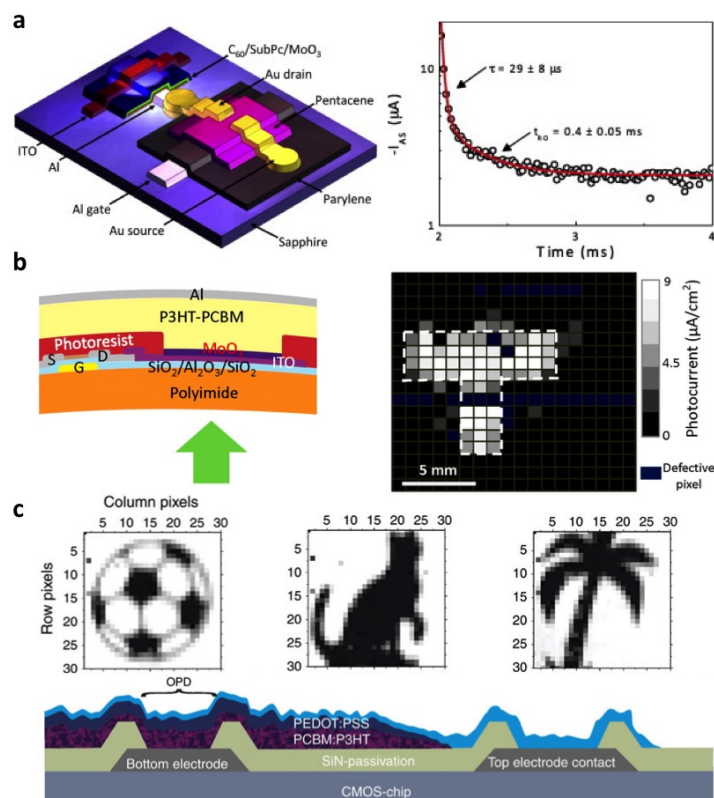


Figure 1.11: (a) Monolithic integration of an organic thin film transistor (TFT) and organic photodiode (OPD) to form a 1T pixel along with the dynamic response. Reprinted with permission from [172]. Copyright 2011 Elsevier. (b) Flexible organic photodiode-carbon nanotube TFT 1T image sensor. Reprinted with permission from [168]. Copyright 2013 American Chemical Society. (c) Top-illuminated spray-coated organic photodiodes on top of a CMOS chip to form a hybrid image sensor. Reprinted with permission from [11]. Copyright 2012 Nature Publishing Group.

tion mode on a flexible substrate[48]. TFTs were processed from a pentacene precursor and patterned with plasma etching, resulting in device yields over 99%, an average mobility of  $0.2 \text{ cm}^2/\text{Vs}$  and negligible crosstalk. This enabled images to be captured at 6.7 Hz at a low light intensity of  $1.1 \mu\text{W}/\text{cm}^2$ . The absorption spectra of the photodiode can also be tuned to suit a wavelength outside the sensitivity of conventional materials. Rauch et. al. demonstrated that PbS quantum dots embedded in a P3HT:PC<sub>60</sub>BM bulk heterojunction photodiodes with amorphous silicon TFTs enabled video capture at 5 frames per second at a wavelength of 1,310 nm[139]. This wavelength is well outside the absorption spectrum of organic semiconductors and silicon. Similar to Rauch et. al., Baierl et. al. also demonstrated that the cutoff wavelength of P3HT:PCBM can be increased to 900 nm by doping the active

layer with Squaraine[11].

Vertical integration of the TFT and photodiode, with the photodiode active area not covered by the TFT, is the most ideal pixel design since this enables the highest possible fill factor. One method of manufacturing an image sensor of this architecture is by fabricating the photodiodes and TFTs on separate substrates then laminating them together with electrical connections through vias as shown by Someya et. al[162]. This enabled the fabrication of a conformable sheet scanner with the photodiode size scalable down to 50  $\mu\text{m}$ . Additionally, laminating these sheets back-to-back could improve mechanical reliability since this places the stress neutral plane where the photodiodes and TFTs are located. Alternatively, vertical integration can be achieved by directly fabricating one device on top of another in such a way that the photodiode area is not obstructed. Ng et. al. deposited a bulk heterojunction photoactive layer on top of an amorphous silicon TFT array (mobility  $0.8 \text{ cm}^2/\text{Vs}$ ) followed by a layer of ITO to form a top-illuminated x-ray sensor[126]. The photodiodes, which have dark currents less than  $1 \text{ nA}/\text{cm}^2$  and an EQE of 35%, have a large fill factor of 76% over the whole array of 180180 pixels with a pitch of 340  $\mu\text{m}$ . Additionally, the symmetry of electron and hole mobility limits the build-up of space charge near one of the electrodes. This build-up would have significantly reduced the internal electric field in the rest of the device, slowing charge extraction from the photodiode. This symmetry in mobility enables a theoretical maximum video rate of 500 Hz for the full array (even though 10 Hz was used for the actual image). Additionally, this array was fabricated on a polyethylene naphthalate (PEN) substrate with processing temperatures below  $150^\circ\text{C}$  and demonstrated a 2.5 cm bending radius before performance degradation. Alternatively, the TFT can be deposited on top of a bottom-illuminated OPD as demonstrated by Jeong et. al[75]. The aluminum cathode shields the TFT from the light, avoiding any undesired phototransistor effects. A 1mm thick PDMS layer was placed between the OPD and TFT in order to electrically isolate them and chemically protect the OPD during fabrication of the TFT. While the charge integrating performance of this pixel was not investigated, the pixel responsivity showed negligible drift during 5 minutes of operation. Vertical integration of passive charge integrating image sensors has also been demonstrated on organic-CMOS hybrids by Baierl et. al[11, 12]. Top-illuminated OPDs were created by spray coating P3HT:PC<sub>60</sub>BM then highly conductive PEDOT:PSS on top of an aluminum electrode on the CMOS chip as shown in Figure 1.11c, with a mean EQE above 40% under reverse bias and negligible crosstalk between pixels (0.26%). A detailed noise analysis confirmed that flicker noise (also known as  $1/f$  noise) is the dominant source of noise as a result of charge trapping and de-trapping. However, it remains unclear as to whether this noise is primarily the result of traps in the transistor or OPD. Finally, vertical integration can be achieved by fabricating transistors transparent to the spectrum of interest. This design concept is well executed with metal oxide transistors due to their large band gap[74]. Sakai et. al. demonstrate that it is possible to create an image sensor using a transparent InGaZnO TFT and an organic photoconductor in a 1T pixel design[146]. While all the layers were vacuum deposited in this report, prior art on transparent metal oxide TFTs[74, 149] suggests that it is possible to create printed

Pixel Architecture	Pixel Device Processing	Frame Rate (Hz) @ lighting conditions	Lowest Imaged Irradiance ( $\mu\text{W}/\text{cm}^2$ ) @ $\lambda$	Bending Radius (mm)	Reference
1T: Horiz integ with patterned photodetector	Evaporated TFT, inkjet photoconductor	DC @ $1\text{mW}/\text{cm}^2$	100 @ 530 nm	Rigid substrate	[124]
	Evaporated TFT & photodiode	60 ms decay (single pixel)	0.25 @ 578 nm (DC)	Rigid substrate	[141]
	Evaporated TFT & photodiode	400 $\mu\text{s}$ readout (single pixel)	12.5 @ 580 nm (DC)	Rigid substrate	[172]
	Evaporated TFT & photodiode	DC @ 130 $\mu\text{W}/\text{cm}^2$ @ 532 nm	3 @ 532 nm (DC)	Flexible but not measured	[117]
Horiz integ with blanket deposited photodetector	Soluble TFT & photodiode	DC @ 100 $\mu\text{W}/\text{cm}^2$ @ 535 nm	2.5 @ 535 nm (DC)	2	[168]
	Soluble TFT & photodiode	6.7 @ $\simeq 1 \mu\text{W}/\text{cm}^2$	1.1 @ 550 nm	Flexible but not measured	[48]
1T: Vertical integration	a-Si TFT, soluble photodiode	5 @ $1.6 \text{ mW}/\text{cm}^2$ @ 1,310 nm	0.6 @ 1,150 nm (DC)	Rigid substrate	[139]
	Evaporated TFT & photodiode	DC @ 80 $\text{mW}/\text{cm}^2$ @ white light	$4 \times 10^4$ @ white light	Flexible but not measured	[162]
	a-Si TFT, soluble photodiode	10	Theoretical NEP of 30 $\text{pW}/\text{cm}^2$	25	[126]
	Evaporated TFT, soluble photodiode	DC (single pixel)	$5 \times 10^4$ @ white light	Flexible but not measured	[75]
	CMOS transistor, soluble photodiode	100 @ 535 & 850 nm	70 @ 535 nm	Rigid substrate	[11, 12]
Phototransistor	Channel current from $\Delta V_{\text{T}}$	1	NA	Flexible but not measured	[119]

Table 1.2: Properties of solution-processed passive pixel image sensors capable of intra-pixel charge integration.

versions of these devices.

Phototransistors can also behave as charge integrating pixels. Milvich et. al. have demonstrated that conventional DNTT transistor arrays can be used as phototransistors without modification of the device structure[119]. Light is detected by observing the shift in threshold voltage while a large positive voltage is applied to the gate to integrate trapped electrons. The shift in threshold voltage increases with integration time but eventually saturates for long integration periods. Additionally, the rate of threshold voltage shift is inversely proportional to channel length resulting from the fact holes are extracted more quickly in short channel devices, decreasing the risk of recombination with electrons. However, the deep trap states of the electrons causes slow refresh rates of at most 1 Hz.

## 1.6 Fabrication Techniques

A wide variety of fabrication methods are necessary in order to create all the components necessary in an image sensor. Conventional silicon-based microfabrication techniques are necessary for the sensor readouts, and microprocessor. Given the poor area-cost scalability of silicon processing[5], printing functional materials on inexpensive substrates is an attractive alternative to maintain desirable device performance while saving cost.

### Transfer of Silicon Devices to Flexible Substrates

Silicon processing is a necessity in order to form the workhorse silicon-based transistor processors that provide advanced communication and computation. The tremendous advances in computational speed and low power consumption of these devices following Moore's law make this technology completely unrivaled by any other processing technology. While these circuits are on fabricated on rigid silicon wafers, it is possible to transfer them to flexible and stretchable substrates that conform well to the body. Such transfer techniques have been demonstrated for a variety of systems ranging from image sensors[93], wearable[86] and even implantable devices and systems[84, 176]. Transferring pre-fabricated devices on silicon can be done using several techniques. A packaged integrated circuit package may flip chip bonded or pick-and-placed onto an elastomeric substrate using a low-temperature solder[86] or adhesive printed electrodes[17] as mentioned in Table 1.3. Devices fabricated on a wafer may also be transferred directly onto an elastomeric substrate such as PDMS by performing a wet etch underneath the fabricated device to loosen the foundation[93]. A buried oxide layer on the wafer is needed in order to act as the detachment point for this transfer. The interconnects between these transferred devices can also be deposited and etched into shape with microfabrication techniques[84, 86, 93]. However, since the transferred wafer-based devices are fairly rigid and not stretchable, the interconnects must be able to accommodate

the all the strain of the substrate to prevent other devices from fracturing. To achieve such a goal, the interconnects can either delaminate off the substrate[93], or be patterned into a serpentine configuration[86] to reduce the stress under strain. Sekitani et. al. demonstrated stretchable interconnects created from printable pastes can connect rigid devices transferred onto an elastomeric substrate[151].

Method	Sensor area scalability	Solution viscosity	Deposition on cheap, flexible substrates	Roll-to-roll throughput	Reference
Microfabrication	Limited, expensive	NA	Need transfer process and bonding layer	Pick and place machines, 0.1-1 m/s	
Spin coating	Limited, wasteful	<1,000 cP	Plastic or elastomeric substrates	Not compatible	[96]
Printing	Medium to high	1-100k cP	Plastic or elastomeric substrates	0.01-1 m/s	[96, 8, 132, 79, 21, 39]
Molding	Medium to high, depends on curing	No requirement	Plastic, elastomeric or textile substrates	0.01-1 m/s	[39]

Table 1.3: Properties of fabrication techniques.

## Printing on Flexible Substrates

Solution processable materials simplify fabrication and reduce cost by eliminating vacuum deposition, photolithography and etch steps used in microfabrication. Common solution processable materials include dielectrics, conductors and semiconductors used to make a wide variety of devices. The most common solution-processed deposition technique is spin coating. While this does produce a uniform film, it does not use ink parsimoniously and is difficult to scale to large areas[96]. These functional inks may be deposited on a variety of substrates, ranging from plastic to textiles, using scalable roll-to-roll compatible printing methods to reduce the cost of large-area sensors mentioned in Table 1.4.

Efficient methods of printing smooth, thin films from low viscosity inks include inkjet printing[96] and doctor blade/slot-die coating[96, 137, 135]. An inkjet printer controls the



Technique	Film uniformity	Film thickness & roughness	Viscosity range	Use of ink	2D patterning	Large area scalability
Inkjet printing	High	Low	1-15 cP	Parsimonious	Yes	Limited
Doctor blade	High	Low	Max of $\simeq 100$ cP	Parsimonious	No	Highly scalable
Screen printing	High	High	1k-100k cP	Parsimonious	Yes	Highly scalable

Table 1.4: Properties of printing techniques.

location of discretely position drops with a two-dimensional actuator and drop volume (1-10 pL) and speed (8 m/s) by a piezoelectric nozzle as illustrated in Figure 1.12a. This digital patterning enables rapid prototyping for sparse features. However, throughput becomes a limiting factor for features with large-area fill factors[132, 161, 167]. Alternatively, ink may be uniformly coated across a substrate by dispensing ink before (doctor blade) or during (slot-die) coating shown in Figure 1.12b. Relevant parameters of optimization include dispensed volume, substrate surface energy, and capillary number, which is described by Equation 1.10, where  $v$ ,  $\eta$ , and  $\gamma$  are coating speed, viscosity, and surface tension, respectively. While this technique is more scalable to large areas than inkjet printing, it is difficult to achieve two-dimensional patterning without patterning the surface energy of the substrate to direct ink flow[135]. Gravure and flexographic printing can achieve two-dimensional patterning at scalable speeds but require higher viscosity inks for reliable printing[96]. Formulating high viscosity inks necessitates the use of highly soluble solutes, which is can be difficult to achieve for many functional materials that are optimized for performance and not solubility. However, proper ink formulation can result in printed features as small as a few micron printed at speeds approaching one meter per second[45, 79].

$$Ca = \frac{v\eta}{\gamma} \quad (1.10)$$

Functional materials with a high paste-like viscosity (1,000-100,000 cP) can be screen printed[21, 137] as described in Figure 1.12c. Ink is first flooded over a patterned mesh (the screen) that is not in contact with the substrate. The screen is then lowered near the substrate before a squeegee presses against the screen and forces ink out through openings in the screen and onto the substrate. Important parameters of optimization include ink viscosity, surface tension, substrate surface energy, squeegee pressure and snap off distance. Molding is also compatible with roll-to-roll manufacturing, but the flow rate into the mold pattern and curing speed is a critical factor in determining the maximum throughput speed[39]. Solution

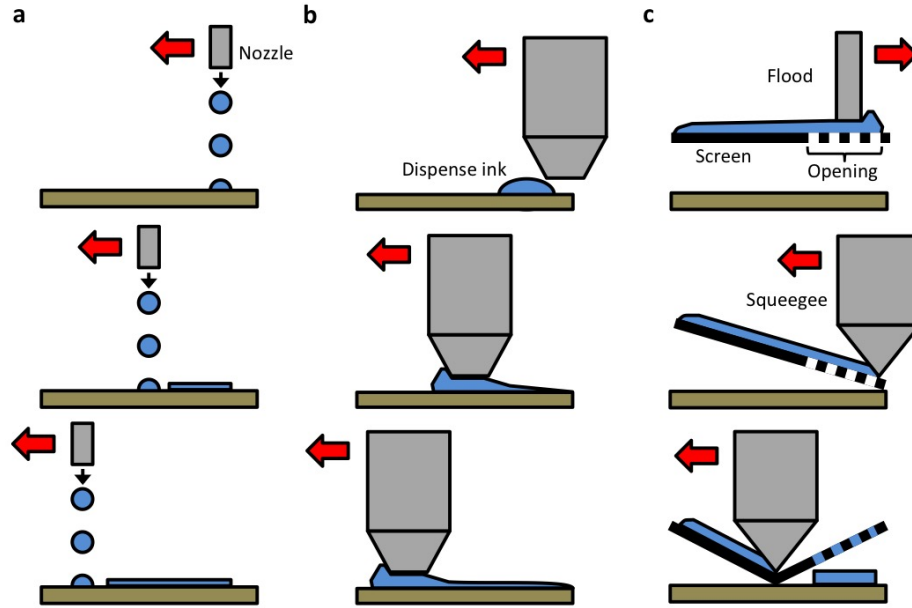


Figure 1.12: (a) Inkjet printing process for a continuous line. (b) Blade coating technique showing ink dispensing followed by coating. (c) Screen printing process depicting flooding of the ink over the screen followed by transfer of the ink through openings in the screen onto a substrate.

processing can even be integrated with textile substrates, which are conformal and robust. However due to the high roughness and porosity of textiles, they are best suited for devices that require thick active layers such as batteries[46, 192].

## 1.7 Thesis Outline

This thesis focuses on the development of printable transistors, photodiodes, and phototransistors on flexible substrates for optical sensing and imaging applications. The figures of merit and architectures introduced for transistors, photodetectors and image sensors will be used to construct and optimize performance.

The second chapter outlines the printing process used to create high performance, high yield, and low variability organic thin film transistor (OTFT) arrays on plastic substrates. A novel surface energy-patterned doctor blade coating technique is used to deposit the source-drain electrodes and isolated semiconductor layers. The effect of printing parameters, capillary number, small molecule-polymer blend ratio, and additive high boiling point solvent

concentrations on film fidelity, pattern design, device performance and yields is investigated.

The development of all-printed organic photodiode (OPD) arrays on plastic is investigated in the third chapter. The doctor blade coating and screen printing process used to create these photodiodes, which are inverted, is first explained. Device optimization is then explained layer-by-layer through the rest of the chapter beginning with the dipole interlayer cathode, then bulk-heterojunction active layer, and finally screen printed anode. The good uniformity over large area of the printing processes enables precise device performance tunability and excellent homogeneity over centimetric scales. Device performance is optimized for implementation in image sensors by having high detectivity under large reverse bias (low dark current and high EQE), wide linear dynamic range, and good bias stress stability.

Chapter four examines the performance of printed capacitive-based photodetectors, which includes organic charge-coupled devices (OCCDs) and organic phototransistors (OPTs). The behavior of charge-coupled devices is examined under illumination in order to develop an understanding of the movement of photogenerated carrier. Using the same foundational architecture of the charge-coupled devices, source-drain electrodes and a high-mobility layer at the dielectric interface is inserted in order to create a phototransistor. A charge integration-readout scheme is developed for these phototransistors in order to create pixels with wide dynamic range and photoconductive gain

Chapter five investigates the implementation of devices for optical sensing and imaging applications. Discrete as well as arrays of organic photodiodes are developed for pulse oximetry in transmission and reflectance mode. The fabrication of conventional photodiode-based image sensors is examined by creating interconnects for arrays of OTFTs (Chapter two) and OPDs (Chapter three). Finally, interconnects are used to create OPT-based image sensors (Chapter four).

The sixth and final chapter focuses on the main conclusions drawn from the culmination of work presented in this thesis. Future directions of research for large area and printed image sensors are also addressed.

## Chapter 2

# Printed Organic Thin Film Transistors

### 2.1 Introduction

While the device performance of solution-processed organic thin film transistors (OTFTs) has improved, it is necessary to investigate novel printing and processing techniques enabling devices with good electrical and mechanical properties while maintaining minimal variability and high device yields[66]. Gravure, flexo, and inkjet printing have been previously used to fabricate fully printed OTFT devices[4, 129, 177]. Flexo printing is highly scalable to large areas by typically results in films that are too rough for OTFTs[187]. Gravure printing is also scalable but has limited lifetime of the doctor blade, which is in contact with the cylinder[91]. This abrasion degrades the doctor blade and results in incomplete wiping of ink from the cylinder, leaving streak marks on the substrate which can cause shorting[49]. On the other hand, inkjet printing is ideal for depositing smooth, well-patterned thin films. However, inkjet printing is challenging to scale to rapid large area patterning, especially for features with large area fill factor, due to the requirement for precisely positioning pL-volume droplets[13, 96]. Blade coating and slot die coating are alternative thin film deposition methods to inkjet printing that enable higher throughputs at the expense of inherently being a one-dimensional coating method as mentioned at the end of the Introduction chapter. OTFTs have been fabricated using a slot die printing technique known as zone-casting in which the solvent controllably evaporates at the tip of the meniscus, depositing high quality crystals with carrier mobilities as high as  $11 \text{ cm}^2/\text{Vs}$ , but with printing speeds limited to few hundreds of  $\mu\text{m/s}$ [26, 35]. Furthermore, device reliability and performance is found to improve through the use of surface energy patterned (SEP) substrates to self-align inkjet-printed source drain electrodes[152] and pattern zone-casted semiconductor for partially printed devices[31, 35, 42, 88, 120, 148, 158]. In order to improve the large area scalability of high performance semiconductors, it is important to move away from the deposition speed of the zone-casting technique[15, 35] and achieve a process in which the

ink can be quickly deposited onto a substrate[177] and then controllably dried[160] to form high quality patterned semiconductor thin films. While in the majority of studies reporting "solution-processed" TFTs comprise a printed or spin-coated semiconductor layer with photolithographically or thermally evaporated metal contacts[15, 31, 42, 72, 88, 120], far fewer reports have strived to achieve high quality printed contacts[78, 152, 177]. Lift-off photolithographic processes and vacuum deposition of expensive metals such as gold must be replaced in order to move to more scalable, simpler, inexpensive, and energy efficient OTFT fabrication. Additionally, the quality of the dielectric-semiconductor interface has a significant impact on mobility[83]. Despite the high mobility of fluoropolymer-semiconductor interfaces[71], few reports provide details on steps to fabricate a fully-printed gate stack with this dielectric[43, 46, 183]. Good printability is also a prerequisite for achieving high performance OTFTs. Poor printing control will result in topographical unevenness, which leads to high device-to-device variability and low yields. As a consequence, low device yields create barriers for circuit designs, application development and overall technology adoption[9].

This chapter will first give an overview of doctor blade coating and how it can be used on SEP substrates in order to create two dimensional-patterned films[135]. A process flow is then developed using this novel printing technique to deposit the source-drain electrodes, semiconductor, gate dielectric, and even gate electrode. The effect of ink rheology and source-drain geometry on yield and channel length variability is also assessed. Then, the printing, device performance, and reliability of polymeric, small molecule, and small molecule-polymeric blend[57] semiconductors are examined deposited from SEP doctor blade coating. Finally, the performance and reliability of printed OTFT arrays are examined for small molecule-polymeric semiconductor blends.

## 2.2 Doctor Blade Coating & Device Process Flow

### Theory

Doctor blade coating is a printing technique in which ink is first dispensed on the edge of a substrate then dragged over the surface by a doctor blade with a fixed height above the substrate as shown in Equation 2.1a. This printing deposits a uniform wet film over the substrate, which eventually dries out to leave behind a solid thin film. During coating, the fluid remains stationary at the boundary of the blade edge and substrate. This creates a Couette flow as shown in the bottom of Equation 2.1a, in which the velocity profile of the ink with respect to the blade is linearly increasing in the gap from zero at the blade to the actual blade velocity at the substrate surface[32, 182]. This linear velocity profile means that the net velocity of fluid exiting the doctor blade is half of the blade speed ( $v_{blade}$ ), resulting in a deposited wet film thickness ( $t_{wet}$ ) on the substrate that is half of the blade height ( $h_{blade}$ ). Experimentally, it has been found that this relationship occurs at high speeds as shown in

Equation 2.1. Coating speeds on the order of several cm/s or less yield film thicknesses under the ideal limit as a result of capillary forces which become more prominent at slower speeds[182]. The thickness of the dry film ( $t_{dry}$ ) is dependent on the ink solute concentration ( $\phi_{conc}$ ) and density of the solute ( $\rho_{solute}$ ) as shown in Equation 2.2.

$$\lim_{v_{blade} \rightarrow \infty} t_{wet} = \frac{h_{blade}}{2} \quad (2.1)$$

$$t_{dry} = \frac{t_{wet} \phi_{conc}}{\rho_{solute}} \quad (2.2)$$

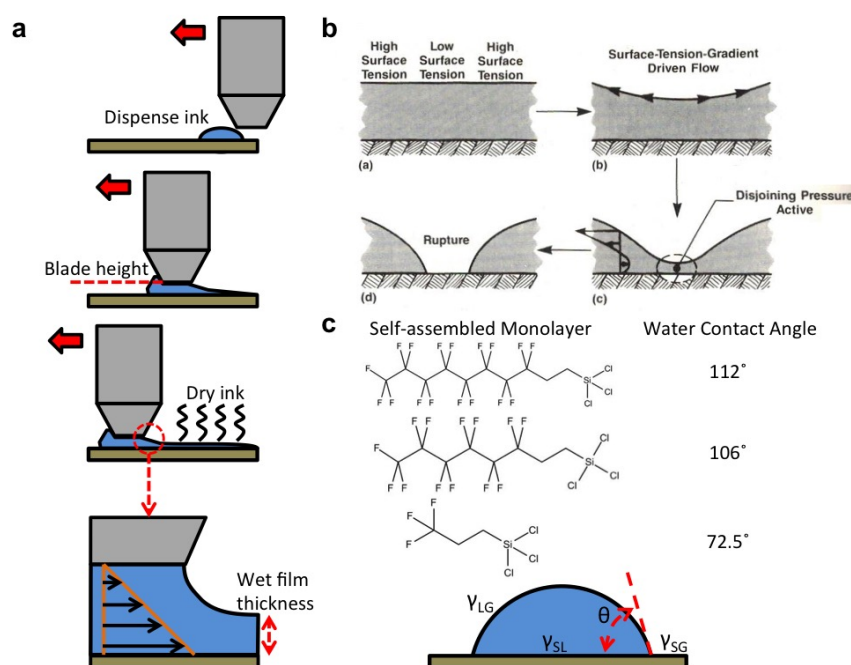


Figure 2.1: Doctor blade coating process (a) and the movement and rupture of fluid on a surface energy-patterned surface (b) (Reprinted with permission from[111]. Copyright 1997 Springer.). The contact angles of water measured on various SAMs (c) showing the liquid (L), gas (G), and solid (S) interface energy interactions on a droplet.

## Surface Energy Patterning

The solutes of the inks used in printing OTFTs comprise of conductors, semiconductors and dielectrics. Methods of patterning wet films must be examined due to the need of isolated source and drain electrodes on the same plane and isolated semiconductor patches between

devices. While the blade can't be used to pattern two dimensional objects since it is not in stationary contact with the substrate, patterning can be done on the substrate to direct flow of the ink. The simplest method of achieving such patterning without the use of photolithographic and subtractive patterning from a blanket coated layer of materials is through surface energy patterning (SEP) of the substrate. Figure 2.1b demonstrates the concept of critical wet film thickness, above which a film will remain stable and uniform but below which the film will spontaneously dewet from the surface of the substrate[111]. Creating regions of high and low surface tension helps guide the splitting of the liquid into desired regions[20]. Additionally, this critical film thickness is inversely proportional to the surface energy of a substrate, which can increase the surface tension-guided driving force to areas of the substrate with higher surface energy.

The first step to achieve the best surface energy patterning is to choose the most hydrophobic (lowest surface energy) surface on a substrate. Water contact angle is a useful method of comparison between materials since it is inversely proportional to surface energy as depicted in Young's equation in Equation 2.3 and Figure 2.1c, where  $\gamma_{SG}$ ,  $\gamma_{SL}$ ,  $\gamma_{LG}$ , and  $\theta$  are the substrate surface energy, ink surface tension, interfacial energy between liquid and substrate, and contact angle, respectively. Figure 2.1c shows the water contact angle measured of various fluoroalkylsilane self-assembled monolayers (SAMs) deposited on a flexible polyethylene naphthalate (PEN) substrate with a planarization layer. The most hydrophobic SAM is the fluoroalkylsilane with the longest chain length at a water contact angle of  $112^\circ$ . Using the Zisman method by measuring the contact angle of various solvents on this SAM, the surface energy is found to be  $21.2 \text{ mN}\cdot\text{m}^{-1}$ .

$$\gamma_{SG} = \gamma_{SL} + \gamma_{LG} \cos \theta \quad (2.3)$$

The blade coating process used to deposit the source-drain electrodes and semiconductor layers on SEP plastic substrates is illustrated in Figure 2.2a. This process is simple and could be scaled to manufacturing as it is compatible with large area processing and it does not require photolithography and lift-off. As a first step in the process, the fluoroalkylsilane SAM is deposited on the plastic substrate by inducing hydroxyl groups on the surface through plasma treatment before exposing it to vapor of the fluoroalkylsilane, causing the trichlorosilane head group to covalently bond to the substrate. The substrate with the SAM is then briefly exposed to low power oxygen plasma through a stainless steel stencil mask in order to define hydrophilic regions. The ink of the desired material is then dragged by a doctor blade and selectively wets the hydrophilic regions.

The common parameters of optimization that will be touched upon include speed, surface energy, platform (substrate) temperature, blade height, and the ink viscosity and surface tension as depicted in Figure 2.2a. Previous work on slot die coating, which has similar mechanics to blade coating, on surface energy patterned surfaces has focused on patterning

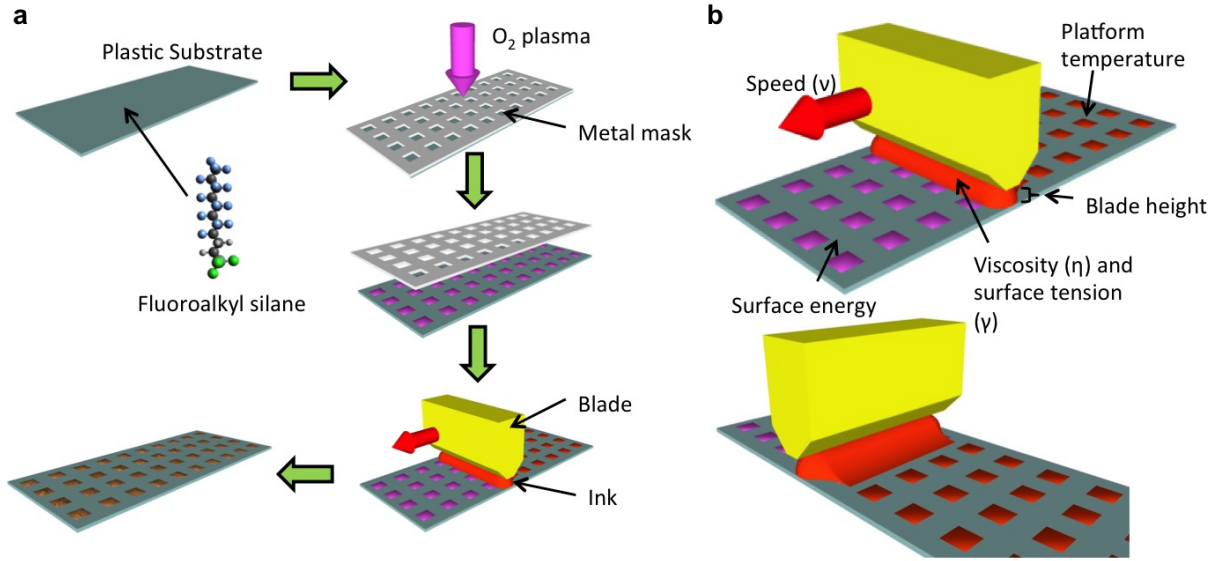


Figure 2.2: The surface energy-patterned doctor blade coating process flow on a substrate (a) and tunable printing parameters (b).

by the dewetting of the ink after coating a uniform liquid film over the substrate[20]. This style of printing deposits an excessive amount of ink on the substrate that uncontrollably segregates onto the hydrophilic regions, creating an inhomogeneous array of features with poor pattern fidelity and increasing the probability of shorted features. It is important to decrease the blade height below the critical thickness at which a wet film of the ink spontaneously dewets from the substrate and use an ink with a low capillary number. By doing so, the meniscus of the ink closely follows the blade and controllably wicks into patterned areas to enable highly uniform arrays as shown in Figure 2.2b. The surface energy-driven patterning process of blade coating on SEP substrates requires an ink with a low capillary number, as written in Equation 2.4, to ensure that viscous forces do not dominate the surface tension forces needed for self-assembled patterning. A slow blade coating speed ( $v$ ), a low ink viscosity ( $\eta$ ) and high ink surface tension ( $\gamma$ ) are ideal for good patterning.

$$Ca = \frac{\eta v}{\gamma} \quad (2.4)$$

## OTFT Fabrication Process

The geometry and configuration of the OTFT is a consideration for performance optimization as well as printing reliability. Bottom contact devices (source-drain electrodes on the



bottom/first layer) are ideal for printed OTFTs since the ideal long channel widths and short channel lengths make this layer the most challenging to print. Fluoroalkylsilane and alkylsilane SAMs deposited on various polymeric gate dielectrics showed far lower SEP printing reliability than on a bare substrate with the fluoroalkylsilane SAM. As a consequence of printing reliability, a bottom-contact top-gate (BCTG) geometry is used for all OTFTs in this thesis. The OTFT fabrication process flow is reported in Figure 2.3 showing the SEP blade-coated source drain electrodes, semiconductor, blanket blade-coated fluoropolymer gate dielectric layer and inkjet-printed gate electrodes. The source-drain electrodes are printed using SEP doctor blade coating, with silver contact pads inkjet printed at the base of each electrode (source & drain, step 4). The outward curving shape of the electrodes enables higher yield since the line width of the electrode is thinner and proximity of the two electrodes is more distant. More findings on source-drain electrode printing optimization will be discussed in the following section. A fluoroalkylsilane SAM is then redeposited on the substrate by plasma treating the whole substrate and exposing it to a vapor of the SAM after the source-drain electrodes are completed. After printing the semiconductor with SEP doctor blade coating, amorphous fluoropolymer is blanket coated over the substrate to form the gate dielectric.

Finally, the gate electrode is formed by either thermal evaporation of aluminum or SEP inkjet printing (gate stack, steps 2 and 3). A surface tension-guided process is also used to print the gate electrode on the fluoropolymer dielectric. Printing on fluoropolymer is particularly challenging because of its hydrophobicity. In previous reports interlayers were deposited in order to improve gate electrode printability and adhesion[46, 183]. Here, four corner dots of metallic nanoparticles are first inkjet-printed then sintered on the blade-coated dielectric. Next, more metallic nanoparticle ink is inkjet-printed over the dots as shown in Figure 2.4a. The surface area of the droplet reduces as the solvent evaporates during the sintering process until the corners become pinned to these dots. Additive concentrations of fluorosurfactant in the metallic nanoparticle ink facilitate self-alignment of the ink during solvent evaporation while minimizing the contact angle so as to prevent the droplet from breaking up. This method avoids the necessity of an interlayer[46], thus maintaining the original gate capacitance. In addition, this method is incredibly robust to the initial form of the large droplet since the silver ink eventually self-aligns to the corner dots with good surface adhesion. Such processing robustness substantially reduces the need for precise drop positioning and volume control, thus enabling higher throughput printing. A schematic representation of the final device is shown in Figure 2.4b. The following sections will cover the optimal ink formulation and patterning for each of these layers.

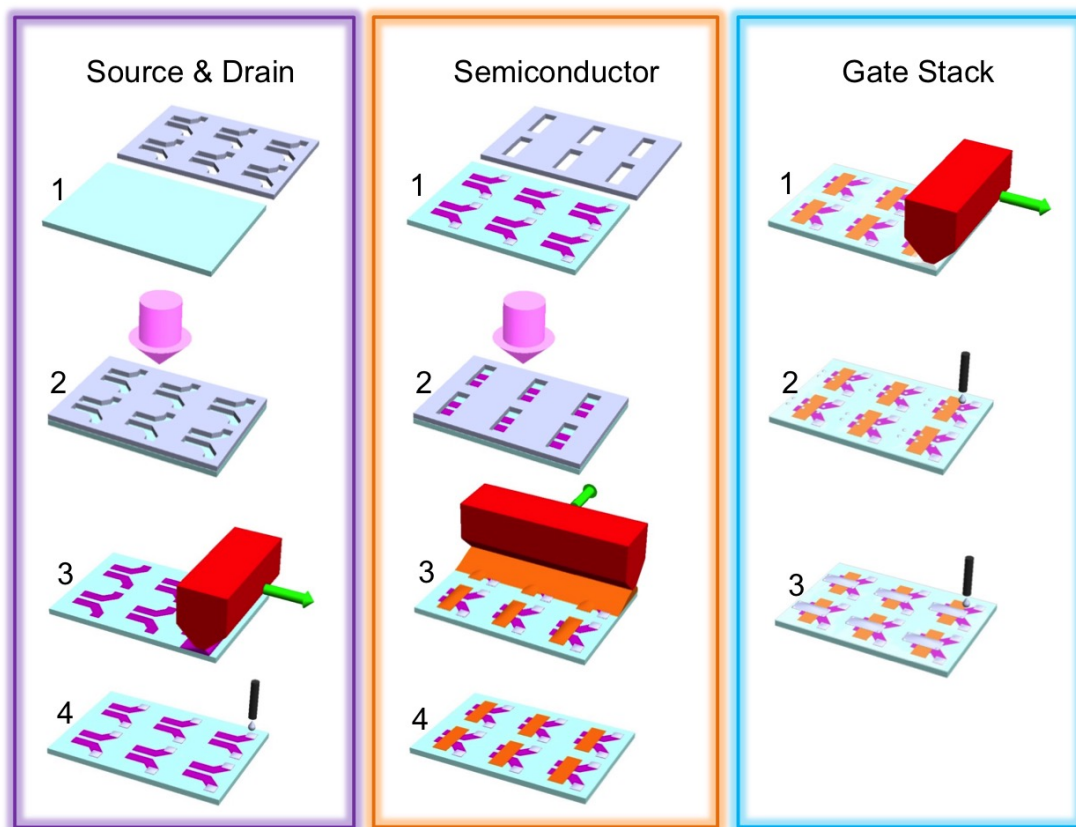


Figure 2.3: Process flow for all-printed OTFT arrays on flexible plastic substrates.

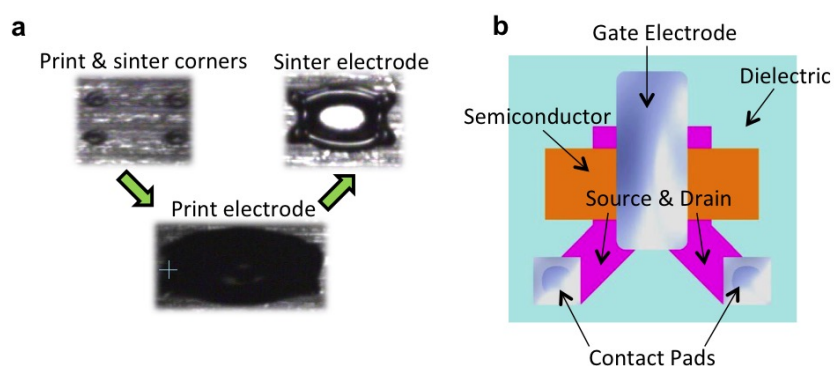


Figure 2.4: The surface energy-patterned inkjet printing process for the gate electrode (a) and the final architecture of the OTFT device (b).

## 2.3 Source-Drain Electrode Optimization

The high surface tension and low viscosity of water make aqueous solutions of PEDOT:PSS ideal for reliable blade coating at higher speeds. Furthermore, PEDOT:PSS is an excellent choice for OTFT source drain electrodes because of its smooth film surface, inexpensiveness, good hole-injection properties, and sufficiently low resistivity[152]. Source-drain electrodes were optimized by varying the line width (LW), channel length ( $L$ ), and channel width or height ( $W$  or  $H$ ) as shown in Figure 2.5a. Figure 2.5b and c show source-drain printing yield (defined as percentage of non-shortcd electrodes) for electrodes of different dimensions processed from as-received 0.8 wt.% PEDOT:PSS solution and from this solution with 50 vol.% water added, respectively. Adding 50 vol.% water to the original solution reduces the capillary number by 41% by changing the viscosity and surface tension of the original solution from 8 cP and 38 mN·m<sup>-1</sup> to 5 cP and 40 mN·m<sup>-1</sup>, respectively. Comparing the two graphs for any given source-drain electrode dimension shows that the lower capillary number of the diluted PEDOT:PSS formulation gives significantly better yield. The yield for 20 measured source-drain for each  $W$  and  $L$  is significantly higher for narrower LWs as a consequence of less ink volume transfer to the hydrophilic patterns, reducing the likelihood of bridging between source-drain electrodes. For 100  $\mu$ m LW electrodes, all 50 and 100  $\mu$ m  $L$  electrodes display 100% yield but 30  $\mu$ m  $L$  electrodes only display 100% yield only for 200  $\mu$ m  $W$ . The cross sectional profile for a 100  $\mu$ m LW 200/30  $\mu$ m  $W/L$  source-drain electrode is shown in Figure 2.5d. The smooth topographical change from the channel to the electrode and thinness of the electrode is ideal to minimize crystallographic disruptions in the device.

In order to deposit uniform thin films it is important to ensure that the spacing between features is greater than the feature size. Figure 2.5e displays the deposited film thickness of diluted PEDOT:PSS solution at several coating speeds for 600  $\mu$ m  $W$  source-drain electrodes of various  $L$  and LWs for a blade height of 125  $\mu$ m above the substrate. For 100  $\mu$ m  $L$  and 100  $\mu$ m LW source-drain electrodes, thickness increases monotonically with minimal variability as coating speed increases. Decreasing the  $L$  to 50  $\mu$ m for these features results in thicker films at lower speeds with more variability due to the short space between features compared to the size of the well-controlled meniscus. The same trend is observed for features using 100  $\mu$ m  $L$  and 200  $\mu$ m LW geometry, albeit thicker films. This increase in film thickness and variability for feature sizes larger than their spacing is likely caused by the rupture of bridging wet source-drain electrodes after the meniscus of the doctor blade has passed. This bridging not only increases the total volume of ink that eventually goes into electrodes, the rupturing process is also poorly controlled and results in an uneven distribution of ink between the source and drain. The substrate surface energy is also another important parameter. Figure 2.5f shows yields for 100  $\mu$ m  $L$  and LW source-drain electrodes using diluted PEDOT:PSS solution of various  $W$  deposited on substrates patterned using the fluoroalkylsilane SAMs shown in Figure 2.1c. The trend of this graph indicates that the more hydrophobic the substrate, the more efficient patterning.

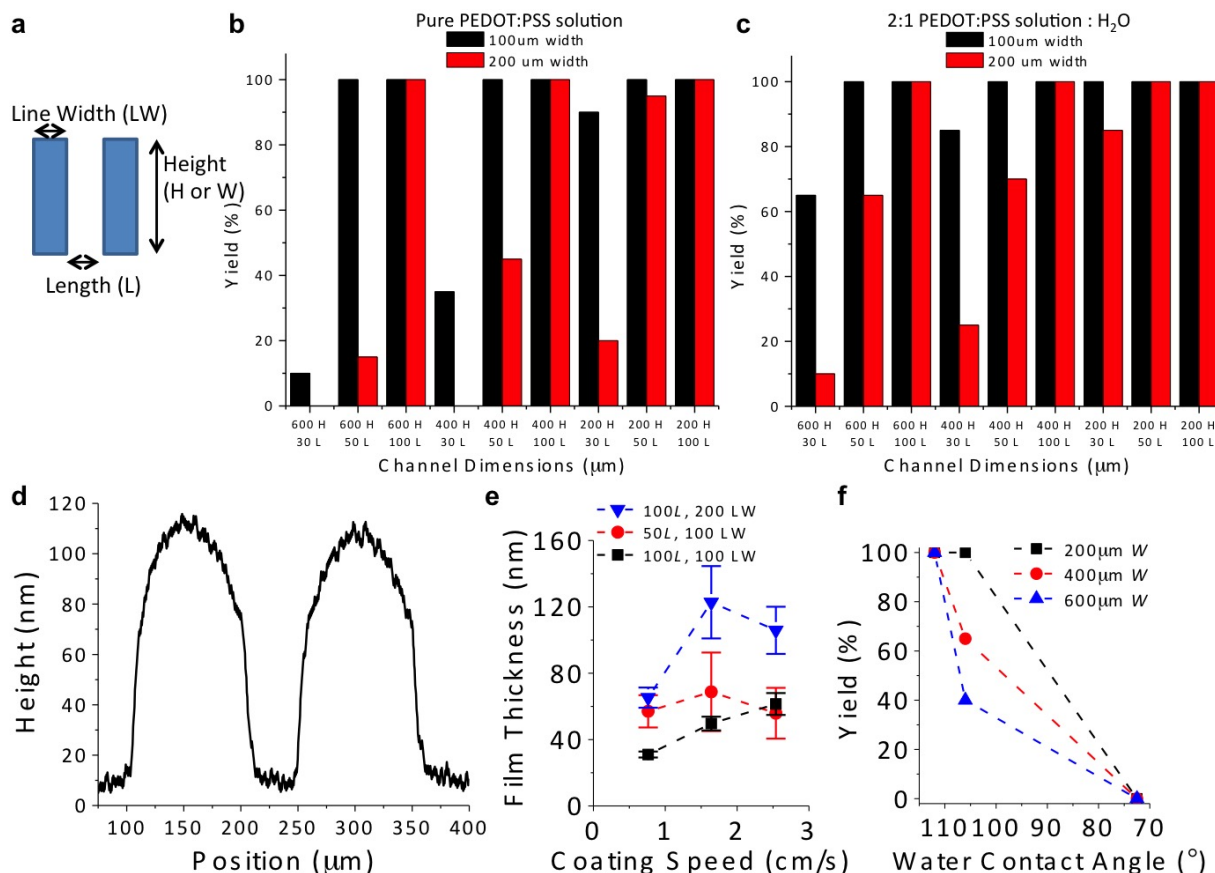


Figure 2.5: SEP source-drain electrode yield as a function of dimensions (a) for as-received ink (b) and optimized ink (c). The profile of a 30  $\mu\text{m}$   $L$  channel with 100  $\mu\text{m}$   $LW$  is measured (d). Film thickness as a function of coating speed (e) and yield as a function of SAM hydrophobicity (f) are quantified as a function of source-drain dimensions.

The final source-drain design for the OTFT uses 100  $\mu\text{m}$   $LW$  electrodes with 400  $W/L$  channel dimensions due to the high reliability as previously shown in Figure 2.5c. The base of the electrodes curve outward to provide sufficient spacing between source and drain contact pads that will be subsequently inkjet printed. Electrodes printed using the as-received 0.8 wt.% PEDOT:PSS solution, shown in Figure 2.6a, exhibit poor pattern fidelity and many shorts between source and drain. In comparison, Figure 2.6b shows that the PEDOT:PSS solution diluted in 50 vol.% water exhibits good pattern fidelity and yield. The electrodes that yielded in printing the as-received PEDOT:PSS show a coefficient of variance (CV) of 12% for 50  $\mu\text{m}$   $L$  with a mean measured channel length of 58  $\mu\text{m}$  as shown in Figure 2.6c. In comparison, the CV and mean channel length of diluted PEDOT:PSS solution is 8% and 41  $\mu\text{m}$ , respectively, measured for 43 devices (100% yield) as shown in Figure 2.6d. A low CV

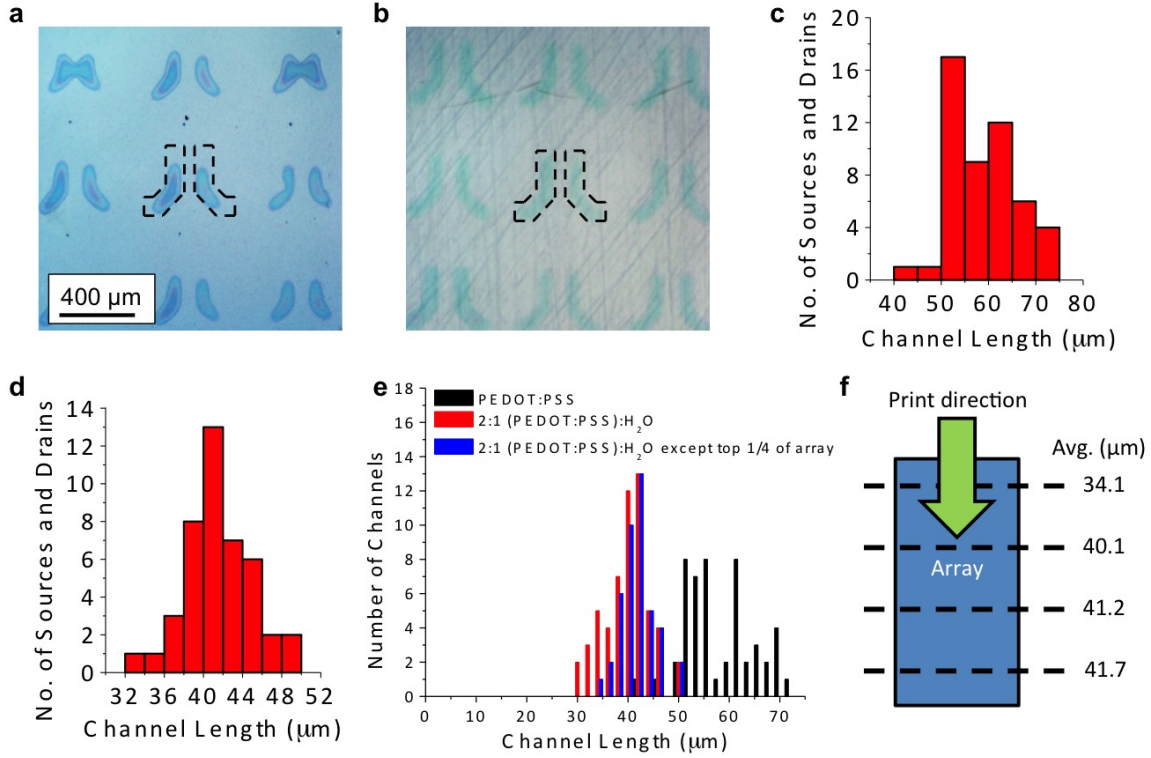


Figure 2.6: Optical micrographs and histogram distribution of channel lengths for source-drain electrodes printed from as-received ink (a,c, respectively) and optimized ink (b,d, respectively). Histogram distribution of channel lengths for various inks for the whole and bottom  $\frac{3}{4}$  of the array (e) along with the mean channel length measured in cross sections perpendicular to the direction of printing (f).

is established as a result of the surface energy patterning, which acts as a driving force for self-assembly into the desired pattern, eliminating line edge roughness effects seen in other printing processes such as gravure and inkjet printing[43]. The resistance of the electrodes is approximately 10 kΩ, which is sufficiently low considering the on-current of these devices ( $\leq 5\mu\text{A}$ ). Device yield is highest and variability is minimal in the bottom  $\frac{3}{4}$  of the array, as shown in the histogram of Figure 2.6e, since the flow of ink on the doctor blade takes a certain time to equilibrate. The mean measured  $L$  is also consistent across the bottom  $\frac{3}{4}$  of the array as shown in Figure 2.6f, with the top row shorter since an excess of ink is deposited onto the electrodes during the equilibration phase.

In addition to depositing PEDOT:PSS on hydrophilic patterned areas on a hydrophobic substrate, it is also possible to use the high surface energy of metallic features to achieve SEP

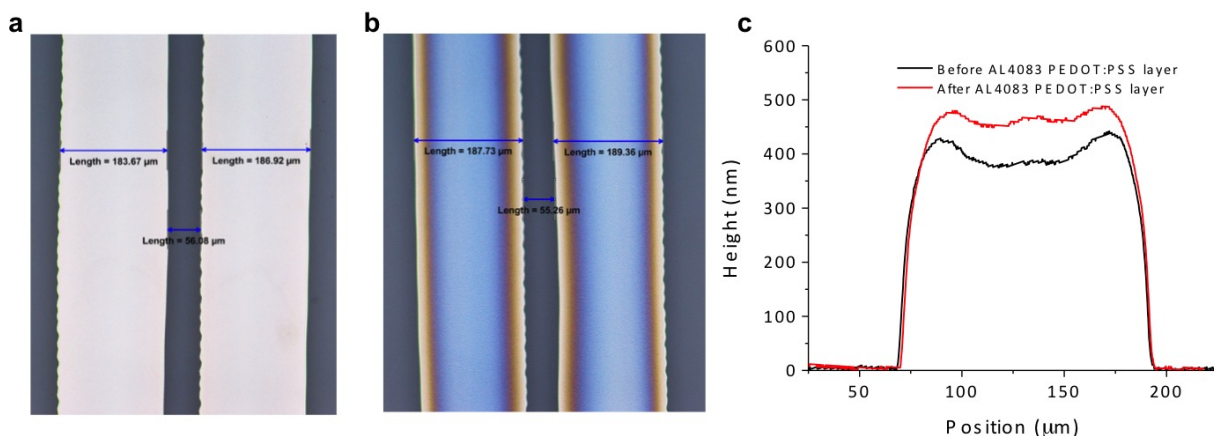


Figure 2.7: Optical micrographs of silver source-drain electrodes before (a) and after (b) coating with PEDOT:PSS with cross-sectional profiles (c).

doctor blade coating. Figures 2.7a and b show the before and after photos, respectively, of a low conductivity, high work function grade of PEDOT:PSS, P VP AI 4083, blade coated on top of inkjet printed silver electrodes. The cross sectional profile in Figure 2.7c shows that approximately 75 nm of PEDOT:PSS is deposited directly on top of the silver. While this bilayer electrode structure was not implemented in a device, it can be highly advantageous since the conductivity of silver reduces the resistance of the electrode while the high work function of PEDOT:PSS enables good hole injection. Furthermore, PEDOT:PSS reduces the surfaces roughness from 7 nm for the sintered silver nanoparticles to 1.2 nm.

## 2.4 Semiconductor Optimization

The deposition of a variety of semiconductors printed using SEP doctor blade coating was investigated as the next printing step after the source-drain electrodes as depicted in Figure 2.3. Each of these sections summarizes the printing optimization and device performance of polymeric, small molecule, and small molecule-polymeric semiconductor blends.

### Polymeric Semiconductor

SEP doctor blade coating of lisicon SP220, a semiconducting polymer with a reported mobility of  $0.1 \text{ cm}^2/\text{Vs}$ , was investigated since the small grain sizes of this polymer lead to less variability in an array of OTFTs. However, the ink of this semiconducting polymer is highly viscous, making it impossible to achieve SEP doctor blade coating using a plasma treated

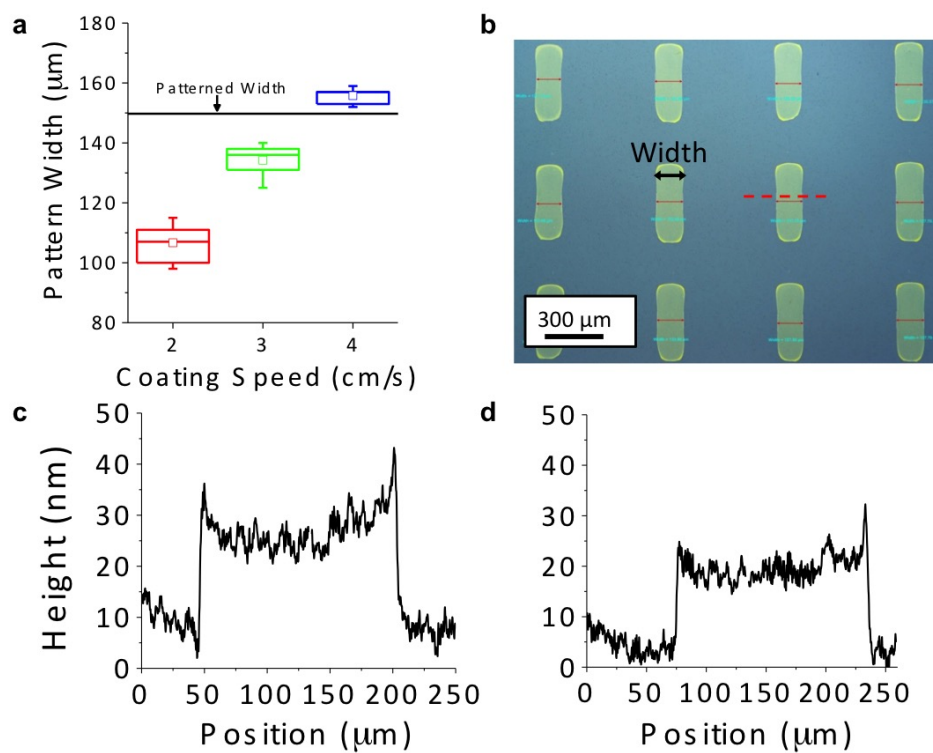


Figure 2.8: Statistical (a) and optical (b) quantification of polymeric semiconductor pattern width along with cross-sections measured at the top left (c) and bottom right (d) of the array as measured through the red dashed line.

pattern on a substrate with fluoroalkylsilane SAMs without overflowing the substrate. This issue is circumvented by exposing the plasma-treated patterns (between step 2 and 3 for the semiconductor layer in Figure 2.3) to hexamethyldisilazane (HMDS) vapor to decrease the surface energy. This treatment decreases the contrast of surface energy between the HMDS-exposed pattern and the rest of fluoroalkylsilane SAM substrate. As a result of the lower surface energy of the pattern, a smaller and more controllable amount of ink is deposited in the patterned areas, making it possible to reliably pattern the semiconductor. In addition, the reduction of surface energy in the patterned areas enables better crystallization of organic semiconductors[94].

Figure 2.8a is a plot of the width of the dry film of the semiconductor, which sets the channel width,  $W$ , of the OTFT, as a function of blade coating speed. More ink is transferred to the pattern at higher coating speeds[182], allowing the pattern to approach  $W$  as defined by the HMDS-treated pattern with decreasing variability. The micrograph of SP220 semiconductor printed at a speed of 4 cm/s on a substrate without source-drain electrodes



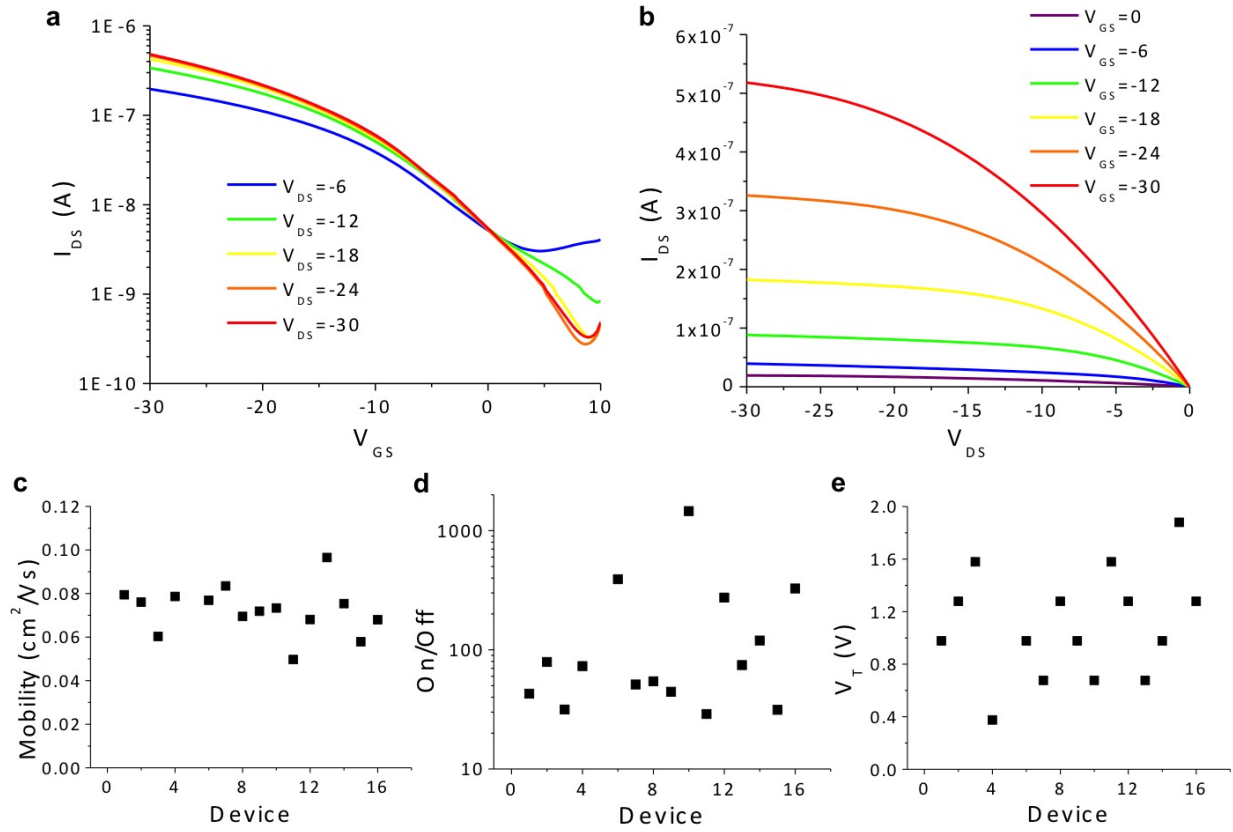


Figure 2.9: Transfer (a) and output (b) characteristics of polymeric SP220 OTFTs along with statistical distribution of saturation mobility (c), on-off ratio (d), and threshold voltage (e).

in Figure 2.8b shows good uniformity with no excess ink deposited on the regions with fluoroalkylsilane SAM. Figures 2.8c and d show the cross sectional profile of SP220 (denoted by the red dashed line in Figure 2.8b) at the top left and bottom right corner of the array, respectively, approximately 5 cm apart. These profiles show that films as thin as 20 nm can be printed with no noticeable coffee ring at the edges induced by rapid solvent evaporation.

OTFTs using SP220 were printed with the optimized PEDOT:PSS source-drain electrodes, amorphous fluoropolymer (AF) gate dielectric, and thermally evaporated aluminum gate electrodes. Despite the low dielectric constant of AF, this material was chosen as a gate dielectric for all OTFTs in this thesis since the low polarization of this material achieves the highest mobility in organic devices since it minimizes scattering of carriers at the dielectric interface[97]. Figures 2.9a and b show the transfer and output characteristics of these OTFTs, respectively. The mobility, on-off ratio, and threshold voltage were extrapolated



for 16 devices as shown in Figures 2.9c, d, and e, respectively. An average mobility of  $0.07 \text{ cm}^2/\text{Vs}$  is extrapolated for these devices with minimal variability, which is in close agreement with the specified mobility of  $0.1 \text{ cm}^2/\text{Vs}$  from the polymer manufacturer. The source-drain electrodes also have no contact resistance with the semiconductor as seen in the linear region of the output plot. However, the on-off ratio is sensitive to fluctuations in film thickness, causing large variability across the array. The high subthreshold slope of approximately 5-7 V/decade also necessitates high voltages to operate these devices with appreciable on-off ratios.

## Small Molecule Semiconductor

A small molecule semiconductor, 6, 13-Bis(triisopropylsilylethynyl)pentacene (TIPS - Pentacene), was also implemented as the semiconductor in the channel for OTFTs. Compared to polymeric semiconductors, the size of the crystalline domains depends strongly on the evaporation conditions of the wet film[35]. Figure 2.10a illustrates a chamber that was placed behind the doctor blade in order to slow down the rate of evaporation, along with polarized micrographs of the semiconductor coated on a plasma-patterned fluoroalkylsilane SAM substrate. TIPS-Pentacene solution cast from toluene without the chamber shows noticeably smaller grain sizes compared to the film coated with the chamber. Additionally, the cross sectional profile of the quickly evaporated film in Figure 2.10b shows significantly thicker edge regions compared to the center region. This non-uniform distribution is the coffee ring effect, which is a result of the flow of liquid from the center of the wet film to replenish the drying film at the edges that leaves behind the solute. This flow is induced by the higher surface tension of the evaporating solvent at the edges. The pileup of TIPS-Pentacene at the edge of the film not only creates a rough surface that can short through the top gate dielectric, but a thick film that makes it difficult to fully deplete the bulk charge of the semiconductor to turn off the device. However, slowing the evaporation as shown in Figure 2.10c eliminates the coffee ring effect since the slower evaporation allows the solvent flowing to the edges to flow back inward and evenly distributes the solute across the pattern[68]. This internal circulation, which is critical to obtaining uniform films, is known as the Marangoni flow.

The direction of coating also has an impact on film quality as shown in the micrographs of Figure 2.11a. Coating perpendicular to the orientation of the patterned areas produces semiconductor films too thick and rough for implementation in OTFTs. Residual material is also deposited on the unwanted fluoroalkylsilane SAM. On the other hand, blade coating along the orientation of the pattern minimizes the perturbation of surface energy along the edge of the meniscus of the doctor blade as the ink is dragged across the substrate. This orientation produces the thin, smooth, uniform films needed for OTFTs without residual material in un-patterned regions. The topography of the source-drain electrodes also influences the quality of the final film. Figure 2.11b depicts the dewetting of the semiconductor

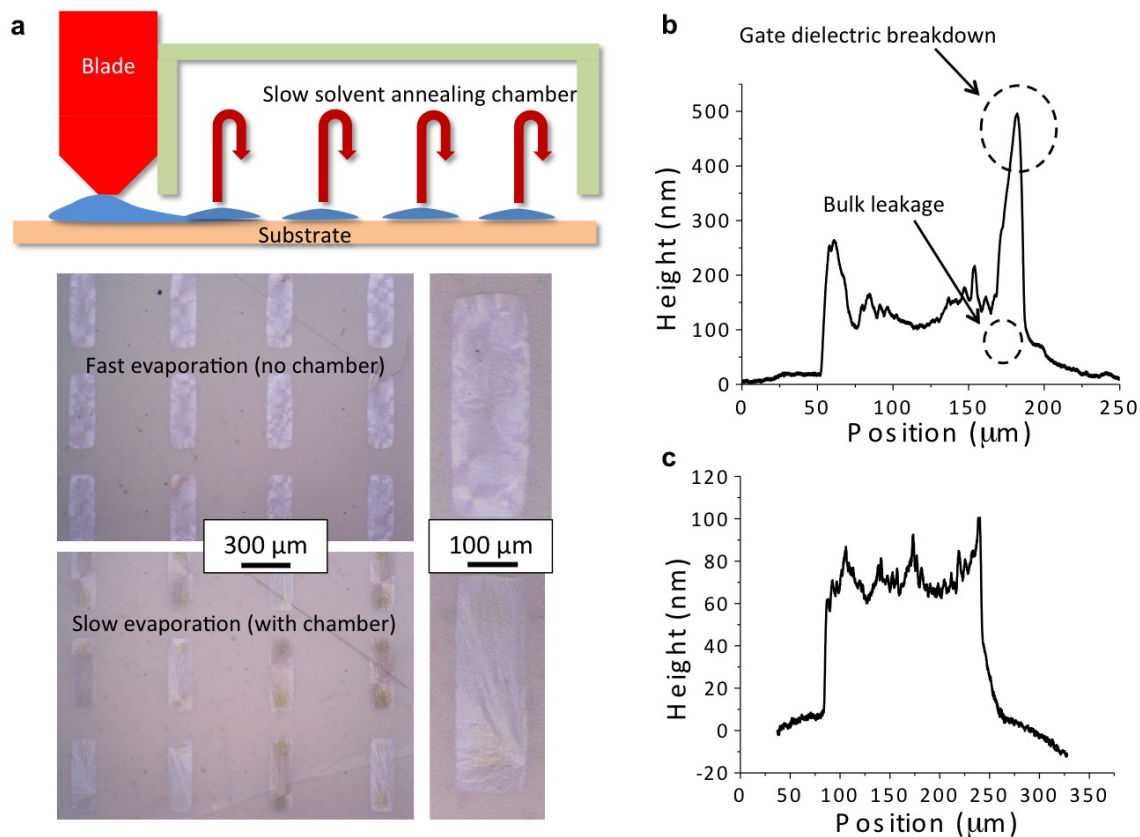


Figure 2.10: Schematic depiction of chamber used to control evaporation rate of toluene with optical micrographs (a) and cross-sectional profiles of TIPS-Pentacene crystals formed by fast (b) and slow (c) solvent evaporation.

that occurs from the edge of the electrodes in the dashed red circles, which effectively reduces the  $W$  of the OTFT, for 40  $\mu\text{l}$  of dispensed ink on the blade and coated at 2 cm/s. This issue is mediated by dispensing more ink on the blade to transfer more ink to the patterned regions. Increasing the volume of ink from 40  $\mu\text{l}$  to 55  $\mu\text{l}$  eliminates most of the discontinuities between the electrodes and the channel as seen in Figure 2.11c.

The final OTFT devices were completed by doctor blade coating the AF dielectric over an array and thermally evaporating aluminum gate electrodes. The larger grain size results in more variability in the output current than the polymeric SP220 semiconductor as seen in Figure 2.11d (mobility is directly proportional to current). Figure 2.11e shows the transfer characteristic of a typical device in the array. While the on-off ratio,  $10^3$ , is higher than that of the SP220 devices, the mobility lags behind at only  $0.014 \text{ cm}^2/\text{Vs}$ . Small molecule organic semiconductors such as TIPS-Pentacene exhibit low mobility when deposited on hydrophilic

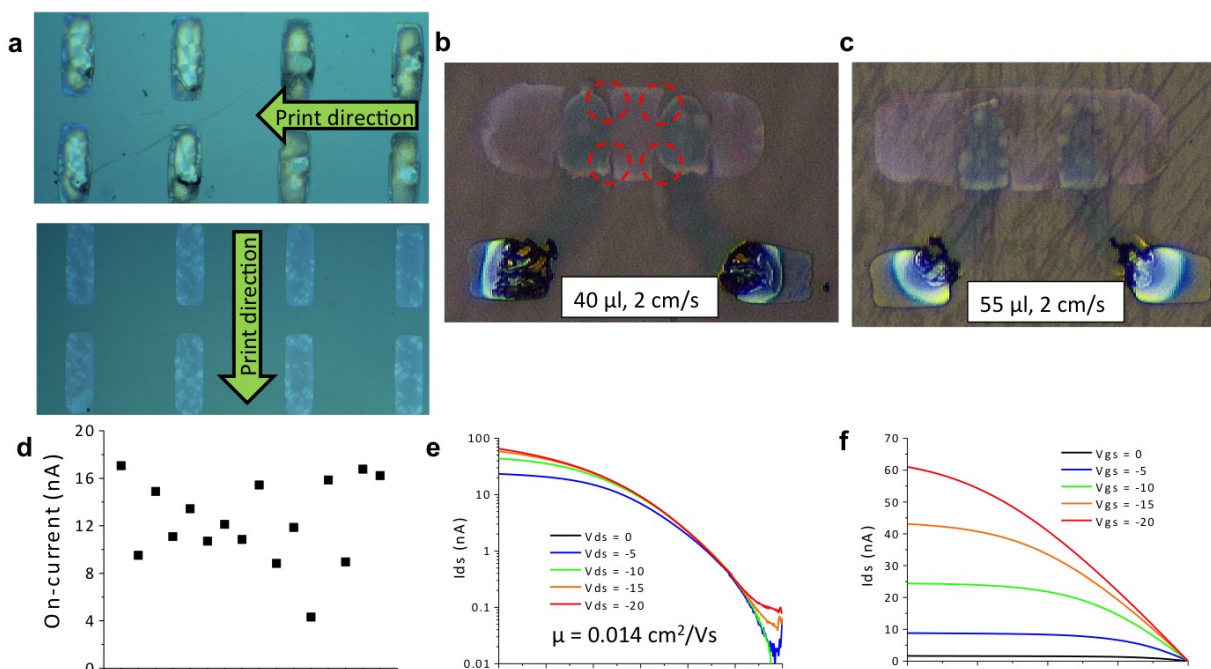


Figure 2.11: Effect of blade coating direction (a) and dispensed ink volume (b and c) on TIPS-Pentacene film morphology and continuity between electrodes and the channel, respectively. The variability of on-current (d) and typical transfer (e) and output (f) curves for a TIPS-Pentacene OTFT.

surfaces since it induces poor  $\pi$ -stacking[88]. HMDS-treated patterns were too hydrophobic for the low viscosity of the TIPS-Pentacene solution, resulting in complete dewetting from the surface. However, the output resistance of the device is high as seen in Figure 2.11f.

## Small Molecule-Polymeric Semiconductor Blends

Blends of polymeric and small molecule semiconductors can be used to combine the high performance of small molecule semiconductors with the rheological properties of polymers to enable reliable printing. The hydrophilic nature of oxygen plasma-treated patterns in our process favors good printability by enabling better ink wetting and decreases hole injection barrier from PEDOT:PSS electrodes[110]. However, as seen previously in the OTFTs made from TIPS-Pentacene, the low viscosity of these solutions results in dewetting from the source-drain electrodes and the hydrophilic surface induces poor  $\pi$ -stacking, leading to poor device performance. Prior art showed that it is possible to achieve high performance OTFTs by blending small molecule semiconductors such as TIPS-Pentacene with a low mobility amorphous polymer poly[bis(4-phenyl)(2,4,6-trimethylphenyl)amine] (PTAA)[57, 71]. The

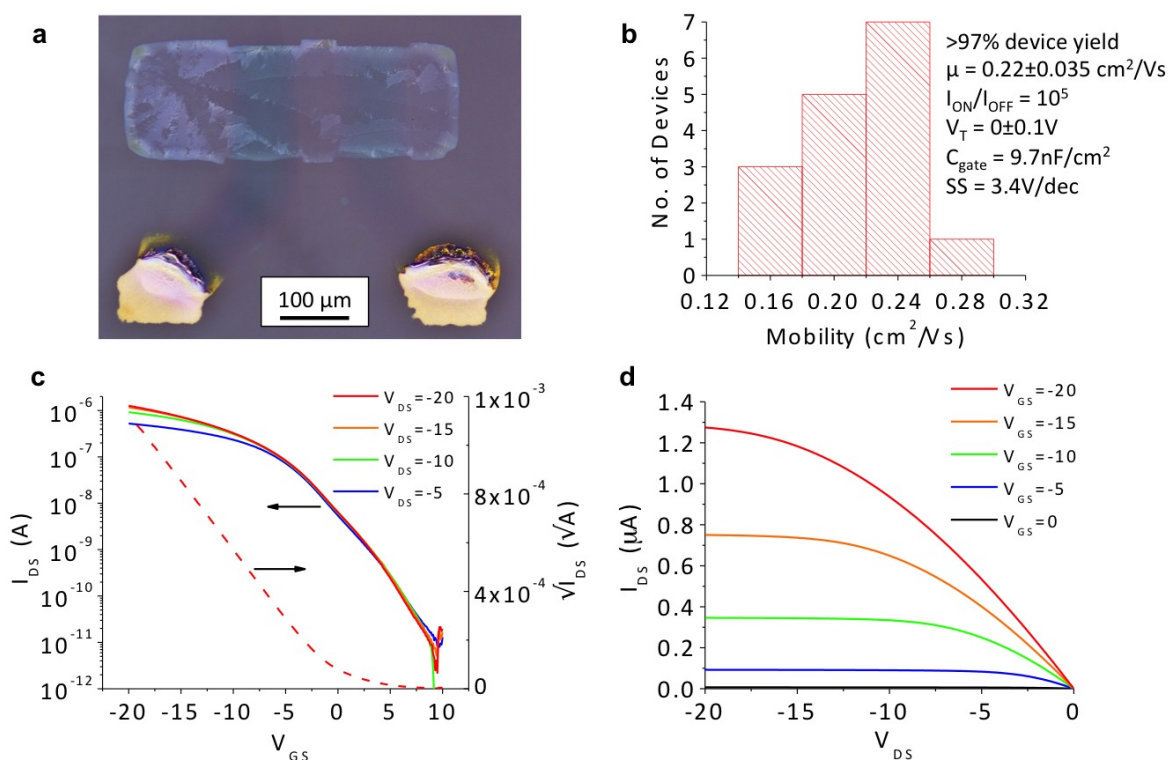


Figure 2.12: An OTFT with a semiconductor composed of 1:1 TIPS-Pentacene : PTAA (a). The distribution of saturation mobility (b) and typical transfer (c) and output (d) plots are shown.

small molecule and PTAA vertically segregate with the high mobility small molecule on top to form top-gate devices. The driving force for this separation increases for hydrophilic substrates, making it compatible with the SEP doctor blade coating process. Figure 2.12a shows a polarized micrograph of a 1:1 TIPS-Pentacene:PTAA blend in mesitylene blade coated on PEDOT:PSS source-drain electrodes. The vertical segregation enables TIPS-Pentacene to form large grains on the surface while the PTAA increases the viscosity sufficiently to prevent dewetting from the electrodes. The complete devices, using AF dielectric and a thermally evaporated gate electrode, have high yield, good mobility and low variability as outlined in Figure 2.12b. The lower subthreshold slope, as seen in 2.12c, enables a high on-off ratio of 105. Additionally, these devices demonstrate good square law behavior (right axis of Figure 2.12c) and no injection barriers from the output characteristic of Figure 2.12d.

The semiconductor used in the final array is a mixture of the high performance small molecule 2,8-difluoro-5,11-bis(triethylsilylethynyl)anthradithiophene (diF TES ADT) with PTAA in Figure 2.13a. Slowly evaporating solvents (low vapor pressure) curtail coffee ring

effects and generally improve transistor performance[108], however the use of these solvents can result in dewetting from lower surface energy substrates as they evaporate[173]. Consequently, it is important to examine the role of high and low vapor pressure solvents in achieving good printing reliability and performance. Figure 2.13b shows the high (mesitylene, 2.49 mmHg) and low (tetralin, 0.37 mmHg) vapor pressure solvents used to print the semiconductor layer.

Figures 2.13c-e shows polarized micrographs of different semiconductor ink compositions. Despite the hydrophilic surface of the plasma-treated pattern, the low viscosity of a pure diF TES ADT solution dewets even for a 9:1 ratio of mesitylene to tetralin. This film formation results in rough semiconducting layers, causing low device yield through severe gate dielectric leakage as reflected in Table 2.1. While dewetting from edges is not an issue when spin coating or blade coating very large patterns or non-patterned films, it becomes apparent that polymer additives are necessary in small molecule solutions in order to modify the rheological properties of the ink to prevent dewetting. As shown in Figure 2.13d, the printability and pattern fidelity is improved when 10 wt.% PTAA is added to diF TES ADT. Further improvement on printability and film formation, in Figure 2.13, is observed as the amount of PTAA is increased to 50 wt.% and the solvent is composed of 2:1 ratio of mesitylene to tetralin.

The quality of the printed semiconductor films was characterized in an OTFT structure with AF gate dielectric and thermally evaporated aluminum gate electrodes. Figure 2.13f shows the transfer characteristics of the devices shown in Figures 2.13c-e with the array and device characteristics summarized in Table 2.1. Furthermore, the subthreshold region for devices with PTAA exhibit an exponential behavior rather than a power law for the

Semiconductor Formulation	Yields	Sat. Mob. ( $\text{cm}^2/\text{Vs}$ )	$\text{Log}(I_{\text{ON}}/I_{\text{OFF}})$	$V_T$
9:1 mesitylene : tetralin, 1:0 diF TES ADT : PTAA	10/16	$0.39 \pm 0.13$	$4.93 \pm 0.23$	$0.78 \pm 0.65$
9:1 mesitylene : tetralin, 9:1 diF TES ADT : PTAA	16/16	$0.47 \pm 0.18$	$4.2 \pm 0.11$	$-0.81 \pm 0.41$
2:1 mesitylene : tetralin, 1:1 diF TES ADT : PTAA	16/16	$0.68 \pm 0.23$	$5.49 \pm 0.15$	$-2.2 \pm 0.37$
2:1 mesitylene : tetralin, 1:1 diF TES ADT : PTAA (spin coated on Au source-drain)	13/16	$0.1 \pm 0.09$	$1.07 \pm 0.2$	$1.11 \pm 4.37$

Table 2.1: Yields and average saturation mobility, on-off ratio and threshold voltage standard deviation for devices with various diF TES ADT : PTAA and mesitylene:tetralin composition.

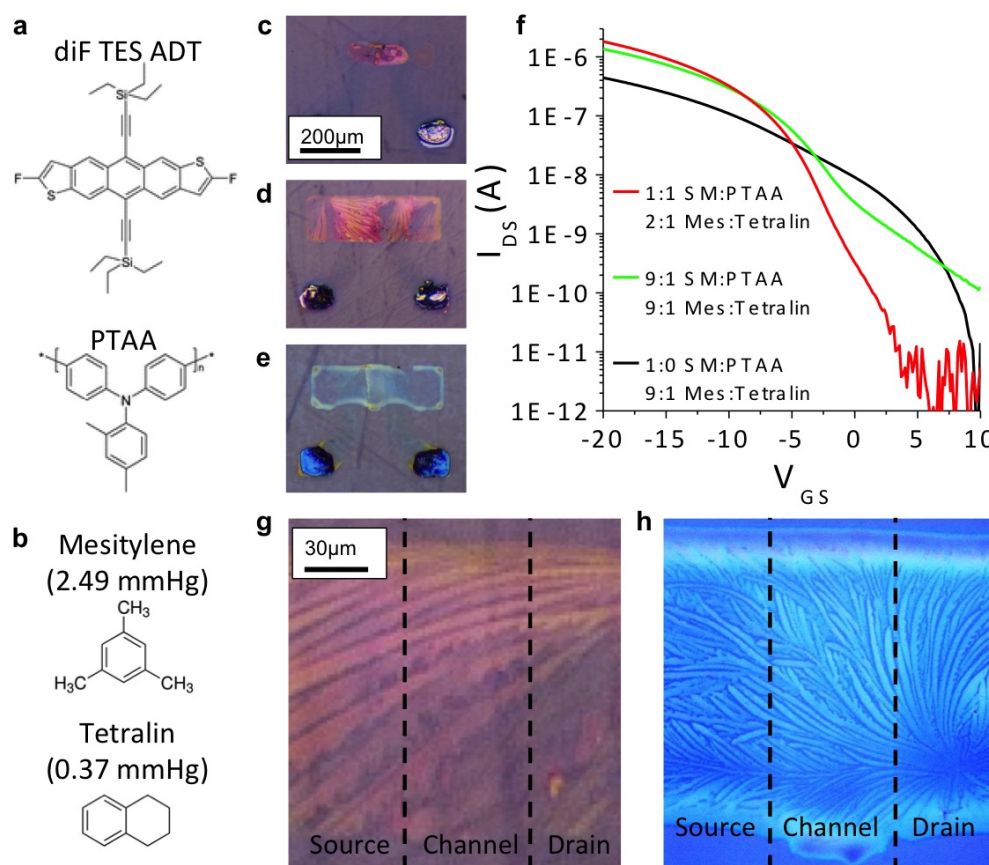


Figure 2.13: Chemical structure of semiconductor (a) and solvent (b) blends used in ink formulation. Polarized optical microscopy of semiconductor films (prior to gate electrode thermal evaporation) printed on plastic from inks composed of 1:0 and 9:1 (c), 9:1 and 9:1 (d), 1:1 and 2:1 (e) diF TES ADT:PTAA and mesitylene:tetralin, respectively. Transfer characteristics of these films (f) and polarized optical microscopy of semiconductor films in the channel regions printed from inks composed of 9:1 and 9:1 (g), 1:1 and 2:1 (h) diF TES ADT:PTAA and mesitylene:tetralin, respectively.

pure diF TES ADT film, which is indicative of a crystalline-behaving band structure[77] and attributed to the vertical segregation of diF TES ADT and PTAA[57]. By further increasing the polymer and tetralin concentration to 50 wt.% and 33 vol.%, respectively, the mobility improves to an average of  $0.68 \text{ cm}^2/\text{Vs}$  with values as high as  $1.6 \text{ cm}^2/\text{Vs}$ , which is comparable to values of  $2 \text{ cm}^2/\text{Vs}$  seen in optimal spin-coated devices[57]. Decreased sub-threshold slope and negative threshold voltage shift (2.1) are also accompanied by increasing the polymer and tetralin concentration. As a figure of comparison, Table 2.1 also reports that control spin-coated devices using the aforementioned semiconductor ink formulation on



pentafluorothiophenol-treated Au source-drain electrodes have worse performance, yield and more variability than printed devices. While there is some dewetting off the topographically higher printed source-drain electrodes seen in Figure 2.13e, the same surface energy of the plasma-treated PEDOT:PSS contacts and underlying plastic substrate in the channel enables a continuous film morphology across the contacts and channel, regardless of ink formulation, as shown in Figures 2.13g and h. This continuity may enable high mobility short channel devices by preventing the small grains seen in short channel metallic bottom contacts as a result of crystal nucleation at the source-drain electrodes[54]. The resulting continuity of morphology is similar to what is seen by the addition of nucleation promoters in OTFTs[173].

## 2.5 Dielectric Optimization

Amorphous fluoropolymer (AF, DuPont™) is used as the gate dielectric for all devices due to its low polarization that minimizes scattering of charge carriers and maximizes mobility. While this layer is un-patterned, it is necessary to ensure good uniformity across the array. Figure 2.14a shows the thickness along the coating direction (y-position) located at several cross sections perpendicular to the coating direction (x-position) for a polymer coated from propylene glycol methyl ether acetate (PGMEA, 45 mmHg vapor pressure) at 70°C. Not only does the thickness taper off with y-position by more than 30%, there is also significant variability in thickness with x-position for a given y-position. Blade coating a higher vapor pressure solvent such as tetrahydrofuran (THF, 150 mmHg) enables a faster evaporation, limiting the spreading of the wet film during the time of drying. Adding 10 vol.% dimethyl-

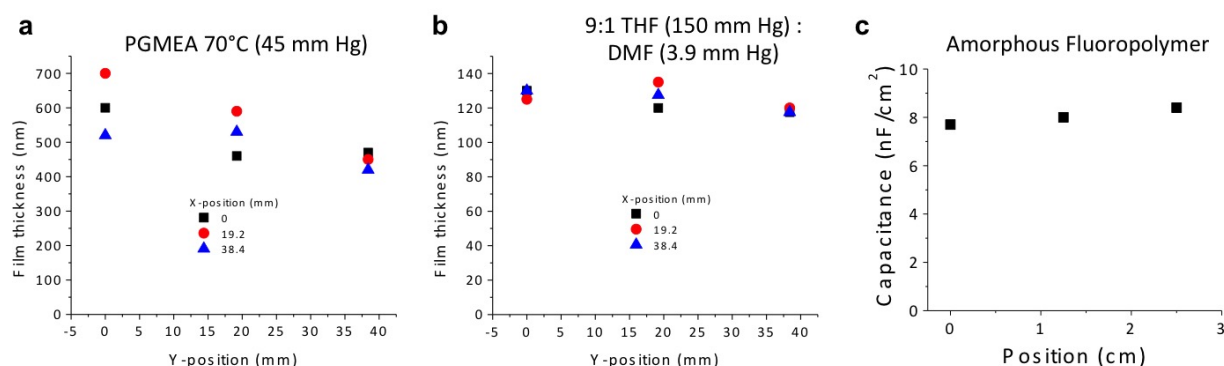


Figure 2.14: Poly(4-vinylphenol) dielectric film thickness along coating (y) and lateral (x) directions printed from a single intermediate vapor pressure solvent (a) and mixture of high and low vapor pressure solvent blend (b). The thickness of amorphous fluoropolymer using a blend of high and low boiling point solvents is also shown (c).

formamide (DMF), with a low vapor pressure of 3.9 mmHg, reduces the roughness of the film since it slowly evaporates from the film after the THF is gone and induces Marangoni flows to uniformly distribute solute. The concentration of high boiling point solvent is kept at an additive concentration ( $\leq 20$  vol.%) to prevent it from affecting the film quality during printing. Figure 2.14b shows how such a ink composition gives more uniform film thickness across the array. The AF dielectric ink was likewise formulated from a high vapor pressure solvent (FC 770, 49 mmHg) with an additive concentration of low vapor pressure solvent. The capacitance per unit area varies only 9% over a distance of 2.5 cm as a result of varying dielectric thickness as shown in Figure 2.14c. This uniformity minimizes variability in TFT arrays.

## 2.6 OTFT Array Performance & Reliability

The uniformity of an array of OTFTs using the optimal semiconductor ink formulation from Table 2.1 and process in Figure 2.3 but with a thermally evaporated gate electrode, shown in Figure 2.15a, is assessed as a function of area and annealing conditions. The mean mobility at various areas in the array annealed at 120°C after thermal evaporation of the gate electrode (post-annealed) is shown in Figure 2.15b is uniform, varying from 0.5 to 0.7 cm<sup>2</sup>/Vs. The large standard deviation is a result of variability in orientation of the large grains of diF TES ADT. Figures 2.15c and f, d and g show that annealing increases both mobility and on-off ratio, respectively. The negative shift in threshold voltage after annealing, as seen by comparing Figures 2.15e and h, is attributed to trapping of positive particles in the bulk of the semiconductor since the mobility increases during annealing.

An all-printed, flexible OTFT array on plastic, as depicted in Figure 2.16a, is finally fabricated according the full process outlined in Figure 2.3. Instead of thermally evaporating a gate electrode, the fully printed OTFT array is finalized by inkjet printing the top gate electrode shown in Figure 2.4a. Device yield is 96% for a 200 nm thick dielectric, the only failure mechanism being dielectric shorting. The transfer and output characteristics of a typical device in Figures 2.16b and c, respectively, demonstrate good square law behavior, high saturation output resistance, and no contact barrier. Figures 2.16d-g show the statistical distribution of saturation mobility, on-off ratio, subthreshold slope, and threshold voltage for this array, respectively. Devices were measured in air as in previous OTFT reports to demonstrate stability[138]. The mean mobility is reduced to 0.31 cm<sup>2</sup>/Vs compared to 0.68 cm<sup>2</sup>/Vs for the devices with evaporated gate electrodes (Table 2.1). This result may originate from residual solvent left in the stack since the array is not placed in the high vacuum and temperature environment of a thermal evaporator. However, all-printed devices demonstrate less variability, with a mobility coefficient of variance (CV) of only 20% compared to 34% for the high mobility devices in Table 2.1. The fully overlapping gate electrode over the channel width prevents leakage current around the gate, enabling devices with mean on-off



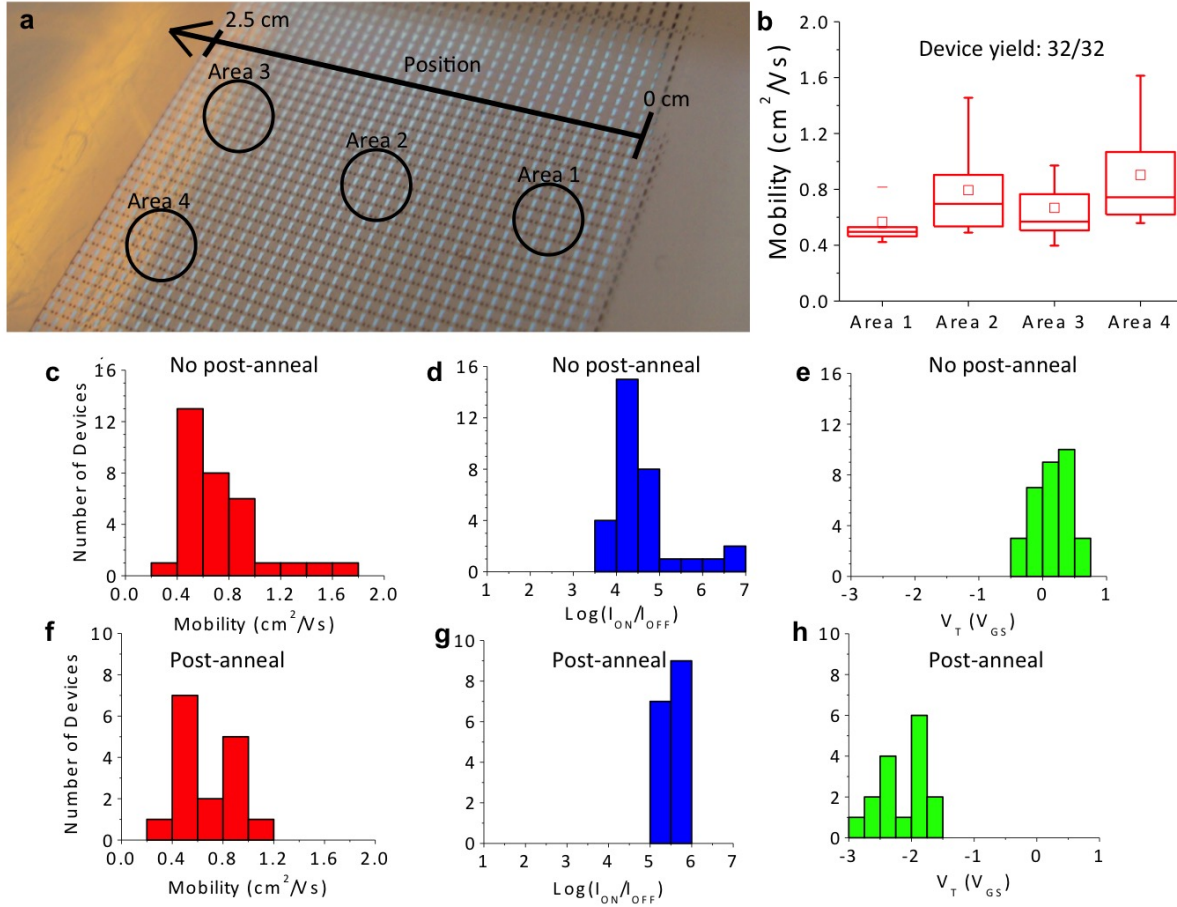


Figure 2.15: Mostly-printed OTFT array with evaporated gate electrodes (a) with mobility measured at various locations in the array (b). Saturation mobility (c and f),  $\text{Log}(I_{\text{ON}}/I_{\text{OFF}})$  (d and g), and threshold voltage (e and h) histograms are shown before and after annealing the complete device (post-annealed) at 120°C for 10 minutes, respectively.

ratios over 105 and subthreshold slopes of 1.17 V/dec with a CV of only 11%. Furthermore, these devices have a mean threshold voltage of -0.07 V with a standard deviation of only 0.21 V, which is far less than values of -10 to -20 V for spin-coated diF TES ADT-polymer blends[159].

Electrical and mechanical reliability measurements were performed on the all-printed array. A bias stress measurement in Figure 2.17a show that the output current of the all-printed OTFT continuously biased for 1000 seconds degrades by 38%. The threshold voltage only shifted by 1V during bias stress, however it was the degradation in mobility which contributes to the decrease in output current as deduced from Figure 2.17b. Mechanical testing

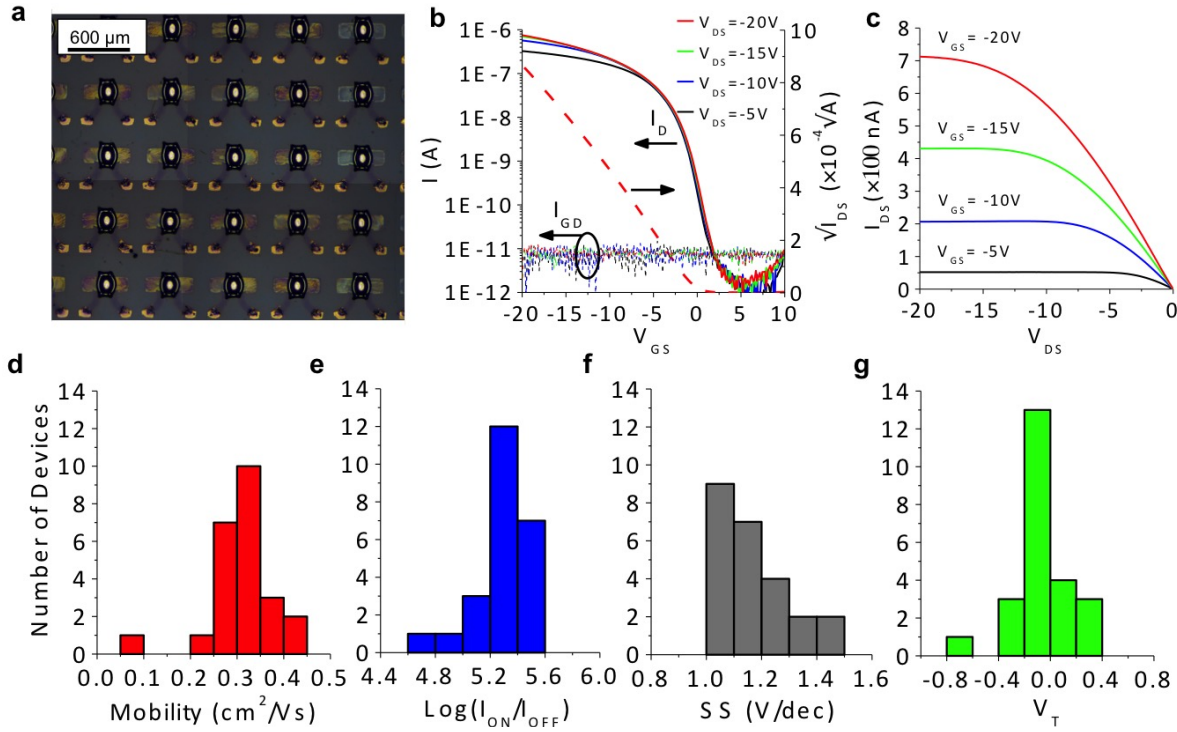


Figure 2.16: Zoomed-out photograph of the all-printed OTFT array (a) with the transfer (b) and output (c) characteristics of a typical device. The statistical distribution of saturation mobility (d),  $\text{Log}(I_{ON}/I_{OFF})$  (e), subthreshold slope (f), and threshold voltage (g) is shown for the array.

reveals less than 20% decrease in on-current at a bending radius of 3mm as shown in Figures 2.17c and d. Devices fail at 1.7 mm radius of curvature as a result of the substrate surface cracking with all other device layers intact as seen in Figure 2.17e.

## 2.7 Conclusion

In summary, novel printing methods were developed and the impact of ink formulations on performance was assessed for fully printed and flexible OTFT arrays. The deposition of each layer, which is processed from solution and deposited and patterned by printing, is optimized to achieve a high device yield. The printed devices exhibit high reliability, low variability, ideal electrical behavior and good mechanical properties. Blade coating on SEP plastic substrates combines the scalable properties of a roll-to-roll compatible printing technique used to fabricate high quality homogeneous thin films with the practicality of generating two-

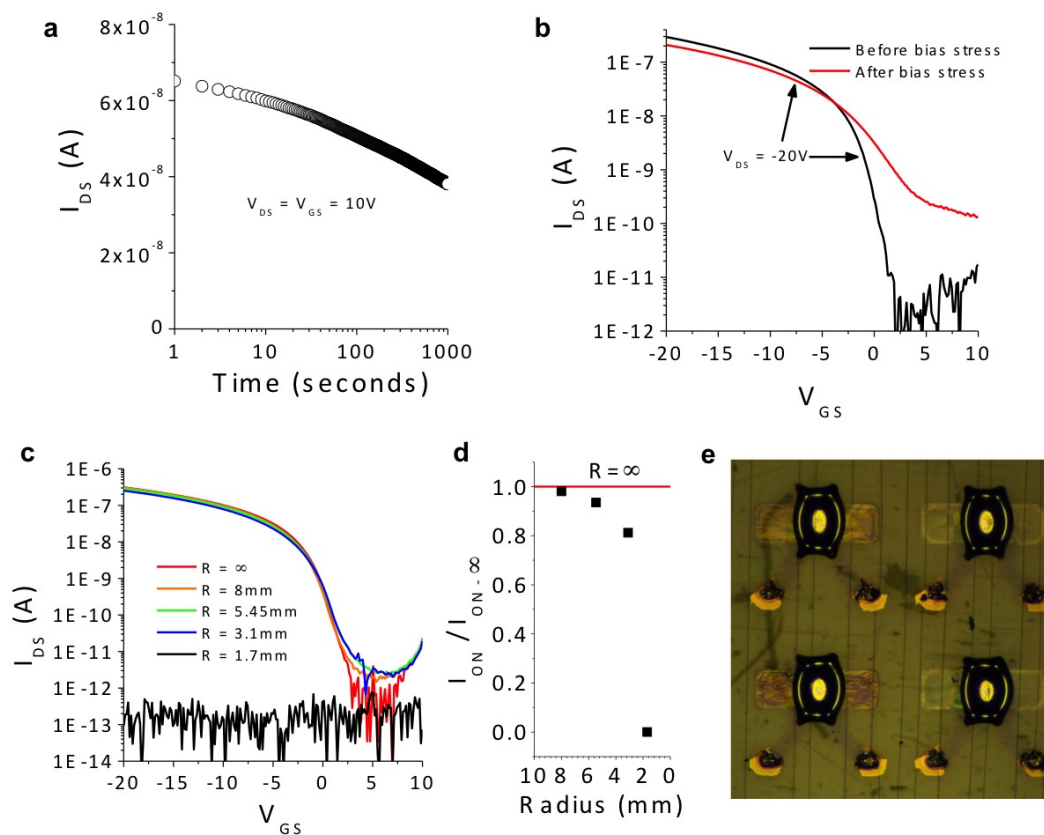


Figure 2.17: Bias stress during measurements (a) and comparison of transfer characteristic before and after (b). Transfer characteristics measured during flex testing (c) showing change in on-current with bending radii (d) that eventually fail due to substrate cracking (e).

dimensional patterns. Using this technique, scalable self-aligned blade-coated SD electrodes with minimal variability can be very reliably printed. Furthermore, blending polymers with high performance small molecules enables more reliable printing with higher boiling point solvents, improved device performance and yields. Finally, surface tension is utilized to print the gate electrodes. Fully-printed devices on plastic demonstrate a high yield of 96% with good carrier mobility (average  $0.31 \text{ cm}^2/\text{Vs}$ ), subthreshold swing (average  $1.17 \text{ V/dec}$ ), high on-off ratio (average  $2.2 \times 10^5$ ), zero threshold voltage, very low variability in all aspects of device performance and good mechanical robustness. The high yields combined with high device performance indicate that SEP blade coating is a scalable and robust technique which can be used to design electronic circuits where device reliability is required and could lead to all-printed systems on plastic.

## Chapter 3

# Printed Organic Photodiodes

### 3.1 Introduction

The recent increase in utilization of image sensors[123, 126, 139] and significant development in the field of wearable and disposable sensors[114] not only demands a decrease in photodiode fabrication costs, but also requires new functional abilities such as operating at extremely low light intensities[18, 41], narrowband and broadband spectral selectivity[6, 51], lightweight and mechanical flexibility[8, 130]. Today, most of these demands cannot be fulfilled by conventional workhorse silicon photodetectors without a significant amount of processing steps to achieve heterogeneous integration[93]. The chemical tunability, mechanical properties and printable processing of organic materials make them promising candidates for fabrication of low-cost, highly scalable and flexible organic photodiodes (OPDs)[5]. In addition, the large area scalability of printing techniques is beneficial for photodiodes since the signal-to-noise ratio (SNR), at a given light intensity, increases with detector size[65, 166]. Since the SNR depends on multiple parameters, such as the external quantum efficiency (EQE)  $\eta$ , the dark current density  $J_d$ , sampling bandwidth and photoactive area, it significantly complicates the comparison of photodetectors. For this reason a useful figure of merit to consider is specific detectivity,  $D^*$ , as mentioned in Chapter 1, which combines these parameters as shown in Equation 3.1, assuming negligible photocurrent shot noise and flicker noise. Azzellino *et al*'s[8] mostly-inkjet printed OPDs with specific detectivity over  $10^{12} \text{ cm}\cdot\text{Hz}^{0.5}\cdot\text{W}^{-1}$  and Tedde *et al*'s[171] low variability partially-spray coated OPDs are a few examples of high performance partially-printed OPDs. However all OPDs reported to date rely on thermal evaporation of oxygen-sensitive metal cathodes, spin-coating or inkjet printing, all of which are not scalable deposition methods in achieving large area coverage or high fill factor (photosensitive area/total area)[10].

$$D^* = \frac{q\lambda\eta}{hc} (2qJ_d + N_{other\ noise})^{-\frac{1}{2}} \text{ cm} \cdot \text{Hz}^{0.5} \cdot \text{W}^{-1} \quad (3.1)$$

This chapter shows that state of the art all-printed, flexible OPDs with average specific

detectivities as high as  $3.45 \times 10^{13} \text{ cm} \cdot \text{Hz}^{0.5} \cdot \text{W}^{-1}$  can be printed using industrially scalable techniques (i.e., blade coating and screen printing) by controlling charge selectivity of organic electrodes[137]. In addition to the high specific detectivity needed to resolve low light intensity, these OPDs are able to sustain high reverse biases. High reverse biases are used to maximize the capacity of the photodiode to capacitatively store photogenerated charge, which is essential for increasing the dynamic range of image sensors[65, 166]. Through optimization and characterization of the properties of each printed layer, device yield is maximized with minimal variability over large areas. The performance of all-printed photodiodes achieved here becomes comparable to silicon photodiodes used in image sensors, which have a specific detectivity of approximately  $6\text{-}7 \times 10^{13} \text{ cm} \cdot \text{Hz}^{0.5} \cdot \text{W}^{-1}$  [65]. These results show that along with advantages such as inexpensive fabrication and mechanical flexibility, all-printed OPDs can have performance competitive with their Si-counterparts.

## Kelvin Probe Force Microscopy

The work function of a conductor is the energy required to remove an electron from the surface of a material to an infinite distance. Knowing this parameter in relation to the HOMO and LUMO of the active layer of the OPD is essential to reduce the contact barrier for the majority carrier and maximize the injection barrier for the minority carrier of that electrode. The ability to tune the work function of the anode and cathode enables arrays of OPDs with high uniformity and precise control of performance. Kelvin probe force microscopy (KPFM) is used to measure the work function of the anode and cathode for the OPDs presented in this chapter. Figure 3.1a shows the initial condition of the isolated probe tip and sample, with the vacuum energy levels ( $E_{\text{Vac}}$ ) and electrochemical potential ( $E_{\text{EC}}$ ) of the tip

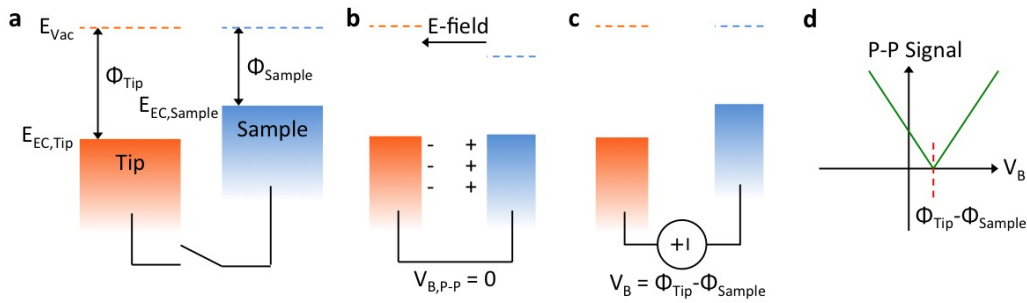


Figure 3.1: Kelvin probe force microscopy (KPFM) theory of operation, showing energy level alignment between the probe tip and sample with no connection (a), short circuit (b), and biased at the flat band potential (c). (d) The peak-to-peak (P-P) output signal characteristics of Kelvin probe measurement as a function of  $V_B$  and denoting the minima that occurs at the flat band potential.

and sample only dependent on the work function of the tip ( $\Phi_{\text{Tip}}$ ) and sample ( $\Phi_{\text{Sample}}$ ), respectively. A direct electrical connection between the two equilibrates the electrochemical potential that is compensated by an electric field between the sample and the probe tip as seen from Figure 3.1b. Figure 3.1c shows that this electric field and injection of charge at the surface is neutralized when the system is biased at the flat band potential, which is the potential at which  $E_{\text{Vac}}$  are lined up in the tip and sample. The amount of charge at the surface is determined by superimposing an alternating voltage on top of the DC voltage of  $V_B$  and reading the peak-to-peak (P-P) signal of the output current. The flat band voltage is determined as the  $V_B$  at which the output signal is minimized as depicted in Figure 3.1d, which is  $\Phi_{\text{Tip}} - \Phi_{\text{Sample}}$ . A known reference for the probe tip is needed to determine  $\Phi_{\text{Sample}}$ . Probe placement closer to the surface of the sample will produce a larger signal due to a stronger capacitive coupling. For this reason, these scans are performed using an atomic force microscopy (AFM) cantilever 10-30 nm above the substrate. In addition, the small tip of the cantilever provides a high resolution to detect pinholes or inhomogeneities in the film.

## Screen Printing Theory

Screen printing is a highly scalable printing technique that is used to deposit patterned thick wet films on a substrates. This printing technique is comprised of a flood phase and a squeegee phase. Flooding is first used to coat a uniform film on the screen without touching it as shown in the step 1 of Figure 3.2a. The screen is a fine mesh (thread diameter 20-30  $\mu\text{m}$ ) with an emulsion layer cast in the mesh to block ink in non-patterned regions. Figure 3.2b illustrates a screen with the underlying mesh (blue) and overlying emulsion (orange) used to define the pattern to be printed. A mesh angle of  $22.5^\circ$  with respect to the print direction is found to provide the best pattern fidelity for low dimensional features[150]. After flooding, a squeegee presses onto the screen as it is dragged across the substrate as shown in step 2 of Figure 3.2a. This squeezes ink from the top of the mesh through openings in the emulsion layer onto the substrate as shown in step 3. The most common parameters of optimization in screen printing occur during the squeegee phase and are the squeegee pressure and snap-off distance, which is the gap between relaxed screen and substrate. A shear thinning viscous paste is needed for screen printing to achieve a contrast in viscosity between flooding and printing as figuratively explained in the graph in Figure 3.2c. Shear rate,  $\dot{\gamma}$ , is defined for a fluid moving between a stationary plate and a moving plate (also known as a Couette flow shown in Chapter 2 Figure 2.1a) as the velocity of the moving plate,  $v$ , divided by the separation between the plates,  $h$ , as shown in Equation 3.2. The large separation between the screen and the flood bar creates a low shear rate at which the paste is too viscous to flow through the openings of the screen. However, pressing the squeegee creates a very small gap with the screen, which increases the shear rate of the ink and decreases the viscosity to the point it can flow through the openings and onto the substrate.

$$\dot{\gamma} = \frac{v}{h} \quad (3.2)$$

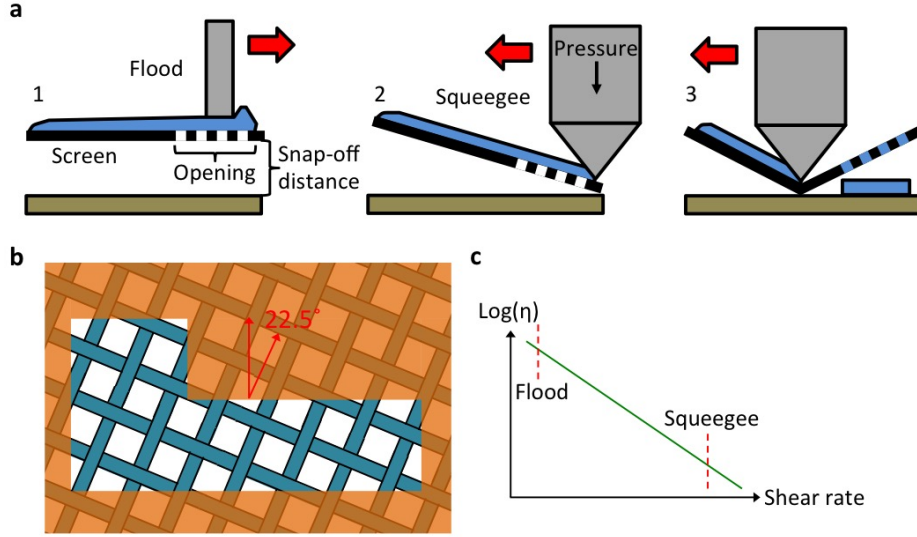


Figure 3.2: (a) Screen printing process showing the flood phase (step 1) and squeegee phase (step 2) with ink pushed through openings in the screen depositing on the substrate as the squeegee is dragged across the screen (step 3). (b) Illustration of a zoomed-in portion of a screen, which consists of an emulsion layer (orange) with openings that define the patterns that is supported by a stainless steel mesh (blue) that is angled  $22.5^\circ$  with respect to the printing direction. (c) Figurative illustration of viscosity ( $\eta$ ) as a function of shear rate for a shear thinning ink, showing regions that are relevant to the flood (step 1) and squeegee (step 2) phases.

## All-printed Organic Photodiode Fabrication Process

There are materials and fabrication limitations to consider when maximizing device performance and reliability that dictate the device architecture. The lack of printable low work function conductors for a cathode demands the use of interlayers. Interlayers not only decrease cathode work function but also have hole blocking properties, which is essential for minimization of reverse bias dark current density[10]. The interlayers are typically cast by spin coating[8, 197] from solvents that are orthogonal to underlying layers. Doctor blade coating is a preferable alternative to spin coating as it is scalable to large areas and can produce large films with well-controlled uniformity[135]. Additionally, this printing technique has been shown to be a suitable deposition method for the active layer as bulk heterojunction



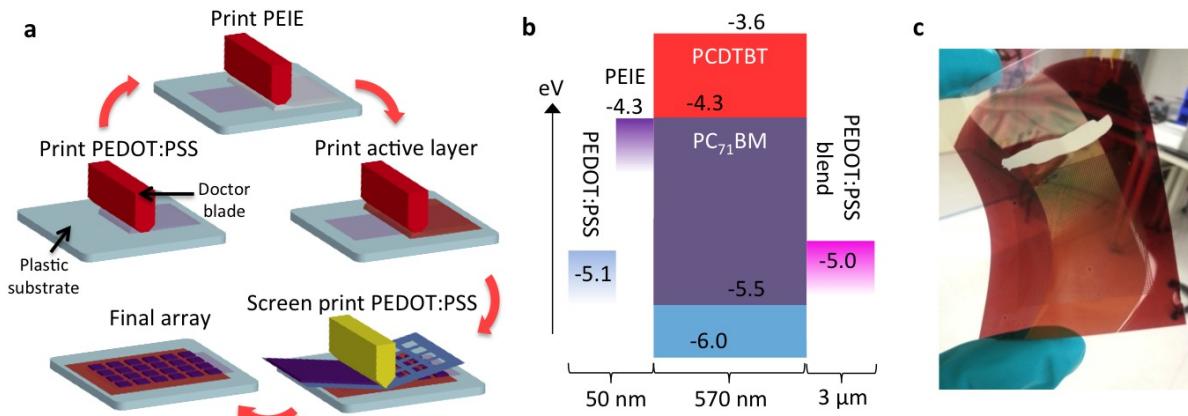


Figure 3.3: (a) Fabrication steps for each layer in an all-printed organic photodiode (OPD) using doctor blade coating (red) and screen printing (yellow). (b) Band diagram and thickness of each layer of the all-printed OPD for a PCDTBT:PC<sub>71</sub>BM active layer. (c) Photograph of  $32 \times 32$  pixel array on a flexible plastic substrate.

(BHJ) morphology can be well controlled[142]. However, printing the low viscosity solutions optimized for doctor blade and spin coating on top of the hydrophobic BHJ active layer leads to dewetting[100]. Screen printing mediates this issue as it is highly scalable and the high viscosity of the pastes minimizes dewetting[8, 100]. While films deposited through screen printing are too thick to be suitable for the poor conductivity of low work function interlayers, conventional high work function conductors can be readily printed. Consequently, an inverted structure offers a better route to achieve printed devices since the cathode interlayer may be deposited on the bottom electrode while the top electrode uses commonplace printable high-work function materials.

This chapter focuses on the development and characterization of a printing process, shown in Figure 3.3a, that allows fabrication of high yield, high performance flexible OPD arrays. The cathode is formed by first blade coating a layer of poly(3,4-ethylenedioxythiophene):poly(styrenesulfonate) (PEDOT:PSS) on a polyethylene naphthalate (PEN) substrate. A low work function cathode is achieved with a second blade coated layer of polyethylenimine ethoxylated (PEIE) on top of the PEDOT:PSS. The highly polarizable imine functional groups of this interlayer create large dipoles on the surface, which can decrease the work function of metallic and polymeric conductors by more than 1 eV[89, 197]. The active layer blade coated on top of the cathode is a BHJ blend of Poly[*N*-9'-heptadecanyl-2,7-carbazole-*alt*-5,5-(4',7'-di-2-thienyl-2',1',3'-benzothiadiazole)] (PCDTBT) and [6,6]-phenyl C<sub>71</sub>-butyric acid methyl ester (PC<sub>71</sub>BM). This blend material was chosen because it is known to be very efficient at generating free-carriers[101, 131] and have good environmental stability[134]. Device fabrication is finished by screen printing an array of anodes of PEDOT:PSS, a well



known hole selective electrode, into the desired shape. The optimal all-printed OPD device structure with the corresponding band diagram and layer thicknesses is shown in Figure 3.3b with an anode and cathode work function of 5 and 4.3 eV, respectively. A photograph of the final 64×64 pixel array in Figure 3.3c demonstrates the mechanical flexibility of this system. It is also possible to fabricate mostly-printed inverted and standard geometry OPDs with evaporated gold or aluminum top electrodes, respectively, which will be compared to the all-printed devices later on. The role of the interlayer work function, active layer thickness, and choice of electrodes on device performance is investigated in order to fabricate OPDs with high specific detectivity at high reverse bias.

## 3.2 Cathode Design

Poor printing reliability has been a limiting factor for improving device yield (the percentage of properly functioning devices) and minimizing variability, with few reports of partially-printed OPDs demonstrating consistent performance over centimetric areas[171]. The main challenge in printing is the uniform deposition of thin interlayers[40] and patterned electrodes without shorting through underlying layers[100]. It has been shown that spin coating PEIE on top of PEDOT:PSS decreases its work function by 1.3 eV[197]. However, very few accounts of variable work function tunability without modification of the interlayer molecule have been demonstrated through any deposition process[40]. The work function of blade coated PEDOT:PSS/PEIE cathode, which is significantly more scalable than spin coating, may be fine-tuned by changing the weight concentration of PEIE in the blade coated solution as summarized by KPFM measurements in Figure 3.4a. Each data point shows the average and standard deviation of the work function measured at three to four data points separated by 2-3 cm on the substrate. The work function of PEDOT:PSS can be lowered from 5.15 eV to anywhere between 4.6 eV and 4.1 eV by changing the PEIE solution concentration between 0.05 wt. % and 1 wt. % in 2-methoxyethanol. Table 3.1 shows, for a given PEIE solution concentration, the work function decrease of PEDOT:PSS is larger in a nitrogen environment than in air. Further studies will need to be done in order to determine whether

PEIE Blade Coating (0.6 wt. %)	Work Function (eV)
Only PEDOT:PSS	$5.15 \pm 0.02$
Coated on PEDOT:PSS in air	$4.73 \pm 0.01$
Coated on plasma-treated PEDOT:PSS in air	$4.96 \pm 0.02$
Coated on PEDOT:PSS in N <sub>2</sub>	$4.17 \pm 0.02$

Table 3.1: Work function of the PEDOT:PSS cathode coated with 0.6 wt. % PEIE in 2-methoxyethanol under various conditions.

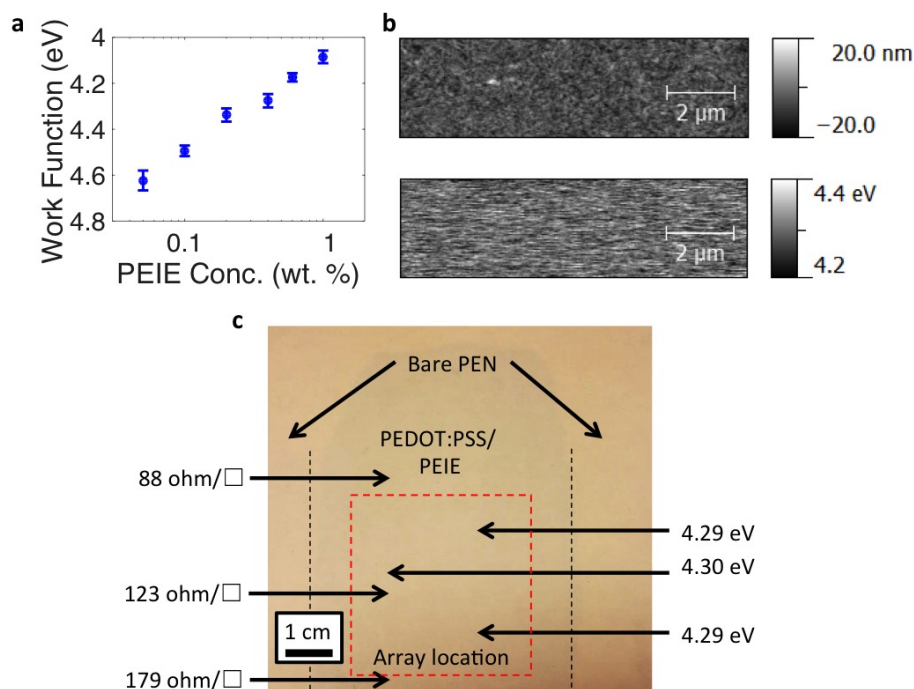


Figure 3.4: (a) Work function of PEDOT:PSS/PEIE cathode measured using KPFM as a function of PEIE solution concentration in 2-methoxyethanol printed with a blade height of 100  $\mu\text{m}$  at a speed of 1.6 cm/s. (b) Atomic force microscopy (AFM) magnitude plot (top) and corresponding KPFM plot (bottom) on PEDOT:PSS coated with a 0.4 wt. % PEIE in solution. (c) KPFM measurements of 0.4 wt. % PEIE in solution coated on PEDOT:PSS and sheet resistance measurement done over centimetric scales depicting the location of the array (red dashed lines) on a polyethylene naphthalate (PEN) substrate.

this is an effects of solvent evaporation or the alignment of imine dipoles. The work function modification of PEDOT:PSS was also uniform on the microscopic scale for all measured samples. Figure 3.4b shows blade coated films of 0.4 wt. % PEIE on PEDOT:PSS with 4.7 nm RMS roughness and 29 meV variability in work function. The high homogeneity in work function seen on micro scale greatly minimizes any effect of pinholes or non-uniformity in coating on device characteristics. Figure 3.4c is a map of work function measurements conducted on different areas of 0.4 wt. % PEIE coated on PEDOT:PSS. The central strip (with its edges marked by black dashed lines) is PEDOT:PSS with the edges being uncoated PEN substrate. The location of the OPD array is denoted by a red dashed square. This map shows uniformity in work function within 10 meV over centimetric scales. Additionally, the sheet resistance of the printed cathode varies from 88  $\Omega/\square$  at the top of the array to 179  $\Omega/\square$  at the bottom. While this non-uniformity in sheet resistance would create noticeable effects for solar cells, the low current densities of organic photodiodes create an insignificant

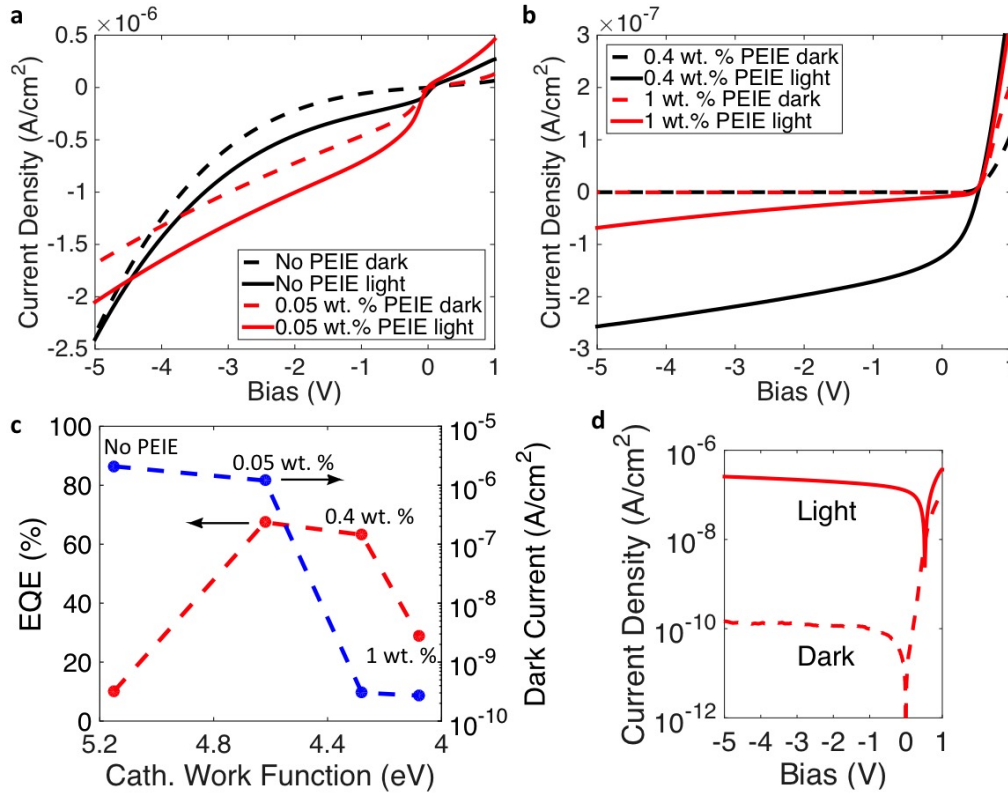


Figure 3.5: (a) Light ( $1 \mu\text{W}/\text{cm}^2$  @ 532 nm) and dark current-voltage characteristics of all-printed OPDs with no PEIE and 0.05 wt. % PEIE in solution deposited for the cathode. (b) Light ( $1 \mu\text{W}/\text{cm}^2$  @ 532 nm) and dark current-voltage characteristics of all-printed OPDs with 0.4 wt. % and 1 wt. % PEIE solution deposited for the cathode. (c) All-printed OPD mean EQE and dark current dependence on PEDOT:PSS/PEIE cathode work function deposited in Figure 3.4a. (d) Light ( $1 \mu\text{W}/\text{cm}^2$  @ 532 nm) and dark current-voltage characteristics in log-scale of the all-printed OPD.

voltage drop to affect device performance. The homogeneity and work function tunability of the cathode established by printing allows for a degree of control through which device performance can be optimized.

The control and reliability of the cathode printing process allows for the examination of the effect of cathode work function on device performance for the all-printed OPDs shown in Figure 3.3b. Light and dark current density-voltage characteristics are plotted in Figures 3.5a and b for devices with no PEIE and PEIE deposited from a concentration of 0.05, 0.4 and 1 wt. % in 2-methoxyethanol. The dependence of EQE and dark current density on the PEDOT:PSS/PEIE cathode work function of these devices is summarized in Figure 3.5c.

The PEDOT:PSS cathode work function without PEIE, 5.15 eV, creates a unipolar hole-transporting photoconductor that results in high dark current density and low EQE at -5 V bias. Lowering the work function to 4.6 eV by printing 0.05 wt. % PEIE in solution significantly improves EQE to 67% but still has approximately the same high dark current density as the unipolar device. Decreasing the cathode work function to 4.3 eV by printing 0.4 wt. % PEIE in solution retains about the same EQE as the device with a 4.6 eV work function electrode, but drastically reduces the dark current density to values below 1 nA/cm<sup>2</sup>. Further decreasing the cathode work function to 4.1 eV by increasing the concentration to 1 wt. % PEIE in solution results in approximately the same dark current density but significantly lower EQE compared to 0.4 and 0.05 wt. % solutions. Initially decreasing the work function of PEDOT:PSS results in an increase in EQE as an ohmic contact is established for electrons between the cathode and active layer. However, approximately the same high dark current density as the device without PEIE is retained because the cathode lacks carrier selectivity and permits hole transport. The abrupt decrease in dark current density with decreasing work function is attributed to the thickness-dependent hole-blocking properties of PEIE[89]. However, using 1 wt. % PEIE in solution to further decrease work function leads to a significant drop in EQE as a result of the insulating nature of PEIE, which causes accumulated charges to recombine at the PEIE/active layer interface and making it a poor electron extractor[106]. The device with the 4.3 eV cathode (0.4 wt. % PEIE in solution) has the highest detectivity (Equation 3.1) since the PEIE interlayer is thick enough to block holes but not too thick to cause electron accumulation and recombination at the cathode. Figure 3.5d shows the light and dark current density-voltage characteristics of the device processed from the optimal PEIE concentration has low dark current with a large shunt resistance. Consequently, charge selectivity, rather than work function, of the cathode needs to be optimized in order to lead to the best OPD detectivity.

### 3.3 Active Layer Design

The thickness of the BHJ layer has been shown to influence device yield and dark current[100, 126, 130], making it an important parameter to control. One method of controlling the thickness is to use a highly soluble donor and acceptor compounds. High solubility not only allows for the deposition of thick films, it also prevents solute aggregation in the film during evaporation of the wet film as figuratively pictured in Figure 3.6a. This aggregation results in pinholes and various other defects in the dry film that lead to low device yield and shorting. Low molecular weight (Mn) PCDTBT is chosen for the active layer since the solubility of polymeric materials increases with decreasing Mn[144]. Additionally, low Mn, 5.99 kDa, and high Mn, 34 kDa, PCDTBT show comparable device performance in these blends[90]. This insensitivity allows for the use of low Mn PCDTBT to create solutions with concentrations of 80 mg/ml in chlorobenzene with a 1:3 ratio of PCDTBT:PC<sub>71</sub>BM. The solubility of the high Mn PCDTBT is lower, with a maximum concentration of 24 mg/ml in

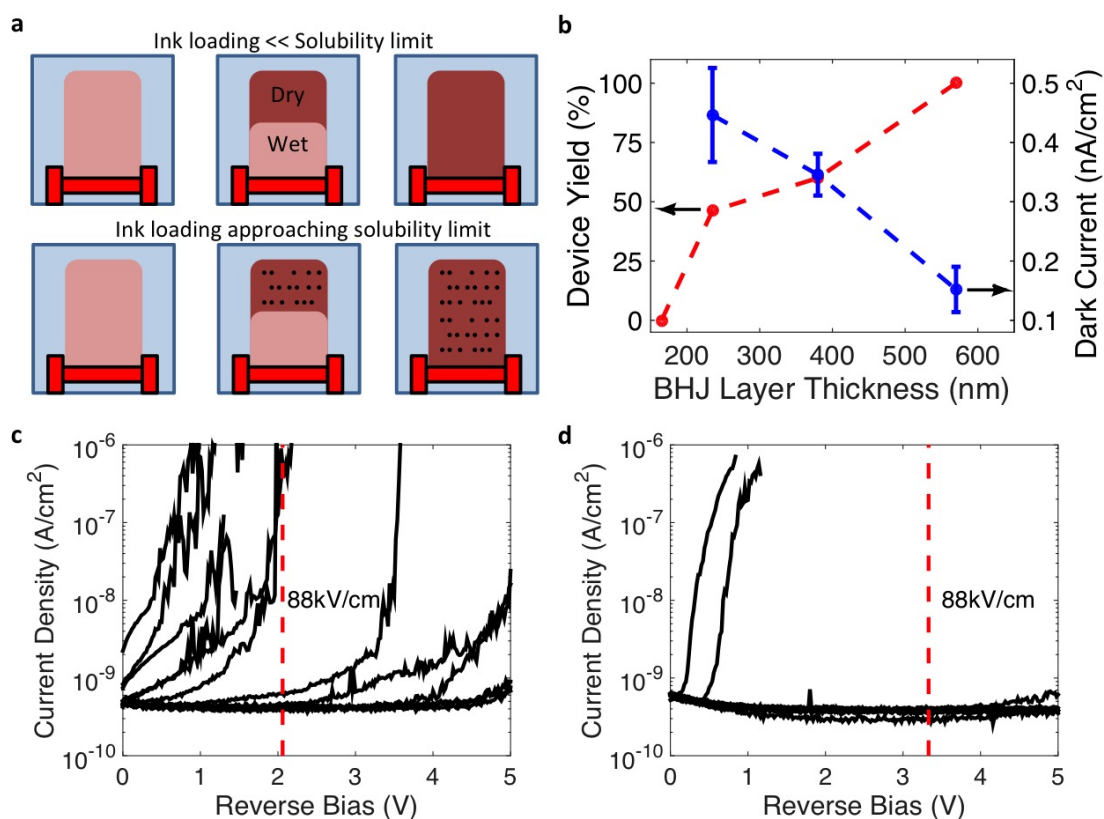


Figure 3.6: (a) Illustrative depiction of the chronological drying process of a blade coated wet film for ink concentrations well below the solubility limit and approaching the solubility limit that leave behind aggregates (black dots). (b) All-printed OPD device yield at an applied reverse bias field of 88 kV/cm and the corresponding dark current for functional devices. Current-voltage characteristics of all-printed OPDs plotted for active layer thicknesses of 235 nm (c) and 380 nm (d) under reverse bias for multiple devices.

chlorobenzene before gelling.

Figure 3.6b shows the device yield and dark current density for the all-printed OPDs (Figure 3.3b) for various BHJ layer thicknesses using the low Mn PCDTBT. A BHJ active layer thickness of 570 nm, the thickness cast from a solution of 80 mg/ml, exhibits perfect yield for 24 measured devices measured at a bias of -5 V. Thinner active layers are achieved by diluting the active layer solution, but result in lower device yields at the same applied field of the 570 nm-device at 5 V reverse bias (88 kV/cm). Figures 3.6c and d show the dark current density-voltage plots of OPDs with 235 nm and 380 nm active layer thicknesses, respectively. Device yield is taken according to whether the device broke down prior

to reaching the applied field of 88 kV/cm (red dashed line in Figures 3.6c and d). It is observed that breakdown occurs at a variety of biases, and that the dark current is similar among all pixels prior to breakdown. For functional devices under the applied field of 88 kV/cm, dark current density decreases for increasing thickness as seen from Figure 3.6b. Film imperfections have a more significant effect for thinner BHJ layers, resulting in more leakage paths that increase dark current density under reverse bias and the likely hood of breakdown. Additionally, the asymmetry in work function of the anode and cathode (0.7 eV) results in stronger built-in fields for thinner active layers. This built-in field renders them more susceptible to increased dark current density and breakdown for a given applied electric field (bias/thickness). Table 3.2 summarizes the performance of all-printed OPDs for these film thicknesses at an applied field of 88 kV/cm. The change in dark current is a larger contributor to change in specific detectivity than the change in EQE with active layer thickness. However, it should be noted the effect of BHJ layer thickness on dark current density is orders of magnitude less significant than the work function of the cathode as seen in Figure 3.5c, which underpins the importance of carrier selectivity at interfaces.

### 3.4 Anode Design

The design of the all-printed printed OPD is finally optimized the top electrode, the anode. The PEDOT:PSS electrode is deposited into a desired pixel geometry via screen printing directly on top of the active layer. Like the cathode, it is also important to tune the work function of the anode to optimize the charge injection and extraction of holes. However, the physical contact and high pressure of screen printing make it impractical to use a thin dipole-modification layer on top of the active layer since it would easily get damaged in the process. A thick dipole-modification layer is also impractical due to the insulating nature of these materials, as seen with PEIE in Figure 3.5c. This issue of work function modification is circumvented by blending the high conductivity PEDOT:PSS paste optimized for screen printing (Orgacon ELP-5015) with a high work function, but low conductivity grade of PEDOT:PSS (Clevios P VP AI 4083) optimized for hole injection. The particle diameter of AI 4083 is 220 nm, which is significantly smaller than the particle diameter of 4  $\mu\text{m}$  for the screen printable PEDOT:PSS (SPP). The smaller particle size of AI 4083 can enable more efficient modification of work function since this enables a flush contact with the surface of the active layer as shown in Figure 3.7a. In addition, blends of these two PEDOT:PSS formulations show the same shear thinning behavior as the original SPP that is needed to enable screen printing (Figure 3.2c) as seen from Figure 3.7b. The EQE and dark current of all-printed OPDs (Figure 3.3b) fabricated using PEDOT:PSS anodes of various blend ratios and gold anodes are shown in Figure 3.7c. Inverted devices fabricated from gold electrodes exhibit the highest EQE and work function, but have a high dark current which limits their specific detectivity (more will be discussed on OPDs with metal electrodes in the next section). Devices fabricated using the original SPP formulation (work function of 4.88 eV) show an

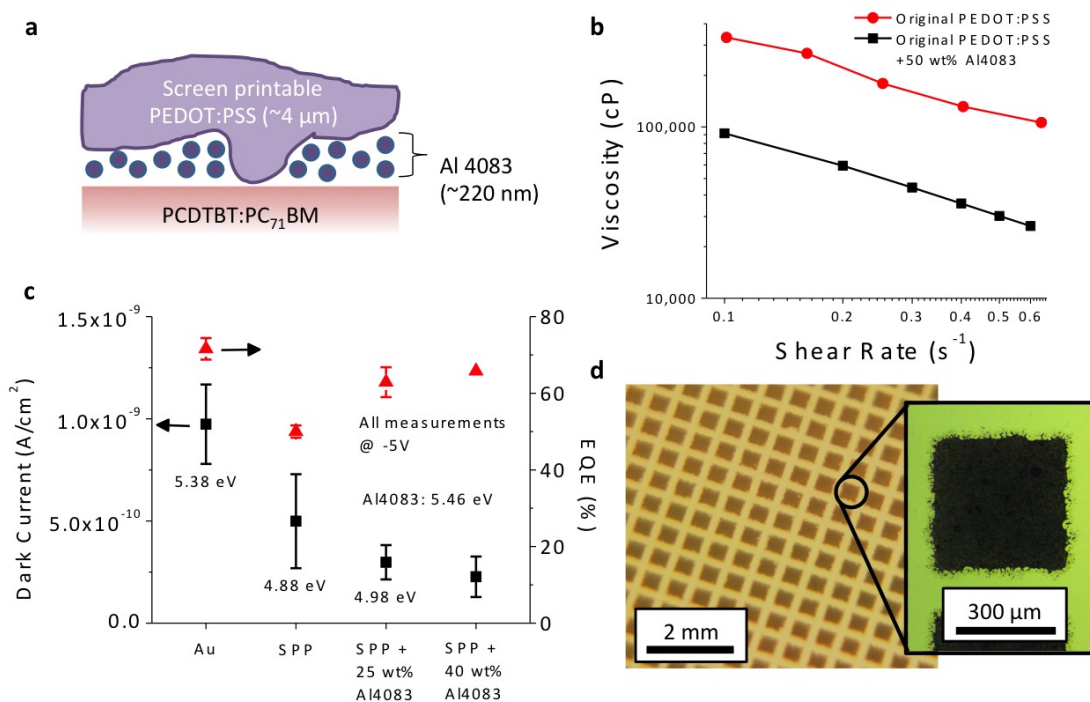


Figure 3.7: (a) Illustrative depiction of a blend of screen printable PEDOT:PSS (SPP) with high work function Al 4083 PEDOT:PSS printed on the active layer. (b) Viscosity of undiluted SPP (courtesy of Agfa Gevaert) and diluted in Al 4083. (c) Dark current density (black) and EQE (red) of inverted OPDs printed with the optimal cathode and active layer for anodes made of gold and blends of SPP and Al 4083 showing the work function of each of these electrodes. (d) Optical micrographs of the anodes on top of the all-printed OPD array.

average EQE and dark current of 55% and 500 pA/cm<sup>2</sup>, respectively. Anodes produced from a blend with 25 wt. % Al 4083 (wt. % referring to the weight of Al 4083 solution added with respect to the undiluted weight of SPP), with a higher work function of 4.98 eV, show an improved EQE and reduced dark current of 62% and 270 pA/cm<sup>2</sup>, respectively. These values are further improved with increasing Al 4083 concentration since the high work function of this PEDOT:PSS formulation, 5.46 eV, improves hole injection and electron blocking[10]. The final OPD array, which is composed of 25 wt. % Al 4083 anodes, is shown in Figure 3.7d to have good printing reliability and uniformity.

In addition to the performance of the anode, the reliability of printing PEDOT:PSS blends on the hydrophobic active layer was examined. Figures 3.8a, b, c, and d show the print quality of blends on the PCDTBT:PC<sub>71</sub>BM active layer with 0, 25, 40 and 50 wt. %



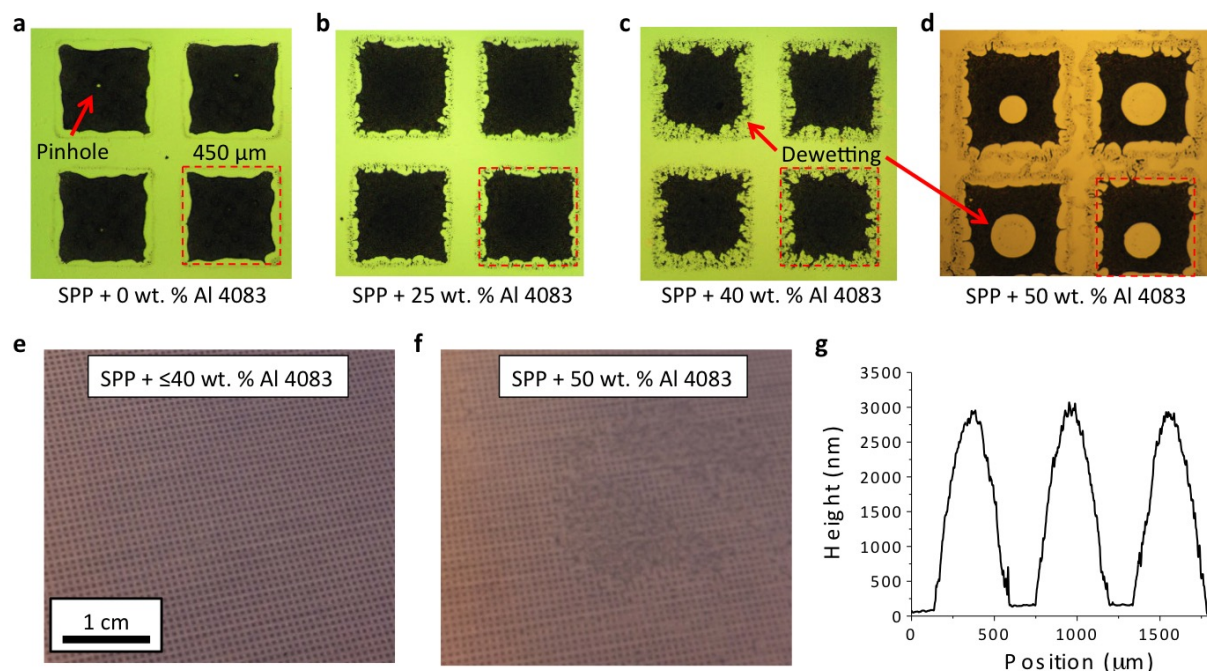


Figure 3.8: Screen printing quality of anode on top of active layer for 0 (a), 25 (b), 40 (c), and 50 (d) wt. % AI 4083 PEDOT:PSS added to SPP. (e) Optical micrograph of PEDOT:PSS blends printed on PEN substrate with at most 40 wt. % AI 4083 (e) and 50 wt. % (f) added to SPP. (g) Cross sectional profile of SPP + 25 wt. % AI 4083 anodes printed on top of the active layer.

AI 4083, respectively. Anodes printed from the original SPP paste show pattern fidelity with respect to the dimensions of the opening in the screen (450 μm) with slight dewetting of 10-15 μm from the edges and small pinholes in the center. Adding 25 wt. % AI 4083 improves the performance as mentioned in Figure 3.7c and eliminates pinholes while retaining the same pattern fidelity and the original paste. However, adding too much AI 4083, while improving EQE and reducing dark current, decreases the viscosity of the paste to the point dewetting becomes more significant from the hydrophobic substrate. Figure 3.8e is a photograph of the anode screen printed on a blank PEN substrate for AI 4083 concentrations of 40 wt. % or under. However, adding 50 wt. % or more decreases the viscosity significantly enough that ink flows through openings in the emulsion during the flood phase of screen printing, causing an excessive amount of ink to transfer to the substrate uncontrollably as pictured in Figure 3.8f. A cross section of the anode printed from the optimal weight loading of 25 wt. % AI 4083 is shown in Figure 3.8g. The 3 μm thickness offers low resistance electrodes, but it transmits too little light to be of practical use for top-side illuminated devices.



### 3.5 Performance & Reliability

#### Influence of Device Architecture on Performance

The top electrodes in OPDs have traditionally been thermally evaporated[6, 10, 18, 51, 55, 114, 139] and therefore constitute a benchmark for printed electrodes. Thermally evaporated top metal electrodes in both inverted and standard device geometries are compared to the all-printed OPD in Figure 3.3b using the optimal anode blend ratio of 25 wt. % AI 4083. Standard devices are fabricated using the same process shown in Figure 3.3a but without depositing a PEIE interlayer or screen printing the PEDOT:PSS electrode. The gold electrode (5.3 eV) has a lower hole barrier than printed PEDOT:PSS (5 eV) while the aluminum (4.1 eV) and silver (4.7 eV) electrodes have a lower and higher electron barrier, respectively, than the printed cathode (4.3 eV) as seen in the band diagrams of Figure 3.9a. The performance of these OPDs is summarized in Table 3.2 and Figure 3.9b.

Silver is investigated as a potential cathode material due to its ubiquitous prevalence in solution-processed conductors and prior implementation in thick-junction OPDs[100]. However, standard geometry devices with silver cathodes have a poor specific detectivity as a result of the high dark current arising from the poor carrier selectivity. Additionally, the EQE drops near short-circuit (Bias = 0 V) conditions since the high work function of 4.7 eV is not sufficient to establish an ohmic contact with the electron transporting PC<sub>71</sub>BM component of the active layer (LUMO 4.3 eV) and necessitates the overdrive of reverse bias to compensate for this energetic barrier. Inverted geometry devices with gold electrodes exhibit

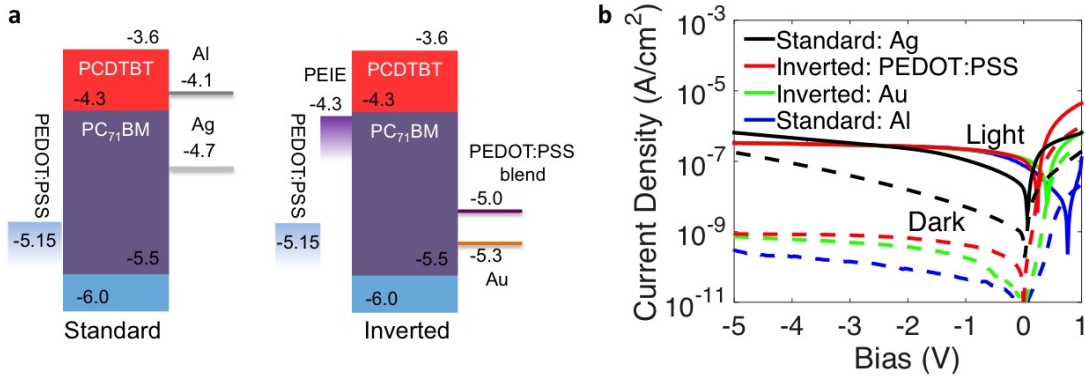


Figure 3.9: (a) Band diagram of standard OPDs with printed anode (no PEIE) and active layer (570 nm-thick) with thermally evaporated aluminum and silver), and inverted OPDs with printed cathode (0.4 wt. % PEIE) and active layer with screen printed PEDOT:PSS (SPP + 25 wt. % AI 4083) or thermally evaporated gold. (b) Current-voltage characteristics of devices under dark and light conditions at 532 nm and 1  $\mu\text{W}/\text{cm}^2$ .

Device Geometry	Cathode / Work Function (eV)	Anode / Work Function (eV)	Active Layer Thickness (nm)	EQE (%) / $V_{\text{Bias}}$ (V)	$J_{\text{Dark}}$ (pA/cm <sup>2</sup> ) / $V_{\text{Bias}}$ (V)	$D^*$ (cm <sup>2</sup> ·Hz <sup>0.5</sup> ·W <sup>-1</sup> ) / $V_{\text{Bias}}$ (V)
Inverted	PEDOT:PSS + PEIE / 4.3	PEDOT:PSS blend / 5	235	61 / -2.06	440 / -2.06	$2.2 \times 10^{13}$ / -2.06
Inverted	PEDOT:PSS + PEIE / 4.3	PEDOT:PSS blend / 5	380	69 / -3.33	350 / -3.33	$2.8 \times 10^{13}$ / -3.33
Inverted	PEDOT:PSS + PEIE / 4.3	PEDOT:PSS blend / 5	570	55 / -5	150 / -5	$3.4 \times 10^{13}$ / -5
Inverted	PEDOT:PSS + PEIE / 4.3	Au / 5.3	570	75 / -5	740 / -5	$2.1 \times 10^{13}$ / -5
Standard	Al / 4.1	PEDOT:PSS / 5.15	200	61 / -1.66	1,760 / -1.66	$1.11 \times 10^{13}$ / -1.66
Standard	Al / 4.1	PEDOT:PSS / 5.15	570	76 / -5	280 / -5	$3.4 \times 10^{13}$ / -5
Standard	Ag / 4.7	PEDOT:PSS / 5.15	600	60 / -5	$1.7 \times 10^5$ / -5	$1.1 \times 10^{12}$ / -5

Table 3.2: OPD characteristics of the various structures illustrated in Figure 3.9a. Measurements were performed under  $1 \mu\text{W}/\text{cm}^2$  at 532 nm at an applied reverse bias field of 88 kV/cm in air without encapsulation.

on average an EQE of 75% at -5 V, which is greater than the 55% seen in the all-printed OPD. However, the gold electrode OPD's dark current density of 740 pA/cm<sup>2</sup> is larger compared to that of the all-printed device at 150 pA/cm<sup>2</sup>. A standard geometry device with an evaporated aluminum electrode has an EQE of 76% at -5 V, similar to the inverted gold anode devices, and a dark current density of 280 pA/cm<sup>2</sup>, which is still higher than that of the all-printed OPD. The lower EQE of the all-printed OPD compared to OPDs with the low charge injection barrier metal electrodes, aluminum and gold, is in accordance to the finding that higher anode and lower cathode work function electrodes in organic diodes are more efficient at charge collection[22]. Albeit the lower aluminum cathode and higher gold anode work functions that improve EQE, devices with a thermally evaporated top electrode exhibit marginally lower detectivities at higher reverse biases than all-printed OPDs as a result of their high dark current.

The current-voltage characteristics in Figure 3.9b show that the differential shunt resistance of the dark current at -5 V of the all-printed OPD,  $1 \times 10^{11} \Omega \cdot \text{cm}^2$ , is significantly higher than that of the OPDs with aluminum or gold top electrodes,  $1.2 \times 10^{10}$  and  $8.7 \times 10^9 \Omega \cdot \text{cm}^2$ , respectively. The high shunt resistance of the all-printed OPD indicates that the

device's lower dark current density is the result of a low density of defect-induced traps at the active layer-electrode interface, which minimizes parasitic leakage paths[125]. Consequently, the higher dark current density of the OPDs with metal electrodes is believed to be the result of the diffusion of evaporated metal into the active layer, which is especially pronounced for gold[128]. Additionally, the hydrophobicity of the active layer could prevent the aqueous screen-printed PEDOT:PSS solution from diffusing into small imperfections in the active layer, thus reducing the amount of shunt paths through the active layer.

## All-printed Organic Photodiode Performance

Despite the inferior charge collection abilities of all-printed OPDs, these devices have a linear dynamic range of at least 5 orders of magnitude (100 dB), with an EQE of 55% at a bias of -5 V as shown in Figure 3.10a. This linearity is indicative of an active layer that does not have low carrier mobilities since this would result in a non-linear dynamic response[10]. Photogenerated carriers with low mobilities lead to higher charge concentrations in the active layer, this space-charge decreases the electric field in regions of high carrier concentration, thus decreasing extraction time that and increasing recombination. The recombination of carrier resulting from this effect, also known as space-charge limited current, creates a non-linear dynamic response with respect to light intensity[61]. Figure 3.10b shows the spectral EQE of the OPD measured at biases from 0 to -5 V. The increase in EQE with reverse bias is indicative of a bimolecular recombination lifetime that is shorter than the transit time of the carriers through the active layer. The transit time decreases with increasing reverse bias, asymptotically increasing the EQE.

The response of all-printed OPDs to sine-modulated light intensity was also measured. Figure 3.10c and d show the frequency response of devices with a 570 and 235 nm-thick active layer ( $t_{OPD}$ ), respectively, measured at various bias voltages at a light intensity of  $\simeq 10^{-4}$  W/cm<sup>2</sup>. Table 3.3 summarizes the results from these figures along with the applied

Active layer thickness (nm)	$V_{Bias}$ (V)	$E_{Applied}$ (kV/cm)	$E_{Int}$ (kV/cm)	$f_{3dB}$ (kHz)
570	0	0	12	0.5
570	-3	53	65	1
570	-5	88	100	2
235	-2.06	88	117	5
235	-5	213	243	50

Table 3.3: All-printed OPD cut off frequencies ( $f_{3dB}$ ) for various active layer thicknesses,  $V_{Bias}$ , and  $E_{Int}$  (Equation 3.3).

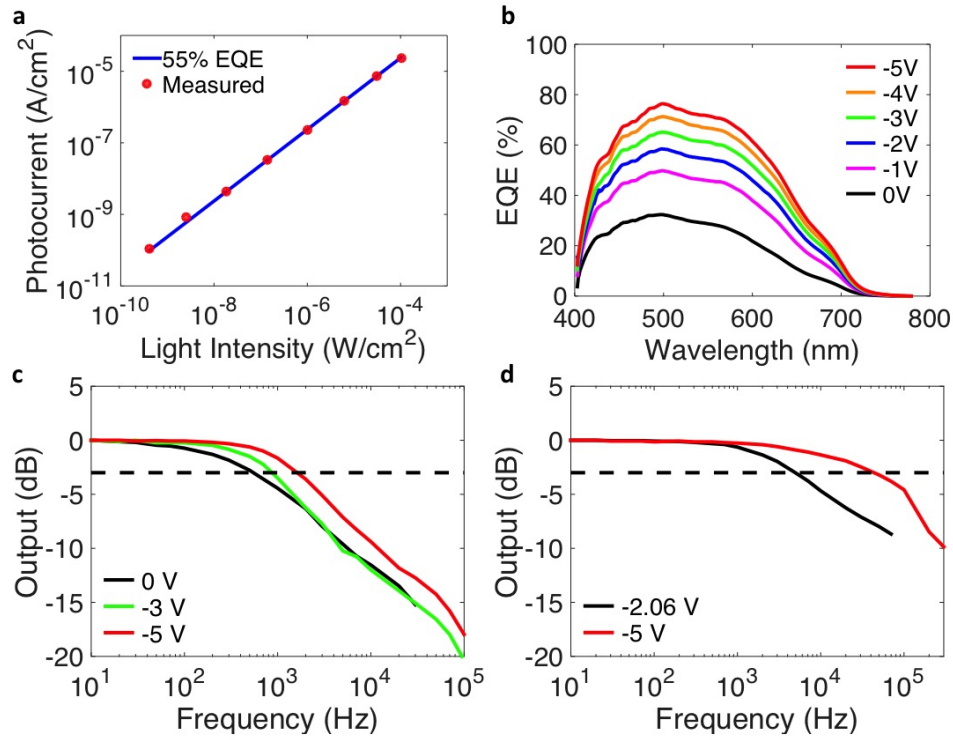


Figure 3.10: (a) Dynamic response of all-printed OPD at 532 nm biased at -5 V. (b) EQE spectral response of all-printed OPD under various  $V_{\text{Bias}}$  under 3-6  $\mu\text{W}/\text{cm}^2$ . Frequency response of all-printed OPDs with a 570 nm- (c) and 235 nm-thick (d) active layer and 0.16  $\text{mm}^2$  active area under sine-modulated light at various biases.

electric field across the active layer ( $t$ ) and the internal electric field,  $E_{\text{Int}}$ , within the active layer that takes into account the asymmetry in work function of the anode,  $\Phi_A$ , and cathode,  $\Phi_C$  as shown in Equation 3.3. The 3-dB cutoff frequency ( $f_{3\text{dB}}$ ) of the 570 nm-thick active layer device increases from 500 Hz at 0 V bias to 2 kHz at -5 V bias or applied field of 88 kV/cm. As shown in Table 3.3, the 235 nm-thick device biased at an internal field of 88 kV/cm has an  $f_{3\text{dB}}$  of 5 kHz, more than double that of the 570 nm-thick device at the same bias. This increase in  $f_{3\text{dB}}$  is a result of the asymmetry in electrode work function that increases  $E_{\text{Int}}$  and the thinness of the active layer, which is less than half the thickness of the 570 nm-thick OPD, which decreases the carrier transit time by more than a factor of two.  $f_{3\text{dB}}$  as high as 50 kHz are achieved for the 235 nm-thick device at an applied bias of -5 V.

$$E_{\text{Int}} = \frac{-V_{\text{Bias}} + (\Phi_A - \Phi_C)}{t_{\text{OPD}}} \quad (3.3)$$

## Impedance Spectroscopy & Noise Measurements of All-printed Organic Photodiodes

Impedance spectroscopy is the study of charge carrier motion in a device by observing the magnitude and phase (or equivalently, resistance and reactance) of the impedance at various frequencies. Figure 3.11a shows the model used to fit the measured impedance frequency response. The model is comprised of a resistor for the PEDOT:PSS electrodes (given a value of  $\simeq 1 \text{ k}\Omega$ ) and a standard dielectric model for interlayers[38] to model PEIE, which is composed of a resistor and capacitor in parallel. The model for the PCDTBT:PC<sub>71</sub>BM active layer is a standardized model developed for organic photovoltaic devices[103], which is the geometric capacitance of the layer in parallel with the bulk resistance of the active layer that is in series with the recombination resistance and capacitance model. The element used to

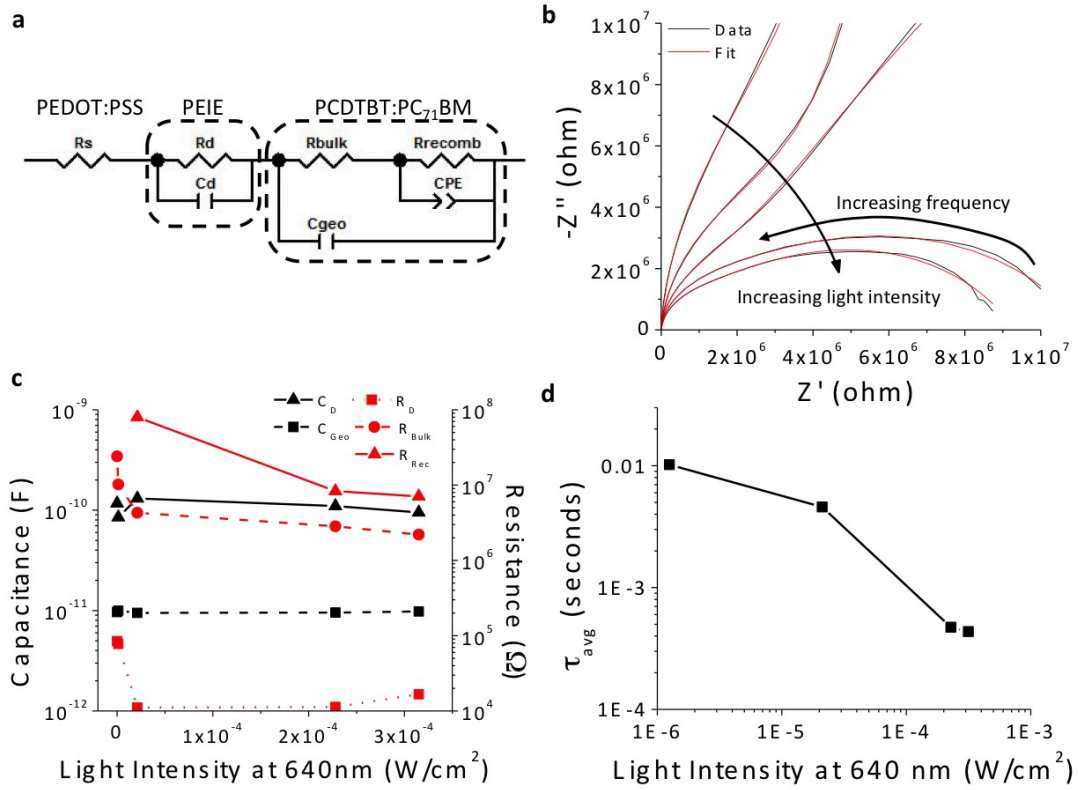


Figure 3.11: (a) All-printed OPD device impedance model with the resistivity of the PEDOT:PSS electrodes and impedance of PEIE and active layers highlighted. (b) Nyquist plot of raw data (black) and fit to the model (red) for various light intensities. (c) Extracted parameters of the model based on the fitted data. (d)  $\tau_{avg}$  (Equation 3.5) measured at  $V_{Bias} = 0 \text{ V}$  for various light intensities.

model the recombination capacitance is a constant phase element (CPE), which is a model for an imperfect capacitor exhibiting resistor-like traits with Equation 3.4 used to describe it where  $0 \leq n \leq 1$  ( $n = 1$  and  $n = 0$  being an ideal capacitor and resistor, respectively). A CPE is used to model recombination because its parallel combination with a resistor can model various distributions in carrier lifetime that is caused by competing recombination mechanisms[103]. Figure 3.11b shows a Nyquist plot of the resistance ( $Z'$ ) and negative reactance ( $-Z''$ ) of the measured impedance (black curve) and of the model fit to the data (red curve), which is measured over a range of frequencies and light intensities.

$$Z_{CPE} = \frac{1}{Q_0 \omega^n} e^{-\frac{\pi}{2}nj} \quad (3.4)$$

The close fit of the model to the data enables reliable determination of the parameters of the OPD model as displayed in Figure 3.11c at various light intensities. The geometric capacitance of the active layer,  $C_{Geo}$ , is independent of light intensity at a value of approximately  $10^{-11}$  F. The theoretical  $C_{Geo}$  of  $9.9 \times 10^{-12}$ , based on the device thickness (570 nm) area ( $400 \times 400 \mu m^2$ ) and permittivity ( $\epsilon_0 = 4$ ), is consistent with the measured value. The recombination,  $R_{Rec}$ , and bulk resistance,  $R_{Bulk}$ , decrease with increasing light intensity since this corresponds to lower recombination lifetimes and increase photoconductivity, respectively. PEIE interlayer resistance also decreases at higher light intensities, which could be a result of carrier concentration-dependent mobility of the material. The average carrier lifetime,  $\tau_{avg}$ , is computed according to Equation 3.5 at each of these light intensities as shown in Figure 3.11d. The carrier lifetime decreases with increasing light intensity, which is indicative of a direct bimolecular recombination process. The carrier lifetime varies from 10 ms at low irradiances to 500  $\mu s$  at high irradiances. These values are within the range of the carrier transit time measured by light frequency response, 2 ms at 0 V and 500  $\mu s$  at -5 V, which gives rise to the large difference in EQE seen between 0 V and reverse bias in Figure 3.10b.

$$\tau_{avg} = (R_{Rec}Q_0)^{\frac{1}{n}} \quad (3.5)$$

The noise floor of a photodetector determines the specific detectivity of the device as shown in Equation 3.1. Since the dark current in the all-printed device is too low (150 pA/cm<sup>2</sup>) for direct noise measurements, the noise spectral density of the photocurrent is measured instead to observe noise mechanisms (See Chapter 1 for background information on noise). Figure 3.12a shows the experimental setup, which consists of a transimpedance amplifier connected at the output of the OPD in order to convert the current output from the light into a voltage that is readable by a power spectrum analyzer. Figure 3.12b shows the noise spectral density for photocurrents of 33 and 56 nA measured at  $V_{Bias}=0$  V. The noise of the photocurrent is found to be spectrally flat, with no trap-induced  $1/f$  noise behavior[11], and in close agreement with the theoretical shot noise at  $1.03 \times 10^{-13}$  and  $1.34 \times 10^{-13}$

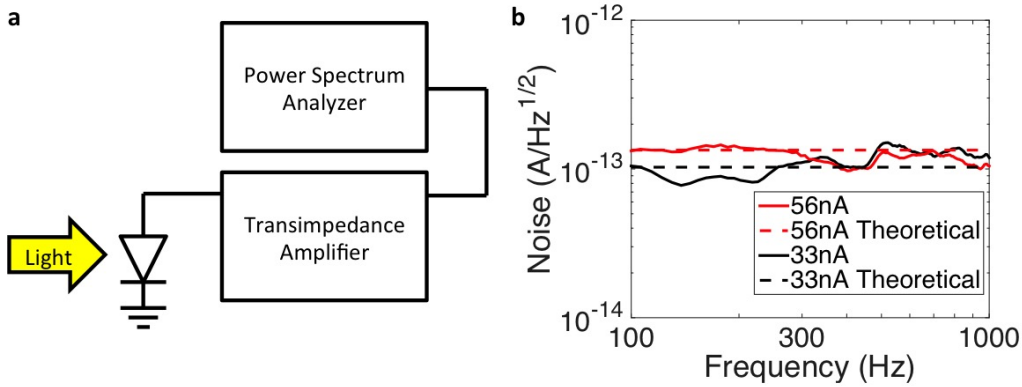


Figure 3.12: (a) Schematic of photocurrent noise measurement setup. (b) Spectral noise density of photocurrent at 33 and 56 nA for all-printed OPDs (solid lines) measured at short circuit and theoretical value based on shot noise (dashed lines) as calculated from Equation 3.6.

A/Hz<sup>1/2</sup> for 33 and 56 nA, respectively, calculated from Equation 3.6. The noise floor of the instrumentation is approximately 10<sup>-14</sup> A/Hz<sup>1/2</sup>, which is an order of magnitude below these measurements. This observation suggests minimal noise generation from other sources, validating the assumptions of no additional noise mechanisms beyond shot noise in Equation 3.1. Using this equation, the all-printed OPDs shown in Figure 3.3b have an average specific detectivity of  $3.4 \times 10^{13}$  cm·Hz<sup>0.5</sup>·W<sup>-1</sup>. Devices with thicker active layers and non-metallic electrodes have higher specific detectivities as summarized in Table 3.2.

$$N_{Shot} = \sqrt{2qI_{Dark}} \quad (3.6)$$

## Reliability of All-printed Organic Photodiodes

Operational bias, stability and device variability are as important as standard photodiode performance metrics when designing devices for systems level applications. The applied reverse bias,  $-V_{Bias}$ , across a photodiode dynamic range of image sensors is determined by the well capacity of the photodiode to store photogenerated charge,  $Q_{Well}$ , according to Equation 3.7, where  $C_{PD}$ ,  $\epsilon$ ,  $t_{OPD}$ ,  $E_{Applied}$  represent areal capacitance, dielectric permittivity, active layer film thickness and applied electric field, respectively[65, 166]. In order to augment the well capacity,  $E_{Applied}$  can be increased by either increasing the reverse bias or thinning the active layer. Figure 3.13a shows the all-printed OPD developed in this chapter offers higher specific detectivity at higher applied fields, maximizing well capacity and thus dynamic range, in comparison to other OPDs in the literature (assuming dielectric constant to be similar between the various BHJ active layers)[3, 6, 8, 18, 51, 55, 100, 114, 126, 130]. It

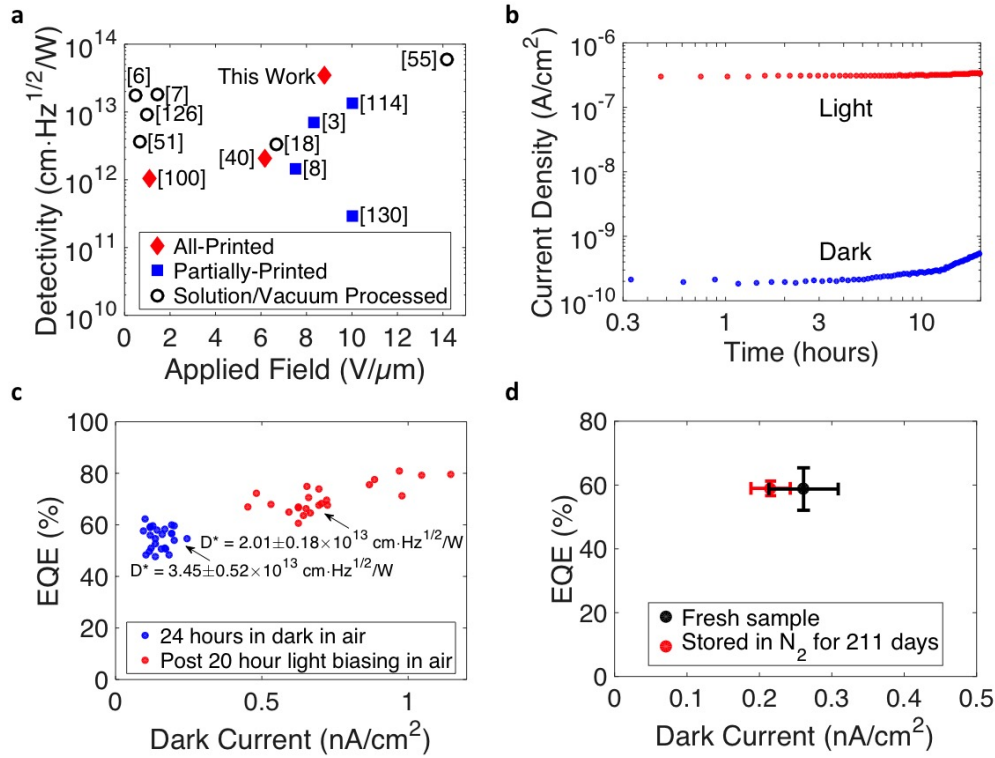


Figure 3.13: (a) Comparison of specific detectivity ( $D^*$ ) calculated according to Equation 3.1 at various applied fields ( $V_{\text{Bias}}/t_{\text{OPD}}$ ) for the all-printed OPDs presented in this chapter and other OPDs published in literature. (b) An all-printed OPD (Figure 3.3b) biased continuously at -5 V for 20 hours in air alternating between light (532 nm) and dark with a 50% duty cycle. (c) Scatter plot of EQE, dark current and  $D^*$  of all-printed OPDs that were left for 24 hours in the dark in air prior to measurement and exposed to the same conditions in Figure 3.13b. (d) EQE and dark current of a batch of all-printed OPDs measured the day of fabrication and after 211 days of storage in nitrogen while exposed to ambient light.

is optimal to examine the stability of specific detectivity by bias stress since photodiodes are continuously biased in most light-sensing and imaging systems[65, 114, 166]. The all-printed OPDs tested in air, which were initially left in the dark for 24 hours, were stable for 3-4 hours when continuously biased at -5 V simultaneously with periodic light-dark exposure (50% duty cycle) as shown in Figure 3.13b. However, Figure 3.13c shows a lengthy periodic light exposure of 20 hours led to a significant increase in both mean EQE, from 55% to 70%, and mean dark current density, from 150 pA/cm $^2$  to 720 pA/cm $^2$ , for 24 OPDs measured in each sample over an area of 4.5 cm $^2$  regardless of whether the OPDs were electrically biased. All 48 measured pixels across these two samples yielded functional device performance. This corresponds to a mean drop in specific detectivity from  $3.45 \times 10^{13}$  to  $2.01 \times 10^{13}$



$\text{cm}\cdot\text{Hz}^{0.5}\cdot\text{W}^{-1}$  while the coefficient of variance (standard deviation/mean) decreases from 15% to 9%. It is believed that the simultaneous increase in EQE and dark current density is the result of photo-oxidation mechanisms which dope the active layer and have been shown to increase both on and off current in organic thin film transistors[116]. This is supported by the observation that devices left in nitrogen and exposed to light continuously for several months exhibit negligible change in average EQE and an increase in average dark current density of approximately  $40 \text{ pA}/\text{cm}^2$  as seen in Figure 3.13d. Despite the decrease of specific detectivity over the course of several hours, the stability of the devices when kept long term in an inert atmosphere and short term in air suggests that even rudimentary encapsulation could preserve as-fabricated device performance for a significantly longer amount of time as has been shown for organic photovoltaic cells[134].

$$Q_{Well} = C_{PD} (-V_{Bias}) \propto \frac{\epsilon (-V_{Bias})}{t_{OPD}} = \epsilon E_{Applied} \quad (3.7)$$

### 3.6 Conclusion

In summary, highly scalable and inexpensive manufacturing techniques such as doctor blade coating and screen printing can be used to deposit each layer of an OPD in order to create high performance devices on plastic substrates. These scalable printing techniques are precise enough to tailor the performance of fully-printed OPDs over large areas with good uniformity. Specifically, the hole blocking properties of the PEIE interlayer has a profound impact on dark current and is well controlled through doctor blade coating. Blends of high conductivity and high work function PEDOT:PSS can be used to improve specific detectivity without compromising printing reliability. Controlling active layer thickness ensures good reliability and minimized dark current even under large applied fields needed to maximize well capacity. Finally, all-printed OPDs display high specific detectivity as a result of their low dark current density in comparison to OPDs with thermally evaporated metal electrodes. Through these considerations, all-printed OPD arrays achieve average specific detectivities as high as  $3.45 \times 10^{13} \text{ cm}\cdot\text{Hz}^{0.5}\cdot\text{W}^{-1}$  under a bias of -5 V with high device yield and low variability. The detectivity of these all-printed OPDs is competitive with conventional inorganic photodiodes and can pave the way to inexpensive, ubiquitous and large area optical systems.

## Chapter 4

# Organic Charge-coupled Devices & Charge-integrating Phototransistors

### 4.1 Introduction

Printable photodetectors have the potential to enable inexpensive yet high performance image sensors on flexible substrates[8, 10, 34, 50, 178, 126, 137, 168] that can open new methods of imaging not possible with rigid substrates[93, 163]. Capacitive-based photodetectors, charge-coupled devices (CCDs) and phototransistors, have unique sensing capabilities compared to photodiodes since they can exhibit photoconductive gain and sublinear responsivity to irradiance. These characteristics enable a logarithmic sensing of irradiance, which is akin to the human eye and has a wider dynamic range than photodiode-based image sensors. Additionally, the structure of capacitive-based devices is more similar to transistors than photodiodes, which facilitates the integration of photodetectors and circuitry in optical and image sensing systems. This chapter will first go over the operation and performance of organic charge-coupled devices (OCCDs). Performance is examined as a function of active layer composition, irradiance and response time. The second portion of this chapter builds off the work on OCCDs towards the development of organic phototransistors (OPTs). Focus is given on the development, operation and performance of OPT pixels geared towards the development of wide dynamic range image sensors.

### 4.2 Organic Charge-coupled Devices

#### Introduction

CCD pixels are commonly implemented in silicon-based systems for image sensing. These devices do not require the high level of patterning in comparison to complimentary metal-oxide-semiconductor (CMOS) image sensor pixel architectures that use short-channel transistors

for high gain. For this reason, CCD image sensors had superior performance to CMOS image sensors throughout a large portion of microfabrication history (70's-90's) since photolithographic capabilities were not sufficiently advanced to create short channel transistors[65]. While advancements in photolithographic patterning in the 2000's have made silicon-based CMOS sensors superior to CCDs, the same lessons can be applied to the emerging field of organic electronics since improvements in short-channel[45, 152, 158] and high mobility transistors[35, 118, 121, 198] are still being made in order to improve the gain of circuits[27]. For this reason, the performance of OCCDs is worth investigating.

## Device Architecture & Quasi-static Characteristics

The architecture of an OCCD consists of a bottom electrode followed by a light absorbing semiconductor, dielectric, and top electrode. Operation of these devices relies on capacitive coupling of photogenerated charge at the semiconductor-dielectric interface that will cause an increase in the effective capacitance of the device. The DC bias across the device also influences the migration of carriers to the semiconductor-dielectric interface and injection of carriers from the back electrode, both of which affect the measured capacitance. Additionally, the lifetime of carriers affects the response time of an OCCD.

Figure 4.1a shows the structure of an OCCD and DC biasing scheme used to assess the performance of all charge-coupled devices in this section. A fluoropolymer (FP) gate dielectric is used since the low polarization of this dielectric induces a minimal amount of carrier scattering at the interface[97]. The bottom electrode is formed by a blade coated bilayer structure of PEDOT:PSS and 0.4 wt. % PEIE solution in 2-methoxyethanol according the cathode optimization performed in Chapter 3 (Figure 3.5c). The bottom electrode (cathode) is biased positively with respect to the top electrode in order to induce the accumulation of photogenerated holes at the semiconductor-dielectric interface with minimal dark injection of holes from the bottom electrode. A hole-accumulating device is preferable for OCCDs since the transport of carriers in organic materials is dominated by hopping transport that gives rise to higher hole than electron mobility[62]. Additionally, the lower surface energy of hole-transporting polymeric donors compared to electron-transporting small molecule acceptors causes a vertical phase segregation of polymers in a bulk heterojunction (BHJ) blend to the surface of a wet film as it is dried and annealed[25, 28]. This results in more hole transporting pathways near the semiconductor-dielectric interface in an OCCD. As a consequence of these factors, hole-accumulating devices are advantageous since carriers could quickly transfer laterally out of the device when a lateral field is applied, with minimal recombination, as in a CCD imager array or phototransistor device. For the particular device illustrated in Figure 4.1a, a 100:1 Poly[N-9'-heptadecanyl-2,7-carbazole-alt-5,5-(4',7'-di-2-thienyl-2',1',3'-benzothiadiazole)] (donor) : [6,6]-Phenyl-C71-butyric acid methyl ester (acceptor) (PCDTBT:PC<sub>71</sub>BM) ratio is used for the active layer. This ratio results in isolated acceptor regions that trap electrons and leads to space charge effects that cause large

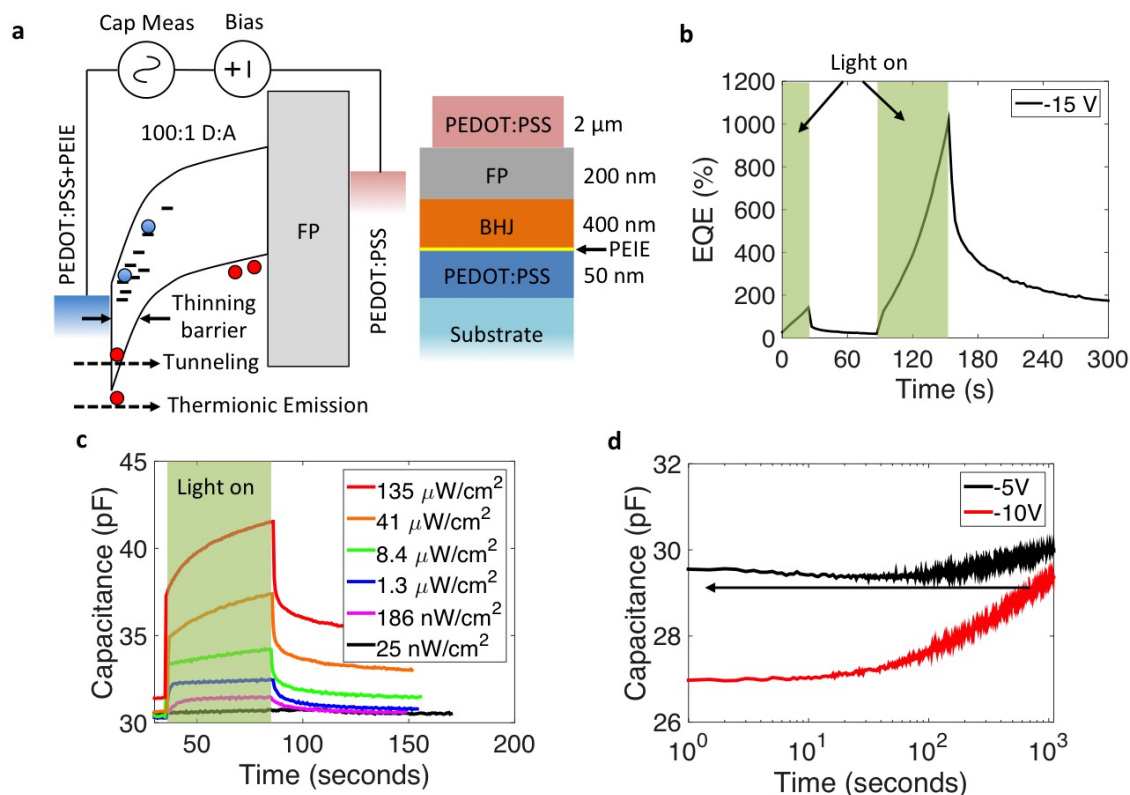


Figure 4.1: (a) Device architecture and cross section of an organic charge-coupled device (OCCD) with an active layer composition of 100:1 PCDTBT:PC<sub>71</sub>BM and the biasing polarities for such devices. (b) External quantum efficiency (EQE) of an all-printed organic photodiode (OPD) as a function of time and biased at -15 V using PEDOT:PSS/PEIE cathode and PEDOT:PSS anode as the device in Chapter 3. (c) Temporal response of the OCCD in (a) illuminated at various irradiances at 532 nm. (d) Bias stress stability in the dark of the OCCD in (a) with an initial run at -10 V immediately followed by a -5 V bias.

amounts of band bending near the cathode where acceptor molecules tend to aggregate[105]. This band bending from trapped charge results photomultiplication since the thinning of the hole barrier permits a greater number of holes to be injected into the active layer via thermionic emission and even through direct tunneling for thinner barriers[67, 170].

Figure 4.1b shows a plot of external quantum efficiency (EQE) versus time for an inverted all-printed organic photodiode (OPD) with a bottom PEDOT:PSS/PEIE cathode, 100:1 PCDTBT:PC<sub>71</sub>BM active layer, and screen printed PEDOT:PSS on top to form the anode when biased at -15 V. A large reverse bias is needed to induce an electric field at the cathode that is high enough to cause hole injected upon electron trapping in acceptor sights.

Exposure of this OPD to light creates photogenerated holes and electrons that are extracted at the anode and trapped in the active layer, respectively. This trapping causes a rise in EQE from 25% from the start of illumination and increases above 100% after 20 seconds as a result of trapped electron-induced hole injection from the cathode. However, the long carrier lifetime of the trapped electrons in acceptor sights results in a slow decay and persistence of photoconductivity in the dark[64]. When the OPD is exposed to light before the persistent photoconductivity decreases to steady-state dark current, the EQE of the light signal starts at a higher value than at the first exposure to light since there are trapped electrons that contribute to hole injection. Figure 4.1c shows the capacitance of the OCCD in Figure 4.1a as a function of time and irradiance. The initial increase in capacitance upon light exposure is caused by the migration of photogenerated holes to the dielectric interface. The gradual rise in capacitance during illumination is attributed to the trapping of electrons in the active layer that induces injection of holes at the cathode, which accumulate at the dielectric interface. The lowest measurable signal at  $186 \text{ nW/cm}^2$  and highest measured signal at  $125 \text{ }\mu\text{W/cm}^2$  lead to a change in capacitance of 1.25 and 10.5 pF, respectively. Increasing the irradiance by a factor of 672 increases the measured capacitance by a factor of 8.4, which is indicative of a logarithmic or sub-linear responsivity that increases the dynamic range of imaging systems[65]. Like the OPD with the same active layer, there is a persistence of photoconductivity in the OCCD. The sudden and gradual drop-off in capacitance after extinguishing the light source are the result of the bimolecular recombination of accumulated holes at the dielectric interface and recombination of trapped electrons in acceptor sights, respectively. Figure 4.1d shows the effect of bias stressing under dark conditions for the OCCD in Figure 4.1a at -10 V followed by a second run at -5 V. The capacitance of the OCCD increases beyond 10 seconds of biasing at -10 V despite the absence of photogenerated electrons. Additionally, parasitic memory effects affect subsequent measurements as seen from the matching final measured capacitance at -10 V and start of -5 V bias. Despite the higher EQE achieved in active layers with charge trapping-induced photomultiplication, the persistence of photoconductivity and instability of these devices under bias stress makes these devices unfit for reliable image sensors that operate at fast frame rates. Consequently, OCCDs with continuous, non-trapping pathways for electrons and holes in the active layer are also investigated.

The performance of OCCDs using the same structure as the device in Figure 4.1a but having an active layer with a composition of 1:3 PCDTBT:PC<sub>71</sub>BM is also assessed. The morphology of this donor-acceptor ratio has minimal charge trapping since it has continuous conductive pathways for electrons and holes in the acceptor and donor, respectively[16, 131]. Figure 4.2a shows the capacitance of this device under dark, 1.3 and  $43 \text{ }\mu\text{W/cm}^2$ . The transient response of this device is significantly faster at reaching a steady state than the OCCD with the 100:1 PCDTBT:PC<sub>71</sub>BM active layer in Figure 4.1c with no noticeable persistence of photoconductivity at this time scale. Additionally, the ratio of capacitance change at 43 and  $1.3 \text{ }\mu\text{W/cm}^2$  (6.1 and 0.5 pF, respectively) is 12.2, which is less than the respective ratio of irradiance of 33.1 and indicates these devices also have logarithmic or

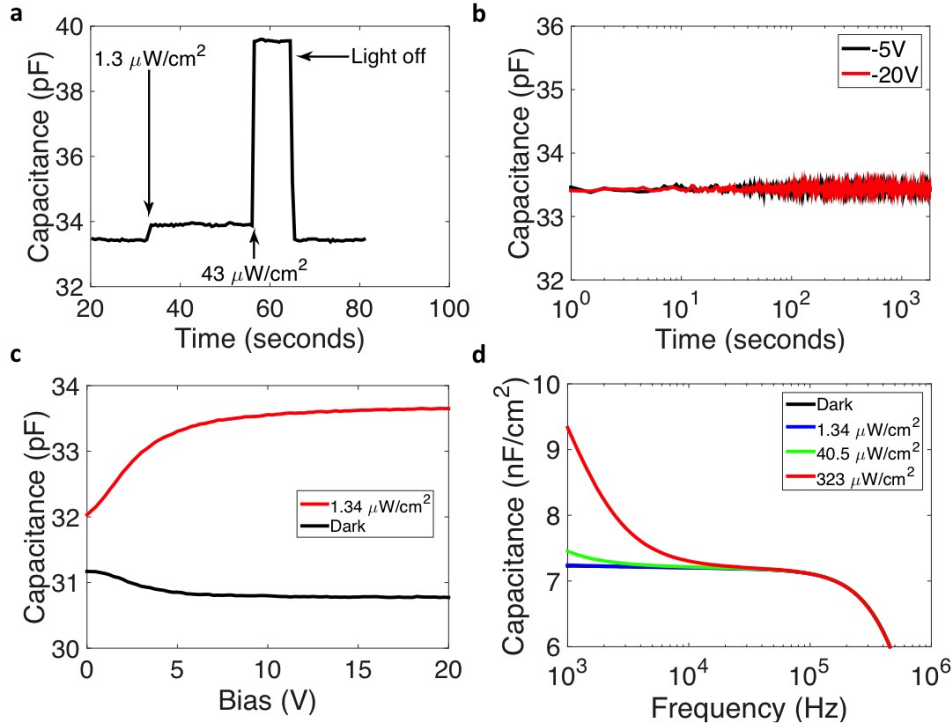


Figure 4.2: (a) Temporal response of an OCCD of the same structure as the device in Figure 4.1a but with an active layer composition of 1:3 PCDTBT:PC<sub>71</sub>BM. (b) Bias stress stability in the dark of the OCCD with 1:3 donor:acceptor with an initial run at -20 V immediately followed by a -5 V bias. (c) Capacitance as function of bias of the same OCCD in the dark and under an irradiance of 1.34  $\mu\text{W}/\text{cm}^2$  at 532 nm. (d) Frequency response of the capacitance for the same OCCD under various irradiances at 532 nm.

sub-linear responsivity that can enable wide dynamic range imaging. Figure 4.2b shows the effect of bias stressing under dark conditions for the this same OCCD at -20 V followed by a second run at -5 V. The measured capacitance is stable throughout the measurement at both voltages and does not show any difference in the measured value at -20 V or -5 V. Given the temporal stability of the active layer of this OCCD, it is possible to reliably examine the dependence of capacitance on bias and frequency. Figure 4.2c shows capacitance on the OCCD as a function of DC bias voltage under dark and illuminated conditions. Increasing the bias depletes the active layer of charge, meaning that the capacitance of the device under dark conditions is determined by the spacing between the bottom and top electrodes beyond a couple volts biasing. This is analogous to reverse biasing an OPD, where the capacitance plateaus after a few volts when the active layer is fully depleted[188]. The capacitance is higher under illumination than dark as a result of the presence of photogenerated carriers at the dielectric interface. Increasing the bias voltage increases the electric field in the active

layer and brings more holes towards the dielectric interface. The motion of carriers in the OCCD is elucidated by examining capacitance as a function of measurement frequency in the dark and under various irradiances as shown in Figure 4.2d. The response of the pixel at low frequencies depends strongly on the light intensity since this influences the amount of photogenerated holes accumulating at the dielectric interface. This response is specific to photogenerated carriers since the capacitance of the OCCD in the dark is independent of frequency. Additionally, lower frequencies increase the capacitance at a given irradiance since this allows more time for photogenerated charge accumulated at the dielectric interface to react to temporal changes in the electric field. The responsivity of these devices to irradiances as low as  $1 \mu\text{W}/\text{cm}^2$  and good stability warrant further characterization as an image sensing pixel.

## Pixel Operation & Performance

The ability for a photodetector to integrate photogenerated charge is essential to maximizing signal-to-noise ratio (SNR) as mentioned in Chapter 1. Given the good stability and quasi-static (constant biasing voltage) performance of the OCCD in Figure 4.2, this device is driven by modulating the bias voltage across the device in order to control charge integration and discharge in order to simulate its performance as an image-sensing pixel. Figure 4.3a is a schematic of the driver circuit used to set the bias across the OCCD and instrumentation amplifier that reads the voltage drop across a resistor in series with the device in order to determine current flow. The bias is of the same polarity as the device in Figure 4.1a. The device is reset by periodically dropping the bias in order to discharge it as shown in Figure 4.3b. The OCCD is only illuminated when it is in integration mode (bias high) in order to examine transient behavior. Figure 4.3c displays the current output from the OCCD pixel at 41 and  $320 \mu\text{W}/\text{cm}^2$  measured at a reset rate of 100 Hz with reference lines marking the current density which corresponds to 100% EQE at both of these irradiances. A large but fast-settling current is seen when resetting the pixel since the change in bias induces a change in charge in the capacitive structure. The EQE of the current being drawn from the OCCD over a duration of 5 ms at an irradiance of  $41 \mu\text{W}/\text{cm}^2$  starts at 80% and ends at 62% while that at  $320 \mu\text{W}/\text{cm}^2$  starts at 50% and decreases to 0% before the end of the light exposure. The decreasing EQE with higher irradiances gives rise to the sub-linear responsivity explained in Figure 4.2a. Additionally, the linear decrease in EQE with exposure time is indicative of the process by which saturation occurs. As charge is accumulated at the dielectric interface, this results in a linear decrease in electric field in the rest of the active layer (where photogenerated carrier are created) since these accumulated charges screen the charge at the top electrode. This screening contributes to a linear decrease in charges reaching the dielectric interface, and thus EQE, since current is proportional to electric field. Saturation occurs at high irradiances due to the large amount of photogenerated carriers as seen with the device under  $320 \mu\text{W}/\text{cm}^2$ . Figure 4.3d shows the OCCD under  $41 \mu\text{W}/\text{cm}^2$  with a reset rate of 100 Hz and 20 Hz, corresponding to a light exposure duration of 5 ms

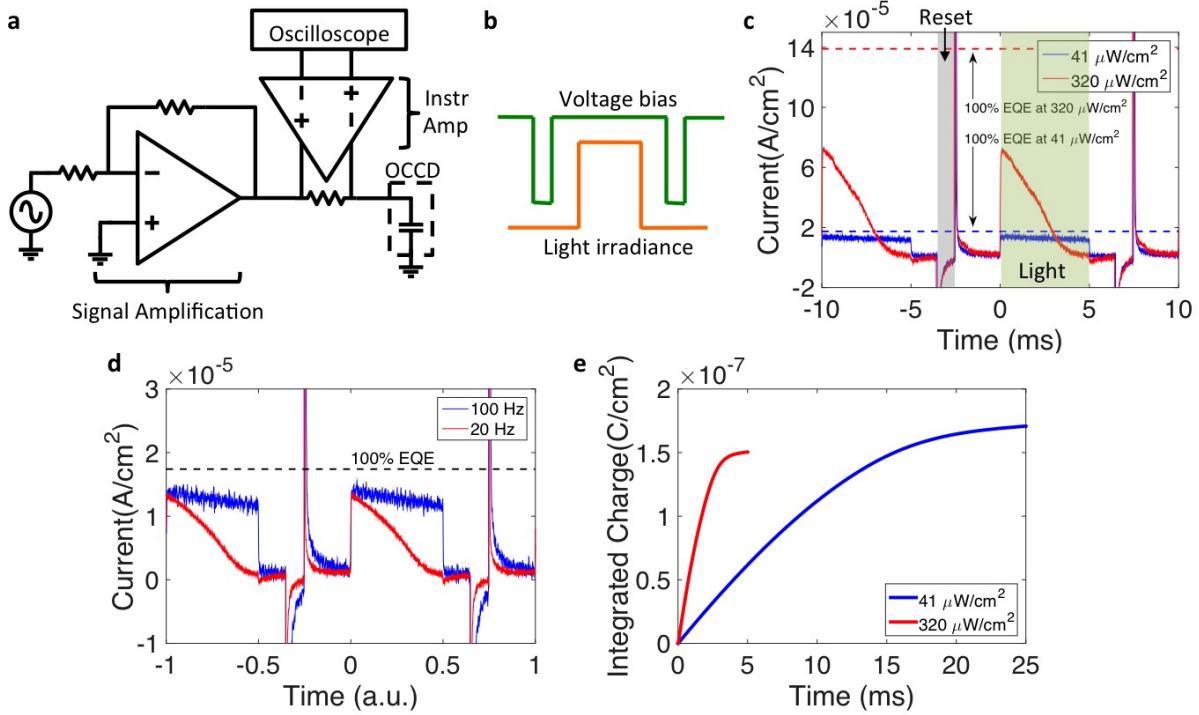


Figure 4.3: (a) Driving and readout circuit used to operate OCCDs as charge-integrating photodetector pixels. (b) Driving scheme used for assessing OCCD charge integration performance by ensuring the light is only on when the OCCD is biased in integration mode (high) and not during reset (low). (c) Temporal response of the OCCD in Figure 4.2 when periodically illuminated at various irradiances at 532 nm for 5 ms at a refresh rate of 100 Hz. (d) Temporal response of the same OCCD illuminated at  $41 \mu\text{W}/\text{cm}^2$  at 532 nm with a 50% duty cycle for a refresh rate of 100 Hz and 20 Hz. (e) Integrated charge as a function of illumination time at various irradiances.

and 25 ms, respectively. The current and EQE vanish to as the pixel saturates in the same linear behavior as the pixel illuminated at  $320 \mu\text{W}/\text{cm}^2$ . This similarity proves that OCCDs are capable of charge integration since either a high irradiance or lengthy exposure results in an accumulation of charge. Additionally, the amount of integrated photogenerated charge at saturation is the same at both  $41$  and  $320 \mu\text{W}/\text{cm}^2$  as seen from Figure 4.3e. This similarity shows that the well capacity (maximum amount of photogenerated charge storage) is independent of irradiance. The well capacity is  $\approx 15 \text{ nF}/\text{cm}^2$ , which is comparable to the geometric capacitance of the gate dielectric ( $\approx 12 \text{ nF}/\text{cm}^2$ ).



## 4.3 Organic Phototransistors

### Introduction

Phototransistors are another capacitive-driven photodetector like CCDs but with a laterally conductive channel. These devices produce photoconductive gain as a result of the unipolar design of the device that traps minority carriers in the channel (see Chapter 1 for background). This gain mechanism is not seen in conventional photodiodes and results in EQEs well over 100% [55, 85, 87, 104, 112, 119]. These devices also have a sublinear responsivity (decreasing EQE) to irradiance [10, 80] as opposed to the linearity (constant EQE) of photodiodes [10]. Figure 4.4a shows the charge output as a function of irradiance from an image sensor pixel using a photodiode and phototransistor. Photoconductive gain in the phototransistor enables higher EQEs than the photodiode-based pixel in low lighting. The sublinear responsivity of phototransistors to light prevents photogenerated charge from saturating the charge capacity of the photodetector in the pixel (well capacity) or readout circuitry at high irradiances. Combining photoconductive gain at low irradiances and sublinear responsivity of a phototransistor-based pixel leads to a wider dynamic range than the linear response of photodiode-based pixel.

Intra-pixel integration of photogenerated charge is necessary to achieve a high SNR at video frame rates. Figure 4.4b illustrates the rolling shutter addressing scheme used in most consumer image sensors [65, 166] in which charge is integrated in the pixel starting at the beginning of the frame. The integrated charge from every pixel in a row of the array is simultaneously readout from the column lines as each row is scanned. The SNR of the readout signal is substantially larger than that from the instantaneous photocurrent when scanning each row. Up until present, only heterogeneously assembled solution-processed organic pho-

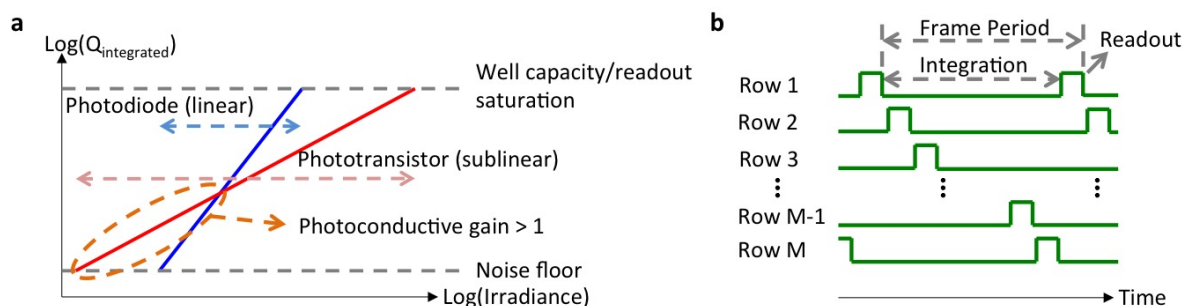


Figure 4.4: (a) Dynamic range of integrated charge for a pixel using a photodiode (linear responsivity) and a phototransistor (sublinear responsivity with photoconductive gain). (b) Rolling shutter row addressing scheme used in commercial image sensors for integration and readout of photogenerated charge during a frame period.

todiodes (OPDs) and thin film transistors (TFTs) have been shown to operate at video frame rates, which are on the order of 30 frames per second (fps)[48, 126, 139]. However, integrating OPDs and TFTs is complicated by differences in geometries, electrodes and active layers. On the other hand, a phototransistor capable of charge integration[119, 194] and a fast response time[104, 143, 184] can operate at higher efficiencies, wider dynamic range, and simplify pixel fabrication. While prior art on high-detectivity solution-processed phototransistors developed for image sensing have high EQEs using direct current sampling[33, 85, 112] or integration on the order of seconds[119, 194], none are shown to integrate photogenerated charge at video frame rates. However, the pixel-driving scheme used to integrate photogenerated charge for the OCCD can also be applied to phototransistors due to their structural similarities.

This chapter shows a novel solution-processed phototransistor architecture based on an organic heterostructure of a high mobility semiconductor deposited on a donor-acceptor bulk heterojunction (BHJ) processed without photolithography on flexible substrates. These devices show a mean mobility of  $1.47 \text{ cm}^2/\text{Vs}$ , on-off ratio of over  $10^5$ , and EQEs above 1200% in the on-state. The fast readout time and photoconductive gain of the OPTs enables charge integration at frame rates up to 100 fps with EQEs over 100% at irradiances below  $1 \mu\text{W}/\text{cm}^2$  at 532 nm. A dynamic range of 103 dB at 30 fps is a result of the sublinear responsivity of these devices. This performance is competitive with consumer image sensors, which have EQEs below 100% and dynamic ranges below 70 dB[65].

## Device Fabrication, Architecture & Characterization

The channel architecture of the phototransistor is essential for maximizing performance. Phototransistors using only a BHJ channel have been shown to exhibit broad absorption spectra[59], but the disordered nature of BHJs makes it difficult to approach mobilities of  $1 \text{ cm}^2/\text{Vs}$  [184]. Conventional high mobility semiconductors such as dinaphtho[2,3-b:2',3'-f]thieno[3,2-b]thiophene (DNTT)[33, 119] and various metal oxides[1] operate as phototransistors, but their photonic performance is limited by low absorption outside the UV region due to their wide band gaps. On the other hand, it is possible to combine the properties of these two devices by forming a heterojunction between a good absorber that efficiently generates electron hole pairs and high mobility semiconductor to rapidly transport the carriers out of the device[112, 143, 193]. Figure 4.5 shows the fabrication process of the OPT device using a bottom contact-top gate architecture. The source-drain electrodes are printed on a flexible plastic substrate using surface energy-patterned doctor blade coating previously developed for organic TFTs[135]. Contacts bumps are printed on the source-drain electrodes in order to create conductive vias through the dielectric that enable probing and inter-device connections from the surface as will be discussed in Chapter 5. A plasma treatment renders the surface hydrophilic to create a uniform coating of PCDTBT:PC<sub>71</sub>BM, a broad absorption BHJ with high internal quantum efficiency[131]. An organic heterojunction is formed

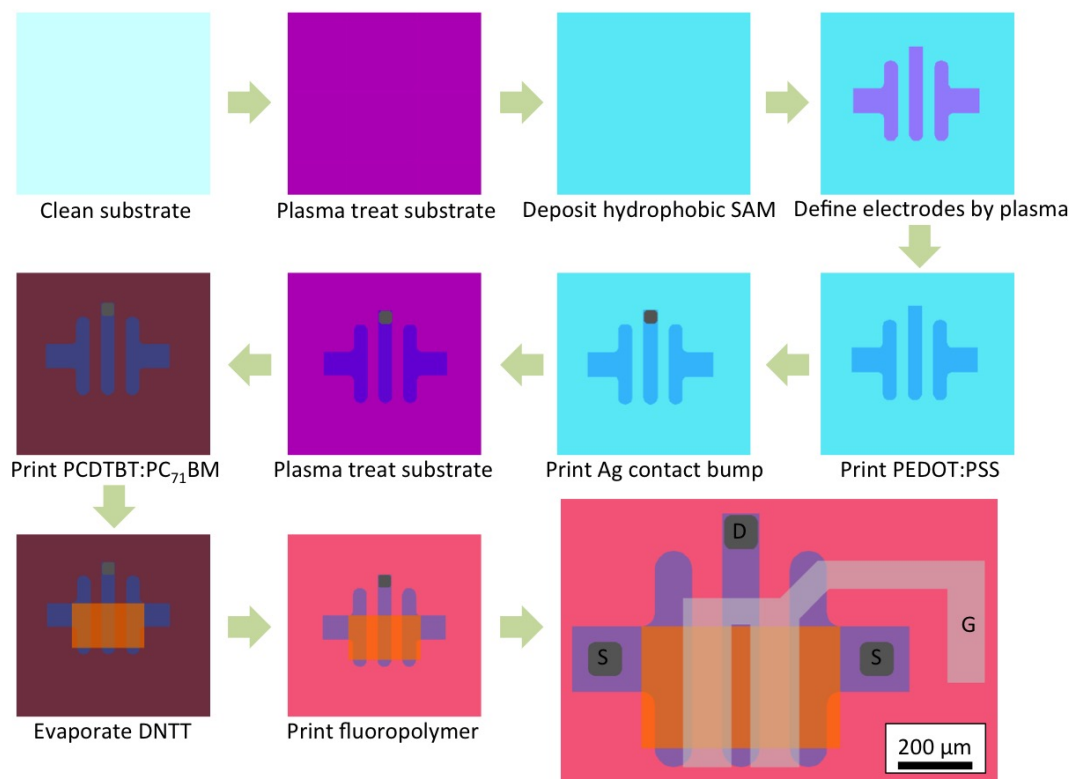


Figure 4.5: Fabrication process flow for the organic phototransistor (OPT) with the final device schematic showing the source (S), drain (D), and gate (G) electrodes.

by thermally evaporating DNTT on top of the absorbing layer. Thermal evaporation also circumvents the lack of organic semiconductor solvents orthogonal to PC<sub>71</sub>BM[47]. A fluoropolymer gate dielectric is blanket coated over the whole substrate with aluminum forming the gate electrode. The final OPT structure is shown at the end of the process flow diagram in Figure 4.5.

The channel of the OPT is comprised of a heterostructure of DNTT and PCDTBT:PC<sub>71</sub>BM BHJ as depicted in the band diagram of Figure 4.6a. It is energetically favorable for photogenerated holes in the highest occupied molecular orbital (HOMO) of PCDTBT to enter DNTT, while electrons are trapped in PC<sub>71</sub>BM due to the high lowest unoccupied molecular orbital (LUMO) of DNTT. This charge carrier selectivity ensures high photoconductive gain, which is dependent on the ratio minority carrier lifetime (electron,  $\tau_n$ ) to the transit time of the majority carrier (hole,  $\tau_t$ ). The effect of the organic heterojunction on device performance is assessed by comparing the complete OPT in Figure 4.6b to partial devices with just the BHJ and DNTT in Figures 4.6b and c, respectively. Figure 4.6e shows the

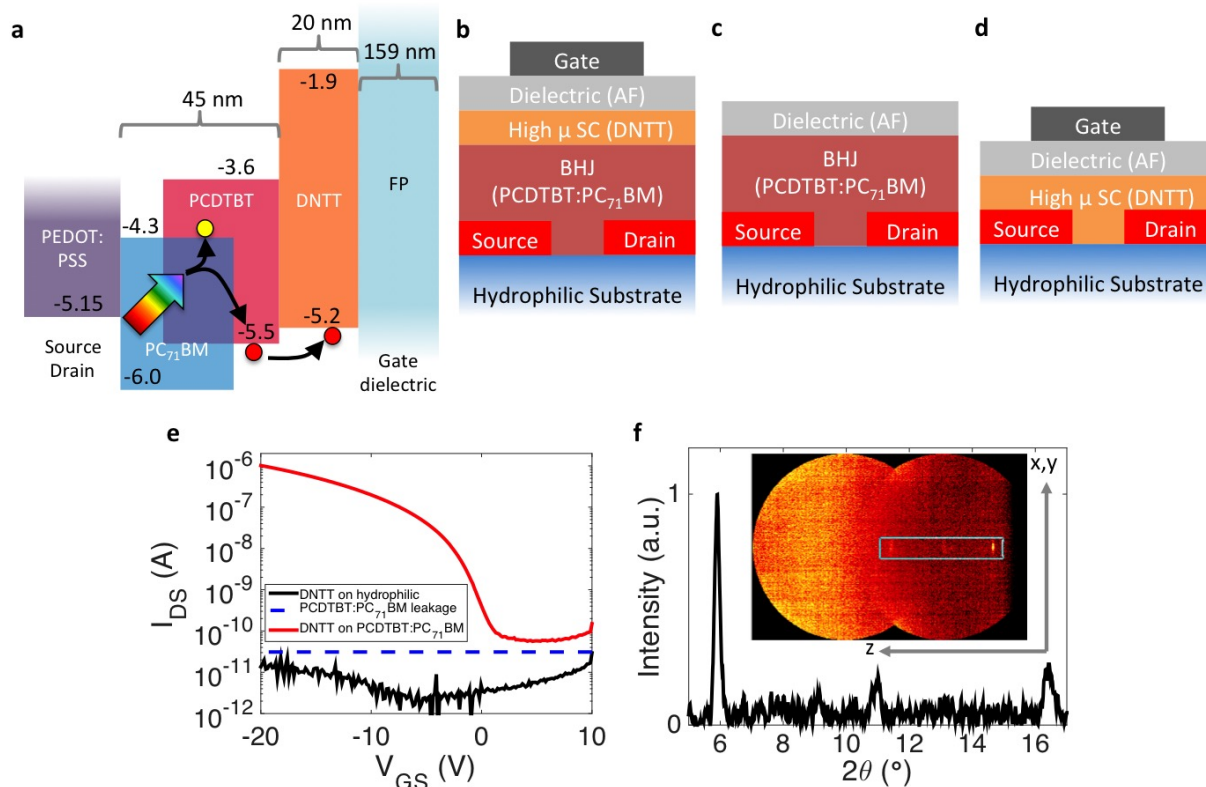


Figure 4.6: (a) Band diagram of the OPT channel along with the thickness of the migration of photogenerated charge and the thickness of each layer. (b,c, and d) Various test structures used to determine the impact of the heterojunction channel. (e) Comparison of transfer characteristics for the devices shown in (b-d). (f) Out-of-plane X-ray diffraction (XRD) measurements on the PCDTBT:PC<sub>71</sub>BM-DNTT channel with the inset showing the 2D diffraction pattern.

typical transfer characteristic of an OPT (Figure 4.6b) in the dark (red), which behaves as a conventional TFT with an on-off ratio of over  $10^5$ . The off-current for this device has a significant contribution from the leakage current between source and drain electrodes through the BHJ as measured from the device in Figure 4.6c. This off-current leakage increases by a factor of 5 when illuminated at high irradiance of  $320 \mu\text{W}/\text{cm}^2$ . Figure 4.6e also shows that the device with DNTT in direct contact with the substrate and source-drain electrodes (Figure 4.6d) does not turn on and remains insulating. This lack of response is attributed to the fact that the crystallization of thermally evaporated organic molecules is highly dependent on the properties onto which it is deposited[83]. The out-of-plane X-ray diffraction (XRD) intensity profile of the DNTT film on top of the BHJ is measured in Figure 4.6f in order to determine the crystal structure of DNTT. The peaks at  $5.9$ ,  $10.95$ , and  $16.4$  are

well matched to the (001), (002), and (003) peaks, respectively, previously reported for high mobility DNTT films[180]. The performance of OPTs is further assessed given the proper crystallization of the semiconductor.

OPT quasi-static performance is examined prior to implementation as a charge-integrating pixel. A transfer characteristic for a typical device with the structure shown in Figure 4.5 in the dark shown in Figure 4.7a. This device exhibits a saturation mobility of  $1.38 \text{ cm}^2/\text{Vs}$ , on-off ratio of  $10^5$ , and very little hysteresis in the on-state and sublinear region. The hysteresis seen in the off-current is attributed to the properties of the BHJ since most of the off-current comes from this film as previously shown in Figure 4.6e and no hysteresis is shown at higher current levels where the DNTT is responsible for majority of the conductivity. The device also shows a close fit to the ideal square-law behavior as observed in Figure 4.7b, validating

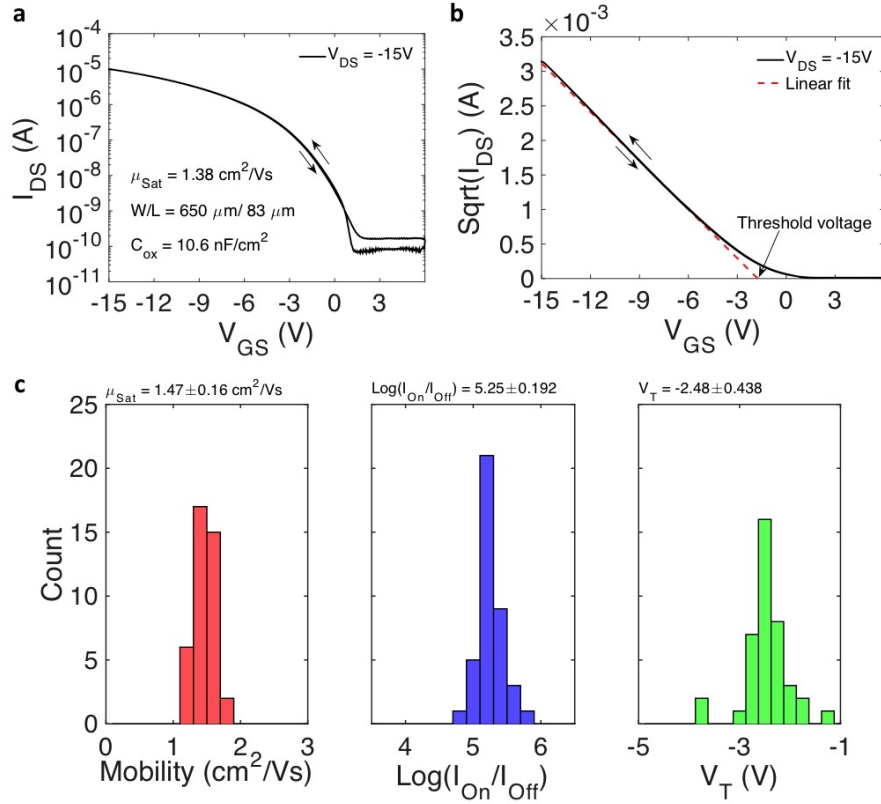


Figure 4.7: (a) Dark transfer characteristic of a phototransistor for forward and backward sweeps at a rate of 5V/s. (b) The transfer characteristic in (a) plotted as  $\sqrt{I_{DS}}$  with respect to a linear fit. (c) Statistical distribution of mobility, on-off ratio, and threshold voltage ( $V_T$ ) for 40 devices.

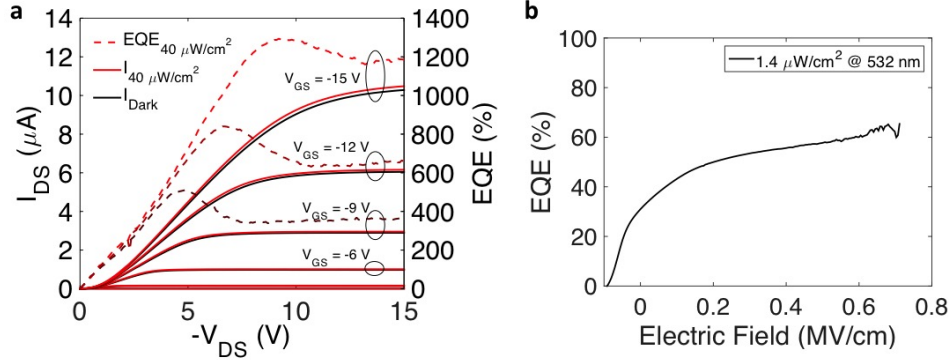


Figure 4.8: (a) Output characteristics of an OPT in dark and under an irradiance of  $40 \mu W/cm^2$  at 532 nm along with the EQE for various  $V_{GS}$ . (b) EQE of an OPD with the same BHJ as the OPT (45 nm of 1:3 PCDTBT:PC<sub>71</sub>BM) using a PEDOT:PSS anode and aluminum cathode as a function of applied electric field.

the use of the square-law model to extrapolate mobility. Multiple TFTs were characterized in the same fashion to examine uniformity across an area of  $1.2 \text{ cm}^2$  as summarized in Figure 4.7c, with a transistor yield of 40 out of 41. The mean and standard deviation saturation mobility,  $\log(I_{On}/I_{Off})$ , and threshold voltage are  $1.47 \pm 0.16 \text{ cm}^2/Vs$ ,  $5.25 \pm 0.192$  and  $-2.48 \pm 0.438$ , respectively. This low variability improves the uniformity of the photoresponse from OPT pixels and can facilitate future circuit designs using these devices as transistor elements for signal routing or additional gain stages. The saturation mobility of these devices is comparable to the value of  $2.1 \text{ cm}^2/Vs$  measured in long channel (40-50  $\mu m$ ) conventional DNTT TFTs deposited on an n-tetradecylphosphonic acid self-assembled monolayer (SAM) with gold top-contact electrodes[98, 198]. The proper diffraction peaks in Figure 4.6f and high performance suggest this BHJ induces crystallization in DNTT similar to alkyl SAMs[94].

The output characteristic of a typical device in dark and under an irradiance of  $40 \mu W/cm^2$  at 532 nm along with the EQE is shown in Figure 4.8a. Contact resistance is seen in the triode region as a result of the hole barrier of 300 meV between PEDOT:PSS and DNTT imposed by PCDTBT, as shown in Figure 4.6a. The PCDTBT-induced contact barrier is further supported by the observation that this effect is not observed for the high-mobility polymeric-small molecule blend TFTs deposited directly on PEDOT:PSS in Chapter 2[135]. Despite the contact resistance, EQE increases linearly with  $-V_{DS}$  in the triode region as described for an ideal photoconductor in Equation 4.1, where  $I_o$ ,  $\mu$ , and  $L$  are the rate of photogenerated electrons in the channel, mobility, and channel length, respectively. These devices have high output saturation resistance and an EQE above 1200% at a  $V_{GS}$  of -15 V. The EQE plateaus in the saturation region since pinch-off at the drain limits

the electric field across the channel, thus also fixing the photoconductive gain. Figure 4.8b shows EQE for an OPD using the same BHJ as the OPT, with an EQE of 63% at the same applied transverse field as the OPT biased at a  $V_{GS}$  of -15 V (670 kV/cm).  $I_{DS, light}$  and  $I_0$  in Equation 4.1 may be replaced with the EQE of the OPT and OPD, respectively, since current is directly proportional to EQE. Given the EQE of the OPD, the electron lifetime ( $\tau_n$ ) in the channel is approximately 80  $\mu$ s in the on-state.

$$I_{DS, light} = I_0 \left( \frac{\tau_n}{\tau_t} \right) = I_0 (\tau_n) \left( \frac{\mu V_{DS}}{L^2} \right) \quad (4.1)$$

## Pixel Operation & Performance

Reading out the integrated photogenerated charge after a frame period, as illustrated in Figure 4.4b, has a significantly higher SNR than sampling the instantaneous photocurrent during each row scan. It is optimal for a device to integrate charge in the regime of maximal SNR, which increases with a higher light-to-dark current ratio. This ratio is 1.02 and 20 for the phototransistor in the on- ( $V_G < V_T$ ) and off-state ( $V_G > V_T$ ), respectively, at 40  $\mu$ W/cm<sup>2</sup> as seen from Figure 4.9a, making it optimal to integrate charge in the off-state. A pixel is created by connecting a biasing capacitor in series with the source of the phototransistor, shown in Figure 4.9b, to minimize dark current through the channel and manage parasitic charge injection from overlapping source-gate electrodes. Figure 4.9c illustrates the mechanisms occurring in the pixel during integration (off-state) and discharge (on-state) for a rolling shutter addressing scheme. Photogenerated electrons are trapped in the channel during integration while holes exit to the drain. Turning on the OPT discharges it by injecting holes that recombine with the accumulated electrons. An external charge amplifier is connected to the drain of the phototransistor in order to monitor hole extraction and injection at the drain electrode and places the electrode at virtual ground.

The biasing capacitor ( $C_B$ ) compensates for the change of charge in the source electrode resulting from parasitic source-gate capacitance ( $C_{GS}$ ) when the device is switched to integration mode as explained in Figure 4.9d. The source electrode is set to 0 V when the OPT is on since the drain is connected to virtual ground, resulting in an accumulated parasitic charge of 15.4 pC for a  $V_{GS}$  of -14 V and  $C_{GS}$  of 1.1 pF. Turning off the device results in a transfer of  $(V_{On} - V_{Off}) C_{GS} = 22$  pC to  $C_B$  assuming no charge dissipation from the source electrode through the channel when turning off the device. This charge transfer biases  $V_{DS}$  at -5.37 V during integration, and is independent of the applied bias voltage,  $V_B$ . Holes are extracted at the drain upon illumination since  $V_{DS} < 0$ , causing a drop in output voltage of the charge amplifier and leaving behind trapped electrons in the channel. Switching the pixel to the on-state discharges the device by injecting holes that recombine with the trapped electrons in the channel. If the charge retention during integration is high, the amount of



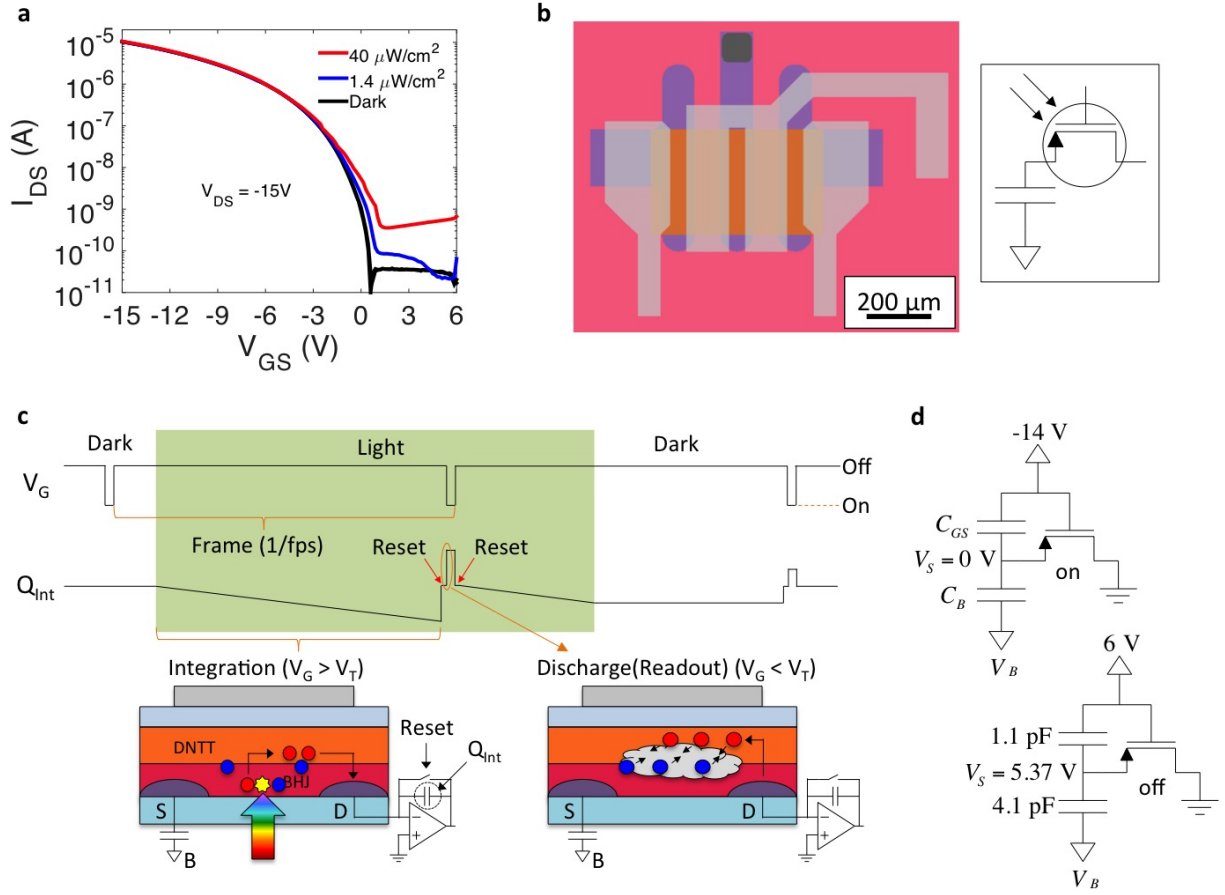


Figure 4.9: (a) Transfer characteristic of OPT at various irradiances at 532 nm. (b) Pixel schematic and equivalent circuit of an OPT-based pixel. (c) Drive ( $V_G$ ) and readout ( $Q_{int}$ ) scheme of pixel operation. The first phase and vast majority of the frame period is charge integration of electrons (blue) followed by a fast discharge of the electrons through recombination with injected holes (red) to quickly readout the signal. (d) Equivalent pixel circuit in the on- and off-state showing relevant parasitic capacitances ( $C_{GS}$ ) and nodal voltages.

integrated charge is equivalent to the discharge during readout.

Charge carrier dynamics during integration are investigated since these are not described by steady-state phototransistor behavior[10, 56]. Figure 4.10a shows the integrated photo-generated charge and the EQE of the rate of integrating charge, labeled as instantaneous EQE, during light exposure for irradiances of  $40 \mu\text{W}/\text{cm}^2$  and  $323 \mu\text{W}/\text{cm}^2$ . The instantaneous EQE initially increases at the same rate for both irradiances, which is attributed to the slow transit time of holes to reach the drain because of the lower mobility in the off-



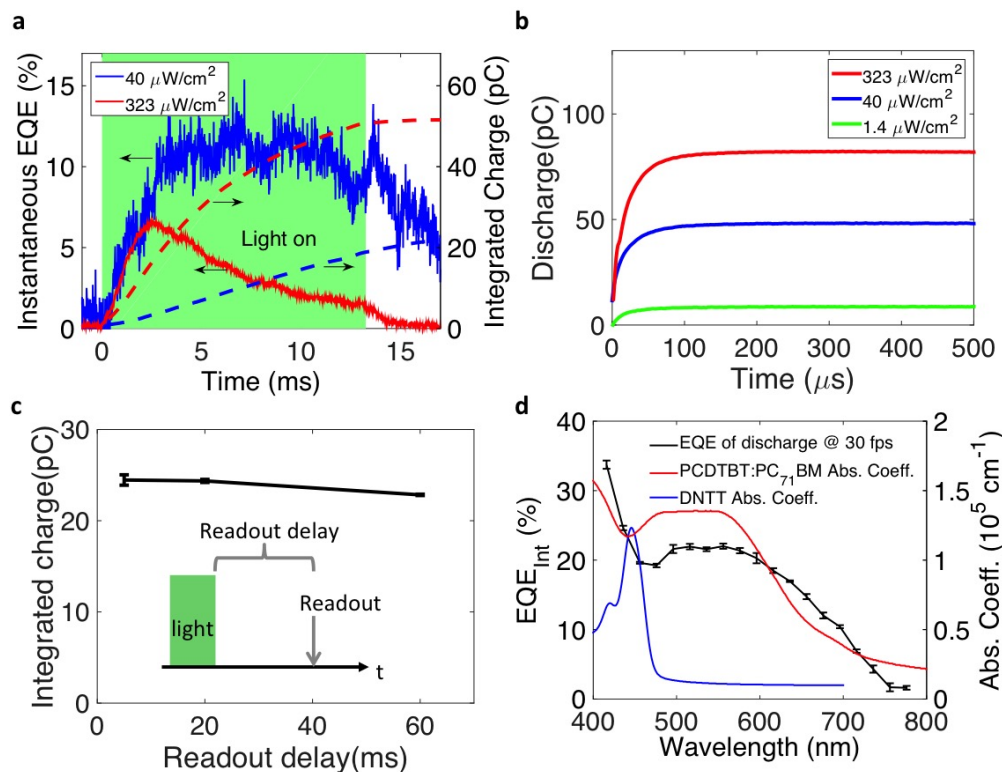


Figure 4.10: (a) Dynamic response of integrating charge and EQE of the rate of integrating charge, labeled instantaneous EQE, at an irradiance of 40 and 323  $\mu\text{W}/\text{cm}^2$  at 532 nm. (b) Dynamic response of the discharge to readout light signals after an integration period of 32 ms for irradiances of 1.4, 40 and 323  $\mu\text{W}/\text{cm}^2$  at 532 nm. (c) Integrated charge as a function of readout delay at an irradiance of 40  $\mu\text{W}/\text{cm}^2$  at 532 nm. (d) EQE of integrated charge ( $\text{EQE}_{\text{Int}}$ ) measured at readout from 416-784 nm at irradiances varying between 5-10  $\mu\text{W}/\text{cm}^2$  at 30 fps. Also shown are the absorption coefficients of the DNTT and PCDTBT:PC<sub>71</sub>BM layers of the phototransistor.

state. This transit time phenomenon is supported by the continuing collection of charge for several milliseconds after the light source is turned off as seen in Figure 4.10a. Persistence of photocurrent from photoconductive gain is negligible at this scale since the minority carrier lifetime in the channel was calculated to be 80  $\mu\text{s}$  under an irradiance of 40  $\mu\text{W}/\text{cm}^2$ . During illumination, the instantaneous EQE peaks before decreasing to a steady-state value. The decrease in efficiency with time is attributed to the accumulation of electrons in the channel, increasing the probability of recombination with holes. Instantaneous EQE also peaks at a higher value at lower irradiances as a result of the slower rate of electron trapping that lowers the probability of recombination.

Irradiance ( $\mu\text{W}/\text{cm}^2$ )	Rise time ( $\mu\text{s}$ )
323	53
40	49
1.4	60

Table 4.1: Rise time (reaches 90% of steady state) of discharge after integration at various irradiances at 532 nm.

Discharge, the phase after integration, is used to readout the amount of integrated charge during a frame period. The discharge dynamics are shown for irradiances of 1.4, 40 and 323  $\mu\text{W}/\text{cm}^2$  after an integration time of 32 ms, which corresponds to 30 fps with a 95% integration duty cycle over the frame period, in Figure 4.10b. Over 90% of the integrated charge is discharged in 60  $\mu\text{s}$  for all irradiances before settling to a steady output as summarized in Table 4.1. The similarity of the discharge time to the minority carrier lifetime of 80  $\mu\text{s}$  suggests that the injected holes recombine with the trapped electrons in the channel as illustrated in Figure 4.9c. In addition to fast response times, high charge retention is desirable during integration to minimize the loss of trapped electrons before discharging. Modulating the readout delay, the time between the end of light exposure and discharge as shown in the inset of Figure 4.10c, is a method that can be used to assess the charge retention of a device[123, 194]. It is found that the pixel retains over 99% of the original stored charge for readout delays of 20 ms and 93% for delays of 60 ms as shown in Figure 4.10c. This charge retention enables the total amount of photogenerated charge integrated at video frame rates, with integration periods on the order of ten to thirty milliseconds, to be accurately determined by reading out the discharge.

Using the rolling shutter scheme in Figure 4.9c and reading out the amount of integrated charge through the discharge, the spectral response of the pixel was measured by the EQE of integrated charge,  $\text{EQE}_{\text{Int}}$ , over a period of 30 fps (32 ms integration time) as shown in Figure 4.10d. The  $\text{EQE}_{\text{Int}}$  is defined in Equation 4.2, where photocharge is the difference in pixel discharge under illumination,  $Q_{\text{Dis, light}}$ , and dark,  $Q_{\text{Dis, dark}}$ . Elementary charge, photon flux ( $\text{mm}^{-2}\text{s}^{-1}$ ), integration time (s) and the photoactive area ( $\text{mm}^2$ ), are denoted by  $q$ ,  $\Phi$ ,  $t_{\text{Int}}$ , and  $A$ , respectively. The similarity between the spectrum of  $\text{EQE}_{\text{Int}}$  and the absorption spectrum of the BHJ below the absorption cutoff of DNTT shows the BHJ layer is responsible for photogeneration. A sharp increase in  $\text{EQE}_{\text{Int}}$  in the blue-UV spectrum is attributed to the onset of absorption in DNTT.

$$\text{EQE}_{\text{Int}} = \frac{\text{Photocharge}}{q\Phi t_{\text{Int}}A} = \frac{Q_{\text{Dis, light}} - Q_{\text{Dis, dark}}}{q\Phi t_{\text{Int}}A} \quad (4.2)$$

The dependence of illuminated region of the OPT-based pixel is examined using another

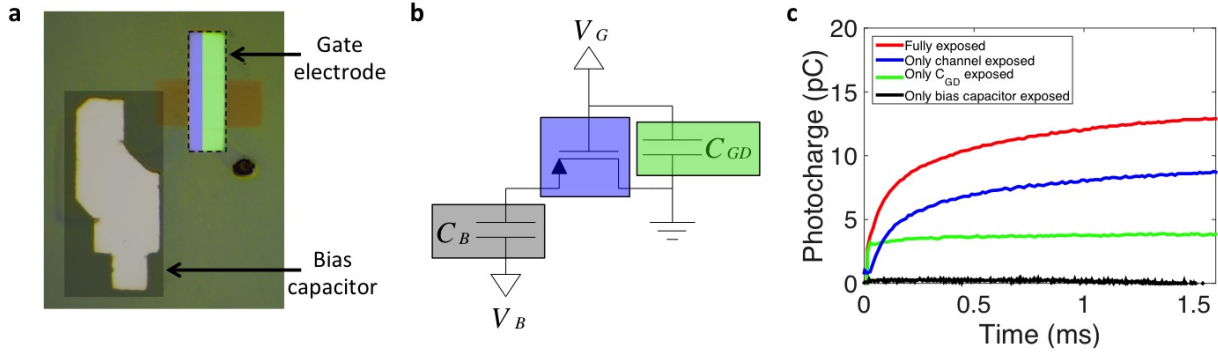


Figure 4.11: (a) Optical micrograph of OPT-based pixel used to test the optoelectronic performance of the device with illumination only on the bias capacitor (black), channel (blue), and drain-gate overlap (green). (b) Equivalent circuit diagram highlighting the same test regions as shown in (a). (c) Discharge characteristics shown for restricted illumination to the regions highlighted in (a) and (b) at an irradiance of  $41 \mu\text{W}/\text{cm}^2$  at 532 nm.

pixel architecture as shown in Figure 4.11a. The equivalent circuit diagram and highlighted regions of the pixel in Figure 4.11a are shown in Figure 4.11b. The optoelectronic performance of each region is assessed by individually illuminating the channel (blue), drain-gate ( $C_{GD}$ ) overlap (green), and bias capacitor ( $C_B$ ) (black) and looking at the discharge as in Figure 4.10b. Figure 4.11c plots these results. The discharge from only illuminating the channel (blue) displays a transient behavior as a result of the transit time of carriers through the channel. However, the discharge of only illuminating  $C_{GD}$  does not exhibit a transient response since carriers are transferred directly between the active layer to the underlying drain electrode without having to go through a resistive channel. No photoresponse is seen from only illuminating  $C_B$  since the one-to-one ratio of photogenerated electrons to holes maintains charge neutrality in the source electrode and does not change biasing. Given these results, the photoactive area for OPTs is considered to be the channel and overlapping gate-drain electrodes.

Dynamic range and  $\text{EQE}_{\text{Int}}$  at various frame rates are used as figures of merit to quantify pixel performance. The integrated charge, as determined by the pixel's charge readout 150  $\mu\text{s}$  after discharge, as a function of irradiance at 532 nm is shown in Figure 4.12a for 5, 30, and 100 fps with a 95% integration time duty cycle. The noise floor is taken as the standard deviation of the readout dark charge and is independent of frame rate. Lower frame rates integrate more charge at a given irradiance since the integration time is longer, giving a higher SNR and decreasing the irradiance at which the integrated signal equals the noise floor (noise equivalent power). For low lighting, ranging from  $10 \text{ nW}/\text{cm}^2$  to several  $\mu\text{W}/\text{cm}^2$ , the integrated charge increases with irradiance by the power of 0.655 for all measured frame

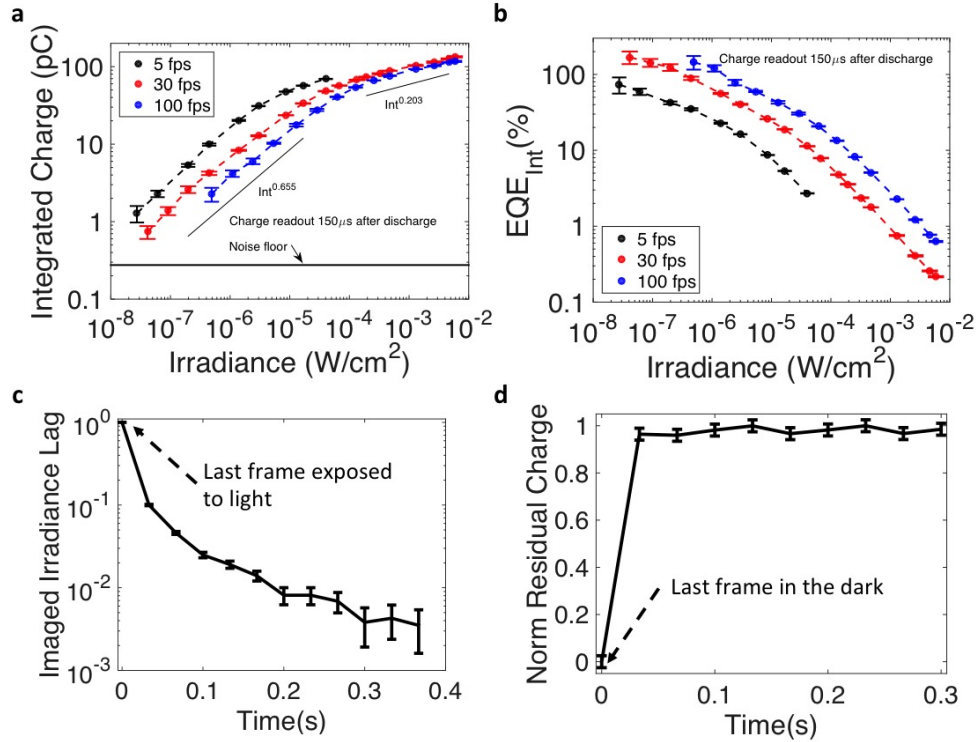


Figure 4.12: (a) Dynamic range of readout signal from an OPT-based pixel measured at 5, 30 and 100 fps with a 95% integration time duty cycle for light at 532 nm. (b)  $\text{EQE}_{\text{Int}}$  measured at readout for the dynamic range measurements in (a). (c) Image lag at 30 fps normalized to imaged irradiance of the last illuminated frame by calibrating the pixel to the plot in (a). (d) Normalized response of pixel to steady illumination after dark.

rates. This power law decreases to 0.203 at higher irradiances, which is indicative of the onset of an additional recombination mechanism at high carrier densities. The sublinear response of the pixel enables wide dynamic range since it prevents saturation of the pixel or readout circuitry at high irradiances as explained in Figure 4.4a. As a result of this response characteristic, the dynamic range of the pixel is measured to be at least 103 dB at 30 fps as shown in Figure 4.12a. Figure 4.12b shows  $\text{EQE}_{\text{Int}}$  of the OPT pixel measurements in Figure 4.12a. The efficiency decreases with longer integration times (lower fps) and higher irradiances since the build-up of electron density in the channel increases the probability of recombination with holes as previously discussed with regards to Figure 4.10a. Photoconductive gain is enabled by stored charge in the biasing capacitor of the phototransistor pixel that is injected into the channel, resulting in  $\text{EQE}_{\text{Int}}$  values above 100% at low irradiances. The decrease of the phototransistor pixel's  $\text{EQE}_{\text{Int}}$  with increasing irradiance creates the sublinear responsivity of these pixels, resulting in wide dynamic range. Image lag, the per-

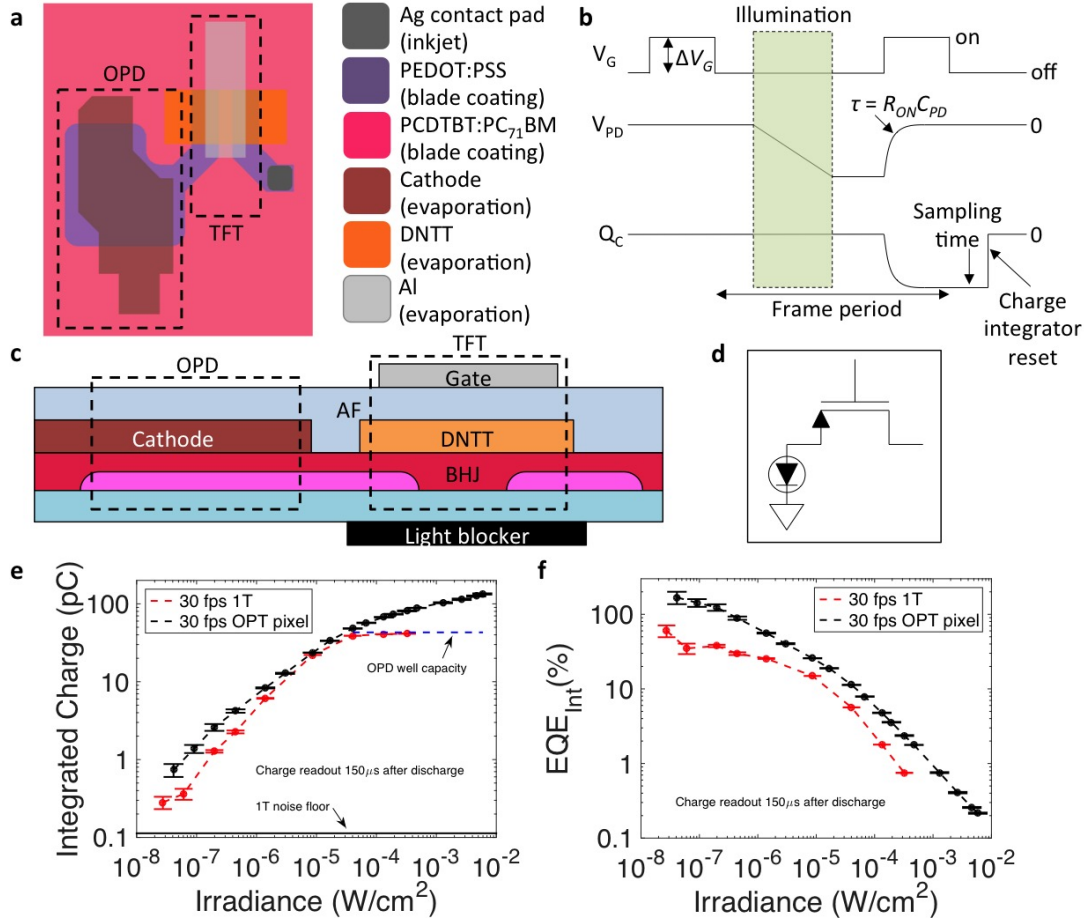


Figure 4.13: (a) Schematic of OPD-based pixel (1T) showing the OPD and TFT element. (b) Driving and charge readout scheme of the 1T pixel, where  $V_G$ ,  $V_{PD}$ , and  $Q_C$  represent gate voltage, voltage at the OPD-TFT node, and collected charge at the drain, respectively, with the drain of the TFT set to ground. (c) Cross sectional profile of the 1T pixel in (a) showing the OPD and TFT regions. (d) Equivalent circuit of 1T pixel. (e) Dynamic response of 1T pixel (red) in comparison to the OPT-based pixel (black). (f)  $EQE_{Int}$  measured at readout for the dynamic range measurements in (e).

sistence of a light signal in a pixel in frames after the light source is turned off, is measured at 30 fps as shown in Figure 4.12c. The measured irradiance decreases to 10% of the original value one frame (33 ms) after the light source is extinguished and to 1% after six frames (200 ms). The response time of the pixel to illumination is also fast as shown in Figure 4.12d with no transient behavior seen between the last dark frame and the following illuminated frames.

A conventional charge-integrating photodiode 1T pixel architecture, comprised of a pho-

todiode in series with a transistor[126, 139, 166], is fabricated from the same material set as the OPT in order to compare the performance of photodiode and phototransistor-based pixel architectures. The pixel schematic and driving-readout scheme are shown in Figures 4.13a and b, respectively (see Chapter 1 for background on the operation of the charge-integrating 1T pixel). The cross section of the pixel, depicting the OPD and transistor area, and equivalent circuit are shown in Figures 4.13c and d, respectively. The TFT has the same channel architecture as the OPT but is covered in order to render it unresponsive to light. Dynamic responses of OPT-based and 1T pixel are compared in Figure 4.13e across a wide range of irradiances at 532 nm. At a sampling rate of 30 fps, the 1T pixel has a dynamic range of 64 dB, which is comparable to the 70 dB of consumer-grade CMOS sensors[65]. The dynamic range of the 1T architecture is limited by the well capacity of the OPD, resulting in a distinct plateau of the responsivity of this pixel at high irradiances while the OPT-based pixel continues to give an irradiance-dependent response. Figure 4.13f shows the 1T pixel is limited to the EQE of the photodiode at low irradiances, which is 63% (Figure 4.8b). The phototransistor pixel is also more efficient than the photodiode pixel across its dynamic range, which ends at the saturation of the OPD's well capacity.

## 4.4 Conclusion

This chapter focused on the development of capacitive-based photodetector elements for implementation in pixels capable of integrating photogenerated charge. OCCDs are promising due to their simple device architecture, excellent bias stress stability and high quantum efficiency of charge integration. These preliminary results suggest device performance that may be capable of efficient inter-pixel charge transfer necessary for CCD image sensors[181] and provided the foundation for the development of the OPT. Light-sensing pixels fabricated using a novel phototransistor architecture comprised of an organic BHJ-high mobility semiconductor heterojunction were also demonstrated in this chapter. The proven synergy of these two material systems can open new avenues of devices and systems research. Efficient intra-pixel integration of photogenerated charge and fast discharging enabled these devices to be operated between 5 to 100 fps with  $\text{EQE}_{\text{Int}}$  above 100% at low irradiances. In addition, the dynamic range of 103 dB measured at 30 fps exceeds the performance of consumer photodiode-based image sensors[65]. Finally, these devices were fabricated without lithography using scalable mass production techniques, opening the possibility of ubiquitous, inexpensive and high performance imaging systems.

## Chapter 5

# Printed Interconnects & Devices for Sensing & Imaging Applications

### 5.1 Introduction

The field of organic and printable semiconductor devices continuously pushes the performance of the materials in order to attain better performance with regards to universal figures of merit. These figures of merit include mobility and on-off ratio for organic thin film transistors (OTFTs). For organic photodiodes (OPDs), these include dark current and external quantum efficiency (EQE). While these figures of merit are universally applicable to all implementations, the performance of nearly all devices must be tailored to meet the specifications for the application in mind[82]. For instance, the channel width to length ratio of complimentary OTFTs may need to be adjusted in order to ensure high gain from a stage[27, 115], or a filter may be needed in front of an OPD to reject unwanted noise.

An array of pixels that is addressable and readable from external components through printed interconnects is necessary for systems with multiple sensors. Using the same device electrodes and dielectrics as read and address lines and dielectric layers between these lines simplifies the fabrication process and is common place for both lithographically-processed[33, 85, 112, 123, 168, 194] and printed arrays[99, 133, 140]. However, highly resistive read lines may result from the fact device electrodes are typically not optimized for conductivity but rather charge injection and extraction from the semiconductor. Additionally, the dielectrics in thin film devices are optimized for high areal capacitance to increase the transconductance, resulting in high parasitic capacitances where address and read lines overlap. The high resistance and capacitance of these lines slows scan rates and causes parasitic charge injection that raises the noise floor of the pixel's signal[166]. In addition to minimizing device performance degradation, interconnects should be mechanically robust. Interconnects have larger dimensions than the thin film devices they connect to and as such experience larger stress for a given strain on the flexible substrate than a thin film device, making them the weakest link.

This chapter applies the OTFTs, OPDs, and organic phototransistors (OPTs) described in Chapters 2, 3, and 4, respectively, to create systems-level applications. First, the implementation of OPDs for wearable and conformal pulse oximetry systems will be discussed. An introduction to the fundamental of pulse oximetry will introduce the fundamental concepts needed to understand transmission and reflectance-based systems. OPD systems with red-infrared and green-red selectivity are tested in their compatibility with inorganic and organic light-emitting diodes (OLEDs). Various system architectures to route interconnects between an array of individually-addressable OPDs to external readout circuits are also discussed. The second part of this chapter outlines the architecture, optimization, and performance of discrete OTFT and OPT arrays connected into row-addressable and column-readable arrays. Finally, an image sensor on flexible substrate is demonstrated using these techniques.

## 5.2 Integration of Organic Photodiodes for Applications in Pulse Oximetry

### Background on Pulse Oximetry

Pulse oximetry is a commonly used non-invasive technique to measure heart rate and arterial blood oxygen saturation ( $\text{SaO}_2$ ). Two LEDs with different transmission peaks are illuminated at one side of a finger then readout by a photodiode on the opposite side as shown in Figure 5.1a. Only one LED is illuminated at a time in order for the photodiode to differentiate between the two signals. Figure 5.1b shows the molar absorptivity spectra of oxygenated hemoglobin ( $\text{HbO}_2$ ) and deoxygenated hemoglobin ( $\text{Hb}$ ). If the peak emission of the LEDs lies where the difference in absorptivity between  $\text{HbO}_2$  and  $\text{Hb}$  is maximal, this results in a maximum difference in the signal received by the photodiode at those two wavelengths. Red ( $\simeq 650$  nm) and infrared ( $\simeq 900$  nm) LEDs are used in commercial pulse oximeter systems since these two wavelengths have the largest difference in absorptivity. The absorptivity at these wavelengths is also low, which means less power is required from the LED to emit light that is received with a strong signal by the photodiode. Figure 5.1c gives a figurative illustration of the signal attenuation from the LED to the photodiode as a function of time. The majority of signal attenuation occurs from tissue, venous blood, and non-pulsatile arterial blood, all of which give a time-invariant signal. However, it is the time-variant signal from the pulsatile arterial blood that is used to determine  $\text{SaO}_2$  and heart rate. The time-invariant signal is subtracted from the total signal to isolate the pulsatile signal, also known as the pulsating photoplethysmogram (PPG). The LEDs are sequentially illuminated and the photodiode current is sampled at a rate of 1 kHz in order to develop a detailed mapping of the PPG.



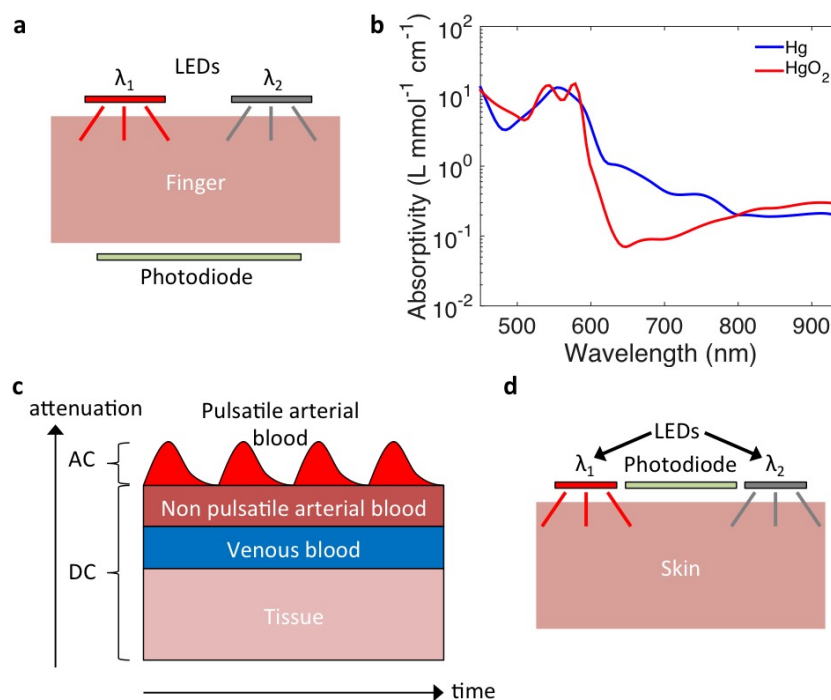


Figure 5.1: (a) Measurement setup of transmission-mode pulse oximetry. (b) Molar absorptivity spectrum of deoxygenated hemoglobin (Hb) and oxygenated hemoglobin (HbO<sub>2</sub>). (c) Schematic representation of a photoplethysmogram (PPG) and the various time-variant and -invariant components that contribute to the signal. (d) Measurement setup of reflectance-mode pulse oximetry.

Oximetry measurements can also be taken in reflection mode by placing LEDs and photodiodes side-by-side on the surface of skin as shown in Figure 5.1d. Unlike transmission-based oximetry, the placement of a reflectance-based oximeter is not constrained to regions on the body with good optical transmittance such as the fingers and earlobes. As such, this oximeter system can be placed on the skin to monitor both SaO<sub>2</sub>, pulse, and skin oxygenation, which is useful metric to quantify wound healing. However, the received light signals are lower and require photodiodes with high specific detectivity (high EQE and low dark current) and readout electronics with high precision.

Organic devices present an opportunity to improve upon the performance of commercial pulse oximeters. Larger sensors capture a larger signal, which increases the signal-to-noise ratio (SNR) as discussed in Chapter 1. The scalable processing used to develop large area arrays of OPDs in Chapter 3 can also be used to realize large-area pixels with applications in pulse oximetry. The scalability of these devices does not lead to increases in cost as with silicon-based devices. Additionally, the thin film structure of these devices directly printed

on conformal plastic substrates reduces packaging and bulkiness compared to conventional silicon wafer-processed devices. For these reasons, large-pixel OPDs capable of sensing both red and infrared wavelength from both LEDs and OLEDs are integrated with drivers and readout circuitry and software to form a complete pulse oximetry system for both transmission and reflectance mode. However, the efficiency of most infrared-emitting OLEDs is quite low and makes it difficult to transmit a sufficiently strong signal to be read by a photodetector after attenuation through a finger. The use of green-emitting OLEDs in conjunction with OPDs is also investigated as replacement for the infrared spectrum since there exists a similar difference in molar absorption coefficient in the green spectrum as with the infrared.

### Transmission Pulse Oximetry with Discrete Organic Photodiodes

OPDs used in pulse oximetry are optimized for large pixels, unlike the pixel density desired for image sensing applications. The architecture and cross section of an array of discrete OPDs is shown in Figure 5.2a and b, respectively. A common PEDOT:PSS anode is blade coated with the edge of the pattern defined through surface energy patterning techniques[135]. Following blade coating of the photoactive layer, a discrete array of aluminum cathodes is thermally evaporated overlapping the anode region. Each pixel has a photoactive area of  $3 \times 7$  mm

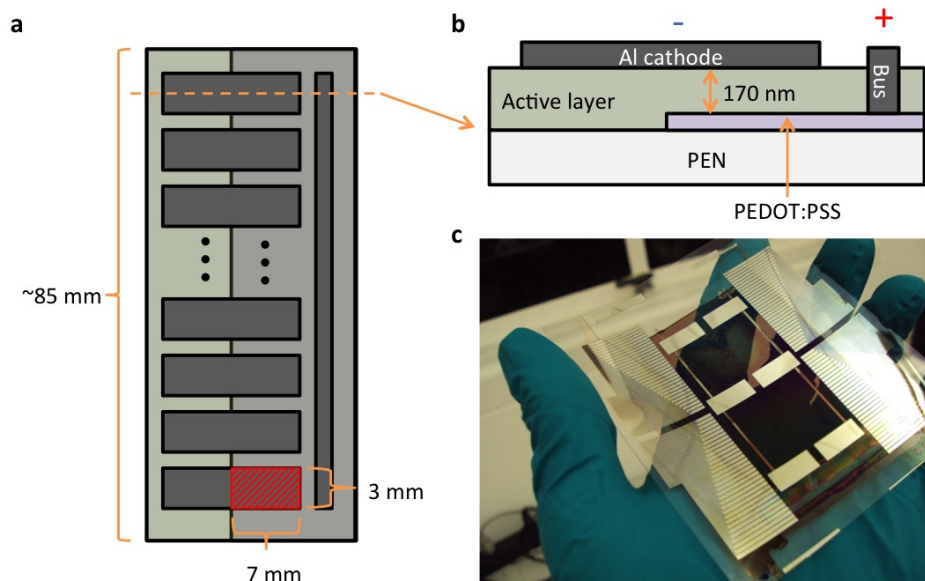


Figure 5.2: (a) Schematic view of a printed array of discrete organic photodiode (OPDs) with the photoactive area highlighted in red. (b) Cross sectional view of an OPD. (c) Photograph of a printed array of discrete OPDs.

per pixel, but multiple devices can be joined to enlarge this area by connecting cathodes in series. A bus line is printed on top of the active layer in close proximity to the photoactive area in order to reduce series resistance. Intra-pixel charge integration is not necessary for the operation of these devices since each pixel has a dedicated readout circuit. Since no photogenerated charge is needed to be capacitively stored, these devices are operated at short circuit (Bias = 0 V) since shot noise and other noise mechanisms from dark current are removed. A transimpedance amplifier, with a feedback resistance of  $R_F$  and open-loop gain of  $A_{OL}$ , is connected in series to the OPD, with a capacitance of  $C_I$ , in order to convert the instantaneous photocurrent signal into a voltage readable by an analog-to-digital converter (DAC). Transimpedance gain is set by the feedback resistance according to Equation 5.1. While the frequency response of the system increases with open-loop gain, it is limited by the capacitance of the OPD and feedback resistance as described by the expression for the corner frequency in Equation 5.2. For this reason, there is a direct trade-off between gain and bandwidth. The 1 kHz operation frequency of OPDs in oximeters necessitates a corner frequency of at least 5 kHz to obtain a square-like response from the OPD at 1 kHz. A feedback capacitor is added in parallel to the feedback resistance in order to remove resonance at this frequency. This addition flattens the frequency response of the transimpedance gain, eliminating any distortions. A picture of the final array is shown in Figure 5.2c.

$$\frac{V_{\text{Out}}}{I_{\text{OPD}}} = R_F \text{ (V/A)} \quad (5.1)$$

$$f_{\text{Corner}} = \frac{A_{OL} - 1}{R_F C_I} \text{ (Hz)} \quad (5.2)$$

### Red- and Infrared-Sensing Organic Photodiodes

OPDs capable of sensing red and infrared light are useful due to their facile integration with conventional LEDs used in commercial pulse oximeters. Polymeric donor and small molecule acceptor bulk heterojunctions (BHJs) are used as the active layer material. Due to the poor electron conductivity of polymeric acceptors and large band gap of fullerene molecules, a polymeric donor is chosen with a small band gap in order to absorb infrared light[175]. Figure 5.3a shows the structures of the two donor polymers and acceptors used to fabricate BHJ active layers for these devices. P3B and P2B both have the same backbone structure, based on 4,4'-difluoro-4-bora-3a,4a-diaza-s-indacene (BODIPY)-thiophene. However, the lengths of the alkyl side chains off of the thiophene units are two carbon units longer in P3B than P2B. Both of these polymers have absorption cutoffs around 900 to 100 nm, absorbing the emission of 850 nm from the infrared LED, and highest occupied molecular orbital (HOMO) and lowest unoccupied molecular orbital (LUMO) levels of -5.05 and -3.8 eV, respectively. Coulombic binding energy of excitons in organic materials is on the order of 500 meV[19]. PC<sub>71</sub>BM is chosen as an acceptor for these donors since the LUMO of -4.3 eV creates a 500 meV ionization potential with respect to the LUMO of the donor, which is sufficient to

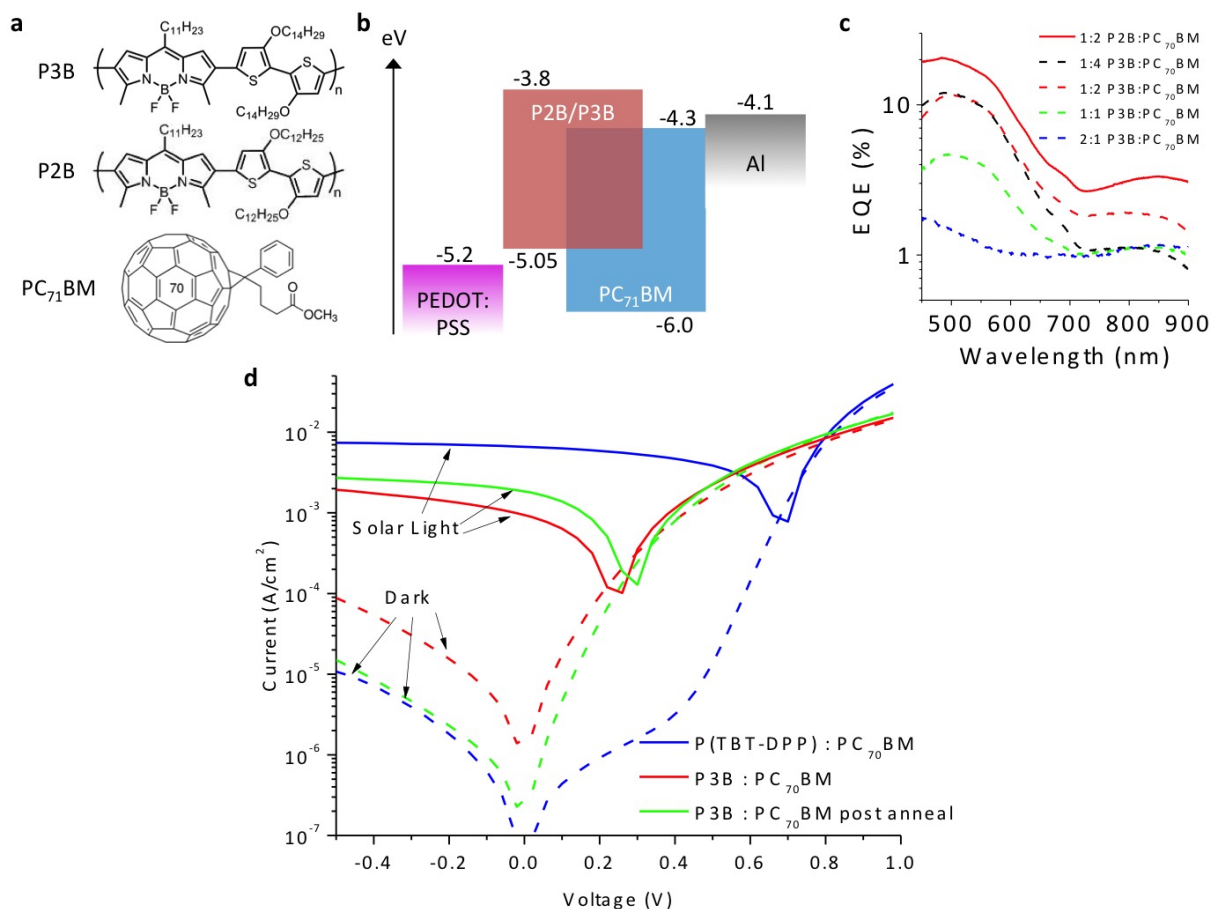


Figure 5.3: (a) Chemical structures of donor polymers (P2B and P3B) and acceptor (PC<sub>71</sub>BM) used to create infrared-sensing OPDs. (b) Band diagram of the OPD at flat band potential. (c) External quantum efficiency (EQE) spectra of various donor:acceptor wt. ratios dissolved in 1,2 dichlorobenzene and spin coated to form devices with the same band diagram as in (b). (d) Light and dark current-voltage characteristics of annealed and unannealed infrared OPDs processed in the same way as the devices in (c) in comparison to a high performance organic photovoltaic material system (P(TBT-DPP):PC<sub>71</sub>BM).

dissociate excitons generated in the donor from infrared light into free charge carriers. Even though PC<sub>60</sub>BM is more commonly available than PC<sub>71</sub>BM, the LUMO of -3.7 eV makes it energetically unfavorable for exciton dissociation. The flat band diagram of the OPD in Figure 5.3b shows the HOMO and LUMO levels of the donor and acceptor along with the work functions of the PEDOT:PSS anode and aluminum cathode. The work function of 5.2 eV of PEDOT:PSS is higher than the HOMO of P2B or P3B and the work function of aluminum is lower than the LUMO of PC<sub>71</sub>BM. These energy level alignments allow for

ohmic contacts with the majority carriers of the electrode and minimize injection of minority carriers.

With a suitable acceptor, anode, and cathode, the active layer is further optimized by determining the optimal donor-to-acceptor ratio to achieve the highest quantum efficiency. Figure 5.3c shows the quantum efficiency spectra of OPDs composed of BHJs with multiple P3B:PC<sub>71</sub>BM weight ratios. These devices were fabricated by spin coating solutions of the BHJ dissolved in 1,2 dichlorobenzene. OPDs of low donor concentrations with 2:1 and 1:1 P3B: PC<sub>71</sub>BM ratios exhibit EQEs of at most 2% in at 650 nm and 1.2% at 850 nm. Decreasing this ratio to 1:2 increases the EQE to 4% at 650 nm and 2% at 850 nm. Further decreasing this ratio to 1:4 maintains the same EQE in the red region but decreases in the infrared back down to 1.2%. The optimal performance of this BHJ with lower donor than acceptor weight concentrations suggests that the BODIPY-thiophene backbone structure of this donor polymer has some amorphous properties. Amorphous donor polymers such as PCDTBT require donor-to-acceptor ratios as high as 1:4 due to the absorption of PC<sub>71</sub>BM in the donor which does not crystallize and phase segregate into its own acceptor domain[164]. On the other hand, highly crystalline polymers such as regioregular poly(3-hexylthiophene-2,5-diyl) (P3HT) perform well for 1:1 ratios since acceptor is not easily trapped in the crystalline domains of the donor[28]. The full EQE spectrum of the OPD nearly doubles when P2B replaces P3B in the BHJ blend with the optimal donor-to-acceptor ratio of 1:2, reaching efficiencies of 7% and 3.5% at 650 nm and 850 nm, respectively. The shorter alkyl side chain lengths of the P2B polymer most likely decrease the size of PC<sub>71</sub>BM domains since donor polymers with long side chain lengths create larger domains of fullerene-based acceptors[127]. Larger domains translate into lower charge conversion efficiencies since the exciton must drift longer to find an interface at which to dissociate, increasing the probability of the exciton recombining with itself[136]. However, shorter side chain lengths also limit the solubility of the polymer, making the printing of thick films more difficult. Figure 5.3d shows the light and dark current-voltage plots of unannealed and post annealed (annealed after aluminum cathode evaporation) 1:2 P3B:PC<sub>71</sub>BM in comparison to a BHJ optimized for visible-light absorption, P(TBT-DPP):PC<sub>71</sub>BM[136]. The increase in light current by 50% at short circuit from post annealing P3B:PC<sub>71</sub>BM is indicative of the same increase in EQE. This improvement in efficiency along with higher open-circuit voltage in the photovoltaic region suggests that annealing causes the formation of a more favorable morphology that improves the efficiency of exciton dissociation at interfaces. The fill factor also improves by 10%, suggesting that carrier mobility is increased or recombination of free carriers is decreased. In addition to increased EQE, the dark current of this BHJ blend decreases after annealing, improving the detectivity of these OPDs. This decrease in dark current after thermal treatment is attributed to the reduction in minority carrier injection caused by the migration of acceptor and donor domains from the anode and cathode, respectively[28, 81].

The optimal donor polymer, donor-to-acceptor weight ratio, and annealing conditions determined from the optimization of spin-coated devices are used to create the printed

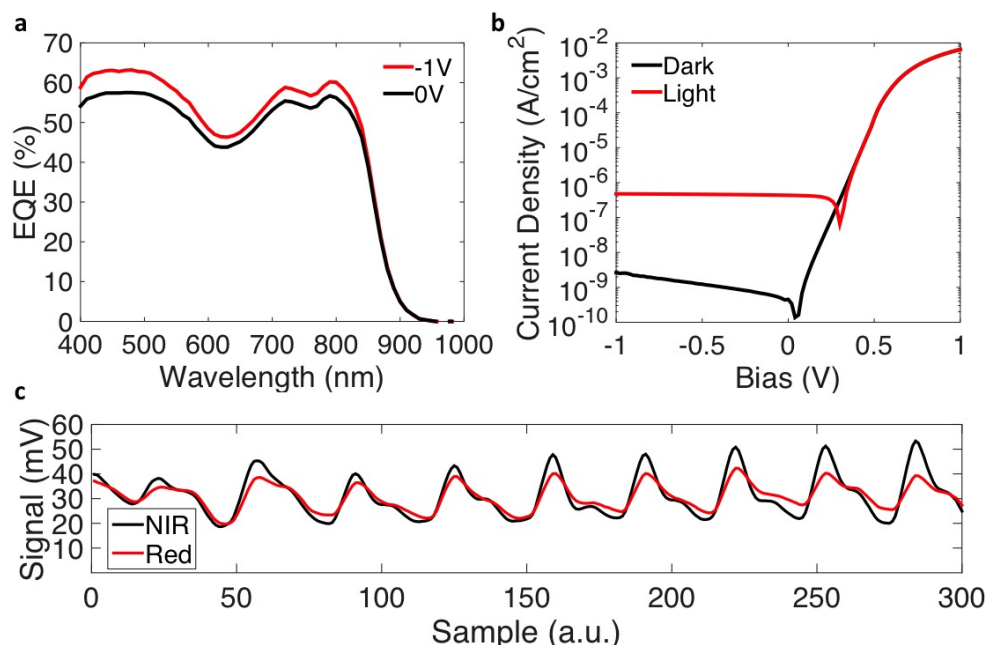


Figure 5.4: (a) EQE of a printed OPD using 1:2 P2B:PC<sub>71</sub>BM by weight dissolved in 2:1 chlorobenzene:1,2 dichlorobenzene by volume. (b) Light and dark current-voltage characteristics of the device in (a). (c) Transmission PPG measurement using near infrared (NIR) and red LEDs.

OPDs shown in Figure 5.2. Figure 5.4a shows the EQE spectrum of a printed OPD using 1:2 P2B:PC<sub>71</sub>BM at short circuit at a bias of  $-1$  V. A 1:2 ratio of 1,2 dichlorobenzene to chlorobenzene is used because the higher vapor pressure of chlorobenzene ensures a uniform deposited film that is mostly dried before it has a chance to dewet[137]. The residual amounts of low vapor pressure 1,2 dichlorobenzene do not cause noticeable dewetting but allow the blend enough time to properly crystallize before the film solidifies[142, 156]. The high EQE of 46% and 25% at 650 nm and 850 nm, respectively, is indicative of sufficiently small domains to induce efficient exciton dissociation. Additionally, a small increase in efficiency of less than 5% across the full spectrum at a bias of  $-1$  V proves that the mobility of the carriers is high and prevents a significant amount of free-carrier recombination[19]. These devices also have dark currents as low as  $2$  nA/cm<sup>2</sup> at a bias of  $-1$  V as seen from the light and dark current measurements. Using this device, pulse oximetry measurements were taken with red and infrared LEDs as shown in Figure 5.4c. The high EQE of these devices and the high transmittance of Hb and HbO<sub>2</sub> in the red and infrared region results in a strong signal from which heart rate and SaO<sub>2</sub> can be easily extracted.

### Green- and Red-Sensing Organic Photodiodes

In addition to red- and infrared-sensitive OPDs, OPDs optimized for green- and red-sensitivity were created in order to be compatible with high performance OLED emitter materials. A green-emitting OLED with a central wavelength of 550 nm is chosen because the difference in molar absorption coefficients of Hb and HbO<sub>2</sub> at this wavelength is comparable to that at 850 nm[114]. Since the OPD doesn't need absorption in the infrared, a wider range of high performance donor polymers optimized for photovoltaics devices with high EQEs is available. As seen in the band diagram of Figure 5.5a, PTB7 is chosen as the donor polymer since BHJ blends of this material with PC<sub>71</sub>BM exhibit high EQEs across the visible spectrum[106]. The HOMO of -5.15 eV for PTB7 makes ohmic contact with the PEDOT:PSS anode at a work function of 5.2 eV. While a PTB7:PC<sub>71</sub>BM ratio of 1:1.5 yields the best

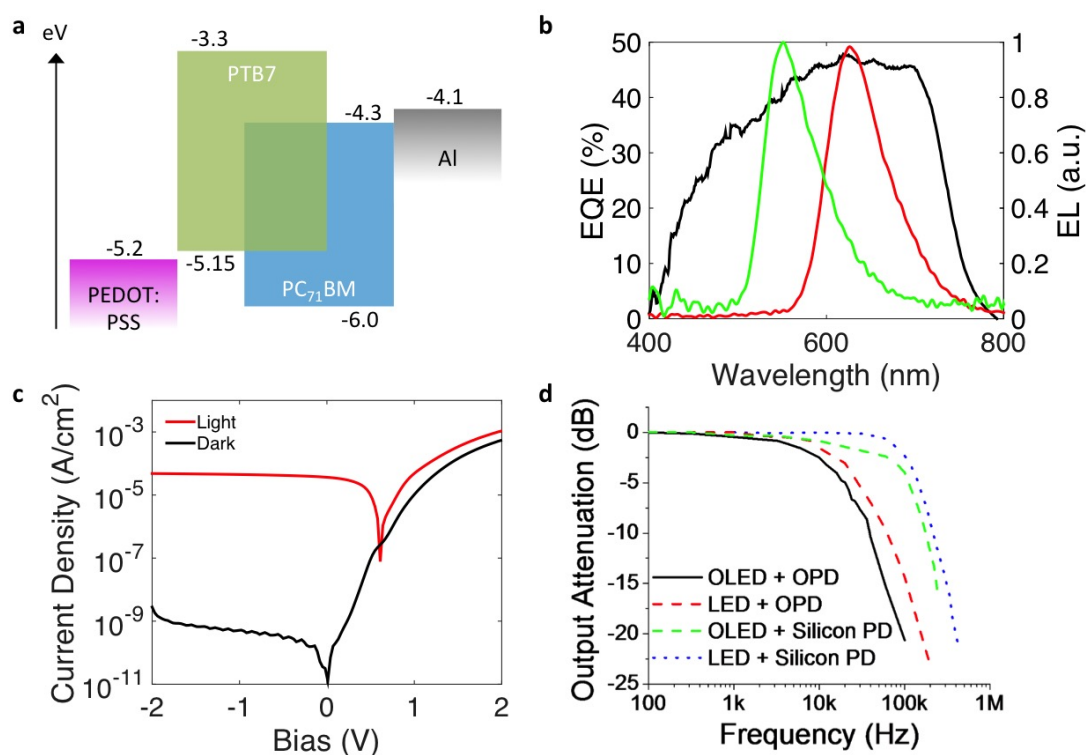


Figure 5.5: (a) Band diagram of PTB7:PC<sub>71</sub>BM (donor:acceptor) OPD at flat band potential. (b) EQE of the printed OPD in (a) cast from 95:5 chlorobenzene:1,8-diiodooctane by volume in relation to the electroluminescent (EL) spectra of the green and red organic light emitting diodes (OLEDs). (c) Light and dark current-voltage characteristics of the device in (a). (d) Attenuation of sine-modulated light dependence on frequency for various LED/OLED and silicon photodiode (PD)/OPD combinations.



photovoltaic performance[107], the effect of blend ratio and thickness on red and green EQE and dark current is examined in order to optimize OPD performance. Testing devices were fabricated by spin coating PTB7:PC<sub>71</sub>BM onto the PEDOT:PSS anode. BHJ blends with 1:1 donor-to-acceptor ratios demonstrate the highest EQEs of 30% and 25% at 550 nm and 625 nm, respectively, with 1:1.5 and 1:5 ratios showing monotonically decreasing efficiencies. Devices with thicker active layers also have lower dark currents and absorb more light to create higher EQE. 1,8-Diiodooctane (DIO) is used with a 3 vol. % additive concentration in chlorobenzene in order to improve absorption and drive donor-acceptor phase segregation in order to drive crystallization to increase carrier mobility and minimize free carrier recombination[195]. Additionally, DIO has been found to reduce dark current in PTB7:PC<sub>71</sub>BM photovoltaic devices[69], improving OPD detectivity.

The EQE spectrum of the printed OPD using the optimal donor-to-acceptor ratio of 1:1 and 3 vol. % DIO in relation to the electroluminescent spectra of the green and red OLEDs is shown in Figure 5.5b. The OPD biased at short circuit yields quantum efficiencies of 38% and 46% at 550 nm and 625 nm, respectively. Figure 5.5c shows the light and dark current of the same device, with dark currents below 1 nA/cm<sup>2</sup> below a bias of -2 V. The negligible increase in photocurrent from short circuit to reverse bias is indicative of good carrier transport and minimal free-carrier recombination[136]. The frequency response of photocurrent from a photodiode biased at short circuit for sine-modulated light is shown for LED and OLED sources and OPD and silicon photodiode received in Figure 5.5d. Silicon photodiodes and LEDs show the highest 3-dB cutoff frequency ( $f_{3dB}$ , reference Chapter 1 for definition) of 120 kHz. A similar  $f_{3dB}$  of 90 kHz is found when an OLED is used to modulate the silicon photodiode, which is indicative of a frequency response that is limited by the photodiode. The combination of LED emitter and OPD received results in a substantially lower  $f_{3dB}$  of 20 kHz. The similar capacitance of the OPD, 3.6 nF, to that of the silicon photodiode, 4.3 nF, means that  $f_{3dB}$  does not decrease as the result of a low-pass filter induced by the photodiode according to Equation 5.2. Instead, it is speculated that the rate of carrier extraction from the BHJ is a limiting factor in the high frequency performance. The full organic systems of OLED and OPD shows an  $f_{3dB}$  of 12 kHz. This cutoff frequency is substantially higher than the 1 kHz operation of the OLEDs and OPD, indicating these devices are suitable for PPG measurements.

The integration of the OLEDs and OPD for the all-organic pulse oximetry system is shown in Figure 5.6a. Parasitic photodetector current is a contributor to failure in pulse oximetry[174]. As such, the OPD is wrapped around the bottom of the finger to minimize photocurrent from ambient light in order to achieve the best PPG signal. The effects of ambient light on the OPD short-circuit current were measured using two finger phantoms with radii of 9 and 5 mm, which are representative of the range of human finger sizes. Under typical room-lighting conditions of 72-76  $\mu\text{W}/\text{cm}^2$ , flexing the OPD around the 9 and 5 mm radii phantoms as opposed to not bending the device reduces the parasitic current from 270 to 20 nA and 280 to 60 nA, respectively. The conformability of the OPD on



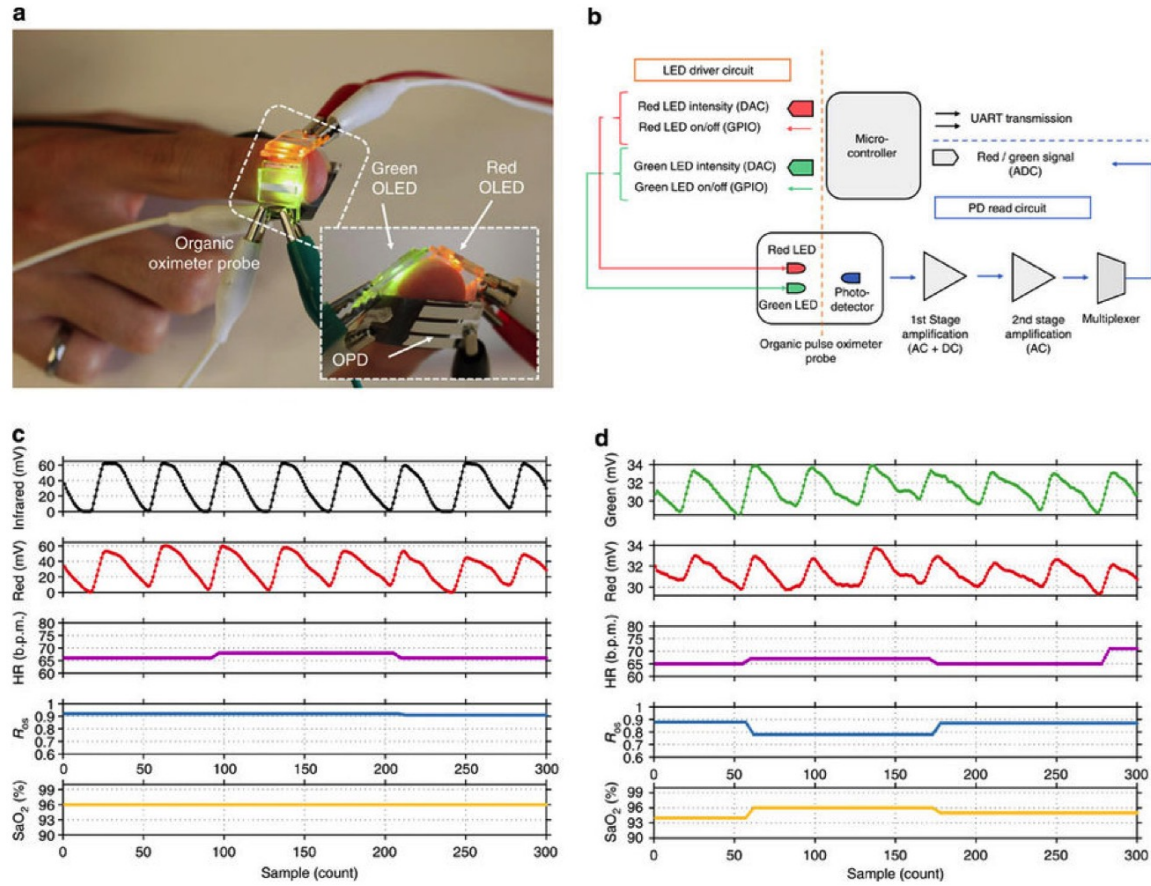


Figure 5.6: (a) Measurement setup of transmission-mode pulse oximetry using all-organic devices. (b) System schematic diagram for driving and reading the oximeter. (c) Reference PPG measurement using LEDs and a silicon PD with the calculated heart rate and blood oxygen saturation ( $\text{SaO}_2$ ). (d) PPG measurement using all-organic devices with the calculated heart rate and  $\text{SaO}_2$ . Reprinted with permission from [114]. Copyright 2014 Nature Publishing Group.

the body thus improves the SNR of the PPG and minimizes motion artifacts. Figure 5.6b shows the system schematic used to drive the OLEDs and readout the OPD current. The OPD current passes through an initial transimpedance amplification stage which converts both time-variant and invariant photocurrent into a voltage according to Equation 5.1. The second gain stage filters out the time-invariant signal but amplifies the time-variant signal in order to extract heart rate and  $\text{SaO}_2$  before being read by an ADC. Figures 5.6c and d show the measured PPG signals and interpreted data for a conventional inorganic-based oximeter and the all-organic system shown in Figure 5.6a, respectively. The lower EQE of the OPD and irradiance of the OLEDs compared to the inorganic pulse oximeter system

results in signals strengths that are an order of magnitude lower than the inorganic system. Despite the lower signal, the measured heart rate and  $\text{SaO}_2$  from both of these probes systems are similar, both indicating 65-70 beats per minutes (bpm) and 94-96%, respectively.

## Reflectance Pulse Oximetry with Addressable Organic Photodiode Arrays

Reflectance-based pulse oximetry enables the measurement of  $\text{SaO}_2$ , pulse, and tissue oxygenation from many more positions on the body than possible with transmission-mode oximetry. In addition, arrays of reflectance-based pixels can map tissue oxygenation to assess the healing of tissue after surgery. However, the low percentage of light that is reflected back through the skin in comparison to what is transmitted necessitates larger pixels in order to capture more light to generate a signal with sufficient SNR. In addition, OPD pixels need to be placed in close proximity to OLED pixels in order to obtain the highest possible flux of reflected light. It is found that the optimal spacing between OLED and OPD is between 3 to 7 mm. As a result of the close proximity of these devices and need for arrays, architectures with addressable arrays of pixels through interconnects on substrate need to be implemented.

Figure 5.7a shows the fabrication process of a four-pixel OPD array using a single OLED pixel, which can be split into two halves to enable two different emissions needed for  $\text{SaO}_2$  measurements. Prior to the first step, a PEDOT:PSS anode is coated on a flexible substrate followed by blade coating of the BHJ photoactive layer. A dielectric film of approximately 10  $\mu\text{m}$  thickness is screen printed on top of the photoactive layer with openings that define the photoactive area of the OPD. As with the discrete array discussed in Figure 5.2, this array also has a common anode for all pixels. Silver interconnect lines are then screen printed on top of the dielectric in close proximity to the photoactive areas (openings) to route the signal from the cathode of each pixel to output contacts at the edge of the array. Screen printing the interconnects on the dielectric prevents shorting to the underlying PEDOT:PSS anode. The OPD is completed by evaporating the aluminum cathode over the defined photoactive area and interconnect line in order to provide a connection from the pixel to the output contacts. Cutting a hole through the center of the OPD array defines the OLED emission area.

A broadband polymeric donor is used that absorbs in the green (550 nm), red (625 nm), and infrared (850 nm) emission regions previously used for measuring  $\text{SaO}_2$ . The large area of the pixels ( $\simeq 1 \text{ cm}^2$ ) and non-modularity of the pixels necessitates BHJ active layers with minimal defects and shunt pathways that decrease device yield. The choice of solvent for the BHJ is investigated since this influences film quality and device performance. BHJ blends with a 1:2 ratio of Donor:PC<sub>71</sub>BM dissolved in chlorobenzene at show poor solubility at a concentration of 20 mg/ml, resulting in poor device yield. The solubility of the

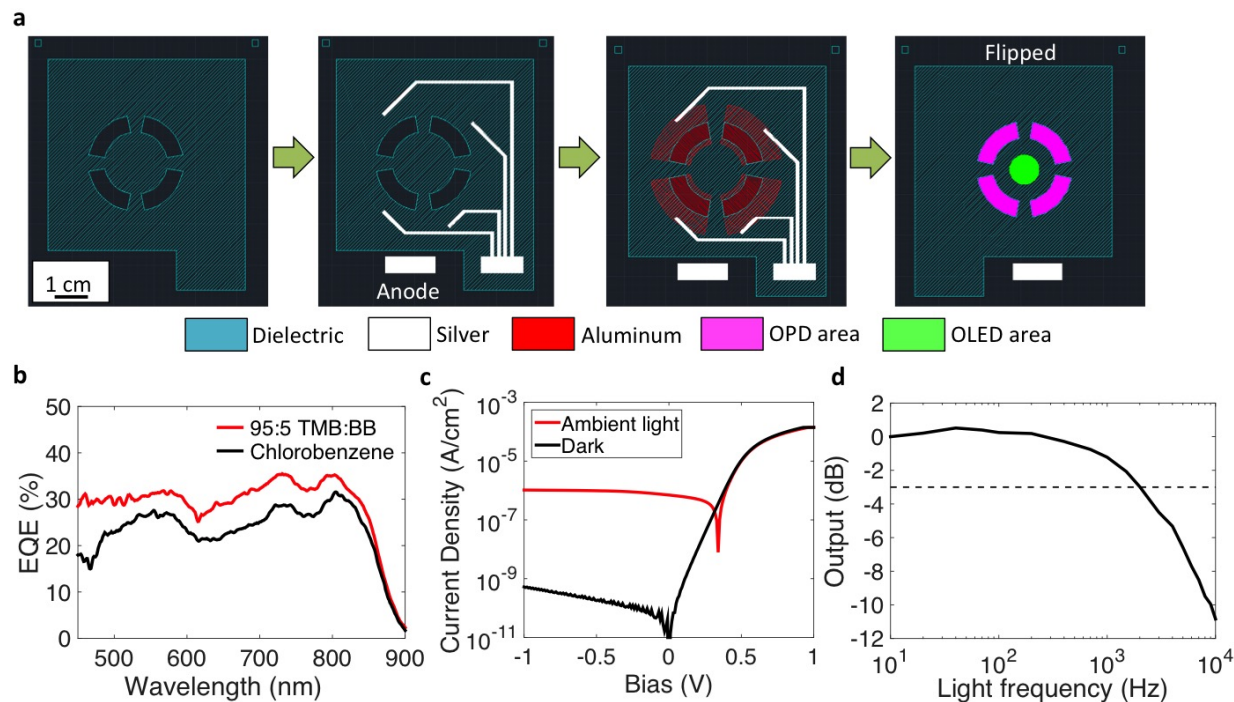


Figure 5.7: (a) Fabrication process for a four-pixel OPD module for reflectance-mode pulse oximetry. (b) EQE spectrum of a BHJ blend of 1:2 donor polymer:PC<sub>71</sub>BM by weight dissolved in 95:5 1,2,4-trimethylbenzene (TMB):benzyl benzoate (BB) by volume. (c) Light and dark current-voltage characteristics of a sample pixel in (a). (d) Signal attenuation of an OPD pixel as a function of the frequency of a sine-modulated light source.

BHJ is significantly improved in 1,2,4-trimethylbenzene (TMB) with additive concentrations of benzyl benzoate (BB), giving significantly smoother films than the previous formulation casted under the same conditions. Figure 5.7b shows EQE measurements at short circuit of OPD pixels from the array design in Figure 5.7a for BHJ films cast from the previously mentioned solvents for a 1:2 ratio of Donor:PC<sub>71</sub>BM at 20 mg/ml to yield the same photoactive layer thickness. For the same thickness, the active layer cast from 95:5 TMB:BB shows a 5% improvement in EQE over the film cast from chlorobenzene. This improvement is likely a result of the high boiling point BB additive (323°C) increasing absorption and charge carrier mobility of this film, similar to the effect of DIO on PTB7:PC<sub>71</sub>BM blends[69].

Figure 5.7c shows the dark and light current-voltage characteristics for the printed OPD array cast from a 95:5 ratio of TMB:BB. The dark current remains below 1 nA/cm<sup>2</sup> at a bias of -1 V and a high shunt resistance of 1.92 GΩ·cm<sup>2</sup>, yielding a noise-equivalent power (NEP) of  $2.28 \times 10^{-14} \text{ W}/\sqrt{\text{Hz}}$  or specific detectivity of  $4.38 \times 10^{13} \text{ cm} \cdot \sqrt{\text{Hz}}/\text{W}$  when biased at short circuit. Despite the high detectivity, there are several issues with this array design that

prevent it from being implemented in a pulse oximeter application. The first issue is that the  $f_{3dB}$  of these pixels is 1 kHz as seen from Figure 5.7d, which means that at least 70% of the photocurrent signal from the photodiode is cutout at the output of the transimpedance amplifier. This attenuation is believed to be the result of the overlap between the common anode and interconnects on the surface of the dielectric adding to the capacitance of the photodiode. Another problem is that the contact resistance between the aluminum cathode on the dielectric and photoactive layer is highly dependent on the thickness of the dielectric layer. This results in inconsistent device yields between batches of arrays. The final issue is that the large unpatterned anode creates a significant amount of noise when the array is placed on the skin as a result of capacitive coupling to tissue. This noise significantly decreases the SNR of the PPG to the point of obfuscation. As a result, an array architecture using alternative patterning techniques and with the minimum amount of anode area is needed in order to eliminate these problems.

An array of OPDs designed for integration with an array of OLEDs to perform reflectance-based pulse oximetry is designed. Figure 5.8a provides a schematic of the array, showing the regions of PEDOT:PSS anode, aluminum cathode and screen printed interconnects. Using the surface energy patterning technique discussed in Chapter 2, the anode is patterned to be the same size as the photoactive area with a little overlap to the left side in order to enable contact to the interconnects. The reservoir at the top of the array for PEDOT:PSS ensures a uniform distribution of ink on the blade prior to blade coating, improving the anode pattern fidelity. Following blade coating of the BHJ layer on top of the anodes, silver interconnect lines are screen printed in top of the array with separate lines for each anode and cathode in every pixel. The screen printed silver ink formulation shorts through the BHJ layer and makes an ohmic contact to the underlying PEDOT:PSS electrode. Finally, aluminum is thermally evaporated on top of the photoactive area with an overlap to the right to make contact to the interconnects. The cathode is deposited after screen printing since the pressure of the screen on the top electrode may increase the probability of shorted devices. OLEDs are placed interdigitated with the OPD array to enable the reflectance pulse oximetry system.

The EQE spectrum of each pixel in the array measured at short circuit is shown in Figure 5.8b color coded to the row position as indicated in Figure 5.8b. Pixels at the bottom row of the array exhibit EQEs of  $\simeq 25\%$  throughout the visible spectrum. This value increases to  $\simeq 30\%$  and  $\simeq 35\%$  moving up to the third and second rows, respectively. This gradual increase in EQE is a result of the tapering thickness of the BHJ caused by the blade coating process as the ink is coated from the top to bottom of the array, causing less absorption in the lower rows. However, the thickness of the PEDOT:PSS also tapers off from top to bottom. The PEDOT:PSS anode in the first row is thick enough to absorb a significant amount of light, especially in the infrared, decreasing the EQE of the OPD as seen in Figure 5.8b. The dark current-voltage characteristics of each pixel in the array is shown in Figure 5.8c. No positional dependence is found on the dark current under reverse bias or equivalent shunt resistance at short circuit. Instead, the dark current and equivalent shunt resistance are higher

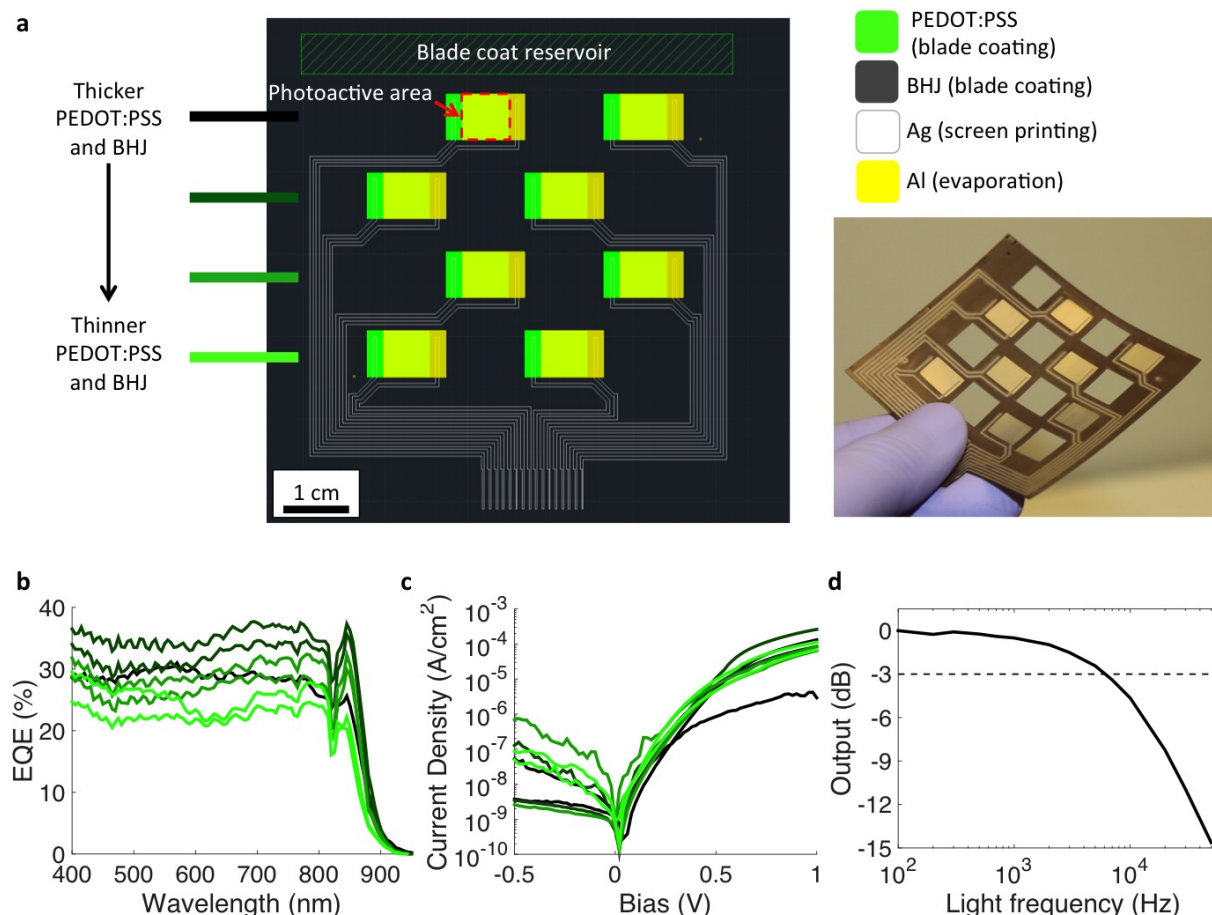


Figure 5.8: (a) Schematic and picture of an eight-OPD pixel array for reflectance-mode pulse oximetry. (b) EQE spectra of the pixels in the array color coded according to row position in (a). (c) Dark current-voltage characteristics of the OPDs in the array color coded according to row position. (d) Signal attenuation of an OPD pixel as a function of the frequency of a sine-modulated light source.

on pixels with visible defects in the BHJ film or underlying PEDOT:PSS electrode. Despite these defects, the highest measured equivalent shunt resistance measured at short circuit, which is used in pulse oximetry mode, is  $2.1 \text{ M}\Omega$  and results in a NEP of  $9.9 \times 10^{-13} \text{ W}/\sqrt{\text{Hz}}$  or specific detectivity of  $7.1 \times 10^{11} \text{ cm} \cdot \sqrt{\text{Hz}}/\text{W}$  that is sufficient to resolve the pulsatile irradiance of  $\simeq 10 \text{ nW}/\text{cm}^2$ . The patterned anode enables low-noise PPG measurements as a result of the reduced capacitive coupling to tissue and a higher  $f_{3\text{dB}}$  of 7 kHz compared to the array design in Figure 5.7a. The absence of dielectric-patterned photoactive areas simplifies the fabrication process and improves the reliability of ohmic contacts to OPDs.

### 5.3 Addressable Organic Thin Film Transistors & Phototransistor Arrays for Image Sensing

Interconnects are essential to drive array elements, such as OTFTs and photodetectors, and readout their signals. It is equally important to address these arrays in a way that requires the least amount of interconnects to external circuitry. This section investigates the use of screen printed interconnects for creating row-addressable OTFT and OPT arrays capable of synchronous readout from column lines. The optimization of screen printing to enable these arrays with applications in image sensing is demonstrated.

#### Optimization of Screen Printed Interconnect Lines & Contact Pads on Discrete Devices

Interconnects and contact pads are screen printed on top of discrete devices, and as such require printing optimization for the top layer of these devices. This layer is the BHJ active layer for OPDs and amorphous fluoropolymer (AF) gate dielectric for OTFTs and OPTs. The surface energy of the substrate is an important consideration for any printing process and is first examined. Figure 5.9a and b show silver screen printed on polyethylene terephthalate (PET) and plasma-treated AF, respectively. The hydrophilic surface energy of PET, with a water contact angle and surface energy of  $72.5^\circ$  and  $39 \text{ mN/m}$ , respectively, results in an overflowing of the silver ink with respect to the intended pattern fidelity. This spreading limits the resolution and proximity of features that can be printed on PET. On the other hand, the pattern fidelity of the silver ink printed on plasma-treated AF is quite high owing to the low water contact angle of  $117^\circ$  that prevents spreading. The high viscosity of the silver paste also prevents dewetting on the hydrophobic substrate. Non-treated AF has a slightly higher contact angle of  $121^\circ$  and surface energy of  $17\text{-}19 \text{ mN/m}$ [102] but results in some pattern dewetting.

Snap-off distance (SOD), the gap between the relaxed screen and substrate, also influences the quality of the printed film. Figures 5.9c and d are micrographs of silver ink printed into column lines on plasma-treated AF using a SOD of  $0.4 \text{ mm}$  and  $1.6 \text{ mm}$ , respectively. For low SOD, the screen remains on the substrate even after the squeegee has passed as a result of the surface tension of the paste. This bondage to the substrate results in the observed spattering in Figure 5.9c once the screen is lifted away from the substrate at the end of the print, which increases the probability of shorted adjacent features. On the other hand, increasing the SOD to  $1.6 \text{ mm}$  significantly minimizes this spattering effect. A larger SOD increases the tension in the screen, causing it to slowly peel off the substrate after the squeegee has passed and before the screen is moved away from the substrate after printing is complete. A larger SOD also applies less pressure on the substrate during printing and maximizes device yield. A screen printed crossover test structure consisting of vertical and



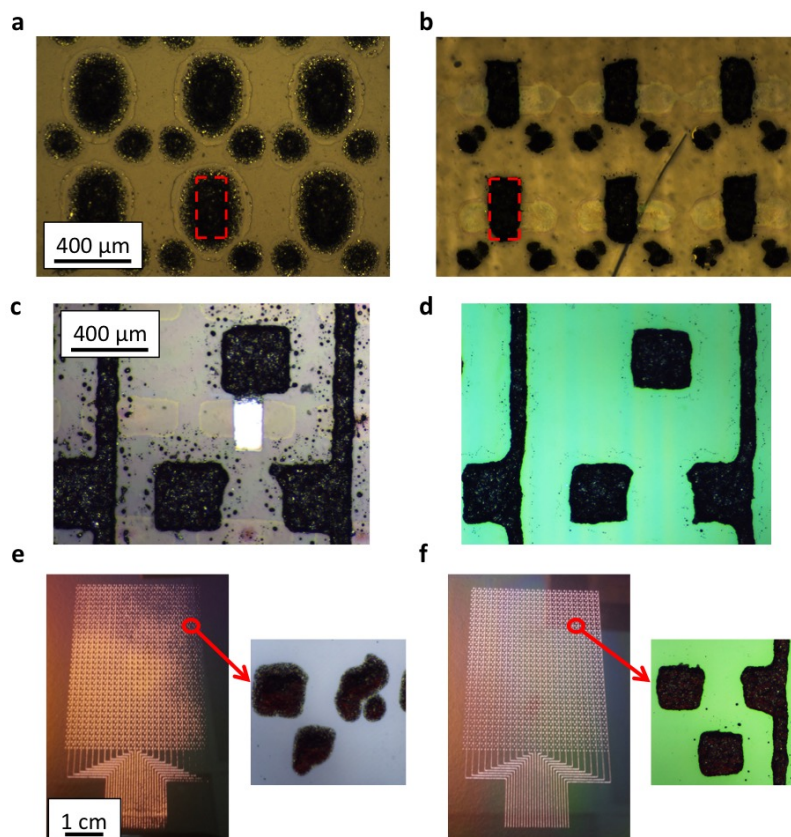


Figure 5.9: Screen printed silver paste on polyethylene terephthalate (PET) (a) and plasma-treated amorphous fluoropolymer (AF) (b). Screen printed silver on plasma-treated AF with a snap-off distance (SOD) of 0.4 mm (c) and 1.6 mm (d). Screen printed features from a screen with a significant amount of drying (e) and negligible amount of solvent evaporation (f).

horizontal silver lines and dielectric separator layer are used to assess the reliability of array interconnects. A SOD of 0.4 mm used for depositing the top conductive trace resulted in shorts for all measured crossovers. However, using 1.6 mm gave good reliability, with no observed shorting or noticeable leakage current for all ten measured crossovers with a bias of 20 V.

Drying of the ink in the screen is a practical concern when printing small feature sizes ( $< 1\text{mm}$ ). Fresh ink from the top of the screen can no longer transfer since dried ink clogs up openings in the emulsion. This effect is more noticeable where ink solvent evaporates more quickly; in smaller patterns or features near the edges as seen in the photographs of Figure 5.9e. Quickly flooding the screen after each print, the phase at which ink solvent evaporates

most quickly in the screen, and minimizing the time between prints mitigates these issues and results in large-area uniformity and good pattern fidelity as seen from Figure 5.9f. Features around the perimeter of an array also slow down the rate of evaporation at the edges of the array.

The screen printing process must not only be compatible with the devices onto which features are printed, but it also must not degrade device performance. Screen printing is compatible with OTFTs and OPTs since the solvents in the silver and dielectric pastes are insoluble in AF and the necessary thermal annealing steps for the interconnects can be used to improve crystallization of the high mobility semiconductor in the channel. On the other hand, screen printing contact pads for the all-printed OPDs in Chapter 3 degrades device performance by increasing the dark current at  $-5$  V bias by a factor of  $\simeq 300$  as shown in Figure 5.10a. This increase in leakage is most likely the result of the solvent of the dielectric or silver being absorbed by PEDOT:PSS and changing the injection properties of the anode.

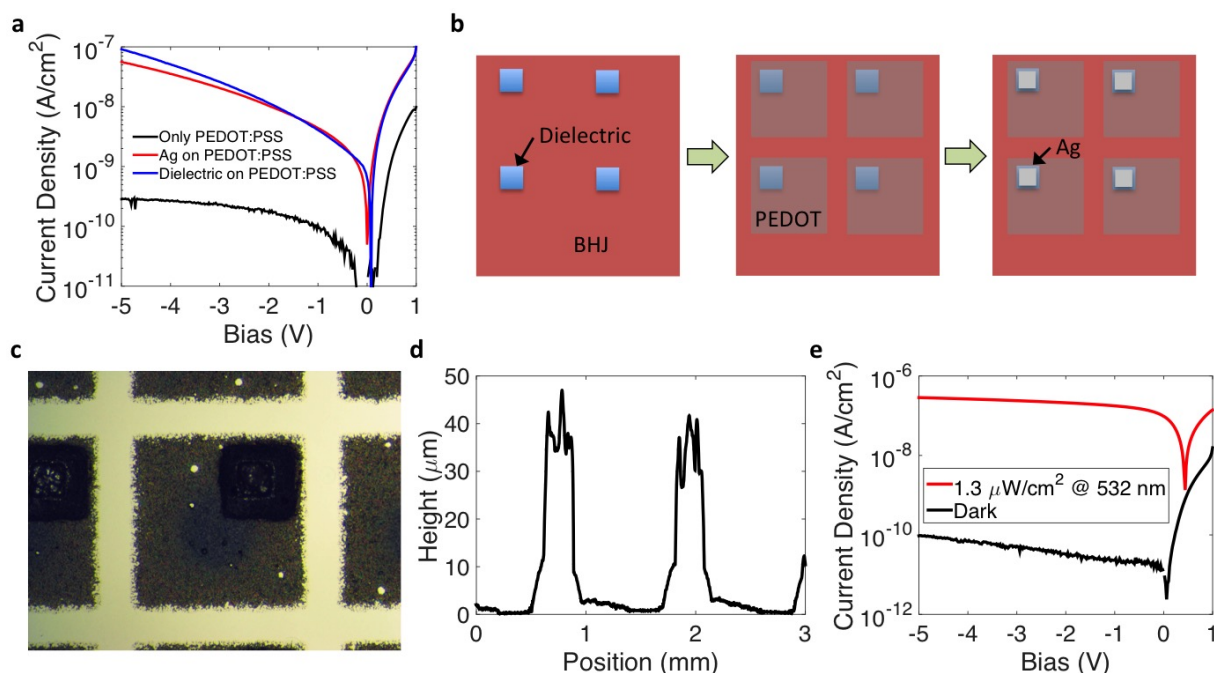


Figure 5.10: (a) Dark current-voltage characteristics of an all-printed OPD (reference Chapter 3) with and without dielectric or silver paste printed on the PEDOT:PSS anode. (b) Screen printing process on top of the BHJ active layer in order to create contact pads for OPD pixels without degrading device performance. (c) Optical micrograph of the final all-printed OPD with a contact pad. (d) Cross sectional profile of the contact pad. (e) Light and dark current-voltage characteristics of the pixel with contact pad.



To circumvent this issue, a dielectric patch is first screen printed on the BHJ layer prior to screen printing PEDOT:PSS. After printing the anode, silver is screen printed on area where dielectric was deposited as shown in a micrograph of the final structure in Figure 5.10c. The contact pad can be as tall as  $30\text{ }\mu\text{m}$  by screen printing silver multiples times as shown in the cross sectional profile of a pixel in Figure 5.10d. By screen printing silver on PEDOT:PSS with an underlying dielectric patch, a low dark current of  $100\text{ pA/cm}^2$  is achieved in reverse bias as seen from Figure 5.10e that is on par with this device without contact pads[137].

## Addressable Organic Thin Film Transistor Arrays

The optimal screen printing techniques discussed in the previous section are applied to the creation of addressable OTFT arrays. Figure 5.11a shows the schematic for the array of these devices. Photographs of the array are shown in Figures 5.11b and c. A device pitch of  $1.2\text{ mm}$  is used in the horizontal and vertical direction instead of the pitch of  $0.6\text{ mm}$  for the

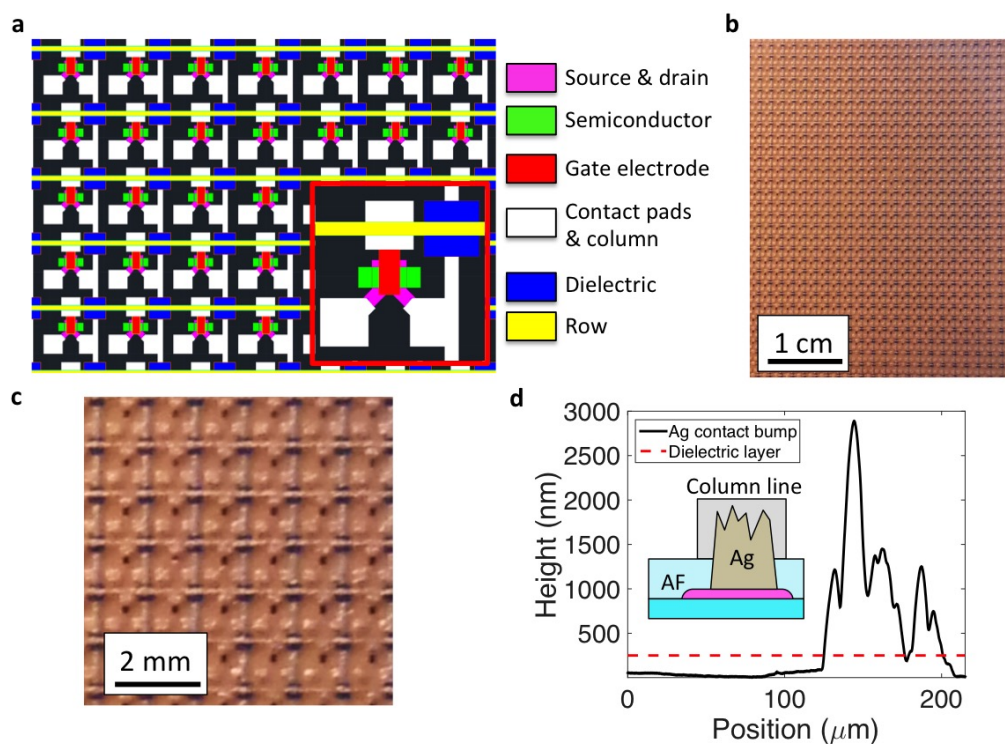


Figure 5.11: (a) Schematic of organic thin film transistor (OTFT) array. (b),(c) Photographs of an array of OTFTs with screen printed interconnects. (d) Cross sectional profile of inkjet printed silver nanoparticle contact bump on a source-drain electrode used to create a conductive via through the gate dielectric (height shown by red dashed line).

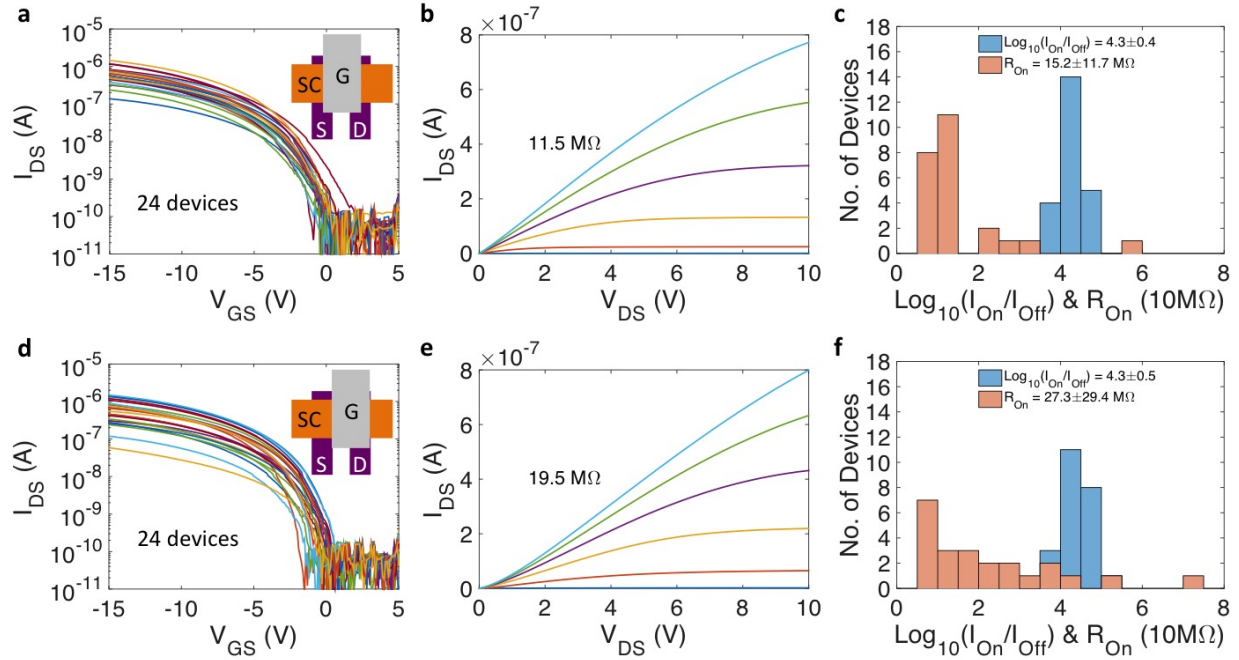


Figure 5.12: (a) Transfer characteristics for OTFTs in the array with sufficient gate-source overlap. (b) Output characteristic of a sample device from (a). (c) Histogram of contact resistance ( $R_{On}$ ) and  $\text{Log}_{10}(I_{On}/I_{Off})$  for the devices in (a). (d) Transfer characteristics for OTFTs in the array with insufficient gate-source overlap. (e) Output characteristic of a sample device from (d). (c) Histogram of  $R_{On}$  and  $\text{Log}_{10}(I_{On}/I_{Off})$  for the devices in (d).

discrete OTFTs in Chapter 2 in order to make room for row and column interconnects. The first printed layer is the column line, which deposits a contact pad on the source electrode and contact pads connecting all the drains of OTFTs in the same column. As mentioned in Chapter 2, contact bumps comprised of inkjet printed silver nanoparticles are also deposited at the base of the source-drain electrodes. These bumps are several  $\mu\text{m}$  in height, far taller than the thickness of the AF dielectric layer covering these electrodes and semiconductor as shown for the cross sectional profile of the silver contact bump in Figure 5.11d. Consequently, screen printing contact pads on top of these bumps provides a conductive via to the underlying source-drain electrodes. Following this, a dielectric patch is screen printed over the column line where the row line will intersect to prevent shorting of these lines. Wider patches are preferable in order to account for imprecise alignment and spreading of silver ink on top of the dielectric. Finally, the row line is printed directly on top of the dielectric and connects to the gate electrode. The anneal steps necessary to bake the electrodes serve as a post-anneal for the OTFT devices, which has been shown to improve mobility and on-off ratio in Chapter 2.

Multiple devices are measured in the array by driving the gate voltage ( $V_{GS}$ ) through the row line and reading out the drain current ( $I_{DS}$ ) through the column line with the source at ground. Two sets of 25 OTFTs are characterized; one with adequate source-gate overlap and the other with a certain degree of underlap. This source-gate overlap influences the contact resistance ( $R_{On}$ ) of the device, which slows down the readout and reset speed of photodiode-based image sensor pixels[65, 166]. Of the 50 measured devices, two failed to exhibit transistor behavior due to a failed connected to a drain contact bump and a shorted gate to source electrode. Figure 5.12a shows the transfer characteristics of devices with sufficient gate-source overlap, all of which exhibit similar threshold voltage and on-off ratio. The output characteristic of a typical OTFT in Figure 5.12b shows an  $R_{On}$  of  $11.5\text{ M}\Omega$  at  $V_{GS}$  of  $-15\text{ V}$ . The mean  $R_{On}$  and  $\text{Log}_{10}(I_{On}/I_{Off})$  are  $15.2\text{ M}\Omega$  and 4.3, respectively. The transfer characteristics of the devices with more gate-source underlap in Figure 5.12d show a similar range of threshold voltages with a slightly steeper subthreshold slope. The output plot of a typical device in Figure 5.12e demonstrates the effect of this underlap on the contact resistance. While this device has higher saturation current than the device with more overlap in Figure 5.12b, the contact resistance in the linear regime is nearly double, at  $19.5\text{ M}\Omega$ . Figure 5.12f shows that, in comparison to the overlap device performance distribution in Figure 5.12c, the contact resistance exhibits not a shift but more of a spreading that can make it more difficult to design circuits. However, the mean  $\text{Log}_{10}(I_{On}/I_{Off})$  is the same as for the overlap devices, at 4.3, which implies gate-source overlap has no effect on on-off ratio.

## Addressable Organic Phototransistor Image Sensor

OPT-based pixels analyzed in Chapter 4 are connected through the same screen printing technique discussed in the previous section to form an image sensor. The fabrication process, as shown in Figure 5.13a, first starts by plasma-treating the substrate to improve the wettability of silver ink on AF followed by screen printing of the row lines to readout discharge from the drain electrode and bias lines for the capacitor in series with the source electrode (reference Chapter 4 for background information on these pixels). A dielectric patch is then printed in order to cover the row and bias lines to prevent shorting to the column line used to control charge integration via the gate electrode. Figure 5.13b provides an overview of the final array design, with insets showing the contact bump via and row-column crossover. Screen printing separate metal and dielectric layers on top of a discrete array of pixels circumvents the issues of using high resistance source-drain electrodes and large overlap capacitance from the gate dielectric for array interconnects. The sheet resistance of the screen printed lines,  $0.1\text{ }\Omega/\square$ , and address-read line overlap capacitance,  $0.2\text{ nF}/\text{cm}^2$ , are far lower than those of the printed source-drain electrodes and gate dielectric,  $1\text{ k}\Omega/\square$  and  $10.6\text{ nF}/\text{cm}^2$ , respectively.

A micrograph of the fully assembled image sensor and circuit diagram depicting addressing (row) and readout (column) are shown in Figure 5.13c. An external charge amplifier is

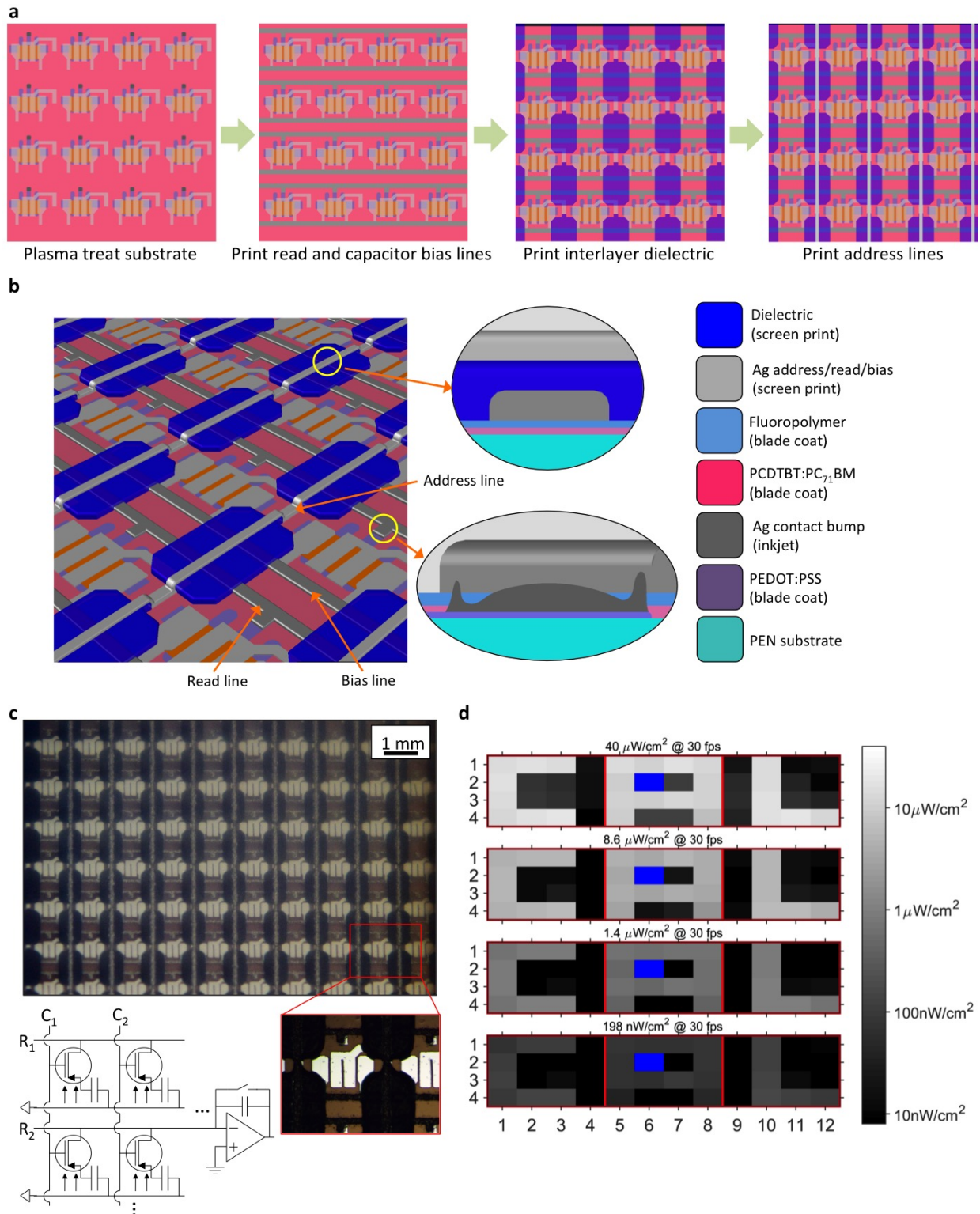


Figure 5.13: (a) Fabrication process for screen printed interconnects on organic phototransistor (OPT)-based pixels. (b) Zoomed-in view of interconnect lines on the image sensor. (c) Photograph of the imager and equivalent circuit diagram. (d) Images taken by the imager at various irradiances.

used to readout the pixel discharge for each row as the charge integration and discharge is controlled via the column line. Image quality is characterized by projection-based images of three letters imaged on separate  $3 \times 3$  sub arrays. Figure 5.13d shows the images taken at various background lighting intensities at 30 fps calibrated according to the dynamic response of these pixels measured in Chapter 4 (reference Figure 4.12a). The photoresponse nonuniformity, which is the ratio of standard deviation to mean integrated charge for illuminated pixels in the array[65], is 19% at  $198 \text{ nW/cm}^2$  and 15% for higher irradiances. This low variability results in good uniformity within both illuminated and dark regions.

## 5.4 Conclusion

OPDs, OTFTs and OPTs have been implemented in various applications ranging from pulse oximetry to image sensors. Screen printing has been shown to be a valuable technique to create interconnects from discrete devices on flexible substrates to external circuitry. Processing condition factors for screen printing such as paste solvents, pressure, and annealing, are compatible with all of these devices and do not degrade device performance. The ability to create large-area arrays of interconnects for these devices opens up new possibilities in developing circuits and more complicated systems on flexible substrates.

# Chapter 6

## Conclusion & Future Work

This thesis contributes to the development of high performance large-area semiconductor devices by using scalable printing techniques as a means of fabrication where wafer-based processing may be prohibitively expensive. Photodetectors are primarily investigated since their sensitivity and dynamic range increase with photoactive area, increasing the performance of sensors and imagers[65]. These photodetector devices include organic photodiodes (OPDs), organic charge-coupled devices (OCCDs), and organic phototransistors (OPTs). Organic thin film transistors (OTFTs) are also investigated in this thesis because of their necessity to interface with OPDs for applications in image sensing. The state-of-the-art in large-area solution-processed image sensors relies on photolithographic steps for processing[48, 117, 139, 168]. Additionally, most of these sensors don't perform intra-pixel integration of photogenerated charge, which severely limits the signal-to-noise ratio (SNR) for short exposure times and high frame rates[126, 166]. In an attempt to move away from wafer-based microfabrication, the foundation of device performance optimization in this thesis stems from the reliability of the printing processes used. This reliability entails good film uniformity over large areas, no pinholes, minimal edge effects, optimal wetting, and good pattern fidelity. Using a well-controlled fabrication process, all of these devices are optimized to give the best performance and reliability for image sensing. Specifically, this application requires high yield, minimal variability, high photodetector specific detectivity,  $D^*$  (Reference Chapter 1), good device stability under biasing for charge integration, and sufficiently fast response times to enable high frame rates.

Chapter 1 performed an assessment on the literature to-date of solution-processed image sensors. Most of these previously published image sensors, whether using photodiodes or phototransistors as the photodetector element, operate under direct photocurrent-sensing mode and not the charge-integration mode needed for achieving an adequate SNR at video frame rates (approximately 30 fps). Only a handful of photodiode-based image sensors were shown to operate at video frame rates using charge integration. Additionally, all of these sensors were fabricated using a combination of wafer-based microfabrication, sacrificial processing, or photolithography and using no additive or printing techniques. Looking at the



state-of-the-art, it was evident that many improvements could be made in solution-processed image sensors.

The development of OTFTs in Chapter 2 was done in order to provide a backplane for OPD-based image sensors. A low contact resistance and high on-off ratio is needed from the transistor element in order to ensure quick discharge and minimal leakage during charge integration. A novel printing deposition method using a surface energy-patterned (SEP) substrate to pattern doctor blade-coated ink is used to create the uniform thin films needed for a high performance and homogenous OTFTs[135]. Following the optimization of the polymeric source-drain electrodes, the semiconductor failed short with low on-off ratio from polymeric materials and low mobility from small molecule materials. However, it was found that blending semiconducting small molecules and polymers gave the best performance with no noticeable contact barrier, high mobility and high on-off ratio. The uniformity of the channel length, semiconductor channel width and gate dielectric thickness enabled discrete arrays of OTFTs with minimal variability, suggesting that SEP doctor blade coating is a viable technique to create OTFT backplanes for image sensors.

Chapter 3 investigated the production of OPDs using the highly scalable and inexpensive manufacturing techniques of doctor blade coating and screen printing. These deposition techniques were precise enough to control factors in the design of the device such as the dipole interlayer thickness in order to tailor external quantum efficiency (EQE) and dark current, or increase anode work function without compromising printing reliability[137]. Thicker active layers prevented shorting, which maximized device yield and minimized dark current. While a polymeric printed top electrode gave a lower EQE than OPDs with top metal electrodes, the absence of defects led to a significantly lower dark current that led to an overall increase in  $D^*$ . This optimization led to devices with high yields and minimal variability in EQE and dark current. Additionally, these devices maintained a high  $D^*$  under large reverse biasing, which increases the dynamic range of image sensors implementing these devices since more charge can be capacitively stored without leakage through dark current.

The approaches used to enable high performance OTFTs and OPDs in Chapter 2 and 3, respectively, were synergized to create capacitive-based photodetector elements in Chapter 4, which included OCCDs and OPTs. It was shown that OCCD devices are capable of efficiently integrating photogenerated charge and exhibit high EQE and excellent bias stress stability. This device provided the foundation upon which the OPT was built. A similar fabrication process as the OTFTs was used to create OPTs. Additionally, a novel organic heterojunction device architecture was implemented, consisting of the light-absorbing active layer previously used for OPDs and high-mobility transport layer. The high level of crystallization enabled transistor performances with high mobilities, high on-off ratios and minimal variability. OPT-based pixels were shown to integrated photogenerated charge with EQEs above 100% at low irradiances owing to photoconductive gain in these devices. The fast discharge after charge integration enabled the operation of these pixel at video frame rates

with superior EQE compared to conventional photodiode-based pixels.

Finally, Chapter 5 integrated and tailored OTFTs (Chapter 2), OPDs (Chapter 3) and OPTs (Chapter 4) into addressable arrays for light and image sensing applications. Various large-area OPDs were designed to have spectrally-matched EQE spectra to the emission of OLEDs used in visible- and infrared-based pulse oximeter applications[114]. Arrays of these devices were made addressable and readable to external circuitry via screen printed conductive traces. Screen printing was also used to connect discrete OTFTs into a row-addressable column-readable backplane with electrodes buried underneath the gate dielectric layer accessed through inkjet printed conductive vias. OPT-based image sensors were also fabricated using screen printed interconnects and enabled quick addressing and fast readout at video frames rates with good reliability even under low lighting conditions.

The primary emphasis of this thesis is on the performance of the individual devices. While most aspects of these devices performed well with respect to the figures of merit, several improvements could be made. The source-drain electrodes for OTFTs deposited using the SEP process could be further developed to achieve shorter channel lengths. Fully-printed OTFTs could be made from semiconductor materials that yield higher mobilities, preferably above  $1 \text{ cm}^2/\text{Vs}$ , and less variability in order to surpass amorphous silicon. Choosing a higher performance semiconductor could also improve the bias stress stability of these devices, which exhibit a large decrease in mobility and on-off ratio for biases of a minute or more. For OPD fabrication, an additive-based modification or alternative to the screen printed top electrode could be developed to minimize the probability of shorts or high leakage currents for devices with thin active layers. These thin-active layer OPDs, when functional, are advantageous owing to their faster response times. Minimizing shorts and leakage current for a printed top electrode could also enable all-printed OPDs with large photoactive areas ( $\geq 10 \text{ mm}^2$ ) without the need for vacuum-deposited electrodes. With regards to the transistor performance of OPTs, using different donor (hole-transporting) materials in the photoactive layer with a lower highest occupied molecular orbital (HOMO) could eliminate contact resistance.

The implementation of these devices in circuits and eventually systems can be achieved once several of the previously mentioned device-level issues are resolved. Active pixel architectures using multiple OPTs as photodetector and gain elements can be integrated in order to further amplify the signal. In addition to solution-processed active pixel circuits, driver and readout circuits are also a relatively untouched area in literature on flexible and solution-processed image sensors. Many advances have been made in monolithic fully printed and flexible circuits, with sensors and digital circuitry manufactured on the same substrate operating in the kHz regime[44, 133]. Printed high gain analog amplifiers have been shown to operate with several millisecond delay with a gain of 50 [115]. However, the amplifier requirements are quite stringent for image sensors as these devices must have very low parasitic input current as to not affect low light measurements, operate at high frequencies to scan thousands of rows per second, and be compact enough to fit within the width of each



column of the imaging array. While a monolithic imaging system is ideal, external circuitry doesn't benefit from large area scaling and flexibility as the image sensor, which makes heterogeneous integration with CMOS drivers and readout circuitry more practical given the state-of-the-art. However, recent advances in printed high frequency transistors[79, 92] could enable printed high gain and high frequency operational amplifiers needed for a monolithic system.

An untouched concept in the literature on solution-processed image sensors is the use of charge-coupled device (CCD) image sensors. These sensors are arrays of transistor gates that accumulate photogenerated charge at the semiconductor-dielectric interface then laterally transfer them out of the array through successive pulsing of adjacent gates (see Holst et. al. for more information[65]). While preliminary reports on OCCDs in this thesis demonstrated high EQE during integration of photogenerated charge, these devices failed to transfer charge laterally when a strip of high mobility semiconductor was deposited at the active layer-dielectric interface. Achieving efficient lateral charge transfer would enable image sensors with a far simpler architecture than OPD or OPT sensors, which could increase the pixel density. The only study on OCCDs has shown 40% lateral charge transfer efficiency between adjacent pixels but very low EQEs[181]. This appreciable charge transfer efficiency suggests that modifications to the OCCD device presented in this thesis could also enable lateral charge transfer while maintaining a high EQE.

There are a number of ways to improve upon what has been demonstrated in the state-of-the-art and this thesis. With regards to light and image sensors, it is important for future work to assess the charge integration performance of pixels as this is the most dominant and highest performance mode of operation even though it is not frequently used in literature. The advantages of large area electronics are fully leveraged when printing is used to deposit as many of the layers as possible despite the fact all literature to date on solution-processed sensors still utilize subtractive photolithography. In terms of applications, many large-area imaging systems in literature are designed for X-ray imaging systems[48, 117, 126, 168] because the absence of optics in these imaging systems makes it easier to push these sensors to market. It is essential for future work on printable large-area image sensors to implement novel optics for flexible and large-area systems[23, 76, 163] to create commercializable high performance cameras ready for conventional photography. These potential improvements coupled with the high performance of the printed devices presented in this thesis pave the way for ubiquitous and high-end light and image sensors.

# Bibliography

- [1] Seung-Eon Ahn et al. “Metal Oxide Thin Film Phototransistor for Remote Touch Interactive Displays”. In: *Advanced Materials* 24.19 (2012), pp. 2631–2636. ISSN: 1521-4095. DOI: 10.1002/adma.201200293.
- [2] Satoshi Aihara et al. “Stacked image sensor with green-and red-sensitive organic photoconductive films applying zinc oxide thin-film transistors to a signal readout circuit”. In: *Electron Devices, IEEE Transactions on* 56.11 (2009), pp. 2570–2576. ISSN: 0018-9383.
- [3] Francesco Arca et al. “Interface Trap States in Organic Photodiodes”. In: *Sci. Rep.* 3 (2013). DOI: <http://www.nature.com/srep/2013/130222/srep01324/abs/srep01324.html>.
- [4] A. C. Arias et al. “All jet-printed polymer thin-film transistor active-matrix backplanes”. In: *Applied Physics Letters* 85.15 (2004), pp. 3304–3306. DOI: [doi:http://dx.doi.org/10.1063/1.1801673](http://dx.doi.org/10.1063/1.1801673).
- [5] Ana Claudia Arias et al. “Materials and Applications for Large Area Electronics: Solution-Based Approaches”. In: *Chemical reviews* 110.1 (2010), pp. 3–24. ISSN: 0009-2665. DOI: 10.1021/cr900150b.
- [6] Ardalan Armin et al. “Narrowband light detection via internal quantum efficiency manipulation of organic photodiodes”. In: *Nat Commun* 6 (2015). DOI: 10.1038/ncomms7343.
- [7] Ardalan Armin et al. “Thick junction broadband organic photodiodes”. In: *Laser & Photonics Reviews* 8.6 (2014), pp. 924–932. ISSN: 1863-8899. DOI: 10.1002/lpor.201400081.
- [8] G. Azzellino et al. “Fully Inkjet-Printed Organic Photodetectors with High Quantum Yield”. In: *Advanced Materials* 25.47 (2013), pp. 6829–6833. ISSN: 1521-4095. DOI: 10.1002/adma.201303473.
- [9] K. J. Baeg, M. Caironi, and Y. Y. Noh. “Toward Printed Integrated Circuits based on Unipolar or Ambipolar Polymer Semiconductors”. In: *Advanced Materials* 25.31 (2013), pp. 4210–4244. ISSN: 0935-9648. DOI: DOI10.1002/adma.201205361.

- [10] Kang-Jun Baeg et al. “Organic Light Detectors: Photodiodes and Phototransistors”. In: *Advanced Materials* 25.31 (2013), pp. 4267–4295. ISSN: 1521-4095. DOI: 10.1002/adma.201204979.
- [11] Daniela Baierl et al. “A hybrid CMOS-imager with a solution-processable polymer as photoactive layer”. In: *Nat Commun* 3 (2012), p. 1175. DOI: doi : 10 . 1038 / ncomms2180.
- [12] Daniela Baierl et al. “Towards a hybrid CMOS-imager with organic semiconductors as photoactive layer”. In: *Ph. D. Research in Microelectronics and Electronics (PRIME), 2011 7th Conference on.* IEEE. ISBN: 142449138X.
- [13] Z. N. Bao. “Fine printing”. In: *Nature Materials* 3.3 (2004), pp. 137–138. ISSN: 1476-1122. DOI: Doi10.1038/Nmat1079.
- [14] Jonathan A Bartelt et al. “Controlling Solution?Phase Polymer Aggregation with Molecular Weight and Solvent Additives to Optimize Polymer?Fullerene Bulk Heterojunction Solar Cells”. In: *Advanced Energy Materials* 4.9 (2014). ISSN: 1614-6840.
- [15] Hector A. Becerril et al. “High-Performance Organic Thin-Film Transistors through Solution-Sheared Deposition of Small-Molecule Organic Semiconductors”. In: *Advanced Materials* 20.13 (2008), pp. 2588–2594. ISSN: 1521-4095. DOI: 10.1002/adma.200703120.
- [16] Z. M. Beiley et al. “Morphology-Dependent Trap Formation in High Performance Polymer Bulk Heterojunction Solar Cells”. In: *Advanced Energy Materials* 1.5 (2011), pp. 954–962. ISSN: 1614-6832. DOI: DOI10.1002/aenm.201100204.
- [17] Meriem Ben Salah Ep Akin. “A Comprehensive Surface Mount Technology Solution for Integrated Circuits onto Flexible Screen Printed Electrical Interconnects”. Thesis. 2014.
- [18] M. Binda et al. “High detectivity squaraine-based near infrared photodetector with nA/cm(2) dark current”. In: *Applied Physics Letters* 98.7 (2011). ISSN: 0003-6951. DOI: Artn073303Doi10.1063/1.3553767.
- [19] Paul W. M. Blom et al. “Device physics of polymer : fullerene bulk heterojunction solar cells”. In: *Advanced Materials* 19.12 (2007), pp. 1551–1566. ISSN: 0935-9648. DOI: 10.1002/adma.200601093.
- [20] C. L. Bower et al. “Continuous coating of discrete areas of a flexible web”. In: *AIChE Journal* 53.7 (2007), pp. 1644–1657. ISSN: 1547-5905. DOI: 10.1002/aic.11215.
- [21] Kyle Braam and Vivek Subramanian. “A Stencil Printed, High Energy Density Silver Oxide Battery Using a Novel Photopolymerizable Poly(acrylic acid) Separator”. In: *Advanced Materials* 27.4 (2015), pp. 689–694. ISSN: 1521-4095. DOI: 10.1002/adma.201404149.
- [22] P. de Bruyn et al. “Diffusion-Limited Current in Organic Metal-Insulator-Metal Diodes”. In: *Physical Review Letters* 111.18 (2013), p. 186801.

- [23] Andreas Brckner et al. "Ultra-thin wafer-level camera with 720p resolution using micro-optics". In: *SPIE Optical Engineering+ Applications*. International Society for Optics and Photonics.
- [24] Richard H. Bube. *Photoelectric properties of semiconductors*. Cambridge: Cambridge University Press, 1992. ISBN: 0-521-40681-1.
- [25] Mariano Campoy-Quiles et al. "Morphology evolution via self-organization and lateral and vertical diffusion in polymer: fullerene solar cell blends RID C-1209-2008 RID F-6068-2011". In: *Nature Materials* 7.2 (2008), pp. 158–164. ISSN: 1476-1122. DOI: 10.1038/nmat2102.
- [26] Joseph Chang et al. "Fully printed electronics on flexible substrates: High gain amplifiers and DAC". In: *Organic Electronics* 15.3 (2014), pp. 701–710. ISSN: 1566-1199. DOI: <http://dx.doi.org/10.1016/j.orgel.2013.12.027>.
- [27] Joseph Chang et al. "Fully printed electronics on flexible substrates: High gain amplifiers and DAC". In: *Organic Electronics* 15.3 (2014), pp. 701–710. ISSN: 1566-1199. DOI: <http://dx.doi.org/10.1016/j.orgel.2013.12.027>.
- [28] Dian Chen et al. "P3HT/PCBM Bulk Heterojunction Organic Photovoltaics: Correlating Efficiency and Morphology RID A-8902-2008". In: *Nano Letters* 11.2 (2011), pp. 561–567. ISSN: 1530-6984. DOI: 10.1021/nl103482n.
- [29] L. M. Chen et al. "Recent Progress in Polymer Solar Cells: Manipulation of Polymer: Fullerene Morphology and the Formation of Efficient Inverted Polymer Solar Cells". In: *Advanced Materials* 21.14-15 (2009), pp. 1434–1449. ISSN: 0935-9648. DOI: DOI10.1002/adma.200802854.
- [30] Huai-An Chin et al. "A flexible barium strontium titanate photodetector array". In: *Extreme Mechanics Letters* (2016). ISSN: 2352-4316.
- [31] Danbi Choi et al. "High-Performance Triisopropylsilylethynyl Pentacene Transistors via Spin Coating with a Crystallization-Assisting Layer". In: *ACS Applied Materials & Interfaces* 4.1 (2011), pp. 117–122. ISSN: 1944-8244. DOI: 10.1021/am201074n.
- [32] Ye T Chou, Ya T Ko, and Man F Yan. "Fluid flow model for ceramic tape casting". In: *Journal of the American Ceramic Society* 70.10 (1987). ISSN: 1551-2916.
- [33] Yingli Chu et al. "Photosensitive and Flexible Organic Field-Effect Transistors Based on Interface Trapping Effect and Their Application in 2D Imaging Array". In: *Advanced Science* (2016). ISSN: 2198-3844.
- [34] Wei Deng et al. "Aligned Single-Crystalline Perovskite Microwire Arrays for High-Performance Flexible Image Sensors with Long-Term Stability". In: *Advanced Materials* (2016). ISSN: 1521-4095.
- [35] Y. Diao et al. "Solution coating of large-area organic semiconductor thin films with aligned single-crystalline domains". In: *Nature Materials* 12.7 (2013), pp. 665–671. ISSN: 1476-1122. DOI: DOI10.1038/Nmat3650.

- [36] Rui Dong et al. “An Ultraviolet-to-NIR Broad Spectral Nanocomposite Photodetector with Gain”. In: *Advanced Optical Materials* 2.6 (2014), pp. 549–554. ISSN: 2195-1071. DOI: 10.1002/adom.201400023.
- [37] Rui Dong et al. “High-Gain and Low-Driving-Voltage Photodetectors Based on Organolead Triiodide Perovskites”. In: *Advanced Materials* 27.11 (2015), pp. 1912–1918. ISSN: 1521-4095.
- [38] B. Ecker et al. “Understanding S-Shaped Current-Voltage Characteristics in Organic Solar Cells Containing a TiO<sub>x</sub> Inter layer with Impedance Spectroscopy and Equivalent Circuit Analysis”. In: *Journal of Physical Chemistry C* 116.31 (2012), pp. 16333–16337. ISSN: 1932-7447. DOI: Doi10.1021/Jp305206d.
- [39] Matthew D. Fagan, Byung H. Kim, and Donggang Yao. “A novel process for continuous thermal embossing of large-area nanopatterns onto polymer films”. In: *Advances in Polymer Technology* 28.4 (2009), pp. 246–256. ISSN: 1098-2329. DOI: 10.1002/adv.20167.
- [40] A. Falco et al. “Spray deposition of Polyethylenimine thin films for the fabrication of fully-sprayed organic photodiodes”. In: *Organic Electronics* 0 (). ISSN: 1566-1199. DOI: <http://dx.doi.org/10.1016/j.orgel.2015.05.003>.
- [41] Yanjun Fang and Jinsong Huang. “Resolving Weak Light of Sub-picowatt per Square Centimeter by Hybrid Perovskite Photodetectors Enabled by Noise Reduction”. In: *Advanced Materials* 27.17 (2015), pp. 2804–2810. ISSN: 1521-4095. DOI: 10.1002/adma.201500099.
- [42] Y. Fujisaki et al. “Direct patterning of solution-processed organic thin-film transistor by selective control of solution wettability of polymer gate dielectric”. In: *Applied Physics Letters* 102.15 (2013). ISSN: 0003-6951. DOI: Artn153305Doi10.1063/1.4802499.
- [43] K. Fukuda et al. “Patterning Method for Silver Nanoparticle Electrodes in Fully Solution-Processed Organic Thin-Film Transistors Using Selectively Treated Hydrophilic and Hydrophobic Surfaces”. In: *Japanese Journal of Applied Physics* 52.5 (2013). ISSN: 0021-4922. DOI: Unsp05db05Doi10.7567/Jjap.52.05db05.
- [44] Kenjiro Fukuda et al. “Fully-printed high-performance organic thin-film transistors and circuitry on one-micron-thick polymer films”. In: *Nat Commun* 5 (2014). DOI: 10.1038/ncomms5147.
- [45] Kenjiro Fukuda et al. “Reverse-Offset Printing Optimized for Scalable Organic Thin-Film Transistors with Submicrometer Channel Lengths”. In: *Advanced Electronic Materials* 1.8 (2015), n/a–n/a. ISSN: 2199-160X. DOI: 10.1002/aelm.201500145.
- [46] Abhinav M. Gaikwad et al. “Highly Flexible, Printed Alkaline Batteries Based on Mesh-Embedded Electrodes”. In: *Advanced Materials* 23.29 (2011), pp. 3251–+. ISSN: 0935-9648. DOI: 10.1002/adma.201100894.

- [47] Abhinav M. Gaikwad et al. "Identifying orthogonal solvents for solution processed organic transistors". In: *Organic Electronics* 30 (2016), pp. 18–29. ISSN: 1566-1199. DOI: <http://dx.doi.org/10.1016/j.orgel.2015.12.008>.
- [48] Gerwin H Gelinck et al. "X-ray imager using solution processed organic transistor arrays and bulk heterojunction photodiodes on thin, flexible plastic substrate". In: *Organic Electronics* 14.10 (2013), pp. 2602–2609. ISSN: 1566-1199.
- [49] Grau Gerd et al. "Gravure-printed electronics: recent progress in tooling development, understanding of printing physics, and realization of printed devices". In: *Flexible and Printed Electronics* 1.2 (2016), p. 023002. ISSN: 2058-8585.
- [50] Pace Giuseppina et al. "Printed photodetectors". In: *Semiconductor Science and Technology* 30.10 (2015), p. 104006. ISSN: 0268-1242.
- [51] Xiong Gong et al. "High-Detectivity Polymer Photodetectors with Spectral Response from 300 nm to 1450 nm". In: *Science* 325.5948 (2009), pp. 1665–1667. DOI: 10.1126/science.1176706.
- [52] O. Goto et al. "Organic Single-Crystal Arrays from Solution-Phase Growth Using Micropattern with Nucleation Control Region". In: *Advanced Materials* 24.8 (2012), pp. 1117–1122. ISSN: 0935-9648. DOI: DOI10.1002/adma.201104373.
- [53] M. Granstrom et al. "Laminated fabrication of polymeric photovoltaic diodes". In: *Nature* 395.6699 (1998), pp. 257–260. ISSN: 0028-0836.
- [54] D. J. Gundlach et al. "An experimental study of contact effects in organic thin film transistors". In: *Journal of Applied Physics* 100.2 (2006). ISSN: 0021-8979. DOI: Artn024509Doi10.1063/1.2215132.
- [55] Fawen Guo et al. "A nanocomposite ultraviolet photodetector based on interfacial trap-controlled charge injection". In: *Nat Nano* 7.12 (2012), pp. 798–802. ISSN: 1748-3387. DOI: <http://www.nature.com/nnano/journal/v7/n12/abs/nnano.2012.187.html>.
- [56] M. C. Hamilton, S. Martin, and J. Kanicki. "Thin-film organic polymer phototransistors". In: *IEEE Transactions on Electron Devices* 51.6 (2004), pp. 877–885. ISSN: 0018-9383. DOI: 10.1109/TED.2004.829619.
- [57] Richard Hamilton et al. "High-Performance Polymer-Small Molecule Blend Organic Transistors". In: *Advanced Materials* 21.10-11 (2009), pp. 1166–1171. ISSN: 1521-4095. DOI: 10.1002/adma.200801725.
- [58] William T. Hammond and Jiangeng Xue. "Organic heterojunction photodiodes exhibiting low voltage, imaging-speed photocurrent gain". In: *Applied Physics Letters* 97.7 (2010), p. 073302. DOI: doi:<http://dx.doi.org/10.1063/1.3481407>.
- [59] Hyemi Han et al. "Broadband All-Polymer Phototransistors with Nanostructured Bulk Heterojunction Layers of NIR-Sensing n-Type and Visible Light-Sensing p-Type Polymers". In: *Scientific reports* 5 (2015).

- [60] Z. C. He et al. “Enhanced power-conversion efficiency in polymer solar cells using an inverted device structure”. In: *Nature Photonics* 6.9 (2012), pp. 591–595. ISSN: 1749-4885. DOI: [Doi10.1038/Nphoton.2012.190](https://doi.org/10.1038/Nphoton.2012.190).
- [61] Zhicai He et al. “Simultaneous Enhancement of Open-Circuit Voltage, Short-Circuit Current Density, and Fill Factor in Polymer Solar Cells”. In: *Advanced Materials* 23.40 (2011), pp. 4636–4643. ISSN: 1521-4095. DOI: [10.1002/adma.201103006](https://doi.org/10.1002/adma.201103006).
- [62] A.J. Heeger, N.S. Sariciftci, and E.B. Namdas. *Semiconducting and Metallic Polymers*. OUP Oxford, 2010. ISBN: 9780198528647.
- [63] Jeanny Herault et al. *Biologically Inspired Computer Vision: Fundamentals and Applications*. John Wiley & Sons, 2015. ISBN: 3527680470.
- [64] Masahiro Hiramoto et al. “Photocurrent multiplication in organic single crystals”. In: *Applied Physics Letters* 81.8 (2002), pp. 1500–1502. DOI: [doi:http://dx.doi.org/10.1063/1.1501764](http://dx.doi.org/10.1063/1.1501764).
- [65] Gerald C Holst and Terrence S Lomheim. *CMOS/CCD sensors and camera systems*. Vol. 408. JCD Publishing, 2007.
- [66] K. Hong et al. “Printed, sub-2V ZnO Electrolyte Gated Transistors and Inverters on Plastic”. In: *Advanced Materials* 25.25 (2013), pp. 3413–3418. ISSN: 0935-9648. DOI: [DOI10.1002/adma.201300211](https://doi.org/10.1002/adma.201300211).
- [67] Chenming Hu. *Modern semiconductor devices for integrated circuits*. Prentice Hall, 2010. ISBN: 0136085253.
- [68] Hua Hu and Ronald G. Larson. “Marangoni Effect Reverses Coffee-Ring Depositions”. In: *The Journal of Physical Chemistry B* 110.14 (2006), pp. 7090–7094. ISSN: 1520-6106. DOI: [10.1021/jp0609232](https://doi.org/10.1021/jp0609232).
- [69] Di Huang et al. “Enhanced performance and morphological evolution of PTB7:PC71BM polymer solar cells by using solvent mixtures with different additives”. In: *Physical Chemistry Chemical Physics* 17.12 (2015), pp. 8053–8060. ISSN: 1463-9076. DOI: [10.1039/C4CP05826G](https://doi.org/10.1039/C4CP05826G).
- [70] Fei Huang et al. “Novel Electroluminescent Conjugated Polyelectrolytes Based on Polyfluorene”. In: *Chemistry of Materials* 16.4 (2004), pp. 708–716. ISSN: 0897-4756. DOI: [10.1021/cm034650o](https://doi.org/10.1021/cm034650o).
- [71] D. K. Hwang et al. “Top-Gate Organic Field-Effect Transistors with High Environmental and Operational Stability”. In: *Advanced Materials* 23.10 (2011), pp. 1293–+. ISSN: 0935-9648. DOI: [DOI10.1002/adma.201004278](https://doi.org/10.1002/adma.201004278).
- [72] M. Ikawa et al. “Simple push coating of polymer thin-film transistors”. In: *Nature Communications* 3 (2012). ISSN: 2041-1723. DOI: [Artn1176Doi10.1038/Ncomms2190](https://doi.org/10.1038/Ncomms2190).
- [73] S James, P Arujo, and A Carlos. “Ferroelectric memories”. In: *Science* 246.4936 (1989), pp. 1400–1405.

- [74] Jaewon Jang et al. “Transparent High-Performance Thin Film Transistors from Solution-Processed SnO<sub>2</sub>/ZrO<sub>2</sub> Gel-like Precursors”. In: *Advanced Materials* 25.7 (2013), pp. 1042–1047. ISSN: 1521-4095. DOI: 10.1002/adma.201202997.
- [75] Shin Woo Jeong et al. “The vertically stacked organic sensor-transistor on a flexible substrate”. In: *Applied Physics Letters* 97.25 (2010), p. 253309. ISSN: 0003-6951.
- [76] Inhwa Jung et al. “Dynamically tunable hemispherical electronic eye camera system with adjustable zoom capability”. In: *Proceedings of the National Academy of Sciences* 108.5 (2011), pp. 1788–1793. ISSN: 0027-8424.
- [77] O. D. Jurchescu et al. “Organic Single-Crystal Field-Effect Transistors of a Soluble Anthradithiophene”. In: *Chemistry of Materials* 20.21 (2008), pp. 6733–6737. ISSN: 0897-4756. DOI: Doi10.1021/Cm8021165.
- [78] Hongki Kang et al. “High-Performance Printed Transistors Realized Using Femtoliter Gravure-Printed Sub-10  $\mu$ m Metallic Nanoparticle Patterns and Highly Uniform Polymer Dielectric and Semiconductor Layers”. In: *Advanced Materials* 24.22 (2012), pp. 3065–3069. ISSN: 1521-4095. DOI: 10.1002/adma.201200924.
- [79] Hongki Kang et al. “Megahertz-class printed high mobility organic thin-film transistors and inverters on plastic using attoliter-scale high-speed gravure-printed sub-5  $\mu$ m gate electrodes”. In: *Organic Electronics* 15.12 (2014), pp. 3639–3647. ISSN: 1566-1199. DOI: <http://dx.doi.org/10.1016/j.orgel.2014.10.005>.
- [80] Hyo-Soon Kang et al. “Characterization of phototransistor internal gain in metamorphic high-electron-mobility transistors”. In: *Applied Physics Letters* 84.19 (2004), pp. 3780–3782. DOI: doi:<http://dx.doi.org/10.1063/1.1739278>.
- [81] Panagiotis E. Keivanidis et al. “The Dependence of Device Dark Current on the Active-Layer Morphology of Solution-Processed Organic Photodetectors”. In: *Advanced Functional Materials* 20.22 (2010), pp. 3895–3903. ISSN: 1616-3028. DOI: 10.1002/adfm.201000967.
- [82] Yasser Khan et al. “Monitoring of Vital Signs with Flexible and Wearable Medical Devices”. In: *Advanced Materials* 28.22 (2016), pp. 4373–4395. ISSN: 1521-4095. DOI: 10.1002/adma.201504366.
- [83] C. Kim, A. Facchetti, and T. J. Marks. “Gate dielectric microstructural control of pentacene film growth mode and field-effect transistor performance”. In: *Advanced Materials* 19.18 (2007), pp. 2561–+. ISSN: 0935-9648. DOI: DOI10.1002/adma.200700101.
- [84] Dae-Hyeong Kim et al. “Materials for multifunctional balloon catheters with capabilities in cardiac electrophysiological mapping and ablation therapy”. In: *Nat Mater* 10.4 (2011), pp. 316–323. ISSN: 1476-1122. DOI: <http://www.nature.com/nmat/journal/v10/n4/abs/nmat2971.html>.



- [85] Jaehyun Kim et al. “Ultrahigh Detective Heterogeneous Photosensor Arrays with In-Pixel Signal Boosting Capability for Large-Area and Skin-Compatible Electronics”. In: *Advanced Materials* 28.16 (2016), pp. 3078–3086. ISSN: 1521-4095. DOI: 10.1002/adma.201505149.
- [86] Jeonghyun Kim et al. “Epidermal Electronics with Advanced Capabilities in Near-Field Communication”. In: *Small* 11.8 (2015), pp. 906–912. ISSN: 1613-6829. DOI: 10.1002/smll.201402495.
- [87] Minseok Kim et al. “Flexible organic phototransistors based on a combination of printing methods”. In: *Organic Electronics* 15.11 (2014), pp. 2677–2684. ISSN: 1566-1199.
- [88] Se Hyun Kim et al. “High-performance solution-processed triisopropylsilylethynyl pentacene transistors and inverters fabricated by using the selective self-organization technique”. In: *Applied Physics Letters* 93.11 (2008), pp. –. DOI: doi:http://dx.doi.org/10.1063/1.2987419.
- [89] Y. H. Kim et al. “Polyethylene Imine as an Ideal Interlayer for Highly Efficient Inverted Polymer Light-Emitting Diodes”. In: *Advanced Functional Materials* 24.24 (2014), pp. 3808–3814. ISSN: 1616-301X. DOI: Doi10.1002/Adfm.201304163.
- [90] J. W. Kingsley et al. “Molecular weight dependent vertical composition profiles of PCDTBT: PC71BM blends for organic photovoltaics”. In: *Scientific Reports* 4 (2014). ISSN: 2045-2322. DOI: Doi10.1038/Srep05286.
- [91] Rungrot Kitsomboonloha. “Modeling and Applications of Highly-Scaled Gravure Printing”. Thesis. 2015.
- [92] Rungrot Kitsomboonloha et al. “MHz-Range Fully Printed High-Performance Thin-Film Transistors by Using High-Resolution Gravure-Printed Lines”. In: *Advanced Electronic Materials* 1.12 (2015). ISSN: 2199-160X.
- [93] Heung Cho Ko et al. “A hemispherical electronic eye camera based on compressible silicon optoelectronics”. In: *Nature* 454.7205 (2008), pp. 748–753. ISSN: 0028-0836. DOI: doi:10.1038/nature07113.
- [94] S. Kobayashi et al. “Control of carrier density by self-assembled monolayers in organic field-effect transistors”. In: *Nat Mater* 3.5 (2004), pp. 317–322. ISSN: 1476-1122. DOI: http://www.nature.com/nmat/journal/v3/n5/supinfo/nmat1105\_S1.html.
- [95] F. C. Krebs, S. A. Gevorgyan, and J. Alstrup. “A roll-to-roll process to flexible polymer solar cells: model studies, manufacture and operational stability studies”. In: *Journal of Materials Chemistry* 19.30 (2009), pp. 5442–5451. ISSN: 0959-9428. DOI: Doi10.1039/B823001c.
- [96] Frederik C. Krebs. “Fabrication and processing of polymer solar cells: A review of printing and coating techniques”. In: *Solar Energy Materials and Solar Cells* 93.4 (2009), pp. 394–412. ISSN: 0927-0248. DOI: http://dx.doi.org/10.1016/j.solmat.2008.10.004.

- [97] Brijesh Kumar, Brajesh Kumar Kaushik, and Yuvraj Singh Negi. “Organic Thin Film Transistors: Structures, Models, Materials, Fabrication, and Applications: A Review”. In: *Polymer Reviews* 54.1 (2014), pp. 33–111. ISSN: 1558-3724. DOI: 10.1080/15583724.2013.848455.
- [98] Kazunori Kuribara et al. “Organic transistors with high thermal stability for medical applications”. In: *Nat Commun* 3 (2012), p. 723. DOI: doi:10.1038/ncomms1721.
- [99] Pak Heng Lau et al. “Fully Printed, High Performance Carbon Nanotube Thin-Film Transistors on Flexible Substrates”. In: *Nano Letters* 13.8 (2013), pp. 3864–3869. ISSN: 1530-6984. DOI: 10.1021/nl401934a.
- [100] L. L. Lavery, G. L. Whiting, and A. C. Arias. “All ink-jet printed polyfluorene photo-sensor for high illuminance detection”. In: *Organic Electronics* 12.4 (2011), pp. 682–685. ISSN: 1566-1199. DOI: DOI10.1016/j.orgel.2011.01.023.
- [101] Balthazar Lechne et al. “Design of intermediate layers for solution-processed tandem organic solar cells: Guidelines from a case study on TiO<sub>x</sub> and ZnO”. In: *Solar Energy Materials and Solar Cells* 120, Part B.0 (2014), pp. 709–715. ISSN: 0927-0248. DOI: <http://dx.doi.org/10.1016/j.solmat.2013.08.032>.
- [102] Sangwha Lee, Joon-Seo Park, and T. Randall Lee. “The Wettability of Fluoropolymer Surfaces: Influence of Surface Dipoles”. In: *Langmuir* 24.9 (2008), pp. 4817–4826. ISSN: 0743-7463. DOI: 10.1021/la700902h.
- [103] B. J. Leever et al. “In Situ Characterization of Lifetime and Morphology in Operating Bulk Heterojunction Organic Photovoltaic Devices by Impedance Spectroscopy”. In: *Advanced Energy Materials* 2.1 (2012), pp. 120–128. ISSN: 1614-6832. DOI: DOI10.1002/aenm.201100357.
- [104] Feng Li et al. “Ambipolar solution-processed hybrid perovskite phototransistors”. In: *Nature communications* 6 (2015).
- [105] Lingliang Li et al. “Achieving EQE of 16,700% in P3HT:PC71BM based photodetectors by trap-assisted photomultiplication”. In: *Sci. Rep.* 5 (2015). DOI: 10.1038/srep09181.
- [106] Ping Li et al. “High-efficiency inverted polymer solar cells controlled by the thickness of polyethylenimine ethoxylated (PEIE) interfacial layers”. In: *Physical Chemistry Chemical Physics* 16.43 (2014), pp. 23792–23799. ISSN: 1463-9076. DOI: 10.1039/C4CP03484H.
- [107] Yongye Liang et al. “For the Bright Future-Bulk Heterojunction Polymer Solar Cells with Power Conversion Efficiency of 7.4%”. In: *Advanced Materials* 22.20 (2010), E135–E138. ISSN: 1521-4095. DOI: 10.1002/adma.200903528.
- [108] J. A. Lim et al. “Self-Organization of Ink-jet-Printed Triisopropylsilylethynyl Pentacene via Evaporation-Induced Flows in a Drying Droplet”. In: *Advanced Functional Materials* 18.2 (2008), pp. 229–234. ISSN: 1616-3028. DOI: 10.1002/adfm.200700859.

- [109] Qianqian Lin et al. “Low Noise, IR-Blind Organohalide Perovskite Photodiodes for Visible Light Detection and Imaging”. In: *Advanced Materials* 27.12 (2015), pp. 2060–2064. ISSN: 1521-4095. DOI: 10.1002/adma.201405171.
- [110] Y. J. Lin et al. “Increasing the work function of poly(3,4-ethylenedioxythiophene) doped with poly(4-styrenesulfonate) by ultraviolet irradiation”. In: *Applied Physics Letters* 91.9 (2007). ISSN: 0003-6951. DOI: Artn092127Doi10.1063/1.2777147.
- [111] *Liquid Film Coating*. Netherlands: Springer, 1997. ISBN: 978-94-011-5342-3.
- [112] Xien Liu et al. “Flexible Organic Phototransistor Array with Enhanced Responsivity via Metal-Ligand Charge Transfer”. In: *ACS applied materials & interfaces* (2016). ISSN: 1944-8244.
- [113] Xingqiang Liu et al. “Scalable Integration of Indium Zinc Oxide/Photosensitive?Nanowire Composite Thin?Film Transistors for Transparent Multicolor Photodetectors Array”. In: *Advanced Materials* 26.18 (2014), pp. 2919–2924. ISSN: 1521-4095.
- [114] Claire M. Lochner et al. “All-organic optoelectronic sensor for pulse oximetry”. In: *Nat Commun* 5 (2014). DOI: 10.1038/ncomms6745.
- [115] Giorgio Maiellaro et al. “High-gain operational transconductance amplifiers in a printed complementary organic TFT technology on flexible foil”. In: *Circuits and Systems I: Regular Papers, IEEE Transactions on* 60.12 (2013), pp. 3117–3125. ISSN: 1549-8328.
- [116] L. A. Majewski et al. “Influence of processing conditions on the stability of poly(3-hexylthiophene)-based field-effect transistors”. In: *Applied Physics Letters* 88.22 (2006), p. 222108. DOI: doi:http://dx.doi.org/10.1063/1.2208938.
- [117] Pawel E Malinowski et al. “Fully Organic Integrated Arrays on Flexible Substrates for X-Ray Imaging”. In: *status: published* (2013).
- [118] Y. C. Mei et al. “High Mobility Field-Effect Transistors with Versatile Processing from a Small-Molecule Organic Semiconductor”. In: *Advanced Materials* 25.31 (2013), pp. 4352–4357. ISSN: 0935-9648. DOI: DOI10.1002/adma.201205371.
- [119] Johannes Milvich et al. “Flexible low-voltage organic phototransistors based on air-stable dinaphtho [2, 3-b: 2', 3'-f] thieno [3, 2-b] thiophene (DNTT)”. In: *Organic Electronics* 20 (2015), pp. 63–68. ISSN: 1566-1199.
- [120] T. Minari et al. “Selective organization of solution-processed organic field-effect transistors”. In: *Applied Physics Letters* 92.17 (2008). ISSN: 0003-6951. DOI: Artn173301Doi10.1063/1.2912822.
- [121] H. Minemawari et al. “Inkjet printing of single-crystal films”. In: *Nature* 475.7356 (2011), pp. 364–367. ISSN: 0028-0836. DOI: Doi10.1038/Nature10313.
- [122] Atsuhiko Miyata et al. “Direct measurement of the exciton binding energy and effective masses for charge carriers in organic-inorganic tri-halide perovskites”. In: *Nat Phys* 11.7 (2015), pp. 582–587. ISSN: 1745-2473. DOI: 10.1038/nphys3357.

- [123] Sebastian Nau et al. “Organic Non-Volatile Resistive Photo-Switches for Flexible Image Detector Arrays”. In: *Advanced Materials* 27.6 (2015), pp. 1048–1052. ISSN: 1521-4095.
- [124] Ivan Nausieda et al. “An organic active-matrix imager”. In: *Electron Devices, IEEE Transactions on* 55.2 (2008), pp. 527–532. ISSN: 0018-9383.
- [125] Jenny Nelson. *The Physics of Solar Cells*. Imperial College Press, 2003.
- [126] T. N. Ng et al. “Flexible image sensor array with bulk heterojunction organic photodiode”. In: *Applied Physics Letters* 92.21 (2008). ISSN: 0003-6951. DOI: [Artn213303Doi10.1063/1.2937018](https://doi.org/10.1063/1.2937018).
- [127] L. H. Nguyen et al. “Effects of Annealing on the Nanomorphology and Performance of Poly(alkylthiophene):Fullerene Bulk-Heterojunction Solar Cells”. In: *Advanced Functional Materials* 17.7 (2007), pp. 1071–1078. ISSN: 1616-3028. DOI: [10.1002/adfm.200601038](https://doi.org/10.1002/adfm.200601038).
- [128] Ronald S. Nowicki. “Diffusion barriers between gold and semiconductors”. In: *Gold Bulletin* 15.1 (1982), pp. 21–24. ISSN: 0017-1557. DOI: [10.1007/BF03216567](https://doi.org/10.1007/BF03216567).
- [129] Y. Ohno. “Carbon nanotube-based thin-film transistors on plastic film”. In: *Active-Matrix Flatpanel Displays and Devices (AM-FPD), 2013 Twentieth International Workshop on*.
- [130] Giuseppina Pace et al. “All-Organic and Fully-Printed Semitransparent Photodetectors Based on Narrow Bandgap Conjugated Molecules”. In: *Advanced Materials* 26.39 (2014), pp. 6773–6777. ISSN: 1521-4095. DOI: [10.1002/adma.201402918](https://doi.org/10.1002/adma.201402918).
- [131] S. H. Park et al. “Bulk heterojunction solar cells with internal quantum efficiency approaching 100%”. In: *Nature Photonics* 3.5 (2009), 297–U5. ISSN: 1749-4885. DOI: [Doi10.1038/Nphoton.2009.69](https://doi.org/10.1038/Nphoton.2009.69).
- [132] Felipe J. Pavinatto, Carlos W. A. Paschoal, and Ana C. Arias. “Printed and flexible biosensor for antioxidants using interdigitated ink-jetted electrodes and gravure-deposited active layer”. In: *Biosensors and Bioelectronics* 67 (2015), pp. 553–559. ISSN: 0956-5663. DOI: <http://dx.doi.org/10.1016/j.bios.2014.09.039>.
- [133] Boyu Peng et al. “High performance organic transistor active-matrix driver developed on paper substrate”. In: *Scientific Reports* 4 (2014), p. 6430. DOI: [10.1038/srep06430](https://doi.org/10.1038/srep06430).
- [134] Craig H. Peters et al. “The Mechanism of Burn-in Loss in a High Efficiency Polymer Solar Cell”. In: *Advanced Materials* 24.5 (2012), pp. 663–668. ISSN: 1521-4095. DOI: [10.1002/adma.201103010](https://doi.org/10.1002/adma.201103010).
- [135] Adrien Pierre et al. “All-Printed Flexible Organic Transistors Enabled by Surface Tension-Guided Blade Coating”. In: *Advanced Materials* 26.32 (2014), pp. 5722–5727. ISSN: 1521-4095. DOI: [10.1002/adma.201401520](https://doi.org/10.1002/adma.201401520).

- [136] Adrien Pierre et al. “Empirically based device modeling of bulk heterojunction organic photovoltaics”. In: *Journal of Applied Physics* 113.15 (2013), p. 154506. DOI: doi : <http://dx.doi.org/10.1063/1.4801662>.
- [137] Adrien Pierre et al. “High Detectivity All-Printed Organic Photodiodes”. In: *Advanced Materials* 27.41 (2015), pp. 6411–6417. ISSN: 1521-4095. DOI: 10.1002/adma.201502238.
- [138] C. Piliego et al. “High Electron Mobility and Ambient Stability in Solution-Processed Perylene-Based Organic Field-Effect Transistors”. In: *Advanced Materials* 21.16 (2009), pp. 1573–+. ISSN: 0935-9648. DOI: DOI10.1002/adma.200803207.
- [139] Tobias Rauch et al. “Near-infrared imaging with quantum-dot-sensitized organic photodiodes”. In: *Nat Photon* 3.6 (2009), pp. 332–336. ISSN: 1749-4885. DOI: doi:10.1038/nphoton.2009.72.
- [140] Xiaochen Ren et al. “A Low-Operating-Power and Flexible Active-Matrix Organic-Transistor Temperature-Sensor Array”. In: *Advanced Materials* 28.24 (2016), pp. 4832–4838. ISSN: 1521-4095. DOI: 10.1002/adma.201600040.
- [141] C Kyle Renshaw, Xin Xu, and Stephen R Forrest. “A monolithically integrated organic photodetector and thin film transistor”. In: *Organic Electronics* 11.1 (2010), pp. 175–178. ISSN: 1566-1199.
- [142] Lee J. Richter et al. “In Situ Morphology Studies of the Mechanism for Solution Additive Effects on the Formation of Bulk Heterojunction Films”. In: *Advanced Energy Materials* (2014), n/a–n/a. ISSN: 1614-6840. DOI: 10.1002/aenm.201400975.
- [143] You Seung Rim et al. “Ultrahigh and Broad Spectral Photodetectivity of an Organic/Inorganic Hybrid Phototransistor for Flexible Electronics”. In: *Advanced Materials* 27.43 (2015), pp. 6885–6891. ISSN: 1521-4095.
- [144] M. Rubinstein and R.H. Colby. *Polymer Physics*. Oxford University Press, 2003. ISBN: 9781613449431.
- [145] Hiroshi Saito et al. “Compound eye shaped flexible organic image sensor with a tunable visual field”. In: *Micro Electro Mechanical Systems, 2005. MEMS 2005. 18th IEEE International Conference on*. IEEE. ISBN: 0780387325.
- [146] Toshikatsu Sakai et al. “A 128 96 pixel, 50  $\mu$ m pixel pitch transparent readout circuit using amorphous In<sub>2</sub>Ga<sub>2</sub>Zn<sub>2</sub>O thin-film transistor array with indium/tin oxide electrodes for an organic image sensor”. In: *Japanese Journal of Applied Physics* 51.1R (2011), p. 010202. ISSN: 1347-4065.
- [147] Bahaa EA Saleh, Malvin Carl Teich, and Bahaa E Saleh. *Fundamentals of photonics*. Vol. 22. Wiley New York, 1991.
- [148] A. Salleo and A. C Arias. “Solution Based Self-Assembly of an Array of Polymeric Thin-Film Transistors”. In: *Advanced Materials* 19.21 (2007), pp. 3540–3543. ISSN: 1521-4095. DOI: 10.1002/adma.200700445.

- [149] William J. Scheideler et al. “Gravure-Printed Sol?Gels on Flexible Glass: A Scalable Route to Additively Patterned Transparent Conductors”. In: *ACS Applied Materials & Interfaces* 7.23 (2015), pp. 12679–12687. ISSN: 1944-8244. DOI: 10.1021/acsami.5b00183.
- [150] *Screen Printing Overview: Basic Mesh Materials*. Web Page. 2016.
- [151] Tsuyoshi Sekitani et al. “Stretchable active-matrix organic light-emitting diode display using printable elastic conductors”. In: *Nat Mater* 8.6 (2009), pp. 494–499. ISSN: 1476-1122. DOI: [http://www.nature.com/nmat/journal/v8/n6/suppinfo/nmat2459\\_S1.html](http://www.nature.com/nmat/journal/v8/n6/suppinfo/nmat2459_S1.html).
- [152] C. W. Sele et al. “Lithography-free, self-aligned inkjet printing with sub-hundred-nanometer resolution”. In: *Advanced Materials* 17.8 (2005), pp. 997–+. ISSN: 0935-9648. DOI: DOI10.1002/adma.200401285.
- [153] Hokuto Seo et al. “A 128 96 pixel stack-type color image sensor: stack of individual blue-, green-, and red-sensitive organic photoconductive films integrated with a ZnO thin film transistor readout circuit”. In: *Japanese Journal of Applied Physics* 50.2R (2011), p. 024103. ISSN: 1347-4065.
- [154] Hokuto Seo et al. “Color sensors with three vertically stacked organic photodetectors”. In: *Japanese Journal of Applied Physics* 46.12L (2007), p. L1240. ISSN: 1347-4065.
- [155] Liang Shen et al. “A Highly Sensitive Narrowband Nanocomposite Photodetector with Gain”. In: *Advanced Materials* 28.10 (2016), pp. 2043–2048. ISSN: 1521-4095. DOI: 10.1002/adma.201503774.
- [156] N. Shin et al. “Effect of Processing Additives on the Solidification of Blade-Coated Polymer/Fullerene Blend Films via In-Situ Structure Measurements”. In: *Advanced Energy Materials* 3.7 (2013), pp. 938–948. ISSN: 1614-6832. DOI: DOI10.1002/aenm.201201027.
- [157] William Shockley and Hans J. Queisser. “Detailed Balance Limit of Efficiency of p?n Junction Solar Cells”. In: *Journal of Applied Physics* 32.3 (1961), pp. 510–519. DOI: [doi:http://dx.doi.org/10.1063/1.1736034](http://dx.doi.org/10.1063/1.1736034).
- [158] H. Sirringhaus et al. “High-resolution inkjet printing of all-polymer transistor circuits”. In: *Science* 290.5499 (2000), pp. 2123–2126. ISSN: 0036-8075. DOI: DOI10.1126/science.290.5499.2123.
- [159] J. Smith et al. “Solution-Processed Small Molecule-Polymer Blend Organic Thin-Film Transistors with Hole Mobility Greater than 5 cm<sup>2</sup>/Vs”. In: *Advanced Materials* 24.18 (2012), pp. 2441–2446. ISSN: 0935-9648. DOI: DOI10.1002/adma.201200088.
- [160] J. Soeda et al. “High Electron Mobility in Air for N,N ’-1H,1H-Perfluorobutyldicyanoperylene Carboxydi-imide Solution-Crystallized Thin-Film Transistors on Hydrophobic Surfaces”. In: *Advanced Materials* 23.32 (2011), pp. 3681–+. ISSN: 0935-9648. DOI: DOI10.1002/adma.201101467.

- [161] D. Soltman et al. “Methodology for Inkjet Printing of Partially Wetting Films”. In: *Langmuir* 26.19 (2010), pp. 15686–15693. ISSN: 0743-7463. DOI: Doi10.1021/La102053j.
- [162] Takao Someya et al. “Integration of organic FETs with organic photodiodes for a large area, flexible, and lightweight sheet image scanners”. In: *Electron Devices, IEEE Transactions on* 52.11 (2005), pp. 2502–2511. ISSN: 0018-9383.
- [163] Young Min Song et al. “Digital cameras with designs inspired by the arthropod eye”. In: *Nature* 497.7447 (2013), pp. 95–99. ISSN: 0028-0836. DOI: 10.1038/nature12083.
- [164] Paul A. Staniec et al. “The Nanoscale Morphology of a PCDTBT:PCBM Photovoltaic Blend”. In: *Advanced Energy Materials* 1.4 (2011), pp. 499–504. ISSN: 1614-6840. DOI: 10.1002/aenm.201100144.
- [165] RA Street et al. “Extended time bias stress effects in polymer transistors”. In: *Journal of applied physics* 100.11 (2006), p. 114518. ISSN: 0021-8979.
- [166] Robert A Street. *Technology and applications of amorphous silicon*. Vol. 37. Springer, 2000. ISBN: 3540657142.
- [167] Sarah L. Swisher et al. “Impedance sensing device enables early detection of pressure ulcers in vivo”. In: *Nat Commun* 6 (2015). DOI: 10.1038/ncomms7575.
- [168] Toshitake Takahashi et al. “Carbon nanotube active-matrix backplanes for mechanically flexible visible light and X-ray imagers”. In: *Nano letters* 13.11 (2013), pp. 5425–5430. ISSN: 1530-6984.
- [169] Yoshifumi Takanashi, Kiyoto Takahata, and Yoshifumi Muramoto. “Characteristics of InAlAs/InGaAs high-electron-mobility transistors under illumination with modulated light”. In: *IEEE Transactions on electron devices* 46.12 (1999), pp. 2271–2277. ISSN: 0018-9383.
- [170] Yuan Taur and Tak H Ning. *Fundamentals of modern VLSI devices*. Cambridge university press, 2013. ISBN: 110739399X.
- [171] S. F. Tedde et al. “Fully Spray Coated Organic Photodiodes”. In: *Nano Letters* 9.3 (2009), pp. 980–983. ISSN: 1530-6984. DOI: Doi10.1021/N1803386y.
- [172] Xiaoran Tong and Stephen R Forrest. “An integrated organic passive pixel sensor”. In: *Organic Electronics* 12.11 (2011), pp. 1822–1825. ISSN: 1566-1199.
- [173] N. D. Treat et al. “Microstructure formation in molecular and polymer semiconductors assisted by nucleation agents”. In: *Nature Materials* 12.7 (2013), pp. 628–633. ISSN: 1476-1122. DOI: Doi10.1038/Nmat3655.
- [174] Narendra S. Trivedi et al. “Effects of motion, ambient light, and hypoperfusion on pulse oximeter function”. In: *Journal of Clinical Anesthesia* 9.3 (1997), pp. 179–183. ISSN: 0952-8180. DOI: [http://dx.doi.org/10.1016/S0952-8180\(97\)00039](http://dx.doi.org/10.1016/S0952-8180(97)00039).

- [175] Hakan Usta et al. “BODIPY-Thiophene Copolymers as p-Channel Semiconductors for Organic Thin-Film Transistors”. In: *Advanced Materials* 25.31 (2013), pp. 4327–4334. ISSN: 1521-4095. DOI: 10.1002/adma.201300318.
- [176] Jonathan Viventi et al. “A Conformal, Bio-Interfaced Class of Silicon Electronics for Mapping Cardiac Electrophysiology”. In: *Science Translational Medicine* 2.24 (2010), 24ra22–24ra22. DOI: 10.1126/scitranslmed.3000738.
- [177] A. D. Vornbrock et al. “Fully gravure and ink-jet printed high speed pBTTT organic thin film transistors”. In: *Organic Electronics* 11.12 (2010), pp. 2037–2044. ISSN: 1566-1199. DOI: DOI10.1016/j.orgel.2010.09.003.
- [178] Ross D. Jansen-van Vuuren et al. “Organic Photodiodes: The Future of Full Color Detection and Image Sensing”. In: *Advanced Materials* (2016), n/a–n/a. ISSN: 1521-4095. DOI: 10.1002/adma.201505405.
- [179] Hanlin Wang et al. “Inkjet Printing Short-Channel Polymer Transistors with High-Performance and Ultrahigh Photoresponsivity”. In: *Advanced Materials* 26.27 (2014), pp. 4683–4689. ISSN: 1521-4095.
- [180] Xinyu Wang et al. “Modifying the thermal conductivity of small molecule organic semiconductor thin films with metal nanoparticles”. In: *Scientific Reports* 5 (2015), p. 16095. DOI: 10.1038/srep16095.
- [181] C. P. Watson and D. M. Taylor. “Demonstration of interfacial charge transfer in an organic charge injection device”. In: *Applied Physics Letters* 99.22 (2011), pp. –. DOI: doi:http://dx.doi.org/10.1063/1.3665190.
- [182] Lukas Wengeler et al. “Comparison of large scale coating techniques for organic and hybrid films in polymer based solar cells”. In: *Chemical Engineering and Processing: Process Intensification* 68 (2013), pp. 38–44. ISSN: 0255-2701. DOI: http://dx.doi.org/10.1016/j.cep.2012.03.004.
- [183] G. L. Whiting and A. C. Arias. “Chemically modified ink-jet printed silver electrodes for organic field-effect transistors”. In: *Applied Physics Letters* 95.25 (2009). ISSN: 0003-6951. DOI: Artn253302Doi10.1063/1.3276913.
- [184] Haihua Xu et al. “A high-sensitivity near-infrared phototransistor based on an organic bulk heterojunction”. In: *Nanoscale* 5.23 (2013), pp. 11850–11855.
- [185] Xin Xu et al. “Direct transfer patterning on three dimensionally deformed surfaces at micrometer resolutions and its application to hemispherical focal plane detector arrays”. In: *Organic Electronics* 9.6 (2008), pp. 1122–1127. ISSN: 1566-1199.
- [186] Feng Yan, Jinhua Li, and Sheung Man Mok. “Highly photosensitive thin film transistors based on a composite of poly(3-hexylthiophene) and titania nanoparticles”. In: *Journal of Applied Physics* 106.7 (2009), p. 074501. DOI: doi:http://dx.doi.org/10.1063/1.3225760.



- [187] H. Yan et al. “A high-mobility electron-transporting polymer for printed transistors”. In: *Nature* 457.7230 (2009), 679–U1. ISSN: 0028-0836. DOI: [Doi10.1038/Nature07727](https://doi.org/10.1038/Nature07727).
- [188] Y. Yao et al. “Plastic Near-Infrared Photodetectors Utilizing Low Band Gap Polymer”. In: *Advanced Materials* 19.22 (2007), pp. 3979–3983. ISSN: 1521-4095. DOI: [10.1002/adma.200602670](https://doi.org/10.1002/adma.200602670).
- [189] Gang Yu et al. “Large-area, full-color image sensors made with semiconducting polymers”. In: *Advanced Materials* 10.17 (1998), pp. 1431–1434. ISSN: 1521-4095.
- [190] Xinge Yu, Tobin J. Marks, and Antonio Facchetti. “Metal oxides for optoelectronic applications”. In: *Nat Mater* 15.4 (2016), pp. 383–396. ISSN: 1476-1122. DOI: [10.1038/nmat4599](https://doi.org/10.1038/nmat4599).
- [191] Yongbo Yuan and Jinsong Huang. “Ultrahigh Gain, Low Noise, Ultraviolet Photodetectors with Highly Aligned Organic Crystals”. In: *Advanced Optical Materials* 4.2 (2016), pp. 264–270. ISSN: 2195-1071. DOI: [10.1002/adom.201500560](https://doi.org/10.1002/adom.201500560).
- [192] Alla M. Zamarayeva et al. “Fabrication of a High-Performance Flexible Silver/Zinc Wire Battery”. In: *Advanced Electronic Materials* 2.5 (2016), n/a–n/a. ISSN: 2199-160X. DOI: [10.1002/aelm.201500296](https://doi.org/10.1002/aelm.201500296).
- [193] Hsiao-Wen Zan et al. “Amorphous indium-gallium-zinc-oxide visible-light phototransistor with a polymeric light absorption layer”. In: *Applied Physics Letters* 97.20 (2010), p. 203506. DOI: [doi:http://dx.doi.org/10.1063/1.3517506](https://doi.org/10.1063/1.3517506).
- [194] Lei Zhang et al. “Large-area, flexible imaging arrays constructed by light-charge organic memories”. In: *Scientific reports* 3 (2013).
- [195] Yifan Zheng et al. “Toward Efficient Thick Active PTB7 Photovoltaic Layers Using Diphenyl Ether as a Solvent Additive”. In: *ACS Applied Materials & Interfaces* 8.24 (2016), pp. 15724–15731. ISSN: 1944-8244. DOI: [10.1021/acsami.6b03453](https://doi.org/10.1021/acsami.6b03453).
- [196] Xiaokang Zhou, Dezhi Yang, and Dongge Ma. “Extremely Low Dark Current, High Responsivity, All-Polymer Photodetectors with Spectral Response from 300 nm to 1000 nm”. In: *Advanced Optical Materials* 3.11 (2015), pp. 1570–1576. ISSN: 2195-1071.
- [197] Y. H. Zhou et al. “A Universal Method to Produce Low-Work Function Electrodes for Organic Electronics”. In: *Science* 336.6079 (2012), pp. 327–332. ISSN: 0036-8075. DOI: [DOI10.1126/science.1218829](https://doi.org/10.1126/science.1218829).
- [198] Ute Zschieschang et al. “Dinaphtho[2,3-b:2',3'-f]thieno[3,2-b]thiophene (DNTT) thin-film transistors with improved performance and stability”. In: *Organic Electronics* 12.8 (2011), pp. 1370–1375. ISSN: 1566-1199. DOI: [http://dx.doi.org/10.1016/j.orgel.2011.04.018](https://doi.org/10.1016/j.orgel.2011.04.018).